Methods in
Molecular Biology 1251

Springer Protocols

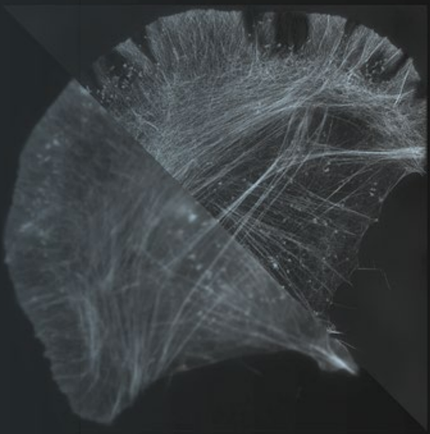

Peter J. Verveer *Editor*

Advanced Fluorescence Microscopy

Methods and Protocols

Humana Press

METHODS IN MOLECULAR BIOLOGY

Series Editor
John M. Walker
School of Life Sciences
University of Hertfordshire
Hatfield, Hertfordshire, AL10 9AB, UK

For further volumes:
http://www.springer.com/series/7651

Advanced Fluorescence Microscopy

Methods and Protocols

Edited by

Peter J. Verveer

Department of Systemic Cell Biology, Max Planck Institute of Molecular Physiology,
Dortmund, Germany

Humana Press

Editor
Peter J. Verveer
Department of Systemic Cell Biology
Max Planck Institute of Molecular Physiology
Dortmund, Germany

ISSN 1064-3745 ISSN 1940-6029 (electronic)
ISBN 978-1-4939-2079-2 ISBN 978-1-4939-2080-8 (eBook)
DOI 10.1007/978-1-4939-2080-8
Springer New York Heidelberg Dordrecht London

Library of Congress Control Number: 2014953904

© Springer Science+Business Media New York 2015
This work is subject to copyright. All rights are reserved by the Publisher, whether the whole or part of the material is concerned, specifically the rights of translation, reprinting, reuse of illustrations, recitation, broadcasting, reproduction on microfilms or in any other physical way, and transmission or information storage and retrieval, electronic adaptation, computer software, or by similar or dissimilar methodology now known or hereafter developed. Exempted from this legal reservation are brief excerpts in connection with reviews or scholarly analysis or material supplied specifically for the purpose of being entered and executed on a computer system, for exclusive use by the purchaser of the work. Duplication of this publication or parts thereof is permitted only under the provisions of the Copyright Law of the Publisher's location, in its current version, and permission for use must always be obtained from Springer. Permissions for use may be obtained through RightsLink at the Copyright Clearance Center. Violations are liable to prosecution under the respective Copyright Law.
The use of general descriptive names, registered names, trademarks, service marks, etc. in this publication does not imply, even in the absence of a specific statement, that such names are exempt from the relevant protective laws and regulations and therefore free for general use.
While the advice and information in this book are believed to be true and accurate at the date of publication, neither the authors nor the editors nor the publisher can accept any legal responsibility for any errors or omissions that may be made. The publisher makes no warranty, express or implied, with respect to the material contained herein.

Printed on acid-free paper

Humana Press is a brand of Springer
Springer is part of Springer Science+Business Media (www.springer.com)

Preface

The fluorescence light microscope has become a common tool in the life sciences, with broad applications in many fields of biology. Recent decades have seen a rapid development in the field, with the introduction of many new techniques to visualize and quantify biological samples at a molecular level.

This book aims to provide an overview of the advanced methods in fluorescence microscopy that have found application in biology, or that are promising to become essential tools in the future. Each chapter focuses on a different method and attempts to provide a practical guide for application in biological systems.

With this book we attempted to cover a broad range of advanced fluorescence microscopy methods. In several cases, the instrumentation that is needed might not be easily available to the biologist, due to their novelty. In these cases, we have attempted to provide instructions for building such equipment, along with protocols for their application.

For some time now, fluorescence microscopy has been a standard tool for the molecular biologist in such fields as cell biology, neurobiology, and development biology. As they become more readily available, the new tools described here will be of tremendous use to those same scientists. We hope that this book will help them to apply these methods in the biological systems that they are interested in.

Dortmund, Germany ***Peter J. Verveer***

Contents

Contributors

NARIMAN ANSARI • *Physical Biology Group, Buchmann Institute for Molecular Life Sciences (BMLS), Goethe Universität Frankfurt am Main, Frankfurt am Main, Germany*
NINA BEIL • *BioQuant, ViroQuant-CellNetworks RNAi Screening Facility, Ruprecht-Karls-Universitat Heidelberg, Heidelberg, Germany*
JÜRGEN BENEKE • *BioQuant, ViroQuant-CellNetworks RNAi Screening Facility, Ruprecht-Karls-Universitat Heidelberg, Heidelberg, Germany*
ULRIKE ENDESFELDER • *Institute of Physical and Theoretical Chemistry, Goethe University, Frankfurt am Main, Germany*
HOLGER ERFLE • *BioQuant, ViroQuant-CellNetworks RNAi Screening Facility, Ruprecht-Karls-Universitat Heidelberg, Heidelberg, Germany*
BART GEVERTS • *Department of Pathology, Josephine Nefkens Institute, Erasmus Optical Imaging Centre, Erasmus MC, Rotterdam, The Netherlands*
MANUEL GUNKEL • *BioQuant, ViroQuant-CellNetworks RNAi Screening Facility, Ruprecht-Karls-Universitat Heidelberg, Heidelberg, Germany*
MIKE HEILEMANN • *Institute of Physical and Theoretical Chemistry, Goethe University, Frankfurt am Main, Germany*
MARK A. HINK • *Department Molecular Cytology, van Leeuwenhoek Centre for Advanced Microscopy (LCAM), University of Amsterdam, Amsterdam, The Netherlands*
ADRIAAN B. HOUTSMULLER • *Department of Pathology, Josephine Nefkens Institute, Erasmus Optical Imaging Centre, Erasmus MC, Rotterdam, The Netherlands*
JANA HÜVE • *Laboratory of Mass Spectrometry and Gaseous Ion Chemistry, The Rockefeller University, New York, NY, USA*
KEES JALINK • *Cell Biophysics Group, Department of Cell Biology B5, The Netherlands Cancer Institute, Amsterdam, The Netherlands*
MARTIN KAHMS • *Laboratory of Mass Spectrometry and Gaseous Ion Chemistry, The Rockefeller University, New York, NY, USA*
KATARZYNA M. KEDZIORA • *Cell Biophysics Group, Department of Cell Biology B5, The Netherlands Cancer Institute, Amsterdam, The Netherlands*
SATYAJIT MAYOR • *National Centre for Biological Science, Bangalore, India*
AMAYA MIQUELAJAUREGUI • *Department of Neurology, David Geffen School of Medicine at UCLA, Los Angeles, CA, USA*
RICARDO MOSTANY • *Department of Neurology, David Geffen School of Medicine at UCLA, Los Angeles, CA, USA*
FRANCESCO PAMPALONI • *Physical Biology Group, Buchmann Institute for Molecular Life Sciences (BMLS), Goethe Universität Frankfurt am Main, Frankfurt am Main, Germany*
AMMASI PERIASAMY • *W.M. Keck Center for Cellular Imaging, Biology, University of Virginia, Charlottesville, VA, USA*
REINER PETERS • *Laboratory of Mass Spectrometry and Gaseous Ion Chemistry, The Rockefeller University, New York, NY, USA*
WILLIAM T.E. PITKEATHLY • *Physical Sciences of Imaging for the Biomedical Sciences (PSIBS) Doctoral Training Centre, University of Birmingham, Edgbaston, Birmingham, UK*

Carlos Portera-Cailliau • *Department of Neurology, David Geffen School of Medicine at UCLA, Los Angeles, CA, USA; Department of Neurobiology, David Geffen School of Medicine at UCLA, Los Angeles, CA, USA*

Natalie S. Poulter • *School of Biosciences, University of Birmingham, Edgbaston, Birmingham, UK*

Riya Raghupathy • *National Centre for Biological Science, Bangalore, India; Shanmugha Arts Science Technology and Research Academy, Thanjavur, India*

Joshua Z. Rappoport • *School of Biosciences, University of Birmingham, Edgbaston, Birmingham, UK*

E. Hesper Rego • *Department of Immunology and Infectious Diseases, Harvard School of Public Health, Boston, MA, USA*

Natalia H. Revelo • *STED Microscopy Group, European Neuroscience Institute, Deutsche Forschungsgemeinschaft Center for Molecular Physiology of the Brain/Excellence Cluster, Göttingen, Germany; International Max Planck Research School for Neurosciences, Göttingen, Germany*

Jürgen Reymann • *BioQuant, ViroQuant-CellNetworks RNAi Screening Facility, Ruprecht-Karls-Universitat Heidelberg, Heidelberg, Germany*

Roli Richa • *Physical Biology Group, Buchmann Institute for Molecular Life Sciences (BMLS), Goethe Universität Frankfurt am Main, Frankfurt am Main, Germany*

Silvio O. Rizzoli • *STED Microscopy Group, European Neuroscience Institute, Deutsche Forschungsgemeinschaft Center for Molecular Physiology of the Brain/Excellence Cluster, Göttingen, Germany; Department of Neuro- and Sensory Physiology, University of Göttingen, Göttingen, Germany*

Martin E. van Royen • *Department of Pathology, Josephine Nefkens Institute, Erasmus Optical Imaging Centre, Erasmus MC, Rotterdam, The Netherlands*

Suvrajit Saha • *National Centre for Biological Science, Bangalore, India*

Lin Shao • *Howard Hughes Medical Institute, Ashburn, VA, USA*

Hari Shroff • *Section on High Resolution Optical Imaging, National Institute of Biomedical Imaging and Bioengineering, National Institutes of Health, Bethesda, MD, USA*

Matthew Shtrahman • *Department of Neurology, David Geffen School of Medicine at UCLA, Los Angeles, CA, USA*

Philip J. Smith • *Physical Sciences of Imaging for the Biomedical Sciences (PSIBS) Doctoral Training Centre, University of Birmingham, Edgbaston, Birmingham, UK*

Ernst H.K. Stelzer • *Physical Biology Group, Buchmann Institute for Molecular Life Sciences (BMLS), Goethe Universität Frankfurt am Main, Frankfurt am Main, Germany*

Yuansheng Sun • *W.M. Keck Center for Cellular Imaging, Biology, University of Virginia, Charlottesville, VA, USA*

Kelsey Temprine • *Section on High Resolution Optical Imaging, National Institute of Biomedical Imaging and Bioengineering, National Institutes of Health, Bethesda, MD, USA*

Yi I. Wu • *Robert D. Berlin Center for Cell Analysis and Modeling, University of Connecticut Health Center, Farmington, CT, USA; Department of Genetics and Developmental Biology, University of Connecticut Health Center, Farmington, CT, USA*

TAOFEI YIN • *Robert D. Berlin Center for Cell Analysis and Modeling, University of Connecticut Health Center, Farmington, CT, USA; Department of Genetics and Developmental Biology, University of Connecticut Health Center, Farmington, CT, USA*
ANDREW G. YORK • *Section on High Resolution Optical Imaging, National Institute of Biomedical Imaging and Bioengineering, National Institutes of Health, Bethesda, MD, USA*

Chapter 1

The Physical Basis of Total Internal Reflection Fluorescence (TIRF) Microscopy and Its Cellular Applications

Natalie S. Poulter*, William T.E. Pitkeathly*, Philip J. Smith, and Joshua Z. Rappoport

Abstract

Total internal reflection fluorescence (TIRF) microscopy has gained popularity in recent years among cell biologists due to its ability to clearly visualize events that occur at the adherent plasma membrane of cells. TIRF microscopy systems are now commercially available from nearly all microscope suppliers. This review aims to give the reader an introduction to the physical basis of TIRF and considerations that need to be made when purchasing a commercial system. We explain how TIRF can be combined with other microscopy modalities and describe how to use TIRF to study processes such as endocytosis, exocytosis, and focal adhesion dynamics. Finally, we provide a step-by-step guide to imaging and analyzing focal adhesion dynamics in a migrating cell using TIRF microscopy.

Key words Total internal reflection fluorescence (TIRF), Endocytosis, Exocytosis, Focal adhesions

1 Introduction

Total internal reflection fluorescence (TIRF) microscopy, also known as evanescent wave/field microscopy, is a technique that uses a special mode of sample illumination to exclusively excite fluorophores that are within approximately 100 nm of the cover glass/sample interface. This mode of illumination is based on an evanescent field which is produced when light rays are totally internally reflected at the cover glass/substrate interface. The evanescent field does not propagate deeper into the sample; therefore, images are not contaminated with fluorescence from out-of-focus planes. As a result, TIRF microscopy provides a means of imaging fluorophores near the cover glass/substrate interface with a high signal-to-noise ratio, thus making it the current gold standard

---

*Authors contributed equally.

Peter J. Verveer (ed.), *Advanced Fluorescence Microscopy: Methods and Protocols*, Methods in Molecular Biology, vol. 1251, DOI 10.1007/978-1-4939-2080-8_1, © Springer Science+Business Media New York 2015

technique for studying events that occur at the adherent plasma membrane of cells [1]. The recent rise in the popularity of this microscopy modality in the field of cell biology has been due, in part, to the work of Daniel Axelrod. Axelrod has been key to the development and promotion of this technique and has written various reviews on the subject [2, 3]. The current availability of "off-the-shelf" objective-based TIRF systems from all major microscope companies has also facilitated its use in the cell biology laboratory, as user-friendly operation makes TIRF microscopy accessible to the general scientific population rather than confining it to those with significant amounts of optical know-how.

When imaging cultured cells, TIRF microscopy has the advantage over confocal and epifluorescence microscopy of providing high-resolution, high-contrast images of the region closest to the glass coverslip (Fig. 1) making it perfect for studying processes such as endocytosis [4–7], exocytosis [8–10], cell adhesion [11–14], and cytoskeletal dynamics [15–18].

Although there now exists numerous commercially available TIRF systems, there are still several considerations that need to be taken into account before purchasing a system to ensure that you meet the requirements of your experiment and achieve the desired image quality.

Most commercially available TIRF microscopes use a "through-the-objective" optical configuration (we describe this and its alternative below). One of the most important considerations for this type of setup is the choice of the objective lens used. High numerical aperture (NA) lenses are always desirable for high-resolution optical microscopy, as they ultimately determine the "resolving power" of a system due to Abbe theory of imaging [19]. It is generally agreed in the literature that the physical minimum for an objective-based TIRF setup is 1.40 NA, but in practice, 1.45 NA is usually the smallest used. The reasons for this are described in detail in the "objective-based TIRF" section. Usually the cost of an objective lens increases with the numerical aperture (NA) of the lens. Therefore, choosing the correct objective for your application, while considering cost implications, is a significant factor when designing your TIRF system.

Another import element that will affect the image quality is the type of camera chosen. Factors influencing camera performance are described in detail in Millis [20], but the main points are summarized here. Monochromatic charge-coupled devices (CCDs) are generally preferable over color-based CCDs. Cameras come with different bit depths; a higher bit depth means that a greater number of gray levels can be detected, increasing dynamic range of intensity measured. For example, a 12-bit camera in our system gives $2^{12} = 4{,}096$ gray levels. If imaging speed is an important factor in your research, an electron-multiplying CCD (EM-CCD) may be more appropriate. EM-CCDs are much more sensitive to low light and therefore allow exposure times to be reduced, allowing

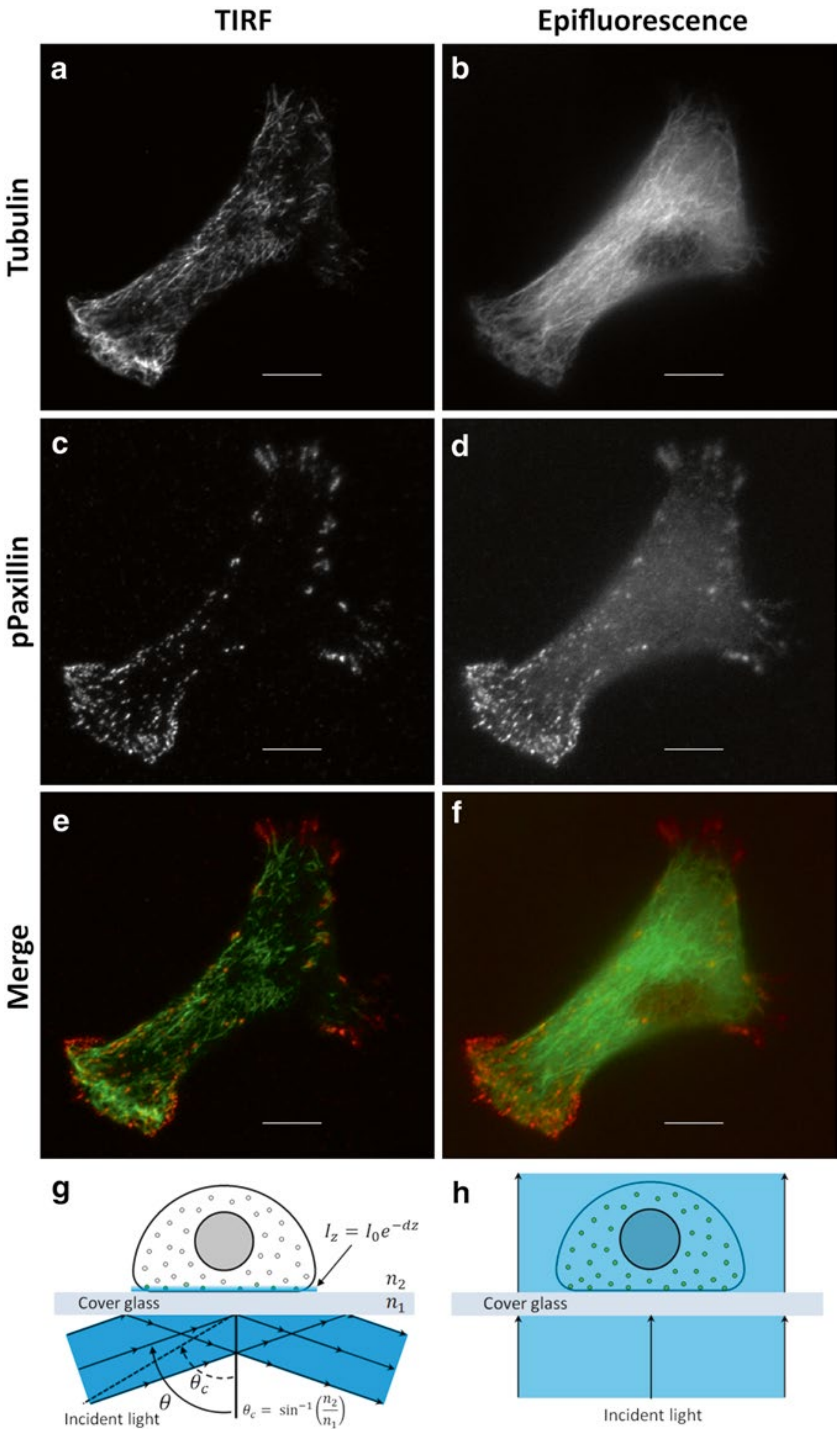

Fig. 1 TIRF versus epifluorescence imaging. A fixed MDA-MB-231 breast cancer cell labeled for alpha-tubulin (**a**, **b**) and phospho-paxillin (**c**, **d**). TIRF imaging (**a**, **c**) results in a much higher signal-to-noise ratio for both structures compared to epifluorescence imaging (**b**, **d**) which has a hazy appearance. Scale bar: 10 μm. (**g**, **h**) Show the illumination schematics for TIRF (**g**) and epifluorescence (**h**)

faster imaging and also reducing photobleaching of the sample. The physical pixel size of EM-CCDs is typically larger than those in standard CCDs, and hence, the resolution of the resulting images is lower. To compensate for this, higher magnification objectives, e.g., 150×, may have to be used to ensure that optical images are sampled above the Nyquist criteria. EM-CCDs are also very expensive and are easily damaged by relatively intense light signals or prolonged low-intensity light signals.

Many applications of TIRF require imaging of more than one color, for example, imaging dynamics of a receptor where the receptor (EGFR) is labeled in green and a vesicle marker (clathrin) is in red [21]. In many other instances, simultaneous acquisition of the two colors would be beneficial as a lot of processes occur very rapidly and switching between different wavelengths might mean that any colocalization may not be detected, when it really does occur. If rapid imaging of two color samples is necessary for your application, it may be worth investing in an emission beam splitter that allows simultaneous imaging of the two colors. This separates the emitted light into two separate beams (one per color) that are each projected onto one half of the camera chip. Although the two colors are imaged simultaneously, there is the drawback that the area that can be imaged is half of that which can be obtained via sequential imaging. Therefore, whether to perform simultaneous or sequential two-color imaging will depend on what is more important to your application.

Once you have your system up and running, the next thing you need to think about is the design of your experiments. Although it is true that an image is worth a thousand words, a TIRF image of a cell without proper quantitative analysis is just a pretty picture. When planning experiments, it is necessary to think about ways to get the most data out of your image and to ensure that you really are measuring the processes that you want to study. In this chapter, we will briefly outline the physical basis of TIRF microscopy, describing the two main different optical configurations, prism- and objective-based, and also introduce another specialist TIRF technique called variable angle TIRF microscopy (VA-TIRFM). We will discuss the benefits of combining TIRF with other microscope modalities and then delve into some of the biological applications of TIRF microscopy and include important tips and tricks for setting up experiments and analyzing the imaging data.

1.1 The Physical Basis of TIRF

Every advantage of using TIRF microscopy emanates from the physical properties of the illumination method that it employs. Therefore, an understanding of the fundamental physical principles behind the formation of TIRF images is absolutely necessary to reap the full benefits of this powerful microscopy technique. This knowledge is also essential when trying to interpret and extract quantitative information from the images obtained through TIRF, as factors such as fluorophore position within the illumination field have a significant influence on the apparent intensity of its fluorescence. This section aims to provide the reader with some of the key physical concepts behind TIRF microscopy as well as important considerations for choosing the appropriate TIRF configuration for various biological applications.

TIRF microscopy relies on what is known as an evanescent field, which serves to exclusively illuminate a thin plane just above the imaging surface, i.e., a glass coverslip. The evanescent field is produced when light rays are totally internally reflected at the interface between the imaging surface and an aqueous medium. Below is a short explanation of the fundamentals of total internal reflection for dielectric media (media that does not conduct electricity; most applications of TIRF in cell biology use dielectric media).

The refractive index, n, of an optical medium tells us how electromagnetic waves, in this case visible light, propagate through it, relative to how it propagates through a perfect vacuum. It is defined as $n = c/v$, where c is the velocity of light in a vacuum and v the velocity of light in the medium. When light rays propagating through one medium (e.g., glass) meet an interface of another medium (e.g., air, water, cytosol) which has a different refractive index, the subsequent direction of the light rays is changed depending on the angle at which the light meets this interface (Fig. 2). Some of the light rays may be reflected from the interface and some may be transmitted into the second medium (Fig. 2a). If the refractive indices of both media are known, n_1 and n_2, as well as the angle of incidence, θ_1, then Snell's law gives us the angle at which light rays are transmitted and/or reflected from this interface, θ_2 Eq. 1.

$$n_1 \sin\theta_1 = n_2 \sin\theta_2 \tag{1}$$

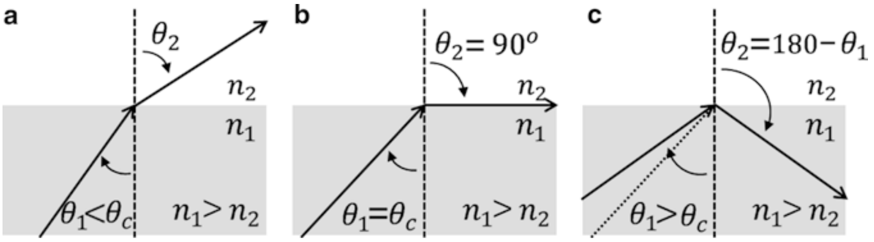

Fig. 2 Ray diagrams for the case of total internal reflection. This figure shows how the direction of light rays changes when they propagate through one medium (*gray*) and encounter an interface of a second medium (*white*), such that they experience an abrupt decrease in refractive index. (**a**) The angle of incidence is less than the critical angle. (**b**) The angle of incidence is equal to the critical angle. (**c**) The angle of incidence is greater than the critical angle

Total internal reflection occurs when the refractive index of the first medium is greater than that of the second, $n_1 > n_2$, and the angle of incidence is greater than what is known as the "critical" angle, θ_c. When the angle of incidence is equal to the critical angle, $\theta_1 = \theta_c$, light rays emerge into the second medium and propagate tangentially along the direction of the interface, or $\theta_2 = 90°$ (Fig. 2b). So Snell's law gives us: $n_1 \sin\theta_c = n_2 \sin 90°$, $\sin 90° = 1$, and therefore, $\theta_c = \sin^{-1}(n_2/n_1)$. For angles of incidence greater than θ_c, light rays are totally reflected back into the first medium (Fig. 2c).

As we have just seen, Snell's law describes which direction light rays leave a boundary between two media for a given angle of incidence, but it tells us nothing about the proportions of the light reflected and transmitted from such a boundary; Fresnel's equations must be used in for this. When Fresnel's equations are solved for the case of total internal reflection, they show that although the propagation of the light rays is totally reflected, there is still an electric component of light which crosses the boundary and, hence, still a field in the second medium. This field is known as the evanescent field, and its intensity decays exponentially with perpendicular distance from the boundary:

$$I_z = I_0 \exp\left(-z/d\right) \tag{2}$$

where I_z is the field intensity at the distance, z, from the interface, d is the decay constant of the field, and I_0 is the intensity of the field at the interface ($z = 0$).

The mathematics behind this is beyond the scope for this article, but interested readers are referred to texts [19, 22] or other good optics text books. In addition, Fresnel's equations demonstrate that there are also implications for the amplitude of an evanescent field for different polarizations of the incident light [2]. However, apart from some specialist experiments [23, 24], the effects of polarization are negligible.

1.2 Penetration Depth

The penetration depth of the evanescent field for a particular TIRF configuration is critical. Local areas of high refractive index within a sample will convert the evanescent field into scattered propagating light which will in turn contaminate images. For that reason, it is often desirable for a TIRF system to have the capability to vary the penetration depth of the evanescent field. The equation below shows what determines the penetration depth of the evanescent field:

$$d = \frac{\lambda_0}{4\pi\sqrt{n_1^2 \sin\theta_1 - n_2^2}} \tag{3}$$

This is perhaps one of the most important equations when designing TIRF-based experiments as there are severe technical/economic implications on the ability to adjust the penetration depth. It shows that the penetration depth is dependent on the wavelength of the excitation beam, λ_0; the angle of incidence of the excitation beam, θ_1; and the refractive indices of the two media: n_1 and n_2. In practice, we do not usually have much control on the refractive index of a biological sample (n_2), and we are usually confined to specific excitation wavelengths (λ_0) of a specific fluorophore once in a sample. We cannot vary the refractive index of the imaging surface once intact during an experiment (n_1). Therefore, experimentally we can only control the penetration depth through variation of the angle of incidence. However, as described below, with many commercially available TIRF objectives, the ability to vary the angle of incident light and thus penetration depth can be limited.

1.3 TIRF Configurations

When TIRF microscopy was first applied in the field of cell biology, the experimental setup consisted of a few basic components added to an inverted fluorescence microscope [25]. Since then, many different optical configurations have been designed and presented in publications, most of which fall into two categories, either prism-based or through-the-objective-based TIRF systems.

1.3.1 Prism-Based TIRF

The key to producing an evanescent field at the imaging surface/sample interface is the delivery of light rays to the interface at the correct angle of incidence. In order to get a "pure" evanescent field, all light rays must meet the interface with the same angle of incidence. A pure evanescent field is one which follows a single exponential profile Eq. 2 with a given decay constant, d. If the incident beam of light meets the interface with a spread of angles, then a field consisting of multiple evanescent fields is created, each with different penetration depths; thus, we no longer follow the profile of a single exponential. Therefore, the excitation beams must be well collimated, and the imaging surface should be as flat as possible. With the aim of imaging cell substrates, glass prisms were optically coupled to glass coverslips, to which cells were adhered, to ensure that these two conditions were met. Hence, the origin of the term "prism-based" TIRF. There are several different configurations for prism-based TIRF microscopes, the first introduced into cell biology studies by Axelrod in 1981 [25].

Although through-the-objective systems are becoming increasingly popular, there are numerous benefits of using prism-based systems. Some of these benefits include:

1. Prism-based systems are typically cost-effective as they can be constructed with "off-the-shelf" components and "home built" in a laboratory/department workshop. Thus, they are

not confined to any particular manufacturer or microscope system.

2. They usually achieve a "purer" evanescent field due to the fact that it is easy to get well-collimated light to the reflective boundary (i.e., minimal scattered light).
3. The resultant evanescent field covers the full field of view, again due to ease of focusing collimated light to the sample interface.
4. Prism-based systems can be designed and built to suit a specific purpose.

Some of the main disadvantages of prism-based systems include:

1. It is difficult to change the angle of incidence (although for simple prism-based setups, a variable angle design is demonstrated in Stock et al. [26]).
2. It is more complicated to set up each experiment as they require the imaging surface (typically a glass coverslip) to be optically coupled to the prism using substances such as glycerol.

1.3.2 Objective-Based TIRF

As the potential of TIRF was realized, and its use in cellular imaging increased, various developments were made to the technology which led to the design of the "through-the-objective"-based systems. The main advantage of this design is that the excitation light is delivered by the objective lens like most other microscopy modalities, therefore making it easier to perform experiments on a high-throughput basis.

The excitation beam is directed off-axis in the back focal plane of the objective and along the periphery of a high NA lens such that it emerges from the front aperture at a sufficiently high angle to achieve total internal reflection at the coverslip/sample interface. In objective-based TIRF systems, high NA objectives are a necessity because of the high angle of incidences required for achieving total internal reflection at the coverslip/sample interface. High NA provides the freedom of a larger range of incident angles and hence variation of penetration depth; therefore, most commercially available lenses are 1.45 and 1.49, but higher NA lenses are available. Olympus has a 100×, 1.65 NA objective which is capable of producing a very pure evanescent field at low penetration depths. The drawback of this lens is that it requires a special immersion oil (which is volatile) and expensive sapphire high refractive index coverslips to match. Fish's review has a good discussion on the NA of an objective and the range of above critical angles [27].

As stated above, in order to get a "pure" evanescent field, the incident light rays need to all meet the coverslip/sample interface at the same angle of incidence. The challenge with the objective-based systems is maintaining a well-collimated beam of light through the special confinements of the margins of the objective lens.

There are many advantages of using an objective-based TIRF system, including:

1. It is easier to use than a prism-based system as it is not restricted by the position of a prism in the setup and does not require the imaging surface to be optically coupled to a prism with a liquid such as glycerol.
2. The user is free to use different off-the-shelf imaging surfaces, i.e., microscope slides, coverslips, and glass-bottom dishes, providing that they have an appropriate refractive index.
3. Light paths can be changed at a "flick of a switch" to image with different wavelengths or imaging modalities.
4. Useful for multipoint, multi-dish, or slide experiments as the excitation and emission beams come from the same side of the objective.

Essentially, all commercially available TIRF microscopes employ objective-based TIRF. These generally allow rapid change of TIRF angle and switching between excitation beams. Some even have simultaneous dual-wavelength or multiwavelength imaging capability by exciting with two or more different wavelengths at the same time and chromatically separating the light emitted from the sample using a beam splitter. Simultaneous wavelength can be achieved in two ways: (1) Use a beam splitter combined with a right-angle prism, so that the separated light paths are projected in adjacent positions on the same CCD chip. (2) A separate CCD could be used for each light path coming from the beam splitter. The former has the obvious disadvantage of sacrificing the field of view for each channel, and the latter is considerably more expansive as it requires additional cameras.

Although through-objective TIRF systems do offer many advantages over the prism-based setups, there are also a few disadvantages:

1. The evanescent waves produced by the through-the-objective-based systems are usually less "pure" than prism-based systems. This is because more rays are scattered as the excitation beam is guided through the back focal plane of the objective than in the prism-based systems.
2. Due to the obscure path the light has to take to leave the objective at the correct angle, the resultant diameter of the beam leaving the objective is very small, typically smaller than the field of view of the microscope. Consequently, the width of the evanescent field is also less than the field of view of the microscope, and hence the image intensity is seen to drop off at the edges of images.

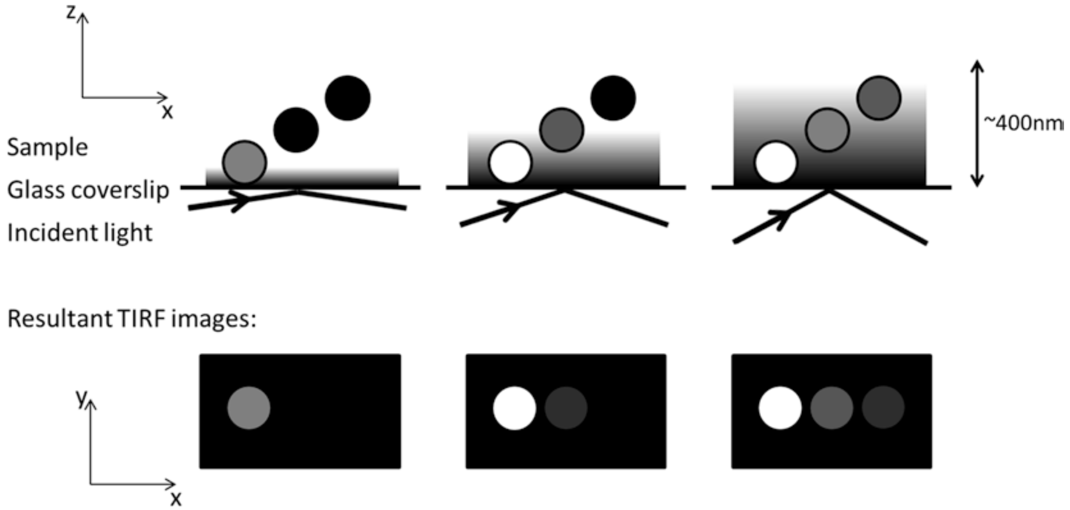

Fig. 3 Variable Angle TIRF. This figure shows how the penetration depth of the evanescent wave varies with incident angle of the incoming laser. The resultant images are shown beneath

3. The maximum angle of incidence achievable with through-the-objective systems is restricted by the NA of the objective, and therefore, smaller penetration depths are achievable with prism-based systems.
4. Purpose-built TIRF objectives are specially engineered so typically cost several thousand pounds.

1.3.3 Variable Angle TIRF Microscopy (VA-TIRFM)

Earlier we discussed the factors that influence the penetration depth of the evanescent field and gave the equation which relates them. We also point out that the only one of these we have any real control over during an experiment is the angle of incidence of the laser beam. Altering this gives us control of the penetration depth of the evanescent field providing the option of illuminating as deep or as shallow into the sample as we wish (Fig. 3), within the constraints of the system (realistically between 100 and 400 nm although 60–600 nm is theoretically possible depending on the specific setup). The technique of VA-TIRF makes possible the measurement of submicroscopic z-distances, with slices up to 10 times thinner than those achieved with a confocal scanning microscope. This allows a much finer level of detail to be resolved in in vitro studies, for example, determining distances between fluorescent probes and cell membranes [28] or the ability to map cell-substrate topology [26]. There are several ways to implement such a technique. The most common models incorporate a single or series of rotating mirrors [26, 28], though setups with an acousto-optic modulator and telecentric lens optics with wavelength-dependant deflection angles and varying image planes are also relatively common [29, 30]. As long as the optics contain a correction for movement of the exciting laser beam in the x–y plane when the angle of incidence is changed, then variable angle TIRF is possible on nearly any system.

Images obtained through this method can be interpreted in a number of different ways. In cell biological applications, qualitative measurements, when the detection of membrane-bound fluorophores is differentiated from those located in the cytosol alone, are possible as are quantitative observations based on relative levels of fluorophore excitation [31]. As of yet, we are not aware of reports of a 3D image stack being created from the images, but the theoretical framework is there.

1.4 TIRF and Other Microscopy Techniques Combined

1.4.1 Epi–TIRF

The addition of a TIRF system to a microscope leaves its optical configuration relatively unchanged; therefore, the sample is still accessible by other microscopy light paths. Most commonly, TIRF is combined with epifluorescence microscopy, due to the fact that they are both widefield techniques and use the same collection optics (filters, dichroics, CCD cameras) which makes it easy to switch between them. Epi-illumination can be achieved in one of the following two ways: (1) through use of an independent epi-light source such as a standard arc lamp light source and (2) by changing the angle of incidence from above the critical angle for TIRF to a subcritical angle such that light is no longer reflected and hence propagates into the sample. The former method is the one more commonly seen in the literature [32–34] as the mechanical switching between each excitation light path can be performed very rapidly (typically a hundreds of milliseconds, some as fast as tens of milliseconds). The latter is less popular due to the speed at which most TIRF systems can "detune" the TIRF beam and then accurately "tune" it again. However, now commercially available microscopes are being produced which can rapidly and accurately change the angle of incidence of the excitation beam for this purpose.

1.4.2 Confocal–TIRF

Combining TIRF with epifluorescence has its obvious limitations, the main being the large depth field of the epi-illumination. In order to overcome this limitation, it can be combined with confocal microscopy because of its optical sectioning capability. Images from confocal microscopes represent a much thinner cross section than epifluorescence images (~1μm compared to ~10μm) because the effective volume of the point spread function (PSF) of confocal is much smaller than that of epi. In conjunction with the sharp PSF, a pin hole is placed before the detector which prevents out-of-focus light rays from reaching the detector. Conventional point-scanning confocal microscopes use a pair of oscillating mirrors to scan the focal point of the excitation light across planar sections through the sample. Any fluorescence from the focal point is then detected using a photon multiplier tube, converted to a digital signal, and the image is recorded serially by a computer. Because images are constructed in this point-by-point manner, the acquisition time per image can be significantly greater than that of the CCD-based acquisition of epi or TIRF (e.g., ~1 s compared to ~100 ms for a 1,000 × 1,000 pixel image). As a result, it would not be possible to perform some of the same experiments which combine epi with TIRF as the distribution of fluorophores within the evanescent field can change significantly in the time it takes to acquire a confocal image. To overcome this limitation, fast confocal systems such as a resonance scanner or spinning disk configurations can be used which are capable of acquiring a 512 × 512 two-dimensional image in ~100 ms (some spinning disk systems can acquire images in less than 20 ms). Resonance scanner systems use high-temporal-resolution photon multiplier tubes and form images in the same way conventional confocal microscopes do. To facilitate colocalization studies with TIRF and resonance scanner images, their data sets must be co-registered as they will generally differ by a rotation, scale, and position within the image. A method for automated co-registration is presented in Pitkeathly et al. [35].

Spinning disk confocal microscopes use an array of micro lenses on a fast rotating disk which is used to simultaneously illuminate multiple points in the sample rather than scanning a single point across it. Images are recorded using a high-grade CCD, and in some setups, the TIRF images are acquired with the same CCD. If the same CCD is used for both light paths, then the images should already be naturally registered. However, this configuration will potentially require significant switch times to alter the light paths.

For all dual modality experiments, the limiting factor is the time it takes to switch from one modality to the other, especially in live-cell experiments. In the case of the TIRF–resonance scanner confocal combination, the switch over can take a few seconds as light paths have to be mechanically switched over. This may prohibit the use of this combination for some experiments.

1.4.3 Dual/Multicolor Experiments

As seen in Eq. 3, the penetration depth is also dependent on wavelength. Hence, when performing simultaneous multiwavelength experiments, this needs to be taken into consideration. If two different excitation wavelengths of light are being used simultaneously, and delivered at the same angle of incidence, then the evanescent field corresponding to the light with the longer wavelength will penetrate deeper into the sample. Moreover, some experiments may require that the penetration depth of both wavelengths of light used to be precisely the same. In this case, the angle of incidence of light of each excitation beam will have to be different. Commercially available microscopes such as the Olympus cell$^{\mathrm{TIRF}}$ microscope are able to control the angle of incidence of each excitation beam independently.

1.4.4 Other Considerations

Some experiments may require precise knowledge of the penetration depth and the profile of the evanescent field. Although the theoretical profile of the evanescent field is described as an exponential function for a given angle of incidence, in practice, this is often not the case. Not all light rays arrive at the same angle of incidence because of scattering on route to the objective lens; therefore, the field is a mixture of exponential functions. Mattheyses and Axelrod developed a method for determining these experimentally [36], and they found that a function consisting of two exponentials accurately described the profile of the field in their through-the-objective-based apparatus.

1.5 Biological Applications of TIRF

1.5.1 Endocytosis

Endocytosis is the process by which a cell internalizes membrane-bound or extracellular material and there are several endocytic pathways in operation in cells [37]. The most well defined of these is clathrin-mediated endocytosis (CME). Clathrin-coated pits (CCPs) form at the plasma membrane before they are pinched off as vesicles inside the cell through the action of the GTPase dynamin [38, 39]. Fluorescently tagged clathrin and dynamin constructs have been developed and validated for use in live-cell imaging studies [40, 41]. The unique properties of TIRF microscopy make it ideal for studying endocytic events [4, 42, 43]. When cells express fluorescently labeled clathrin, the CCPs appear as spots at the cell surface. As clathrin-coated vesicles (CCVs) form, they are still seen at the plasma membrane, but as they are pinched off and moved into the cell, and therefore out of the TIRF field, they seem to "disappear" (Fig. 4). If you want to ascertain if your protein of interest is really undergoing endocytosis, there are various criteria that need to be met [44]. Firstly, the putative endocytic event must be seen to disappear over successive frames and not move laterally out of the field of view. To ensure that this can be detected, you must make sure that you are imaging frequently enough to capture the endocytic process. We tend to image with "no delay." This means that if the exposure time was set to 400 ms, then the camera will take an image every ~400 ms. This mode of camera capture is called streaming and occurs through continuous "frame grabbing" from the CCD chip. Secondly, appropriate controls are needed to verify that a spot disappearing from the TIRF field is due to an endocytic event and not photobleaching.

To ensure that events of endocytosis are not actually misidentified occurrences of photobleaching, it is important to quantify the intensity of other neighboring spots in the field of view (Fig. 4b, c). If the intensity of the spot of interest decreases over the period of analysis but a nearby spot shows no change in intensity, then you can be fairly sure that photobleaching is not playing a role in spot disappearance. Another way of checking that a spot is being endocytosed is if it disappears from the TIRF image but is still visible in an epifluorescence image, indicating that it has moved further than

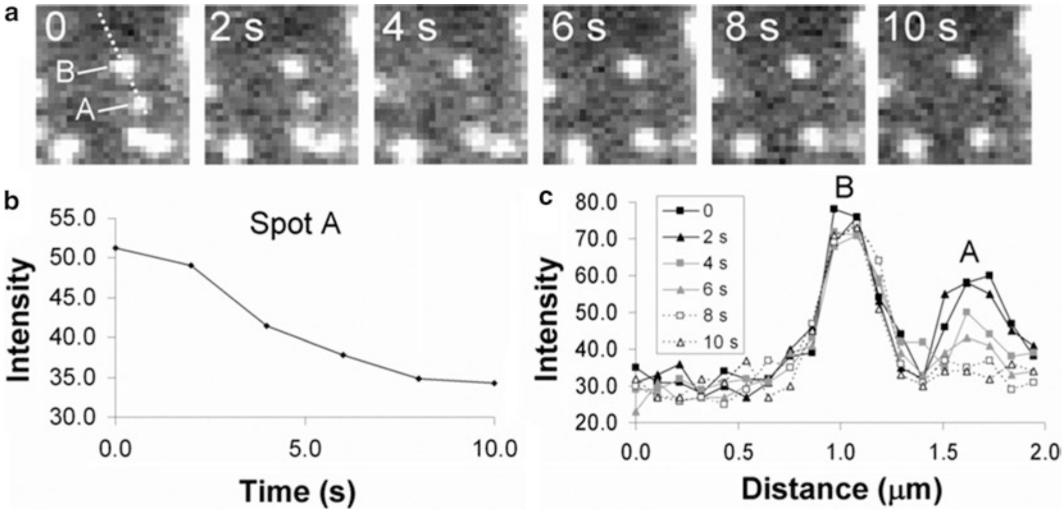

Fig. 4 Quantifying endocytosis. A clathrin-coated pit labeled with clathrin-dsRed (spot A) is seen to disappear from the TIRF field over time (**a**). A neighboring CCP (spot B) does not disappear and serves as a control for photobleaching. Quantification of the fluorescence intensity of both spots is shown in the graphs below. (**b**) shows the total intensity of spot A decreases over time and (**c**) shows the intensity of spots A and B taken across the dotted line shown in (**a**). The intensity of spot B remains unchanged throughout the imaging so the disappearance of spot A is due to endocytosis and not photobleaching. This research was originally published in Biochemical Journal, J.Z. Rappoport, focusing on clathrin-mediated endocytosis. Biochemical Journal. 2008; 412: 415–423 © the Biochemical Society

100 nm into the cell. This has been used in various studies [6, 45, 46], but as the TIRF and epi images are generally not taken at the same time, care needs to be taken in subsequent analysis. Additionally, if your protein of interest is undergoing endocytosis, then it should colocalize with other markers of endocytosis and its internalization/disappearance from the TIRF field should be coincident with the disappearance of these independent endocytic markers. As mentioned previously, fluorescently tagged clathrin and dynamin constructs have been developed and these can be used in combination with your protein of interest to see if they colocalize and disappear together. Dynamin is also involved in some clathrin-independent endocytic pathways, so it may be a good marker to use if your protein is not internalized via CME. However, in our opinion, the gold standard for scoring a bona fide event of endocytosis depends upon the observation that an extracellular soluble ligand which has bound to a receptor on the cell surface internalizes at the same time, place, and rate as your intracellular endocytic markers. In one example, we incubated cells in transferrin (Tf), the ligand for the Tf receptor, which is internalized by CME, and simultaneously imaged clathrin and Tf entering the cell [5]. The co-disappearance of the endocytic marker within the cell (clathrin) with a soluble ligand placed outside the cell (Tf) clearly demonstrates that endocytosis was occurring in these cells.

1.5.2 Exocytosis

Exocytosis occurs when an intracellular vesicle fuses with the plasma membrane, releasing its contents to the extracellular environment [47]. Exocytosis is important for many processes such as insertion of particular receptors at defined areas of the plasma membrane, release of neurotransmitters at the pre-synaptic terminal, and removal of waste products from the cell. TIRF microscopy is ideal for studying exocytosis as the evanescent wave decays over a distance that is roughly the same thickness as a secretory vesicle [48], so as the vesicles move towards the plasma membrane, they are seen to get brighter. Again, certain criteria must be met to ensure that a true exocytic event is occurring as there have been instances where dyes that accumulate in vesicles previously used to show exocytic events (e.g., acridine orange (AO)) have not been appropriately employed. The "flash" of increased intensity previously thought to depict fusion of an AO-labeled vesicle with the membrane actually can be due to rupture of the vesicle carrying the dye triggered by photodamage caused through imaging [48, 49]. As a result, an integral membrane protein is deemed to be better for visualizing exocytosis as its diffusion in the membrane is slower (2D, rather than 3D). Thus, it is both easier to visualize and to quantify a membrane protein moving laterally within a membrane rather than a soluble protein diffusing in solution. Figure 5 shows the exocytosis of a GFP-tagged transferrin receptor (TfR-GFP) in HeLa cells. The vesicle carrying the receptor can be seen to get brighter as it nears the plasma membrane and moves deeper into the evanescent wave. In this instance, the GFP tag is intraluminal, and as GFP fluorescence is partially quenched at low pH, when fusion begins and the acidic vesicle interior is neutralized by the extracellular medium, the fluorescence intensity is observed to peak at the onset of fusion. The fluorescence intensity then starts to decline as the TfR-GFP spreads out into the plasma membrane, increasing the width of the intensity profile as this lateral diffusion continues.

Strict quantitative criteria have been set out by the laboratory of Sanford Simon to explicitly demonstrate the delivery of membrane-associated cargo to the cell surface via exocytosis [48, 50], and this should be applied to confirm a suspected exocytic event. These criteria are based upon the fact that while the total intensity of the cargo from within the fusing vesicle will not change immediately post-fusion, the area of that signal will. However, it must be emphasized that the speed of acquisition is critical for imaging exocytosis. From Fig. 5, you can see that this exocytic event is completed within just over 1 s so imaging needs to be as rapid as possible. Simultaneous dual-color imaging is also useful when studying exocytosis. To confirm that your protein is involved in exocytosis, it is good practice to co-express it with known markers of exocytosis such as the soluble protein neuropeptide Y (NPY) and the membrane protein vesicular stomatitis virus glycoprotein

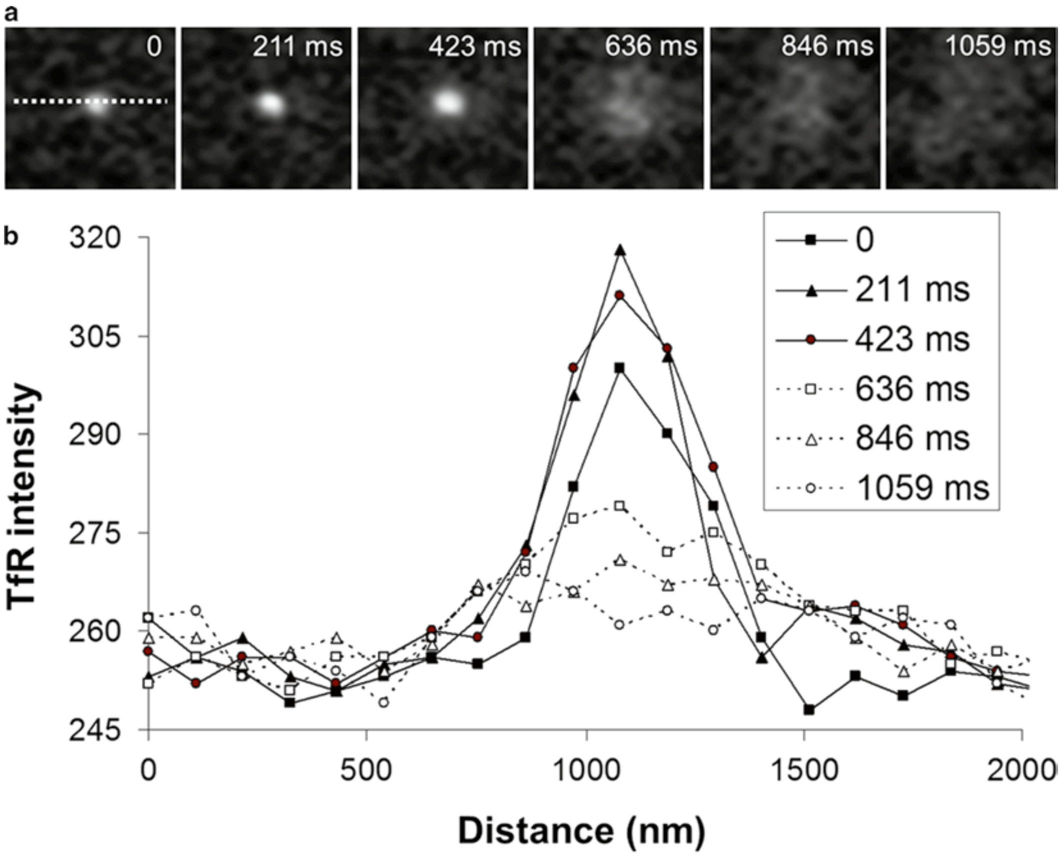

Fig. 5 Analyzing exocytosis by TIRF. (**a**) A TIRF timelapse showing a vesicle carrying transferrin receptor (TfR)-GFP fusing with the plasma membrane. (**b**) Quantification of the GFP intensity across the dotted line shown in (**a**) over time. As the vesicle fuses with the plasma membrane, the fluorescence intensity peaks and then declines as the receptor diffuses within the plane of the membrane

(VSVG), tagged with a different color to your protein of interest. This type of analysis was carried out by Grigoriev et al. [10] in a study looking at the role of Rab6 in exocytosis. You can then use TIRF to quantify colocalization and time of appearance and fusion with the membrane of the two proteins to confirm whether exocytosis is occurring. As exocytosis is a rapid process, sequential acquisition of the two colors would not be appropriate in this instance as the events would be completed before the filters had time to move into place and any colocalization would be missed.

1.5.3 Focal Adhesion Dynamics

Focal adhesions (FAs) are large, multiprotein complexes that act to link the actin cytoskeleton of cells to the extracellular matrix through heterodimeric transmembrane proteins called integrins [51, 52]. Regulation of these structures is important for cell migration; new focal contacts form at the front of migrating cells, and these can either be quickly turned over or can mature into more stable FAs that allow the cell to transmit traction forces (through the actin cytoskeleton) to the ECM and vice versa [53]. FAs need to be disassembled at the back of the cell so the rear can be retracted and the cell can move forward. As FAs form at the adherent cell membrane, they are best visualized through the use of TIRF microscopy to eliminate unwanted signal that might obscure their pattern and position in the cell. Any treatment that affects cell migration, be it through genetic means or application of a pharmaceutical agent, could be acting on the formation or disassembly of FAs in the cell and this is often a topic of investigation. For example, inhibiting CME in fibroblast cells resulted in a reduction in cell migration and prevented efficient disassembly of FAs in these cells [54]. The effect of a treatment on FAs can be assessed by measuring the intensity, the size, and the position of the FAs in the cell over time. However, using the intensity and size of a structure in a TIRF image is perhaps not the best measurement because other factors can affect them. The number of fluorophores in a structure will affect the intensity, as will the position of the fluorophore in the *z*-direction. Objects closer to the coverslip appear brighter and bigger than those further away, and due to the sensitivity of TIRF, even nanometer differences in vertical position can cause noticeable changes in intensity. Thus, FA turnover (the time it takes for an FA to form and then disassemble) is generally the most direct measure of FA dynamics. Figure 6 shows a FA labeled

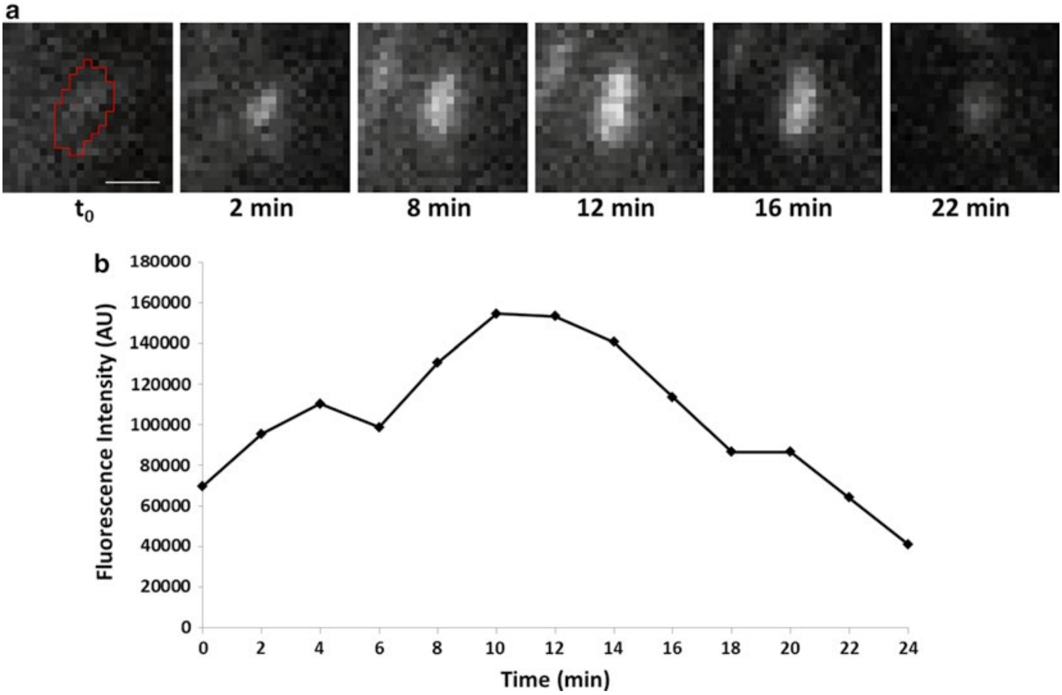

Fig. 6 Focal adhesion turnover. (**a**) A focal adhesion (FA) labeled with paxillin-RFP forming, maturing, and disassembling in an MDCK migrating at a wound edge seen via TIRF microscopy. (**b**) Quantification of the total fluorescence intensity of the FA over time. The region being measured is shown as a red ROI in the first image in (**a**)

with paxillin-RFP in an MDCK migrating in a wound healing assay. A FA can be manually identified and a region of interest (ROI) drawn around it. Information such as area and intensity can be taken from the ROI for each time point and plotted in a graph to show how the FA increases in size and intensity over time before decreasing as it disassembles. The absolute size and intensity cannot be determined due to the reasons detailed above, but they give an indication of any relative differences over time, and in combination with the time scale, comparisons between treatments can be made. It should be noted though that slower moving cells may have decreased FA turnover rates; thus, perturbations that affect FA dynamics may represent indirect effects.

Manual analysis of FA turnover is laborious and subject to bias as the FA chosen to be analyzed is often the biggest and easiest to identify. Thus, these FAs may not be representative of the population. As such, automated FA detection programs have been developed that allow the identification, tracking, and analysis of various FA properties over time, and one from the Gomez lab has been made publically available at http://gomezlab.bme.unc.edu/tools [11]. An additional advantage of automated tracking over manual identification is that a large number of FAs can be identified and analyzed, increasing confidence in the results seen. If an automated program does not work on your data sets, it is important to manually analyze as many FAs as possible within each cell. In the next section of this chapter, we will provide a step-by-step guide to imaging focal adhesion dynamics on a Nikon TIRF system using the breast cancer MDA-MB-231 cells migrating in a scratch wound assay as an example.

2 Materials

2.1 Biological

1. MDA-MB-231 cells from the Health Protection Agency Cell Culture Collection.
2. Complete medium: DMEM (Lonza), 10 % fetal calf serum (FCS) (Labtech International), 1 % penicillin/streptomycin (Gibco).
3. 1× trypsin (Gibco).
4. Lipofectamine 2000 (Invitrogen).
5. Paxillin-RFP construct (courtesy of Dr. Maddy Parsons, King's College London).
6. Cell imaging medium (CIM): Hanks balanced salt solution (HBSS; Sigma) dissolved into 10 mM HEPES at pH 7.4, with FCS at 5 % (V/V).
7. Neubauer cell counting chamber.
8. 35 mm glass-bottomed imaging dishes (MatTek Corporation, USA).

2.2 Hardware

1. Nikon TIRF system based on a Nikon Eclipse Ti inverted microscope, utilizing illumination through the microscope objective (CFL Plan Apo 60× NA 1.49, Nikon).
2. Microscope incubator (Okolab S.r.l) set at 37 °C for live-cell imaging.
3. Green diode 561 nm laser.
4. 12-bit iXon 1 M EM-CCD camera.
5. Nikon NIS-Elements Advanced Research v3.2 software.

3 Methods

1. Trypsinise a T75 flask of MDA-MB-231 cells and count the number of cells per 1 ml using a counting chamber. Seed 6×10^5 cells onto each 35 mm glass bottom dish and incubate in complete medium at 37 °C, 5 % CO_2 for 24 h.
2. On day 2, transiently transfect cells with paxillin-RFP using Lipofectamine 2000 according to the manufacturer's instructions using a ratio of 4 μg DNA to 10 μl Lipofectamine 2000 per 35 mm dish of cells. Remove transfection medium after 3 h to prevent cell death, replace with fresh complete medium, and leave the cells in the incubator to express the construct for 24 h.
3. On day 3, wound the confluent layer of cells using a pipette tip, remove the medium, and replace with CIM that has been pre-warmed to 37 °C (*see* **Note 1**). Before using the microscope, observing laser safety guidelines, ensure that the TIRF laser is aligned and focused for the objective you are going to use.
4. Place the dishes of cells onto the microscope stage within a microscope incubator that has been pre-warmed to 37 °C for at least several hours before imaging (*see* **Note 2**). Ensure that the glass bottom of the dish is clean and it is completely level on the microscope stage (*see* **Note 3**).
5. Using a 60× TIRF oil objective (NA 1.45) in bright-field mode, focus the cells using the course focus and then fine-tune using the extra-fine focus setting before turning on the perfect focus system (PFS).
6. Search for transfected cells at the wound edge using the 563 nm laser (for RFP) at a "detuned" angle (*see* **Note 4**).
7. Once a transfected cell has been identified gently, adjust the laser angle until TIRF has been reached (*see* **Note 5**).
8. Set the exposure time for the image; ensure that no pixels are saturated but structures are bright enough to be seen. Typical exposure times are 200–500 ms.
9. Once all the cells to be imaged have been identified and their XY positions saved, set up a timelapse (*see* **Note 6**). For focal

adhesion (FA) turnover assays, we generally image the cell every 1 min for 1 h, but this can be adjusted depending on the speed the cells are moving (i.e., faster cells need imaging more often and vice versa). Timelapse imaging files are saved automatically on the NIS-Elements software as .nd2 files.

10. Use the timelapse files to get quantitative information on FA dynamics. The ROI tool can be used to select FAs and measure their fluorescence intensity over time, indicating their assembly and disassembly rates. Other parameters such as area and number of FAs can also be determined in the NIS-Elements AR software.

4 Notes

1. If your microscope setup does not have CO_2 capabilities, then buffering the pH of the cell environment using CIM is a good alternative. Alternatively, if CO_2 is available, you can image cells in DMEM in a 5 % CO_2 atmosphere containing the appropriate supplements but *without* phenol red.
2. To minimize stage drift during the course of a timelapse experiment, it is important to ensure that the microscope incubator, and therefore the microscope components, is up to the required temperature (usually 37 °C). It helps to have the temperature probe immersed in water in the incubator as this gives a better indicator of the temperature in the dish being imaged and is also a more constant temperature so the heater will not be switching on and blowing on your samples every time there is a slight dip in temperature.
3. Any dirt or liquid on the coverslip area of the dish can hinder good TIRF imaging. Clean the coverslip with ethanol and ensure it is dry before imaging. Also make sure the imaging dish is flat and there is enough oil. If you see a circular interference pattern when imaging, remove the dish, clean the oil from objective and the dish, and apply fresh oil and ensure dish is replaced so that the coverslip is flat and try again (see Mattheyses et al. [1] for more detailed troubleshooting information).
4. Detuning the TIRF involves changing the angle of the laser so that the cells can be visualized via propagated light, in an epifluorescence-like state. This helps you to see transfected cells and also identify the edge of the wound, which is very difficult in TIRF mode.
5. TIRF is when there is no "haze" visible around the cell; generally, the cell gets dimmer as the laser angle is moved towards TIRF and then it suddenly gets brighter just before TIRF is reached. You know when you are in TIRF when all the out-of-focus light disappears and when you focus up and down only

the structures you are looking at go in and out of focus; no other fluorescent molecules deeper in the cell come into focus (i.e., only a single focal plane can be visualized). There are several websites that provide useful information on TIRF microscopy, along with interactive tutorials and example images, for example:

http://www.microscopyu.com/articles/fluorescence/tirf/tirfintro.html

http://www.olympusmicro.com/primer/techniques/fluorescence/tirf/tirfhome.html.

6. If your system has an automated XY stage and allows XY positions to be saved (i.e., allowing more than one cell to be imaged in a timelapse), make sure that the number of positions being imaged fits into the time interval between images or else you will not be imaging as frequently as you think you are.

Acknowledgments

The authors would like to acknowledge funding through BBSRC Project grant BB/H002308/1. WTEP and PJS are funded through the Physical Sciences of Imaging for the Biomedical Sciences (PSIBS) Doctoral Training Centre, and NSP is funded through British Heart Foundation New Horizons grant NH/11/6/29061. The TIRF microscope used in this research was obtained *through Birmingham Science City Translational Medicine Clinical Research and Infrastructure Trials Platform*, with support from Advantage West Midlands (AWM).

References

1. Mattheyses AL, Simon SM, Rappoport JZ (2010) Imaging with total internal reflection fluorescence microscopy for the cell biologist. J Cell Sci 123:3621–3628
2. Axelrod D (2001) Total internal reflection fluorescence microscopy in cell biology. Traffic 2:764–774
3. Axelrod D (2008) Total internal reflection fluorescence microscopy. Methods Cell Biol 89:169–221
4. Rappoport JZ, Simon SM (2003) Real-time analysis of clathrin-mediated endocytosis during cell migration. J Cell Sci 116:847–855
5. Rappoport JZ, Benmerah A, Simon SM (2005) Analysis of the AP-2 adaptor complex and cargo during clathrin-mediated endocytosis. Traffic 6:539–547
6. Merrifield CJ, Perrais D, Zenisek D (2005) Coupling between clathrin-coated-pit invagination, cortactin recruitment, and membrane scission observed in live cells. Cell 121:593–606
7. Merrifield CJ, Feldman ME, Wan L et al (2002) Imaging actin and dynamin recruitment during invagination of single clathrin-coated pits. Nat Cell Biol 4:691–698
8. Fix M, Melia TJ, Jaiswal JK et al (2004) Imaging single membrane fusion events mediated by SNARE proteins. Proc Natl Acad Sci U S A 101:7311–7316
9. Akopova I, Tatur S, Grygorczyk M et al (2011) Imaging exocytosis of ATP-containing vesicles with TIRF microscopy in lung epithelial A549 cells. Purinerg Signal 8:59–70

10. Grigoriev I, Splinter D, Keijzer N et al (2007) Rab6 regulates transport and targeting of exocytotic carriers. Dev Cell 13:305–314
11. Berginski ME, Vitriol EA, Hahn KM et al (2011) High-resolution quantification of focal adhesion spatiotemporal dynamics in living cells. PLoS One 6:e22025
12. Partridge MA, Marcantonio EE (2006) Initiation of attachment and generation of mature focal adhesions by integrin-containing filopodia in cell spreading. Mol Biol Cell 17:4237–4248
13. Fletcher SJ, Poulter NS, Haining EJ et al (2011) Clathrin-mediated endocytosis regulates occludin, and not focal adhesion, distribution during epithelial wound healing. Biol Cell 104:238–256
14. Lock FE, Ryan KR, Poulter NS et al (2012) Differential regulation of adhesion complex turnover by ROCK1 and ROCK2. PLoS One 7:e31423
15. Manneville JB (2006) Use of TIRF microscopy to visualize actin and microtubules in migrating cells. Meth Enzymol 406:520–532
16. Webb RL, Rozov O, Watkins SC et al (2009) Using total internal reflection fluorescence (TIRF) microscopy to visualize cortical actin and microtubules in the drosophila syncytial embryo. Dev Dynam 238:2622–2632
17. Dixit R, Ross JL (2010) Studying plus-end tracking at single molecule resolution using TIRF microscopy. Method Cell Biol 95:543–554
18. Gardner MK, Charlebois BD, Jánosi IM et al (2011) Rapid microtubule self-assembly kinetics. Cell 146:582–592
19. Graham-Smith SF, King TA (2000) Optics and photonics: an introduction. Wiley, Chichester, UK
20. Millis BA (2012) Evanescent-wave field imaging: an introduction to total internal reflection fluorescence microscopy. Methods Mol Biol 823:295–309
21. Rappoport JZ, Simon SM (2009) Endocytic trafficking of activated EGFR is AP-2 dependent and occurs through preformed clathrin spots. J Cell Sci 122:1301–1305
22. Born M, Wolf E, Bhatia AB (1999) Principles of optics: electromagnetic theory of propagation, interference and diffraction of light. Cambridge Univ Press, Cambridge, UK
23. Anantharam A, Onoa B, Edwards RH et al (2010) Localized topological changes of the plasma membrane upon exocytosis visualized by polarized TIRFM. J Cell Biol 188: 415–428
24. Sund SE, Swanson JA, Axelrod D (1999) Cell membrane orientation visualized by polarized total internal reflection fluorescence. Biophys J 77:2266–2283
25. Axelrod D (1981) Cell-substrate contacts illuminated by total internal reflection fluorescence. J Cell Biol 89:141–145
26. Stock K, Sailer R, Strauss W et al (2003) Variable-angle total internal reflection fluorescence microscopy (VA-TIRFM): realization and application of a compact illumination device. J Microsc 211:19–29
27. Fish KN (2009) Total internal reflection fluorescence (TIRF) microscopy. Curr Protoc Cytom Chapter 12, Unit 12.18
28. Olveczky BP, Periasamy N, Verkman A (1997) Mapping fluorophore distributions in three dimensions by quantitative multiple angle-total internal reflection fluorescence microscopy. Biophys J 73:2836–2847
29. Oheim M, Loerke D, Chow RH et al (1999) Evanescent-wave microscopy: a new tool to gain insight into the control of transmitter release. Philos T Roy Soc B 354:307–318
30. Rohrbach A (2000) Observing secretory granules with a multiangle evanescent wave microscope. Biophys J 78:2641–2654
31. Loerke D, Stühmer W, Oheim M (2002) Quantifying axial secretory-granule motion with variable-angle evanescent-field excitation. J Neurosci Methods 119:65–73
32. Weisswange I, Bretschneider T, Anderson KI (2005) The leading edge is a lipid diffusion barrier. J Cell Sci 118:4375–4380
33. Millán J, Hewlett L, Glyn M et al (2006) Lymphocyte transcellular migration occurs through recruitment of endothelial ICAM-1 to caveola-and F-actin-rich domains. Nat Cell Biol 8:113–123
34. Saffarian S, Kirchhausen T (2008) Differential evanescence nanometry: live-cell fluorescence measurements with 10-nm axial resolution on the plasma membrane. Biophys J 94: 2333–2342
35. Pitkeathly WT, Poulter NS, Claridge E et al (2011) Auto-align – multi-modality fluorescence microscopy image co-registration. Traffic 13:204–217
36. Mattheyses AL, Axelrod D (2006) Direct measurement of the evanescent field profile produced by objective-based total internal reflection fluorescence. J Biomed Opt 11: 014006
37. Doherty GJ, McMahon HT (2009) Mechanisms of endocytosis. Annu Rev Biochem 78:857–902

38. Damke H (1996) Dynamin and receptor-mediated endocytosis. FEBS Lett 389:48–51
39. Roth MG (2005) Clathrin-mediated endocytosis before fluorescent proteins. Nat Rev Mol Cell Biol 7:63–68
40. Gaidarov I, Santini F, Warren RA et al (1999) Spatial control of coated-pit dynamics in living cells. Nat Cell Biol 1:1–7
41. Cao H, Garcia F, McNiven MA (1998) Differential distribution of dynamin isoforms in mammalian cells. Mol Biol Cell 9:2595–2609
42. Rappoport JZ, Taha BW, Lemeer S et al (2003) The AP-2 complex is excluded from the dynamic population of plasma membrane-associated clathrin. J Biol Chem 278: 47357–47360
43. Yarar D, Waterman-Storer CM, Schmid SL (2005) A dynamic actin cytoskeleton functions at multiple stages of clathrin-mediated endocytosis. Mol Biol Cell 16:964–975
44. Rappoport JZ (2008) Focusing on clathrin-mediated endocytosis. Biochem J 412:415–423
45. Soulet F, Yarar D, Leonard M et al (2005) SNX9 regulates dynamin assembly and is required for efficient clathrin-mediated endocytosis. Mol Biol Cell 16:2058–2067
46. Lee D, Wu X, Eisenberg E et al (2006) Recruitment dynamics of GAK and auxilin to clathrin-coated pits during endocytosis. J Cell Sci 119:3502–3512
47. Jahn R, Südhof TC (1999) Membrane fusion and exocytosis. Annu Rev Biochem 68: 863–911
48. Simon SM (2009) Partial internal reflections on total internal reflection fluorescent microscopy. Trends Cell Biol 19:661–668
49. Jaiswal JK, Fix M, Takano T et al (2007) Resolving vesicle fusion from lysis to monitor calcium-triggered lysosomal exocytosis in astrocytes. Proc Natl Acad Sci U S A 104: 14151–14156
50. Schmoranzer J, Goulian M, Axelrod D et al (2000) Imaging constitutive exocytosis with total internal reflection fluorescence microscopy. J Cell Biol 149:23–32
51. Burridge K, Fath K, Kelly T et al (1988) Focal adhesions: transmembrane junctions between the extracellular matrix and the cytoskeleton. Annu Rev Cell Biol 4:487–525
52. Burridge K, Chrzanowska-Wodnicka M (1996) Focal adhesions, contractility, and signaling. Annu Rev Cell Dev Biol 12:463–519
53. Webb DJ, Parsons JT, Horwitz AF (2002) Adhesion assembly, disassembly and turnover in migrating cells-over and over and over again. Nat Cell Biol 4:E97–E100
54. Ezratty EJ, Bertaux C, Marcantonio EE et al (2009) Clathrin mediates integrin endocytosis for focal adhesion disassembly in migrating cells. J Cell Biol 187:733–747

Chapter 2

Two-Photon Excitation Microscopy and Its Applications in Neuroscience

Ricardo Mostany, Amaya Miquelajauregui, Matthew Shtrahman, and Carlos Portera-Cailliau

Abstract

Two-photon excitation (2PE) overcomes many challenges in fluorescence microscopy. Compared to confocal microscopy, 2PE microscopy improves depth penetration, owing to the longer excitation wavelength required and to the ability to collect scattered emission photons as a useful signal. It also minimizes photodamage because lower energy photons are used and because fluorescence is confined to the geometrical focus of the laser spot. 2PE is therefore ideal for high-resolution, deep-tissue, time-lapse imaging of dynamic processes in cell biology. Here, we provide examples of important applications of 2PE for in vivo imaging of neuronal structure and signals; we also describe how it can be combined with optogenetics or photolysis of caged molecules to simultaneously probe and control neuronal activity.

Key words 2-Photon, Axonal bouton, Calcium imaging, Channelrhodopsin, Confocal microscopy, Dendritic spine, Electroporation, Green fluorescent protein, Optogenetics, Oregon Green BAPTA, Photomultiplier tube, Synaptic plasticity, Turnover, ScanImage, Uncaging

1 Introduction

1.1 Fluorescence Microscopy

Fluorescence microscopy has emerged as the preferred tool for studying the structure and dynamics of biological systems both in vivo and in vitro. In recent decades, we have witnessed unprecedented technological advances in molecular and cellular imaging, which was fueled in large part by the discovery of fluorescent molecules that can be used to image cellular structure and the dynamics of organelles or even single proteins [1]. The sensitivity of fluorescence detection for these molecules (e.g., fluorescent proteins from a variety of aquatic invertebrate species such as jellyfish, synthetic fluorescent dyes, and quantum dots) is exquisite [2]. Chemists and molecular biologists have also modified fluorescent proteins such that individual proteins can be used to monitor changes in intracellular calcium, pH, protein–protein interactions,

Peter J. Verveer (ed.), *Advanced Fluorescence Microscopy: Methods and Protocols*, Methods in Molecular Biology, vol. 1251, DOI 10.1007/978-1-4939-2080-8_2,

or the function of single enzymes such as kinases or the ubiquitin proteasome system [1].

In parallel with these discoveries, rapid advances in fluorescence microscopy techniques have led to creative new ways to study biological processes [3]. For example, confocal microscopy allowed scientists to visualize these fluorescent molecules with improved spatial resolution, fluorescence lifetime imaging microscopy (FLIM) and Forster resonance energy transfer (FRET) led them to study protein–protein interactions and fluorescence recovery after photobleaching (FRAP) made it possible to investigate protein turnover and trafficking, to name a few. In addition, the diffraction resolution limit of light microscopy was recently broken with novel methods, such as stimulated emission depletion (STED), bringing us to a new era of super-resolution microscopy [4–6].

1.2 Two-Photon Excitation Microscopy

Besides the discovery of fluorescent proteins, perhaps the most significant advance in bio-imaging of the last 25 years was the invention, in 1990, of two-photon excitation (2PE) microscopy [7]. Since then, 2PE has become widely popular for in vivo imaging of neuronal structure because of its superior depth penetration and reduced photobleaching compared to confocal or epifluorescence microscopy [8]. Imaging deeper with 2PE is achieved by means of excitation with an infrared laser and optics that collect much of the scattered emitted light, while maintaining excellent spatial resolution. An added bonus is that 2PE greatly decreases photodamage (such as photobleaching and phototoxicity) and is therefore more compatible with experiments requiring prolonged continuous tissue illumination (e.g., calcium imaging). Both advantages make 2PE ideally suited to chronic in vivo imaging in the intact brain.

Single-photon excitation requires the absorption of a high energy photon to excite an orbital electron of a fluorophore to a vibrationally and electronically excited state (excitation; Fig. 1a). When this electron relaxes to its ground state, it emits a photon of light of a different wavelength than the excitation photon (fluorescence emission). In 2PE this process is achieved by the quasi-simultaneous absorption of two photons: the first one excites the electron to a virtual intermediate state, and the second one completes its excitation to reach the final excited state.

The main shortcoming of single-photon excitation is its inefficient fluorescence excitation: because light absorption occurs throughout much of the specimen, a pinhole in front of the detector is required in confocal microscopy to reject fluorescent photons emanating from outside the focus (Fig. 1b). Unfortunately, the pinhole similarly rejects in-focus photons that subsequently scatter, and as a result only unscattered photons contribute to the signal. This inefficiency demands high laser power for imaging, which creates unwanted photodamage [9] and limits imaging depth to the free mean path of visible light (≤100 μm in biological tissue [10]).

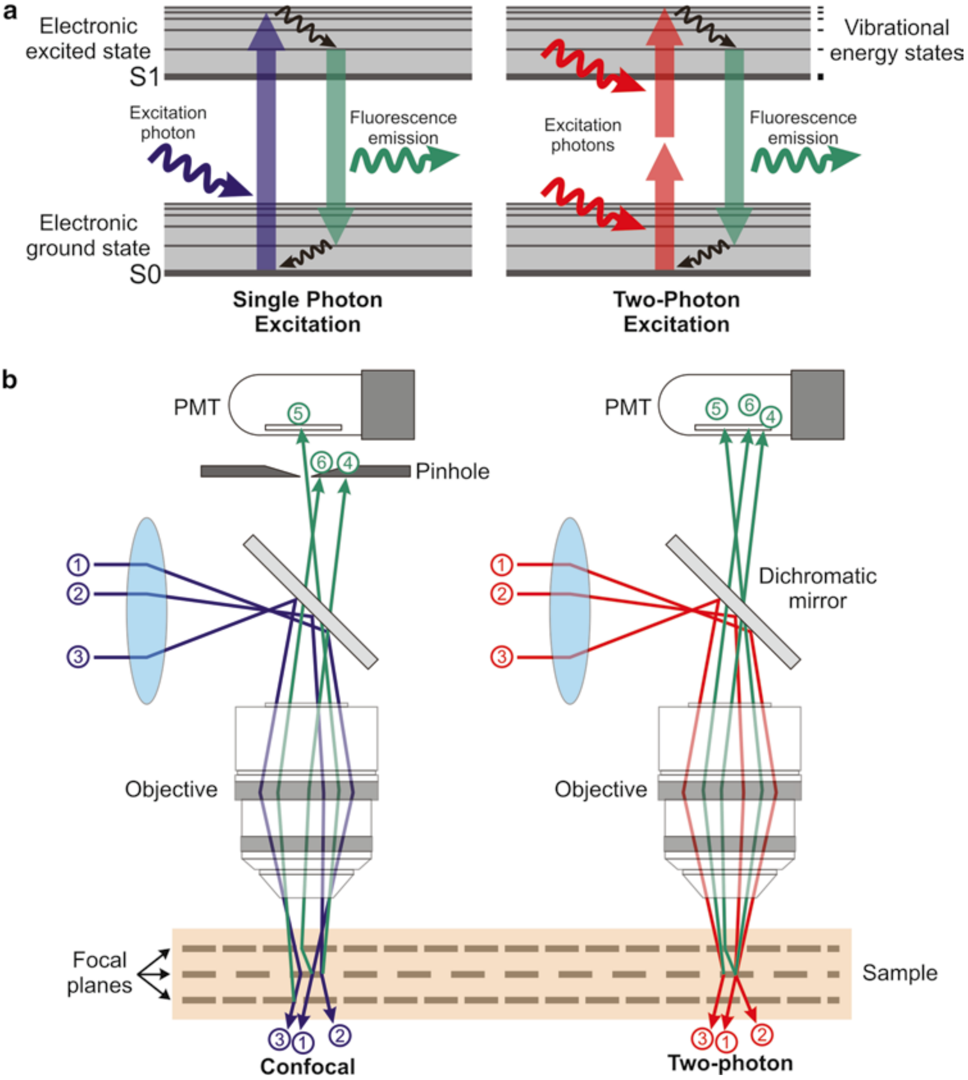

Fig. 1 Principles of 2PE microscopy. (**a**) Jablonski energy diagram showing the electron excitation process in single- (*left*) and two-photon (*right*) fluorescence microscopy. Single-photon excitation (*left*) requires the absorption of a high energy photon to excite an orbital electron of a fluorophore to a vibrationally and electronically excited state (excitation). When this electron relaxes to its ground state, it emits a photon of light of a different wavelength than the excitation photon (fluorescence emission). In 2-photon excitation (2PE; *right*), this process is achieved by the quasi-simultaneous absorption of two photons; the first one excites the electron to a virtual intermediate state, and the second one completes the excitation to reach the electronic excited state. (**b**) Confocal versus 2PE microscope systems. In confocal systems (*left*), the presence of a pinhole *right* before the photodetector rejects the photons emitted from outside the focus (e.g., photon #6), as well as those scattered on their way to the PMT (e.g., photon #4). Only unscattered photons coming from the focal plane are able to pass through the pinhole (e.g., photon #5) and contribute to the signal. In 2PE systems (*right*) there is no need for a pinhole since photons contributing to the signal come only from the geometrical focus of the excitation spot (e.g., photon #5), even if they were scattered on their path to the PMT (e.g., photon #4)

In 2PE, two lower energy photons are absorbed simultaneously to excite the fluorophore. Because of the steep dependence of absorption rate on photon concentration (light intensity), fluorescence is confined to the geometrical focus of the laser excitation spot, which provides inherent optical sectioning. A pinhole is not required because all emitted photons (regardless of how much they scatter on their path to the detector) convey a useful signal (Fig. 1b). Greater tissue penetration is possible in 2PE (compared to confocal microscopy) thanks to the longer excitation wavelength used and to the ability to collect scattered emission photons as a useful signal. These properties of 2PE also limit photodamage since the absorption is confined to a tiny focal volume, and fewer excitation events are required to achieve the same signal due to the improved collection efficiency. In addition, because 2PE microscopy requires photons of lower energy than those used in one-photon excitation, this reduces photodamage further.

2 Materials

2.1 Instrumentation: Laser and Microscope

Although commercial systems are available for multiphoton microscopy, some users may prefer to custom build their 2PE microscope (Fig. 2). Because the hardware and software needed for laser beam scanning and data acquisition in 2PE and confocal microscopy are so similar, commercial confocal systems can sometimes be converted into a two-photon microscope [11]. For further reading on configuring a 2PE system, please refer to the following resources [3, 8, 9, 12].

Mode-locked lasers are well matched to the requirements for efficient 2PE (short pulse width of 50–100 fs and high repetition rates of ~100 MHz). In particular, tunable femtosecond Ti:Al_2O_3 (titanium:sapphire) lasers are commonly used in most laboratories because the spectral range (690–1,050 nm) is sufficient to excite a wide variety of available fluorophores. Fixed wavelength mode-locked lasers in the 1,000–1,250 nm range (e.g., Nd:YLF, Yb:KYW, or Cr:forsterite) can also be used, for example, to image red-shifted fluorescent proteins [13], and they are more affordable than tunable lasers. Longer wavelengths of ~1,300 nm can be achieved when an optical parametric oscillator (OPO) is coupled to a standard Ti:Al_2O_3 laser; this configuration may be desirable to achieve deeper tissue penetration [14] or multicolor imaging [12]. Others have reached record depths of imaging using regenerative amplifiers as the excitation source, which lower the laser repetition rate and thereby increase the yield of nonlinear optical processes [10, 15].

In addition to the laser, the main components in a standard 2PE microscope are a beam expander, a fast shutter, scanning mirrors (closed loop or resonant), photomultiplier tubes (PMT), and the different optical components (e.g., scan and tube lenses, reflecting and dichroic mirrors, objective lens), needed to guide the laser beam to the sample and the emitted light to the PMTs (Fig. 2).

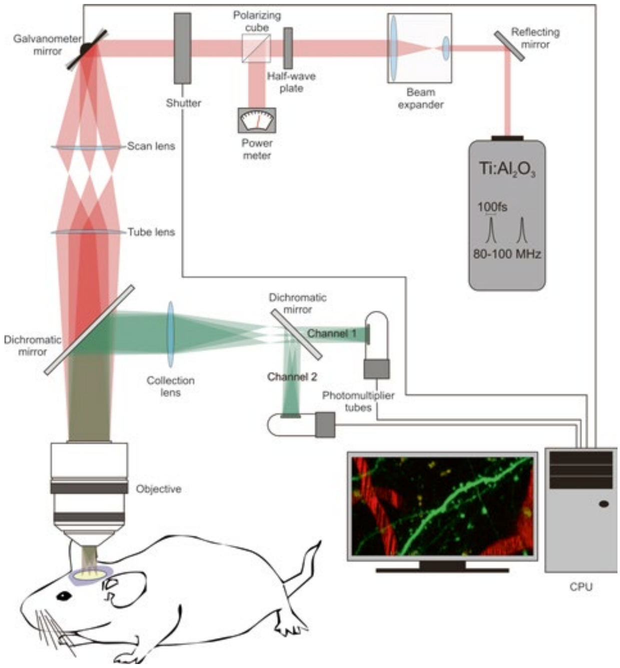

Fig. 2 Components of a 2PE microscope. The basic components of a 2PE microscope include the following elements: the two-photon laser (Ti:sapphire laser), a beam expander (the goal is to fill the back aperture of the objective lens), a half-wave plate combined with a polarizing cube to control and measure the laser power, a fast shutter to control exposure, scanning mirrors (vertical and horizontal, in this example they are closed-loop galvanometer mirrors), a scan lens, a tube lens, a dichromatic mirror, the objective, a collection lens, the photomultiplier tubes, and a CPU to integrate and control the image acquisition process

2.2 Image Acquisition and Image Processing Tools

For custom microscopes several image acquisition and image processing tools have been developed:

1. ScanImage [16] is an image acquisition application for controlling laser scanning microscopes. It was developed in MATLAB (The MathWorks, Inc.) and is currently used by >150 laboratories worldwide (https://openwiki.janelia.org/wiki/display/ephus/ScanImage). This versatile software uses simple graphical user interfaces to operate the scan mirrors

(scan speed, zoom, rotation) and define the properties of the images to be acquired (e.g., number of slices in a stack, step size), as well as settings to carry out uncaging experiments.

2. Another helpful application is ImageJ (http://rsbweb.nih.gov/ij/) and some of its plug-in collections (www.macbiophotonics.ca/imagej; http://www.uhnresearch.ca/facilities/wcif/imagej/), which are used for image processing and analysis.
3. Neurolucida (MicroBrightField, Inc.) and its confocal image stack module is a commercial software that can be used to trace and analyze complete axonal and dendritic arbors of neurons within image stacks acquired with 2PE and extract useful information (e.g., length, branching nodes, branch order, complexity index, etc.) to characterize the neuron imaged. Standard tools for analysis of calcium imaging data (*see* Subheading 3.4) are still being developed [17], and individual labs use custom routines usually written in MATLAB.

3 Methods

3.1 Making the Brain Visible for 2PE Microscopy: Fluorescent Labeling of Cells and Tissues

Both synthetic dyes and fluorescent proteins are available to image the structure of neurons and glia in the brain (e.g., tracing the dendrites and axons of particular neuronal types) or to record neuronal activity with calcium imaging. Commonly used synthetic dyes for imaging neuronal structure with 2PE include Lucifer yellow, Alexa fluor, DiI, and fluorescein. Intravascular injection of fluorescent dextrans permits the study of blood flow dynamics at the level of capillaries in the superficial layers of the cortex [18–21]. In addition, methoxy X-O4 is a fluorescent compound that crosses the blood-brain barrier and binds to amyloid plaques in mouse models of Alzheimer disease [22]. Synthetic calcium indicator dyes include Fluo-4, Fura-2, and OGB-1. Suforhodamine 101, a red dye that labels glia [23], is commonly used in calcium imaging experiments to distinguish neurons from glia.

A wide array of fluorescent proteins also exists over a rainbow palette of colors that allow an increasing number of applications [24, 25]. For example, EGFP, YFP, mCherry, and td-Tomato are frequently used for imaging neuronal structure with 2PE, while TNXXL, YC3.60, and GCaMP6 have been developed as genetically encoded fluorescent calcium indicator proteins [26–29] (*see* **Note 1**). For in vivo imaging of brain cells, specific cell subsets can be labeled with fluorescent proteins through an array of genetic methods (alone or combined). Below we discuss briefly the most commonly used methods for labeling cells for imaging with 2PE:

1. Filling cells with synthetic dyes: For live imaging of neural structure with 2PE microscopy, cells can be labeled with fluorescent dyes using Diolistics [30], by direct injection of dyes

into the brain or by filling them with a particular dye during whole-cell recordings [31]. Similarly, synthetic calcium dyes can be introduced directly into cells or electroporated using a patch pipette [32]. Alternatively, the acetoxy-methyl ester (AM) variants of dyes like Fluo-4 or OGB-1 can be bulk-loaded into the brain, which allows for recording the activity of large ensembles of neurons [33–35].

2. Transgenic and gene targeting (*see* **Note 2**): Mice engineered to express fluorescent proteins under the control of specific promoters (e.g., thy1 promoter; [36]) have been used for chronic imaging neuronal structure in vivo for a decade [37, 38]. The use of conditional gene expression (e.g., Cre-loxP, Flp-FRT) and inducible systems (e.g., Tet-ON/Tet-OFF) provides further spatial and temporal control of gene expression [39].
3. Transfection methods: In the context of live cell imaging with 2PE, nucleic acids (DNA or shRNA constructs) are most commonly introduced in neurons using plasmid electroporation or viral infection. These methods can be used in Cre mice for conditional gene activation to obtain higher labeling specificity [39]. For in vivo electroporation, the delivery of a plasmid into neurons of living mice is achieved by injecting a DNA solution into the brain (or into a single cell with patch-clamp electrophysiology) followed by short electric pulses that permeabilize cell membranes temporarily and allow plasmid entry [40]. For in utero electroporation, the DNA is injected into the cerebral ventricles in mouse embryos in order to target subpopulations of neuron precursors (e.g., layer 2/3 pyramidal neurons of the cerebral cortex) [41–43]. Recombinant viruses (e.g., adenoviruses, lentiviruses, herpes viruses) are increasingly used for gene delivery into neurons, typically via stereotaxic intracranial injections targeted to a particular brain region [44–46].

3.2 Cranial Window for In Vivo 2PE Microscopy

Two different surgical preparations, glass-covered cranial window and thinned skull, have been developed to get optical access to the brain and image structure and functionality of labeled neurons [47–50]. The cranial window preparation requires the removal of a piece of skull (leaving the dura intact), and then the craniotomy is covered with a tiny glass coverslip (Fig. 3). The thinned skull preparation requires mechanical thinning of the superficial layers of the skull, preserving a thin layer of the bone that allows imaging through it. There is also a variant of the thinned skull approach, in which the skull is thinned, polished, and ultimately reinforced with a layer of cyanocrylate glue and a cover glass [51]. With any of these methods, one can achieve sufficient spatial resolution with 2PE microscopy to detect individual dendritic spines or axonal boutons.

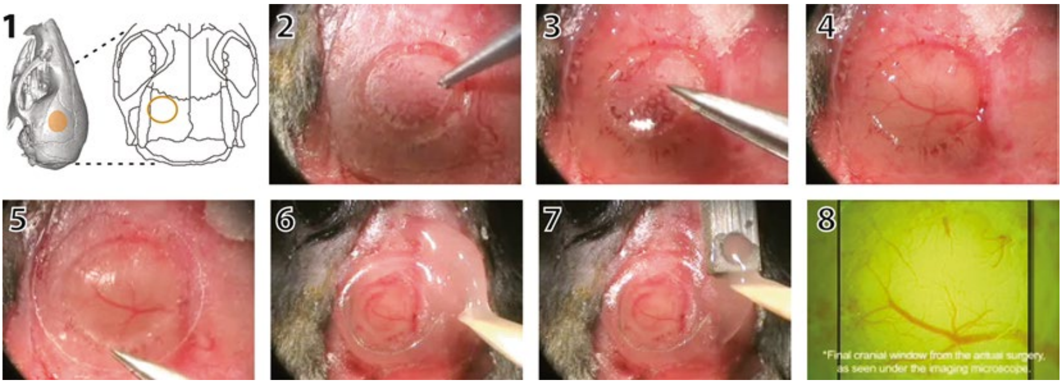

Fig. 3 Cranial window surgery for in vivo imaging with 2PE microscopy. The location of the cranial window is selected based on anatomical landmarks or functional imaging (1). In this case, the window was placed over the *left* barrel cortex. Under anesthesia, the skull is exposed, and a circular portion of the bone is gently carved with a pneumatic drill (2). Next, the bone flap is removed with small forceps (3) taking care not to damage the underlying meninges and vasculature (4). A glass coverslip is gently placed over the craniotomy (5). The edges of the glass window are sealed with cyanoacrylate glue and dental cement (6). A small well is also made around the window with dental acrylic to accommodate the objective lens and a drop of water for imaging. A titanium bar is then embedded in the dental acrylic (7), which can later be used to attach the mouse on to the microscope stage. The cortical vasculature can be seen under the microscope objective (7). Please refer to Mostany R and C Portera-Cailliau (2008) for a video of the procedure

The main advantage of the glass-covered cranial window method is that it allows for multiple imaging sessions to be conducted for longitudinal imaging of the same neuronal or glial processes within large fields of view. The cranial window approach (but not the thin skull preparation) also makes it possible to perform certain manipulations of the brain before sealing the craniotomy with a cover glass (e.g., electrode implantation, direct intracortical pharmacology, bolus loading of calcium dyes, viral injections). In addition, craniotomies are necessary for implanting gradient refractive index lenses (GRIN) in experiments that require imaging of deep brain structures [52] (*see* **Note 3**). The main drawback of the cranial window method is that it is more technically demanding as only the best preparations remain optically transparent for weeks or months, and even the slightest perturbation of the dura mater will cause a quick worsening of the quality of the imaging. Because the skull is never breached with the thinned skull technique, the incidence of infection and inflammation is minimal, and the success rate is much higher [53]. One downside of transcranial imaging is that skull thinning, which has to be repeated before every imaging session, can only been done a limited number of times (<3), or else the quality of imaging deteriorates. In this regard, the polished and reinforced preparation avoids the bone inflammation that results from repeated thinning [51].

3.3 Imaging Neuronal Structure with 2PE Microscopy

The structure and function of different cell types in the brain that express fluorescent dyes or proteins can be imaged in vivo using 2PE microscopy allowing the study of dynamic anatomical and functional changes as a result of learning and memory or in response to sensory inputs from the environment, or how they compensate for or degenerate in disease. The extraordinary resolution of the images acquired with 2PE microscopy makes it possible to observe tiny neuronal structures, such as spines and axonal boutons (~1 μm in diameter), and even quantify the turnover and trafficking of synaptic proteins (e.g., PSD95, Ras) within these structures [13, 54]. In the last decade, several studies that imaged synaptic structure in vivo with 2PE were able to record changes in synapses that were either associated with sensory experience and learning motor tasks (reviewed in [55, 56]), or triggered by stroke [18]. Chronic 2PE microscopy in vivo can also be used to image neuroglial [57] and neurovascular [51] interactions, blood flow dynamics [21, 19], and amyloid plaques [58, 59], among others. By imaging neurons in the intact brain of living mice, such longitudinal, high-resolution imaging studies of dendritic and axonal segments have provided valuable information about dynamic aspects of synapses that could not previously be examined using histological studies in fixed tissue (Fig. 4).

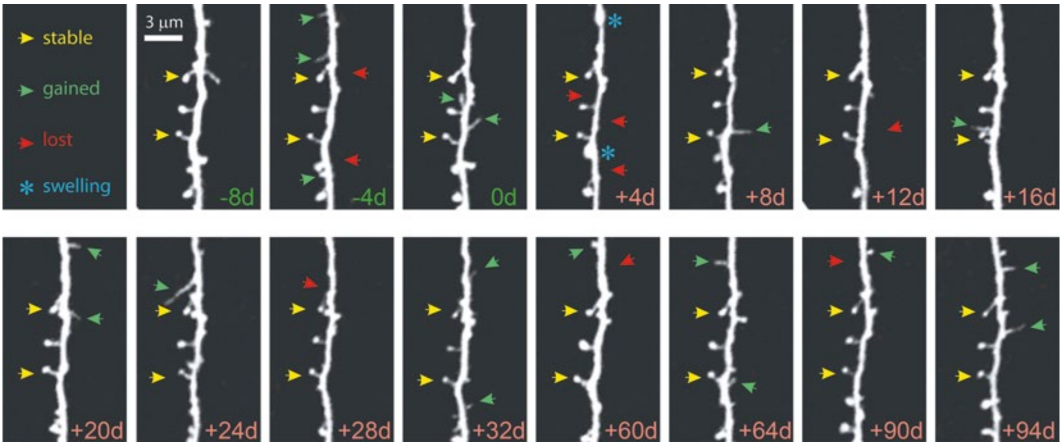

Fig. 4 Chronic high-resolution imaging of dendritic spines with in vivo 2PE microscopy. High-resolution images of dendritic spines acquired with in vivo 2PE microscopy before and after stroke. The day of imaging is shown in the *lower right-hand* corner. Shown is an apical dendritic segment from a layer 5 pyramidal neuron in peri-infarct cortex before (*green*) and after (*red*) unilateral permanent middle cerebral artery occlusion (MCAO) in mice. All images are maximum intensity projections (4–7 slices, 1.5 μm apart). A few examples of always present spines (*yellow arrowheads*), gained spines (*green arrowheads*), and lost spines (*red arrowheads*) are shown. Blue asterisks at +4 d post MCAO denote transient dendritic swelling after stroke. See Mostany et al. [18] for details

3.4 Recording Neuronal Signals with 2PE Microscopy

3.4.1 Calcium Imaging

When neurons fire action potentials, the intracellular concentration of calcium ions rises. One can record neuronal activity optically by using fluorescent dyes (or proteins) that respond to binding of calcium by changing their spectral properties (e.g., their fluorescent intensity increases or decreases, or their excitation/emission spectra change). Calcium imaging using 2PE microscopy is an ideal tool for interrogating large ensembles of neurons in the intact brain [32] because it offers advantages over traditional single unit recordings using microelectrodes. First, with calcium imaging one can record signals from hundreds (potentially thousands) of neurons simultaneously. When combined with mouse genetics to label individual subpopulations of neurons, one can also be certain of which cell types the calcium signals are being recorded from. Second, calcium imaging is less invasive, and circuits can be recorded without penetrating electrodes that might disrupt normal activity.

For calcium imaging, one can use 2PE microscopy to record calcium transients in single dendritic spines [60, 61] or to monitor the spontaneous or evoked activity of large ensembles of neurons simultaneously with single cell resolution [62–64] (Fig. 5).

Unfortunately, two-photon calcium imaging suffers from important drawbacks, such as poor temporal resolution and low signal-to-noise ratio [17, 65]. Newer generation genetically encoded calcium indicators with improved signal-to-noise will overcome

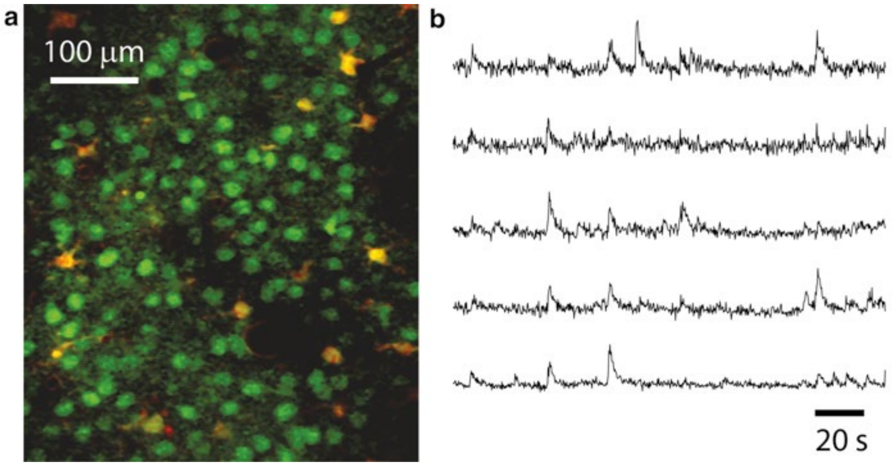

Fig. 5 Calcium imaging of neuronal ensemble activity with 2PE microscopy. (**a**) Typical field of view of layer 2/3 neurons (*green*) and glia (*yellow*) stained with the calcium indicator dye Oregon Green BAPTA-1AM and imaged with in vivo 2PE microscopy. Sulforhodamine 101 (a red dye) was used to stain glia. The image is a single frame (~120 μm below the dura) in a representative calcium imaging movie (3 min, 3.9 frames per second) from a 14-day-old mouse. (**b**) Calcium traces showing the relative changes in fluorescence intensity over the baseline fluorescence (ΔF/F) of 5 different layer 2/3 neurons from a representative calcium movie. The upward deflections represent spiking events within those neurons

some of these limitations. For example, although synthetic indicators are superior for detecting single spikes, some of the newer genetically encoded indicators (YC3.60, GCaMP6f) may detect action potentials quite reliably [66]. Importantly, recent developments in faster scanning (e.g., acousto-optical deflectors), parallelization of 2PE (e.g., multifocal multiphoton microscopy), and improved photodetectors suggest that over the next decade optical probing of neural activity with calcium imaging could eventually be an excellent alternative to electrophysiology, offering a less invasive approach to record action potential firing in large ensembles of identifiable neurons in three dimensions (*see* Subheading 4, **step 2**).

3.4.2 Voltage-Sensing Proteins

Another way to optically probe neuronal activity is to image changes in membrane potential. For this purpose several voltage-sensing proteins (e.g., FLaSh, VSFP2, SPARC, Flare, Opto-patch) have been designed that work well with 2PE microscopy and could in theory be useful to monitor the activity of thousands of individual neurons simultaneously [67–69]. These sensors are usually FRET based and can report both subthreshold changes in membrane potential and spiking activity of neurons. Unfortunately, most current approaches for voltage sensing with genetically encoded or synthetic indicators have poor spatial resolution and very low signal-to-noise ratio, requiring the averaging of many stimuli to detect responses.

3.5 Combining 2PE Microscopy with Optogenetics, Glutamate Uncaging

Another advantage of 2PE microscopy is that it can easily be combined with optogenetics and be used to uncage neurotransmitters for temporally and spatially precise manipulation and probing of neuronal activity within intact neural circuits.

3.5.1 Optogenetics

This technique enables researchers to silence or stimulate genetically specified classes of neurons (or other electrically excitable cells) with exquisite temporal precision using light-sensitive molecules [70, 71]. For example, channelrhodopsin-2 (ChR2) is a light-activated cation channel that depolarizes neurons, whereas halorhodopsin (NphR) and archaerhodopsin-3 (Arch) are a chloride channel and an outward proton pump, respectively, that enable almost complete silencing of neurons. Using optogenetic tools, cell type-specific and minimally invasive photostimulation has revealed causal relationships between activity of neuronal populations and animal behavior. In addition to evoked behaviors, electrophysiological recordings (e.g., patch-clamp or "optrodes") [72] or calcium imaging [73] can be used as the readout of neuronal activity. Thus, by combining 2PE microscopy with calcium dyes or voltage-sensitive dyes, subsets of neurons expressing optogenetic sensors could be specifically modulated with light to reveal and mimic patterns of connectivity with phenomenal temporal and spatial precision [74]. In the future, as improved red-shifted calcium indicator dyes become available, it will be easier to combine optogenetics with two-photon calcium imaging. Although optogenetic manipulations are by enlarge done with single-photon excitation, 2PE of ChR2 is possible in vivo [75], and this option may be preferable when precise stimulation of individual synapses or portions of circuits is desired.

3.5.2 Two-Photon Uncaging

The photorelease of caged, biochemically inert effector molecules (e.g., nucleotide, neurotransmitter, second messenger) can be used to control molecular interactions in cells [76]. With two-photon uncaging, the absorption energy is used to release the caged molecule, typically a neurotransmitter, from its protective chemical group, in order to mimic normal synaptic activity. The photoactivation of caged neurotransmitters has achieved synapse-specific resolution with the use of 2PE in brain tissue. By combining 2PE and uncaging (e.g., of MNI-glutamate), postsynaptic receptors of individual spines can be stimulated with excellent temporal and spatial resolution while structural and activity changes are assessed. These techniques have been successfully applied to the study of postsynaptic signaling and local circuit mapping at the level of individual dendritic spines [77–79]. An exciting recent advance was the successful stimulation of identified dendritic spines in vivo, in adult mice, using two-photon uncaging [80].

3.6 Future Directions

The invention of 2PE microscopy has revolutionized fluorescence imaging over the last 2 decades, thanks to the vision of physicists, chemists, engineers, and biologists working towards a common goal. Over the next few years, we will continue to witness unprecedented advances that lead to additional improvements in this powerful tool. In particular, developments that will enhance our ability to image deeper in the brain and with better temporal resolution in awake behaving mice will be especially useful.

3.6.1 Deeper and Brighter Imaging

Light scattering of both the near-infrared excitation wavelengths used in 2PE microscopy and of the emitted fluorescence imposes limits on how deep one can image [81]. As a result, in vivo calcium imaging with conventional 2PE has been restricted to the superficial layers of the neocortex. A variety of approaches have been established to increase the depth range for in vivo calcium imaging, including the use of high numerical aperture objectives and longer wavelengths (e.g., with fixed-wavelength laser sources or OPOs), using adaptive optics and wavefront optimization to correct for spherical aberrations and lensing effects [82, 83] or implementing ultrashort-pulsed regenerative amplifiers [15]. An alternative approach to deeper imaging is to improve on the collection of scattered fluorescent emissions that are not transmitted through the objective and would otherwise be a wasted signal, for example, by using a ring of optical fibers around the objective [84]. A different approach entirely is to use microendoscopes to reach deep brain structures, such as the hippocampus [52, 85]. In addition, signal-to-noise ratios will improve as better fluorophores become available. For calcium imaging this is a critical issue, because when faster scanning is implemented (see below), the pixel dwell time of the laser will be reduced, resulting in less signal from the indicator. Major efforts are underway to design better genetically encoded calcium indicators to solve these problems [28].

3.6.2 Faster Imaging

A major problem with calcium imaging is that it is hard to relate changes in fluorescence of the indicator molecule to neuronal spiking both in terms of determining the exact numbers of action potentials and especially the timing between them. This is due to limitations in the signal-to-noise ratio of most indicators (see above) and in the speed of acquisition. Recent solutions have been put forward to improve image acquisition speed. For example, spatiotemporal multiplexing of multibeam scanning with 2PE can improve temporal resolution and make it possible to record neurons at different depths simultaneously [86]. Alternatively, one can record only useful signals from cell bodies using targeted path scanning [87] or acousto-optical deflectors [88, 89]. Lastly, there is considerable effort in the field to shape the excitation beam to minimize or eliminate scanning, in order to rapidly excite large numbers of cells in parallel without significantly compromising the pixel dwell time. These novel geometries include the use of Bessel beams [90] and light sheets [91] to achieve thin 2PE planes perpendicular to the emission path or the implementation of spatial light modulators that shape the laser beam into an arbitrary light pattern, which allows for simultaneous imaging (or uncaging) at different locations [92] (*see* **Note 4**). Further developments in years to come will no doubt bring us closer to our goal of being able to record, with millisecond precision, the firing of thousands of neurons, distributed over a volume of brain tissue in behaving animals.

3.6.3 2PE Microscopy in Behaving Animals

An important goal of neuroscientists is to link changes in the structure and function of neuronal circuits to changes in behavior. It is therefore critically important to study these phenomena in the intact behaving animal. In the case of calcium imaging of neuronal activity, this has been accomplished by recording in head-restrained mice while they navigate virtual environments [93] or by miniaturizing 2PE microscopes into portable devices that allow investigators to image freely moving animals [84, 94].

4 Notes

1. GECIs come in two varieties: single-fluorophore sensors and sensors involving FRET between two proteins. A good example of single-fluorophore GECIs is the GCaMP family of sensors, which is composed of a circularly permuted EGFP molecule

that is flanked on one side by the calcium-binding protein calmodulin and on the other by the calmodulin-binding peptide M13. FRET-based sensors (e.g., the yellow cameleon dye YC 3.60) require a nonradiative energy transfer between an excited donor fluorophore (e.g., enhanced cyan fluorescent protein) and an acceptor fluorophore (e.g., circularly permuted Venus protein). The two fluorophores are connected by a linker sequence that is composed of a calcium-binding protein (e.g., calmodulin-M13, troponin); upon calcium binding, a conformational change in the linker protein brings the distance between the donor and acceptor fluorescent proteins to less than 10 nm, which is necessary for FRET to occur. This is reflected by a decrease in the fluorescence intensity of the donor protein (blue) and an increase in the acceptor fluorescence (green), and the calcium signal is therefore expressed as the ratio of the two.

2. Additional information on specific gene expression patterns in available mouse lines can be found in Allen Brain Atlas (http://www.alleninstitute.org), Genepaint (http://www.genepaint.org), GENSAT (http://www.gensat.org), or The Jackson Laboratory (http://jaxmice.jax.org).
3. The microendoscopy approach to image deep structures relies on the use of GRIN lenses, which use internal variations in the refractive index (as opposed to curved refractive surfaces of conventional lenses) to guide light. In essence, GRIN lenses act as an optical relay that projects the scanning pattern of the 2PE microscope to a focal plane deep inside the tissue sample. A wide array of microendoscopes is available with varying physical length, optical working distance and numerical apertures, and field of views. An important shortcoming of microendoscopy is that it is associated with some degree of tissue damage because it relies on the insertion of a GRIN lens into the brain.
4. Unfortunately, because these light-sheet approaches are currently limited in their depth penetration, it will be challenging to adapt them for live imaging in the intact rodent brain.

Acknowledgments

This work was supported by the Stein Oppenheimer Endowment Award and by grants from the US National Institutes of Health (5R01HD054453 from the Eunice Kennedy Shriver National Institute of Child Health and Human Development and 5RC1NS068093 from the National Institute of Neurological Disorders and Stroke).

References

1. Miyawaki A (2011) Proteins on the move: insights gained from fluorescent protein technologies. Nat Rev Mol Cell Biol 12:656–668
2. Eigen M, Rigler R (1994) Sorting single molecules: application to diagnostics and evolutionary biotechnology. Proc Natl Acad Sci U S A 91:5740–5747
3. Wilt BA, Burns LD, Wei Ho ET et al (2009) Advances in light microscopy for neuroscience. Annu Rev Neurosci 32:435–506
4. Hell SW, Wichmann J (1994) Breaking the diffraction resolution limit by stimulated emission: stimulated-emission-depletion fluorescence microscopy. Opt Lett 19:780–782
5. Hell SW (2003) Toward fluorescence nanoscopy. Nat Biotechnol 21:1347–1355
6. Sigrist SJ, Sabatini BL (2012) Optical super-resolution microscopy in neurobiology. Curr Opin Neurobiol 22:86–93
7. Denk W, Strickler JH, Webb WW (1990) Two-photon laser scanning fluorescence microscopy. Science 248:73–76
8. Svoboda K, Yasuda R (2006) Principles of two-photon excitation microscopy and its applications to neuroscience. Neuron 50:823–839
9. Denk W, Svoboda K (1997) Photon upmanship: why multiphoton imaging is more than a gimmick. Neuron 18:351–357
10. Theer P, Hasan MT, Denk W (2003) Two-photon imaging to a depth of 1000 microm in living brains by use of a $Ti:Al_2O_3$ regenerative amplifier. Opt Lett 28:1022–1024
11. Nikolenko V, Nemet B, Yuste R (2003) A two-photon and second-harmonic microscope. Methods 30:3–15
12. Entenberg D, Wyckoff J, Gligorijevic B et al (2011) Setup and use of a two-laser multiphoton microscope for multichannel intravital fluorescence imaging. Nat Protoc 6:1500–1520
13. Gray NW, Weimer RM, Bureau I et al (2006) Rapid redistribution of synaptic PSD-95 in the neocortex in vivo. PLoS Biol 4:e370
14. Kobat D, Durst ME, Nishimura N et al (2009) Deep tissue multiphoton microscopy using longer wavelength excitation. Nat Protoc 17: 13354–13364
15. Mittmann W, Wallace DJ, Czubayko U et al (2011) Two-photon calcium imaging of evoked activity from L5 somatosensory neurons in vivo. Nat Neurosci 14:1089–1093
16. Pologruto TA, Sabatini BL, Svoboda K (2003) ScanImage: flexible software for operating laser scanning microscopes. Biomed Eng Online 2:13
17. Grewe BF, Helmchen F (2009) Optical probing of neuronal ensemble activity. Curr Opin Neurobiol 19(5):520–529
18. Mostany R, Chowdhury TG, Johnston DG et al (2010) Local hemodynamics dictate long-term dendritic plasticity in peri-infarct cortex. J Neurosci 30:14116–14126
19. Mostany R, Portera-Cailliau C (2008) A method for 2-photon imaging of blood flow in the neocortex through a cranial window. J Vis Exp. (12). pii: 678. doi:10.3791/678. PMID: 19066563
20. Schaffer CB, Friedman B, Nishimura N et al (2006) Two-photon imaging of cortical surface microvessels reveals a robust redistribution in blood flow after vascular occlusion. PLoS Biol 4:e22
21. Kleinfeld D, Mitra PP, Helmchen F et al (1998) Fluctuations and stimulus-induced changes in blood flow observed in individual capillaries in layers 2 through 4 of rat neocortex. Proc Natl Acad Sci U S A 95:15741–15746
22. Klunk WE, Bacskai BJ, Mathis CA et al (2002) Imaging Abeta plaques in living transgenic mice with multiphoton microscopy and methoxy-X04, a systemically administered Congo red derivative. J Neuropathol Exp Neurol 61: 797–805
23. Nimmerjahn A, Kirchhoff F, Kerr JN et al (2004) Sulforhodamine 101 as a specific marker of astroglia in the neocortex in vivo. Nat Methods 1:31–37
24. Shaner NC, Steinbach PA, Tsien RY (2005) A guide to choosing fluorescent proteins. Nat Methods 2:905–909
25. Chudakov DM, Matz MV, Lukyanov S et al (2010) Fluorescent proteins and their applications in imaging living cells and tissues. Physiol Rev 90:1103–1163
26. Lutcke H, Murayama M, Hahn T et al (2010) Optical recording of neuronal activity with a genetically-encoded calcium indicator in anesthetized and freely moving mice. Front Neural Circ 4:9
27. Tian L, Hires SA, Mao T et al (2009) Imaging neural activity in worms, flies and mice with improved GCaMP calcium indicators. Nat Methods 6:875–881
28. Looger LL, Griesbeck O (2012) Genetically encoded neural activity indicators. Curr Opin Neurobiol 22:18–23
29. Mank M, Santos AF, Direnberger S et al (2008) A genetically encoded calcium indicator for

chronic in vivo two-photon imaging. Nat Methods 5:805–811

30. Gan WB, Grutzendler J, Wong WT et al (2000) Multicolor "DiOlistic" labeling of the nervous system using lipophilic dye combinations. Neuron 27:219–225
31. Portera-Cailliau C, Pan DT, Yuste R (2003) Activity-regulated dynamic behavior of early dendritic protrusions: evidence for different types of dendritic filopodia. J Neurosci 23: 7129–7142
32. Grienberger C, Konnerth A (2012) Imaging calcium in neurons. Neuron 73:862–885
33. Garaschuk O, Milos R, Konnerth A (2006) Targeted bulk-loading of fluorescent indicators for two-photon brain imaging in vivo. Nat Protoc 1:380–386
34. Golshani P, Portera-Cailliau C (2008) In vivo 2-photon calcium imaging in layer 2/3 of mice. J Vis, Exp
35. MacLean J, Yuste R (2005) Imaging action potentials with calcium indicators: practical guide. In: Yuste R, Konnerth A (eds) Imaging neurons a laboratory manual, 2nd edn. Cold Spring Harbor Laboratory Press, Cold Spring Harbor, NY, pp 351–355
36. Feng G, Mellor RH, Bernstein M et al (2000) Imaging neuronal subsets in transgenic mice expressing multiple spectral variants of GFP. Neuron 28:41–51
37. Grutzendler J, Kasthuri N, Gan WB (2002) Long-term dendritic spine stability in the adult cortex. Nature 420:812–816
38. Trachtenberg JT, Chen BE, Knott GW et al (2002) Long-term in vivo imaging of experience-dependent synaptic plasticity in adult cortex. Nature 420:788–794
39. Jefferis GS, Livet J (2012) Sparse and combinatorial neuron labelling. Curr Opin Neurobiol 22:101–110
40. Judkewitz B, Rizzi M, Kitamura K et al (2009) Targeted single-cell electroporation of mammalian neurons in vivo. Nat Protoc 4:862–869
41. Saito T, Nakatsuji N (2001) Efficient gene transfer into the embryonic mouse brain using in vivo electroporation. Dev Biol 240:237–246
42. Dixit R, Lu F, Cantrup R et al (2011) Efficient gene delivery into multiple CNS territories using in utero electroporation. J Vis Exp. (52). pii: 2957. doi:10.3791/2957. PMID: 21730943
43. Cruz-Martin A, Crespo M, Portera-Cailliau C (2010) Delayed stabilization of dendritic spines in fragile X mice. J Neurosci 30:7793–7803
44. Atasoy D, Aponte Y, Su HH et al (2008) A FLEX switch targets Channelrhodopsin-2 to multiple cell types for imaging and long-range circuit mapping. J Neurosci 28:7025–7030
45. Lowery RL, Majewska AK (2010) Intracranial injection of adeno-associated viral vectors. J Vis Exp. (45). pii: 2140. doi: 10.3791/2140. PMID: 21113119
46. Schultz BR, Chamberlain JS (2008) Recombinant adeno-associated virus transduction and integration. Mol Ther 16:1189–1199
47. Holtmaat A, Bonhoeffer T, Chow DK et al (2009) Long-term, high-resolution imaging in the mouse neocortex through a chronic cranial window. Nat Protoc 4:1128–1144
48. Mostany R, Portera-Cailliau C (2008) A craniotomy surgery procedure for chronic brain imaging. J Vis Exp. (12). pii: 680. doi:10.3791/680. PMID: 19066562
49. Cruz-Martin A, Portera-Cailliau C (2010) In vivo imaging of axonal and dendritic structures in developing cortex. In: Sharpe J, Wong R (eds) Imaging in developmental biology: a laboratory manual, 1st edn. Cold Spring Harbor Laboratory Press, Cold Spring Harbor, NY, pp 513–522
50. Yang G, Pan F, Parkhurst CN et al (2010) Thinned-skull cranial window technique for long-term imaging of the cortex in live mice. Nat Protoc 5:201–208
51. Drew PJ, Shih AY, Driscoll JD et al (2010) Chronic optical access through a polished and reinforced thinned skull. Nat Methods 7: 981–984
52. Jung JC, Mehta AD, Aksay E et al (2004) In vivo mammalian brain imaging using one- and two-photon fluorescence microendoscopy. J Neurophysiol 92:3121–3133
53. Xu HT, Pan F, Yang G et al (2007) Choice of cranial window type for in vivo imaging affects dendritic spine turnover in the cortex. Nat Neurosci 10:549–551
54. Yasuda R, Harvey CD, Zhong H et al (2006) Supersensitive Ras activation in dendrites and spines revealed by two-photon fluorescence lifetime imaging. Nat Neurosci 9:283–291
55. Holtmaat A, Svoboda K (2009) Experience-dependent structural synaptic plasticity in the mammalian brain. Nat Rev Neurosci 10: 647–658
56. Yu X, Zuo Y (2011) Spine plasticity in the motor cortex. Curr Opin Neurobiol 21:169–174
57. Nimmerjahn A, Kirchhoff F, Helmchen F (2005) Resting microglial cells are highly dynamic surveillants of brain parenchyma in vivo. Science 308:1314–1318
58. Spires TL, Meyer-Luehmann M, Stern EA et al (2005) Dendritic spine abnormalities in amyloid precursor protein transgenic mice demonstrated

by gene transfer and intravital multiphoton microscopy. J Neurosci 25:7278–7287

59. Tsai J, Grutzendler J, Duff K et al (2004) Fibrillar amyloid deposition leads to local synaptic abnormalities and breakage of neuronal branches. Nat Neurosci 7:1181–1183
60. Sabatini BL, Svoboda K (2000) Analysis of calcium channels in single spines using optical fluctuation analysis. Nature 408:589–593
61. Chen X, Leischner U, Rochefort NL et al (2011) Functional mapping of single spines in cortical neurons in vivo. Nature 475:501–505
62. Cossart R, Aronov D, Yuste R (2003) Attractor dynamics of network UP states in the neocortex. Nature 423:283–288
63. Kerr JN, Greenberg D, Helmchen F (2005) Imaging input and output of neocortical networks in vivo. Proc Natl Acad Sci U S A 102: 14063–14068
64. Ohki K, Chung S, Ch'ng YH et al (2005) Functional imaging with cellular resolution reveals precise micro-architecture in visual cortex. Nature 433:597–603
65. Gobel W, Helmchen F (2007) In vivo calcium imaging of neural network function. Physiology 22:358–365
66. Hendel T, Mank M, Schnell B et al (2008) Fluorescence changes of genetic calcium indicators and OGB-1 correlated with neural activity and calcium in vivo and in vitro. J Neurosci 28:7399–7411
67. Perron A, Mutoh H, Akemann W et al (2009) Second and third generation voltage-sensitive fluorescent proteins for monitoring membrane potential. Front Neural Circ 2:5
68. Ahrens KF, Heider B, Lee H et al (2012) Two-photon scanning microscopy of in vivo sensory responses of cortical neurons genetically encoded with a fluorescent voltage sensor in rat. Front Neural Circ 6:15
69. Chanda B, Blunck R, Faria LC et al (2005) A hybrid approach to measuring electrical activity in genetically specified neurons. Nat Neurosci 8:1619–1626
70. Fenno L, Yizhar O, Deisseroth K (2011) The development and application of optogenetics. Annu Rev Neurosci 34:389–412
71. Bernstein JG, Garrity PA, Boyden ES (2012) Optogenetics and thermogenetics: technologies for controlling the activity of targeted cells within intact neural circuits. Curr Opin Neurobiol 22:61–71
72. Deisseroth K (2011) Optogenetics. Nat Methods 8:26–29
73. Zhang YP, Oertner TG (2007) Optical induction of synaptic plasticity using a light-sensitive channel. Nat Methods 4:139–141
74. Peron S, Svoboda K (2011) From cudgel to scalpel: toward precise neural control with optogenetics. Nat Methods 8:30–34
75. Papagiakoumou E, Anselmi F, Begue A et al (2010) Scanless two-photon excitation of channelrhodopsin-2. Nat Methods 7:848–854
76. Ellis-Davies GC (2009) Basics of photoactivation. Cold Spring Harb Protoc. pdb top55
77. Matsuzaki M, Ellis-Davies GC, Nemoto T et al (2001) Dendritic spine geometry is critical for AMPA receptor expression in hippocampal CA1 pyramidal neurons. Nat Neurosci 4:1086–1092
78. Sobczyk A, Scheuss V, Svoboda K (2005) NMDA receptor subunit-dependent [Ca2+] signaling in individual hippocampal dendritic spines. J Neurosci 25:6037–6046
79. Ashby MC, Isaac JT (2011) Maturation of a recurrent excitatory neocortical circuit by experience-dependent unsilencing of newly formed dendritic spines. Neuron 70:510–521
80. Noguchi J, Nagaoka A, Watanabe S et al (2011) In vivo two-photon uncaging of glutamate revealing the structure-function relationships of dendritic spines in the neocortex of adult mice. J Physiol 589:2447–2457
81. Oheim M, Beaurepaire E, Chaigneau E et al (2001) Two-photon microscopy in brain tissue: parameters influencing the imaging depth. J Neurosci Methods 111:29–37
82. Rueckel M, Mack-Bucher JA, Denk W (2006) Adaptive wavefront correction in two-photon microscopy using coherence-gated wavefront sensing. Proc Natl Acad Sci U S A 103: 17137–17142
83. Booth MJ (2007) Adaptive optics in microscopy. Philos Transact A Math Phys Eng Sci 365:2829–2843
84. Engelbrecht CJ, Gobel W, Helmchen F (2009) Enhanced fluorescence signal in nonlinear microscopy through supplementary fiber-optic light collection. Opt Express 17:6421–6435
85. Flusberg BA, Cocker ED, Piyawattanametha W et al (2005) Fiber-optic fluorescence imaging. Nat Methods 2:941–950
86. Cheng A, Goncalves JT, Golshani P et al (2011) Simultaneous two-photon calcium imaging at different depths with spatiotemporal multiplexing. Nat Methods 8:139–142
87. Lillis KP, Eng A, White JA et al (2008) Two-photon imaging of spatially extended neuronal network dynamics with high temporal

resolution. J Neurosci Methods 172: 178–184

88. Grewe BF, Langer D, Kasper H et al (2010) High-speed in vivo calcium imaging reveals neuronal network activity with near-millisecond precision. Nat Methods 7:399–405
89. Duemani Reddy G, Kelleher K, Fink R et al (2008) Three-dimensional random access multiphoton microscopy for functional imaging of neuronal activity. Nat Neurosci 11: 713–720
90. Planchon TA, Gao L, Milkie DE et al (2011) Rapid three-dimensional isotropic imaging of living cells using Bessel beam plane illumination. Nat Methods 8:417–423
91. Truong TV, Supatto W, Koos DS et al (2011) Deep and fast live imaging with two-photon scanned light-sheet microscopy. Nat Methods 8:757–760
92. Nikolenko V, Watson BO, Araya R et al (2008) SLM microscopy: scanless two-photon imaging and photostimulation with spatial light modulators. Front Neural Circ 2:5
93. Dombeck DA, Harvey CD, Tian L et al (2010) Functional imaging of hippocampal place cells at cellular resolution during virtual navigation. Nat Neurosci 13:1433–1440
94. Kerr JN, Nimmerjahn A (2012) Functional imaging in freely moving animals. Curr Opin Neurobiol 22:45–53

Chapter 3

Live Spheroid Formation Recorded with Light Sheet-Based Fluorescence Microscopy

Francesco Pampaloni, Roli Richa, Nariman Ansari, and Ernst H.K. Stelzer

Abstract

We provide a detailed protocol for a three-dimensional long-term live imaging of cellular spheroids with light sheet-based fluorescence microscopy. The protocol allows the recording of all phases of spheroid formation in three dimensions, including cell proliferation, aggregation, and compaction. We employ the human hepatic cell line HepaRG transfected with the fusion protein H2B-GFP, i.e., a fluorescing histone. The protocol allows monitoring the effect of drugs or toxicants.

Key words Light sheet-based fluorescence microscopy, LSFM, SPIM, Three-dimensional cell cultures, Live-cell assay, Tumor spheroids, Spheroid formation, HepaRG cells, Live-cell imaging

1 Introduction

Data gathered during long-term fluorescence imaging provides the basis for the analysis of spatiotemporal processes in single cells, tissues, and whole organisms [1]. Three-dimensional imaging is required to investigate cellular processes under close-to-natural conditions, especially in three-dimensionally organized cell cultures. The issues of phototoxicity, photobleaching, high recording speed, and three-dimensional imaging capability have been assessed by employing spinning-disk confocal fluorescence microscopy [2], heavily optimized wide-field fluorescence microscopy with subsequent deconvolution (OMX) [3], and light sheet-based fluorescence microscopy (LSFM) [4, 5]. Among these three microscopies, LSFM (Fig. 1) is particularly gentle towards living samples. The light sheet-based illumination irradiates the specimen with an extremely low energy of about 2 μJ at 488 nm in the illumination plane [6, 7]. Since LSFM takes advantage of modern cameras, a very high stack recording speed is possible. While in our first implementation of a Digital Scanned Light Sheet Microscope (DSLM), a speed of six planes/second was achieved, where each plane consisted of 2,048 × 2,048 pixels [6], an entire stack of 100 or

Peter J. Verveer (ed.), *Advanced Fluorescence Microscopy: Methods and Protocols*, Methods in Molecular Biology, vol. 1251, DOI 10.1007/978-1-4939-2080-8_3, © Springer Science+Business Media New York 2015

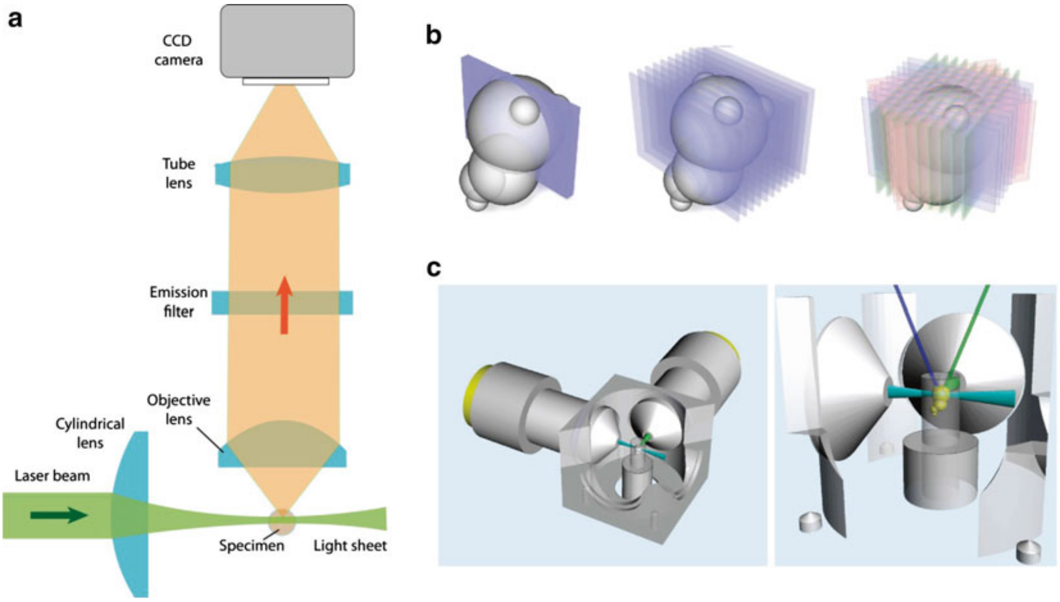

Fig. 1 Light sheet-based fluorescence microscopy (LSFM). (**a**) Setup of a single plane illumination microscope (aka SPIM) [5]). (**b**) Principles of LSFM imaging. *Left*: a single plane in the specimen is illuminated by a light sheet. Only the plane that is observed is also illuminated, resulting in lower photobleaching and lower phototoxicity. *Center*: by moving the specimen through the stationary light sheet, a three-dimensional stack of images is recorded. *Right*: by rotating the specimen multiple-view image stacks are obtained. Combining multiple different views of the specimen increases the resolution along the *z*-axis. (**c**) Close-up of a specimen chamber, showing both the illumination and detection objective lenses oriented at a 90° angle with respect to each other

more images should now become available every second. Another important advantage of LSFM is the high dynamic range, which supports very complex image processing. With LSFM, long-term fluorescence imaging of developing *Arabidopsis thaliana* lateral roots [8], fruit fly (*Drosophila melanogaster*) embryos [5, 9], and zebra fish (*Danio rerio*) embryos for up to 72 h has been performed without impairing the development [6]. The high speed allows one to follow, e.g., the mitosis and migration of more than 10,000 cells in a zebra fish embryo [6].

LSFM is also extremely well suited to record the behavior of live mammalian cells for long periods of time [10] and is the tool of choice for imaging three-dimensional cell cultures, such as cellular spheroids. The latter become more and more popular in basic research [11], for drug screening [11–15], and for personalized medicine [16]. Most immortalized and tumor cell lines, primary cells, as well as stem cells can form spheroids by spontaneous aggregation on nonadhesive substrate [17]. The spheroid formation consists of aggregation, delay, and compaction phases. The entire process takes 3–7 days [18]. Previous work has shown that LSFM is particularly well suited to image tumor cell spheroids in three dimensions at high resolution [19] and with live cells [20].

We show how to perform long-term live imaging by combining the LSFM with a perfusion chamber. Agarose beakers are employed to allow the cell aggregation in a confined environment. As an example, we record the complete formation of a spheroid over a time period of 6 days. We use the recently developed hepatic human cell line HepaRG, which is well suited for drug and toxicity screenings [21].

2 Materials

2.1 Chemicals and Reagents

1. *Cell growth medium*: Add 50 ml FBS (100 % fetal bovine serum), 5 ml penicillin/streptomycin, and 5 ml 200 mM L-glutamine to 445 ml DMEM (1× Dulbecco's modified eagle medium phenol-free). Mix 500 ml of medium. Store at 4 °C.
2. *Cell dissociation*: StemPro Accutase Cell Dissociation Reagent (Life technologies, #A1110501).
3. *Agarose aliquots*: Prepare a 1 % solution of high-melting point agarose (Sigma, A9539) in PBS. Aliquot the agarose solution in 2 ml tubes. Store at 4 °C.
4. *Transduction reagent*: BacMam viral particles containing a histone 2B-GFP expression cassette (Invitrogen C10594).

2.2 Cell Culture Equipment

1. 25 cm^2 tissue culture flask (e.g., from greiner bio-one, www.greinerbioone.com).
2. Hemocytometer (e.g., Neubauer hemocytometer).

2.3 Cell Line

HepaRG, terminally differentiated hepatic cells derived from a human hepatic progenitor cell line that retains many characteristics of primary human hepatocytes (e.g., from Life Technologies, HPRGC10).

2.4 Templates for the "Agarose Beakers"

Custom templates, see further in the text.

2.5 Further Equipment

1. Sharp angled-tip precision forceps (e.g., Excelta SKU 50-SA, http://www.excelta.com).
2. 1 ml syringes.
3. 0.55 × 25 mm (24 G × 1″) hypodermic needles.
4. Custom LSFM mounting system for the agarose beaker (details further in the text).

2.6 Imaging

1. Various suitable LSFM implementations are described in details in [5, 22, 23] (SPIM), *(6)* (DSLM), and [8] (monolithic DSLM, mDSLM). A commercial LSFM is available from Zeiss (Lightsheet Z.1, http://microscopy.zeiss.com/microscopy/en_de/products/imaging-systems/lightsheet-z-1.html#Introduction).

2. Long working water-dipping distance objective lenses (e.g., Carl Zeiss W N-Achroplan 10×/0.3 NA).

2.7 Temperature and Gas Control System for Time-Lapse Live Imaging

1. A compact cell incubator (e.g., Galaxy® 14S CO_2 incubator, New Brunswick http://eshop.eppendorfna.com/products/New_Brunswick_Galaxy_14S_CO₂_Incubator).
2. Heated hose for tubing system (e.g., series WSKW from Winkler http://en.winkler.eu).
3. Microprocessor-controlled table-top temperature controller (e.g., WRT2000X, from Winkler http://en.winkler.eu).
4. A 4 meter-long gas-permeable silicon tubing (e.g., from Reichelt Chemietechnik, Germany, 1 mm internal diameter, 2 mm external diameter, http://www.rct-online.de).
5. Gas-impermeable rubber tubing (e.g., from Reichelt Chemietechnik, Germany—EPDM/PP pharmaceutical tubing, 1.6 mm internal diameter, 4.8 mm external diameter, http://www.rct-online.de).
6. Peristaltic pump (e.g., REGLO digital from Ismatec, Germany, http://www.ismatec.de/de_d/pumpen/s_reglo/reglo_digital.htm).
7. Two-stop tubing for the peristaltic pump (e.g., 1.30 mm two-stop PharMed BPT tubing, Ismatec SC0328).
8. Autoclavable Luer-Lok connectors, mini tubing olive connectors (inner Ø 2 and 1.5 mm), and quick-disconnect coupling/nipple systems with valve (e.g., THOMAFLUID-POM with 1.6 mm nozzle). All this part can be purchased, e.g., from Reich elt Chemietechnik, Germany, http://www.rct-online.de).

2.8 Software for Image Acquisition and Image Processing

Image processing software (e.g., Fiji, a variant of ImageJ, http://fiji.sc).

3 Methods

3.1 Thawing of the HepaRG Cell and Transduction with the Histone 2B-GFP Nuclear Marker

1. Rapidly thaw the frozen HepaRG cells (within 5 min) in a 37 °C water bath. Dilute the thawed cells in a 5 ml pre-warmed growth medium. Centrifuge cells for 4 min at 300×*g*. Resuspend the pellet in 5 ml pre-warmed cell growth medium. Plate cells at high density in a 25 cm^2 cell culture flasks to speed up recovery. Change medium after 24 h. Propagate cells at 90–100 % confluence. Detach cells with 500 ml StemPro Accutase Cell Dissociation Reagent, and resuspend cells in 4.5 ml cell growth medium.

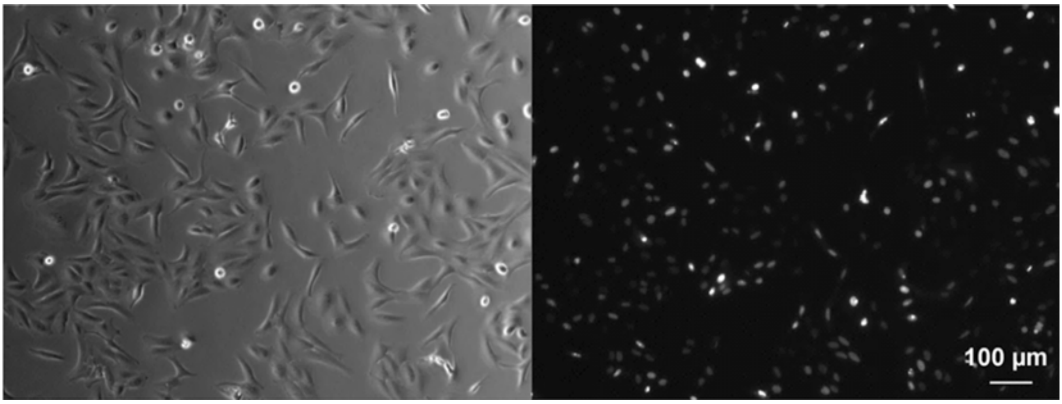

Fig. 2 HepaRG cells transduced with nuclear marker H2B-GFP. *Left*: transmitted light image. Right: fluorescence image. Objective lens: CZ Achroplan 10×/0.3. Ex/Em: 488/520 nm. Microscope Zeiss Axiovert 40 CFL

2. Determine the concentration of cells in the medium with a hemocytometer (e.g., Neubauer hemocytometer).
3. Expand HepaRG cells as monolayer on a 75 cm^2 tissue culture flask, until they reach a 70 % confluence.
4. Add the BacMam transduction reagent with a histone 2B-GFP expression cassette to the plated cell, by pipetting the viral particles directly in the media at the density recommended by the company data sheet. Baculoviral vectors for fluorescent labeling of the cell nuclei have a relatively low cellular toxicity [24]. After 24 h of incubation with the BacMam particles, cells are detached by employing StemPro Accutase and the cell suspension is diluted to 2×10^3 cells in 25 μl (the volume of the measuring chamber mounted in the LSFM). The transduction efficiency approaches 90 % (Fig. 2).
5. Perform a control experiment by forming HepaRG spheroids in a suitable U-well plate (e.g., the HydroCell Surface™ 96-well plate). The original cell suspension is diluted in growth medium, and 100 μl is transferred in each well. An 8-channel pipette can be employed to reduce the pipetting time. Incubate the multiwell plate under standard cell culture conditions. Spheroid formation is completed after 2–6 days (Fig. 3).

3.2 Agarose Beaker Molding

1. A caster can be made from an aluminum tube and an aluminum plunger (Fig. 4a, b). Employ aluminum or stainless steel for both the tube and the plunger to support the rapid cooling of the agarose gel. Use a conically shaped plunger tip to simplify the aggregation of the cells in the center of the beaker (Fig. 4a, b, *see* **Note 1**).
2. Autoclave the caster.
3. Prepare a 1 % solution of high-melting point agarose in PBS and aliquot it in 1.5 ml tubes.

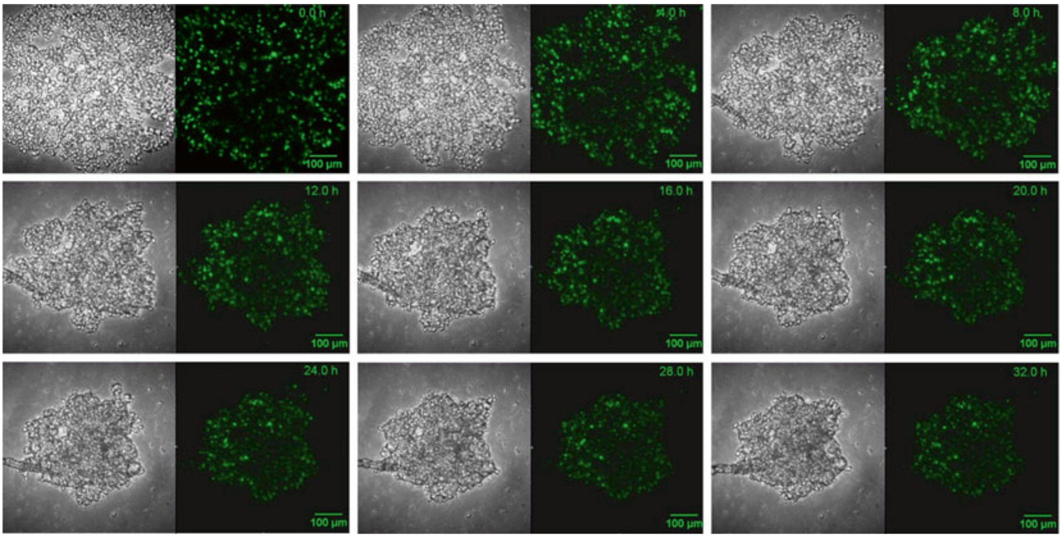

Fig. 3 Aggregation of a HepaRG spheroid for 32 h. 2,000 cells/well expressing H2B-GFP were seeded into a 96-well plate coated with an agarose layer. The cells do not adhere to the agarose layer and form compact spheroids within days (aka liquid overlay method). Transmitted light and fluorescence images are shown. Objective lens: Nikon CFI Plan Fluor 10×/0.30, WD 16 mm. Ex/Em: 488 nm/515 nm. Time-lapse interval: 30 min. Microscope: Nikon Eclipse confocal fluorescence microscope

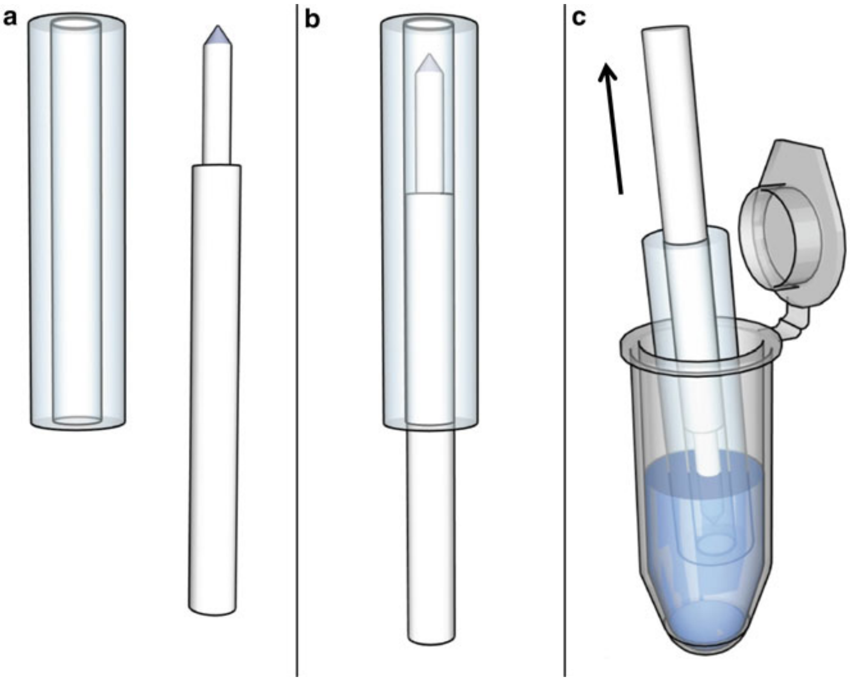

Fig. 4 Schematic representation of the template and the production of agarose beakers. (**a**) The template consists of a stainless steel barrel and a plunger. (**b**) The assembled template. (**c**) The liquid 1 % high-melting agarose is sucked into the template by pulling the plunger

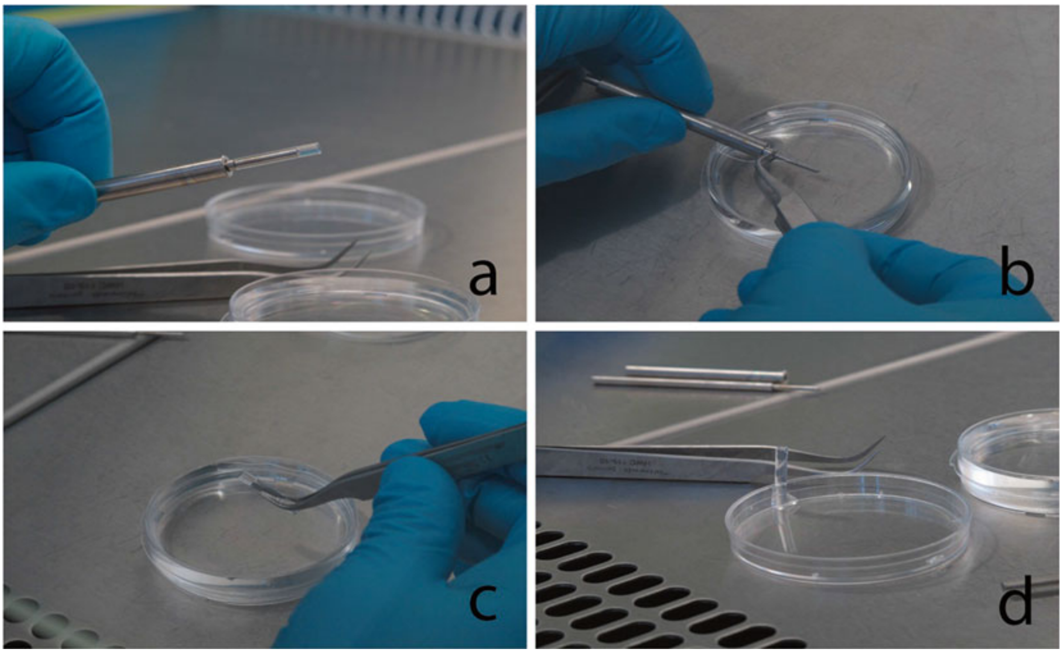

Fig. 5 The photographs illustrate the extraction procedure of the agarose beaker from the stainless-steel template. (**a**) The agarose beaker is still on the template. (**b**) The agarose beaker is immersed into sterile PBS and gently pushed out of the template with a sharp-tip angled forceps. (**c**) The agarose beaker is carefully manipulated with the forceps, and (**d**) the beaker is placed vertically in an empty petri dish in order to fill it with the cell suspension

4. Place few aliquots of the 1 % agarose solution in a heating block at 95 °C for 15 min in order to completely melt the agarose.
5. Working under the laminar flow sterile hood, immerse the caster in one 1.5 ml tube with the liquid agarose solution. Suck the agarose into the template by pulling up the plunger (Fig. 4c). Place the caster at 4 °C for 5 min to allow a fast hardening of the agarose gel.
6. After agarose hardening, push the plunger out of the template. Separate the agarose beaker from the plunger by completely immersing it in PBS and by gently pushing the beaker out with a sharp angled tip precision forceps (Fig. 5).
7. Store the agarose beakers at 4 °C in PBS with 1 % penicillin/streptomycin.

3.3 Cell Seeding in the Agarose Beaker

1. Work under the laminar flow sterile hood.
2. With sharp angled tips forceps, place one agarose beaker vertically inside a petri dish. Place the beaker in contact with the wall of the petri dish in order to have a stable support during the cell seeding (Fig. 5d).

3. Remove any residual storage PBS from within the beaker with a 1 ml syringe connected to a 0.55 × 25 mm needle (24G × 1″).
4. Slowly inject in the beaker the cell suspension by employing a 1 ml syringe with a 0.55 × 25 mm needle (24G × 1″). Avoid the formation of air bubbles in the cell suspension during injection (*see* **Note 3**).
5. Insert the beaker vertically into a 1.5 ml tube, and centrifuge it at 300 × *g* for 5 min. The centrifugation allows for a rapid seeding of the cells at the beaker's bottom.

3.4 Preparation of the LSFM Perfusion Chamber

1. Most of the LSFM chambers have a large volume of about 10 ml. Thus, a perfusion system is necessary in order to maintain a constant pH during long-term time-lapse experiments.
2. Provide the LSFM perfusion chamber with an inlet hole at the bottom of the chamber and with an outlet hole at the top of the chamber (Fig. 6, inset).
3. Connect mini tubing olive connectors to the inlet and the outlet.
4. Autoclave the chamber.

3.5 Assembly of the Inlet and Outlet Perfusion Tubing

1. *Gas exchange tubing*: wrap the 4 m-long gas-permeable thin silicon tube around a stable aluminum cylinder forming a tight spiral (Figs. 6 and 7). The long and thin silicon tube allows fast equilibration of the flowing media with the outside gas environment. By placing the silicon spiral in a CO_2 incubator set to 5 % CO_2, the pH of the cell culture media can be stably maintained at 7.4.

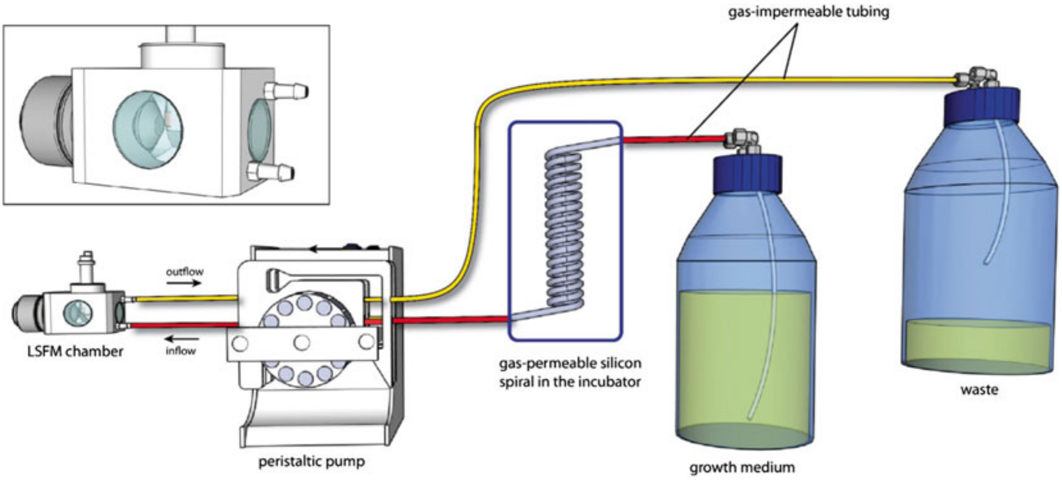

Fig. 6 Schematic representation of the assembled cell culture media perfusion system. *Inset*: a specimen chamber equipped with inlet and outlet connectors

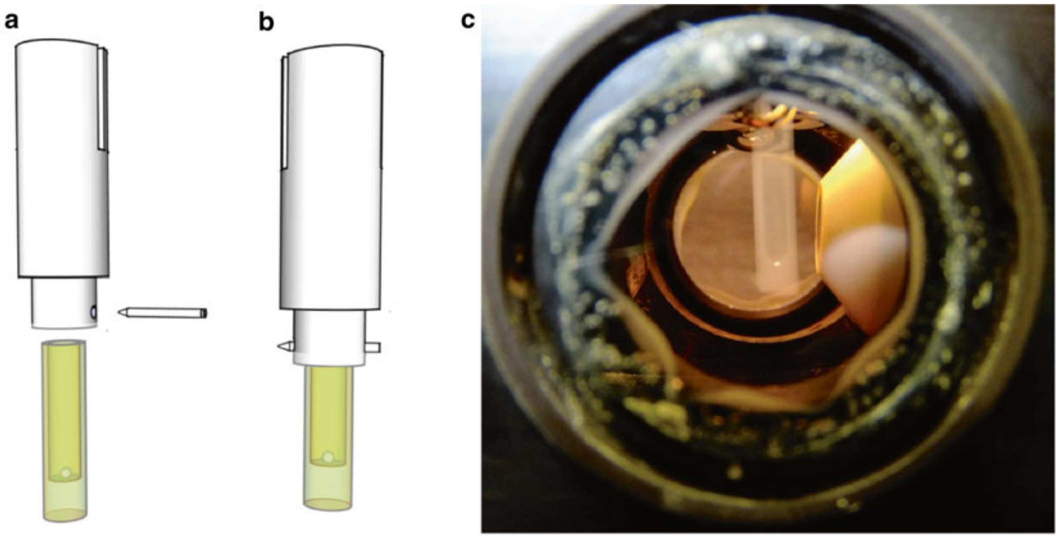

Fig. 7 Mounting the agarose beaker that contains the seeded cells with the specimen holder. (**a**, **b**) The *bottom* part of the specimen holder is first immersed in sterile media or PBS. The capillary force facilitates the insertion of the agarose beaker in the holder. A sharp-tip pin prevents it from dropping down. (**c**) The photograph shows the specimen inside the LSFM chamber

2. *Inlet tubing*: connect with Luer-Lok connectors both ends of the silicon tube spiral to about 1 m-long gas-impermeable tube. The gas-impermeable tubing ensures that no gas exchange between the perfusion media and the environment outside the CO_2 incubator occurs. Connect one end to the two-stop tubing for the peristaltic pump, as well as the extension tubing that will be connected with the perfusion chamber. Use quick-disconnect valve coupling nipples to connect the tube with the perfusion chamber. Connect the tube at the other end with the growth media supply bottle (Fig. 6, *see* **Note 2**).
3. *Outlet tubing*: connect with Luer-Lok connectors one approximately 1 m-long gas-impermeable tube to the two-stop tubing for the peristaltic pump. Connect the extension tubing that will be linked with the perfusion chamber. Use a quick-disconnect valve coupling nipple to connect the tube with the perfusion chamber (Fig. 6).
4. Autoclave both the inlet and the outlet tubing.

3.6 LSFM Holder for the Agarose Beaker

1. Prepare a custom-made LSFM holder for the agarose beaker similar to the one shown in Fig. 7. The bottom part of the holder must fit the agarose beaker. The material of the holder must be autoclavable (e.g., POM, *see* **Note 4**). Notice the sharp-tip pin used to stably anchor the beaker to the holder (Fig. 7a, b). The upper part of the holder must be designed to

ensure a stable connection with the LSFM *xyz*-stage once inserted in the LSFM chamber (Fig. 7c).

2. In the laminar flow sterile hood, vertically position the agarose beaker containing the cell suspension in one petri dish (see e.g., Fig. 5d).
3. Wet the bottom part of the beaker holder with sterile PBS or medium. This facilitates the insertion of the beaker into the holder.
4. Insert the agarose beaker into the holder. The easiest procedure is keeping the beaker vertically in a petri dish and approaching the holder from the top. The wet bottom part of the holder will "suck" the agarose beaker facilitating the connection.
5. Insert with forceps the pin laterally through the holes of the holder, and punch the agarose beaker so that it will not drop down during the experiment.

3.7 Assembly and Testing of the Temperature-Controlled Heating System

1. A commercially available tube heating system is a simple solution to control the temperature in the LSFM perfusion chamber.
2. Insert the inlet tube into the tube heating system as shown in Fig. 8.
3. Connect the inlet and outlet tubing to the LSFM perfusion chamber as shown in Subheading 3.4 and Fig. 6.
4. The final medium temperature at equilibrium depends also on the flow speed. Perform a test in order to find the optimum flow speed in order to reach a medium temperature of 37 °C.

3.8 Assembly of the Whole System and Start of the Time Lapse

1. Sterilize the objective lens of the LSFM with ethanol.
2. Connect the autoclaved LSFM chamber to the objective lens.
3. Pipette at the bottom of the empty chamber 1 ml of sterile silicon oil. A thin layer of silicon oil prevents bacterial contamination by effectively isolating the media in the chamber from the outside environment.
4. Cover the chamber with a petri dish lid in order to maintain the inside sterile.
5. Place the gas exchange silicon spiral in the CO_2 incubator (Fig. 9). Both ends of the spirals are provided with Luer-Lok connectors and go outside the incubator through the standard cable aperture (visible in Fig. 9, inset).
6. Assemble the inlet and outlet tubing system in a sterile hood as illustrated in Subheading 3.5 and in Fig. 6.
7. Put the growth media supply bottle on ice, in order to prevent bacterial contamination of the media over several days.
8. Insert the final part of the inlet tubing in the heating system as illustrated in Subheading 3.7 and in Fig. 8.

Fig. 8 Assembly of the temperature-controlled heating system. The final part of the inlet tube is inserted through the heating system, which warms the perfused medium

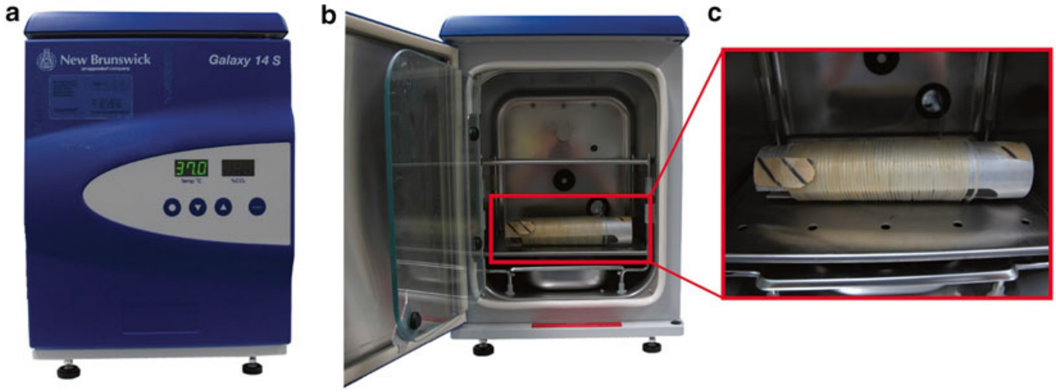

Fig. 9 Photograph of the gas exchange spiral placed inside a small CO_2 incubator (**a**) ensuring a constant pH 7.4 of the perfusion medium. A 5 % CO_2 concentration is set in the incubator. (**b**, **c**) The silicon tube spiral wrapped around an aluminum cylinder

9. Connect the inlet and outlet tubing to the LSFM chamber by employing a quick-disconnect valve coupling nipple, and start both the peristaltic pump and the heating system in order to fill up the chamber with growth media at 37 °C.
10. Once the chamber is filled up and the media temperature is stable, insert the mounted agarose beaker prepared as illustrated in Subheading 3.6 and Fig. 7.
11. Start the time lapse.

3.9 Results

We observed the formation of a HepaRG spheroid from 2,000 seeded cells with a Carl Zeiss W N-Achroplan 10×/0.3 objective lens. Figure 10 shows the entire process in both transmitted light (Fig. 10a) and fluorescence contrast (shown as a three-dimensional isosurface rendering, Fig. 10b). We recorded in total 600 three-dimensional stacks with two channels (transmitted light and fluorescence) with an interval of 15 min between two stacks.

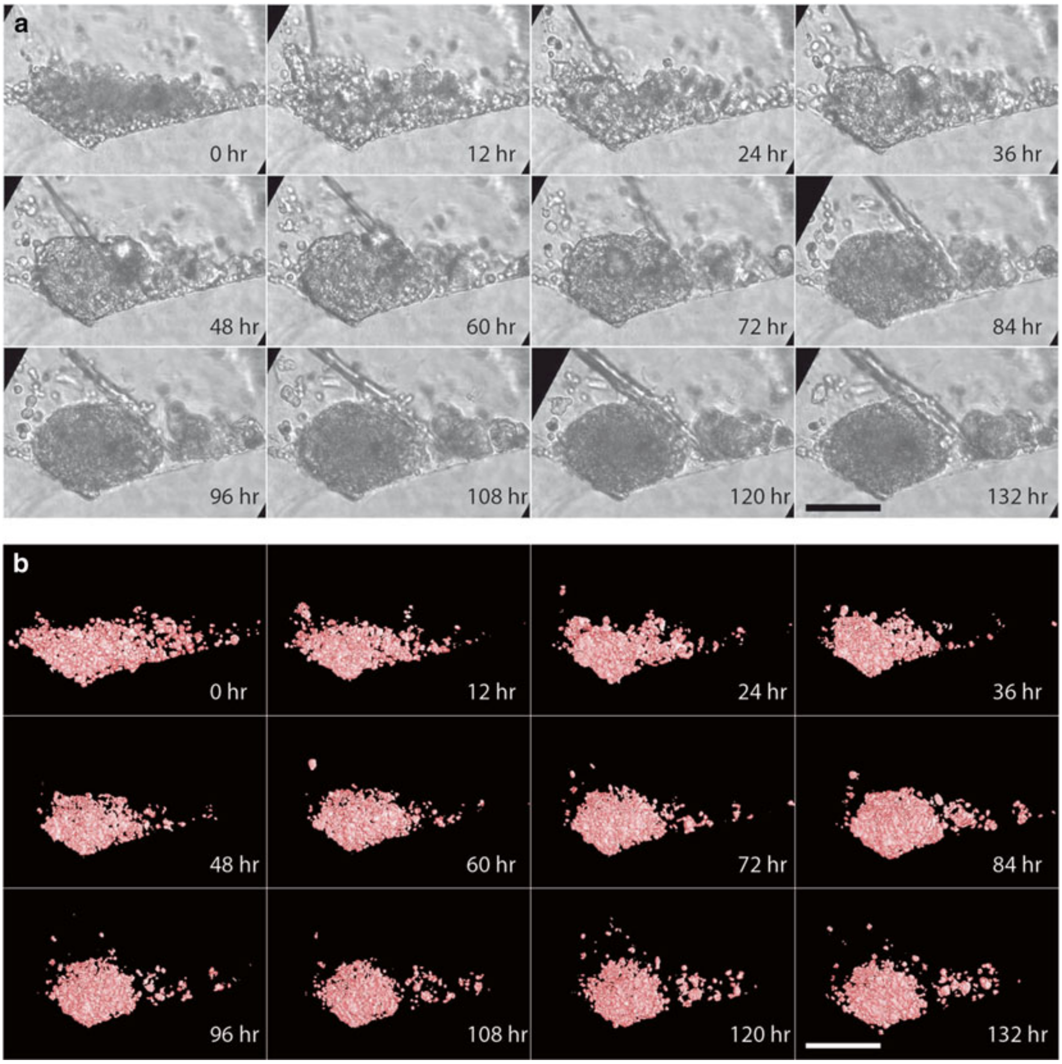

Fig. 10 Formation of a HepaRG spheroid during a period of 6 days. 2,000 cells were seeded into the 1 % agarose beaker. (**a**) The transmitted light frames were recorded during the fluorescence time-lapse imaging with the TC-LSFM. (**b**) Three-dimensional surface rendering of the corresponding fluorescence stacks. The fluorescence fusion protein employed for nuclei visualization was H2B-GFP. The rendering of the fluorescence data was performed with the ImageJ plugin "3D view." Scale bar 100 μm. For both transmitted light and three-dimensional fluorescence imaging the same objective lens, Zeiss W N-Achroplan 10×/0.3 was employed

Each three-dimensional stack contains 135 single frames spaced 2.6 μm along the *z*-axis (81,000 frames within 150 h). The progressive aggregation and compaction of the HepaRG cells proceeds for approximately 60 h. From 60 h onwards, spheroid compaction occurs, as inferred from the volume reduction of the spheroid shown in Fig. 10b. We counted the mitotic events during the spheroid formation. The three-dimensional stacks were visually inspected plane by plane in their entirety and over time with ImageJ

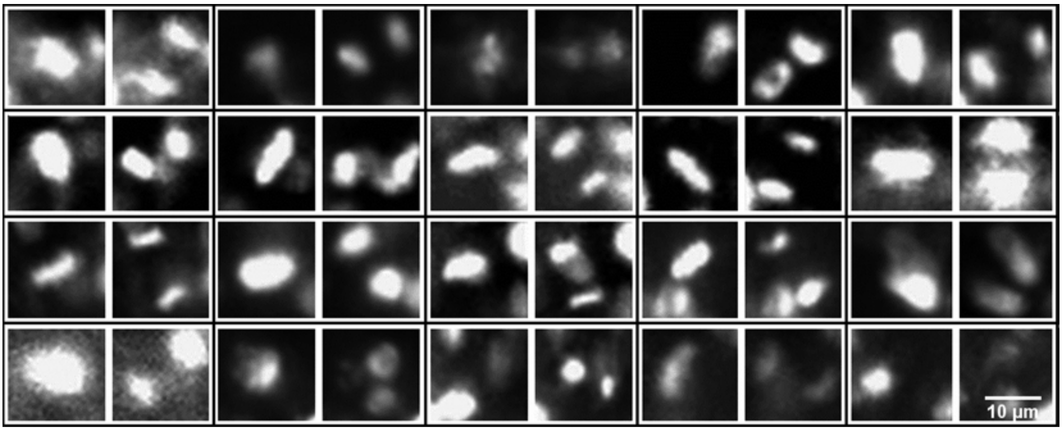

Fig. 11 Representative mitosis events recorded during the HepaRG spheroid formation. Each pair of frames represents a mitotic event, showing the nucleus before and after mitosis at a time interval of 15 min. The cells express the fusion protein H2B-GFP. Objective lens: CZ N-Achroplan 10×/0.3

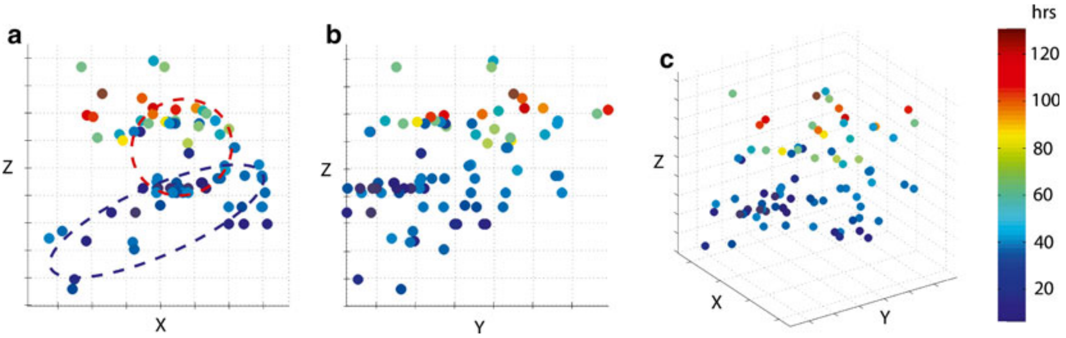

Fig. 12 Analysis of mitotic events during the formation of the HepaRG cells spheroid. The temporal axis is color coded according to the color bar. (**a**) Maximum projection of the mitotic events on the *xz* plane. As shown in the diagram, the majority of the mitotic events occur during the first 50 h. The *blue* and *red dashed circles* represent the approximate shape and position of the aggregating cells during the initial phase of the spheroid formation (*blue*) and in the finally formed spheroid. Please note the majority of the mitotic events that occur in the outer cell layer of the forming spheroids. (**b**) Maximum projection on the *yz* plane. **c**) Complete *xyzt* representation of mitotic events during the spheroid's formation

and its *Bio-importer* plug-in. Figure 11 provides representative examples of the detected mitotic events. Due to the excellent signal-to-noise ratio of the LSFM stacks over the whole recording period, this procedure can be automated. In total, we recorded 90 cell divisions, which is sufficient to provide a representative picture of the cell divisions profile in the spheroid.

The results of the analysis are plotted in Fig. 12. The data shows that the majority of the mitotic events occur prior to the onset of the compaction phase, which takes place 60 h after seeding the cells. The cell divisions decrease during the compaction phase of the spheroid. Mitosis occurs primarily at the periphery of the spheroid rather than in the core, as apparent from the three-dimensional data plotted in Fig. 10a.

These results show that an LSFM equipped with a perfusion system can be used to monitor the complete process of spheroid formation in three dimensions for a period of at least 6 days.

4 Notes

1. The caster tip can have other shapes than a conical one. Possible shapes are flat or truncated cone. In order to have a U-shaped bottom, just produce an agarose open tube with the caster, and then close one end with a droplet of agarose. The surface tension will induce a U-shaped bottom.
2. It is convenient to pre-fill the inlet tubing with medium before connecting it with the LSFM perfusion chamber. This avoids air bubbling and the formation of foam in the chamber once the peristaltic pump is started.
3. The filling of the agarose beaker with the cell suspension can be alternatively conducted with thin glass capillaries connected to a normal plastic hypodermic syringe with a 20 cm-long flexible silicon tube. This allows a very precise control over the flow. In this way, the cell suspension can be dispensed without the formation of air bubbles.
4. The LSFM holder for the agarose beakers as well as the perfusion chamber should be made of an autoclavable plastic material, e.g., POM. Metals should in general be avoided due to potential cellular toxicity.

Acknowledgments

The authors thank the Deutsche Forschungsgemeinschaft (DFG) and the German Federal Ministry of Education and Research (BMBF) for financial support (project ProMEBS). We thank Berit Langer for her outstanding support.

References

1. Baker M (2010) Cellular imaging: taking a long, hard look. Nature 466:1137–1140
2. Homem CCF, Reichardt I, Berger C et al (2013) Long-term live cell imaging and automated 4D analysis of drosophila neuroblast lineages. PloS One 8(11):e79588. doi:10.1371/journal.pone.0079588
3. Carlton PM, Boulanger J, Kervrann C et al (2010) Fast live simultaneous multiwavelength four-dimensional optical microscopy. Proc Natl Acad Sci U S A 107:16016–16022
4. Huisken J, Stainier DY (2009) Selective plane illumination microscopy techniques in developmental biology. Development 136:1963–1975
5. Huisken J, Swoger J, Del Bene F et al (2004) Optical sectioning deep inside live embryos by selective plane illumination microscopy. Science 305:1007–1009

6. Keller PJ, Schmidt AD, Wittbrodt J et al (2008) Reconstruction of zebrafish early embryonic development by scanned light sheet microscopy. Science 322:1065–1069
7. Keller PJ, Stelzer EH (2008) Quantitative in vivo imaging of entire embryos with digital scanned laser light sheet fluorescence microscopy. Curr Opin Neurobiol 18:624–632
8. Maizel A, von Wangenheim D, Federici F et al (2011) High-resolution live imaging of plant growth in near physiological bright conditions using light sheet fluorescence microscopy. Plant J 68:377–385
9. Keller PJ, Schmidt AD, Santella A et al (2010) Fast, high-contrast imaging of animal development with scanned light sheet-based structured-illumination microscopy. Nat Methods 7:637–642
10. Pampaloni F, Kroschewski R, Berge U et al (2014) Tissue-Culture Light Sheet Fluorescence Microscopy (TC-LSFM) allows long-term imaging of three-dimensional cell cultures under controlled conditions. Integrative Biology. doi:10.1039/C4IB00121D
11. Harma V, Virtanen J, Makela R et al (2010) A comprehensive panel of three-dimensional models for studies of prostate cancer growth, invasion and drug responses. PLoS One 5:e10431
12. Friedrich J, Seidel C, Ebner R et al (2009) Spheroid-based drug screen: considerations and practical approach. Nat Protoc 4:309–324
13. Matsuda M, Shiratori S (2011) Correlation of antithrombogenicity and heat treatment for layer-by-layer self-assembled polyelectrolyte films. Langmuir 27:4271–4277
14. Takano S, Tian W, Matsuda M et al (2011) Detection of IDH1 mutation in human gliomas: comparison of immunohistochemistry and sequencing. Brain Tumor Pathol 28:115–123
15. Lee MY, Kumar RA, Sukumaran SM et al (2008) Three-dimensional cellular microarray for high-throughput toxicology assays. Proc Natl Acad Sci U S A 105:59–63
16. Goto A, Hoshino M, Matsuda M et al (2011) Phosphorylation of STEF/Tiam2 by protein kinase A is critical for Rac1 activation and neurite outgrowth in dibutyryl cAMP-treated PC12D cells. Mol Biol Cell 22: 1780–1790
17. Kelm JM, Timmins NE, Brown CJ et al (2003) Method for generation of homogeneous multicellular tumor spheroids applicable to a wide variety of cell types. Biotechnol Bioeng 83:173–180
18. Lin RZ, Chou LF, Chien CC et al (2006) Dynamic analysis of hepatoma spheroid formation: roles of E-cadherin and beta1-integrin. Cell Tissue Res 324:411–422
19. Verveer PJ, Swoger J, Pampaloni F et al (2007) High-resolution three-dimensional imaging of large specimens with light sheet-based microscopy. Nat Methods 4:311–313
20. Lorenzo C, Frongia C, Jorand R et al (2011) Live cell division dynamics monitoring in 3D large spheroid tumor models using light sheet microscopy. Cell Div 6:22
21. Guillouzo A, Corlu A, Aninat C et al (2007) The human hepatoma HepaRG cells: a highly differentiated model for studies of liver metabolism and toxicity of xenobiotics. Chem Biol Interact 168:66–73
22. Greger K, Swoger J, Stelzer EH (2007) Basic building units and properties of a fluorescence single plane illumination microscope. Rev Sci Instrum 78:023705
23. Huisken J, Stainier DY (2007) Even fluorescence excitation by multidirectional selective plane illumination microscopy (mSPIM). Opt Lett 32:2608–2610
24. Zeng J, Du J, Lin J et al (2009) High-efficiency transient transduction of human embryonic stem cell-derived neurons with baculoviral vectors. Mol Ther 17:1585–1593

Chapter 4

Fluorescence Microscopy-Based RNA Interference Screening

Manuel Gunkel, Nina Beil, Jürgen Beneke, Jürgen Reymann, and Holger Erfle

Abstract

Using RNAi interference (RNAi), it is possible to study the effect of specific gene knockdowns in mammalian cells. In this protocol we present the automated preparation of "ready to transfect" multiwell plates and cell arrays, on which cells can be grown which are then reversely transfected with one type of siRNA in every individual well or spot. Additionally, different microscope types for screening approaches are compared and considerations about the information workflow are made.

Key words High-throughput screening, High content screening, Automated sample preparation, Automated microscopy, Data mining

1 Introduction

Microscopy-based RNA interference (RNAi) screening has become a powerful tool to elucidate gene function in mammalian cells in a previously inconceivable manner [1]. In this chapter we describe the workflow of the ViroQuant-CellNetworks RNAi screening facility in BioQuant, Heidelberg University, from automated sample preparation to screening microscopy [2], supported by sophisticated data mining tools [3, 4].

The ideal specific gene knockdown experiment by RNAi allows addressing controlled gene silencing independent of any stochastic gene expression and cell cycle effects. This generates an unambiguous cellular phenotype for the assay of interest. Unfortunately, this does not reflect the reality of RNAi experimentation, especially not in high-throughput RNAi workflows. Uncontrolled knockdown efficiencies in combination with stochastic gene expression and cell cycle effects, just to mention a few, cause the occurrence of populations of phenotypes after gene knockdown [5]. To increase the information content of RNAi knockdown experiments, single-cell

Peter J. Verveer (ed.), *Advanced Fluorescence Microscopy: Methods and Protocols*, Methods in Molecular Biology, vol. 1251, DOI 10.1007/978-1-4939-2080-8_4,

information should be collected and considered for evaluation [6]. Besides that, many biological assays require an image resolution sufficient to resolve subcellular structures or to obtain information on physical interactions between cellular components. Many RNAi screens taking cellular population into consideration have been published, and the need for microscopy-based image acquisition is steadily growing.

As different processes of interest within a biological system occur at defined points in space and time, different microscopic observation and investigation methods have to be considered. Nowadays, advanced and fully automated data acquisition (DAQ) techniques are needed for performing large-scale screening assays. The techniques are optimized in terms of throughput (number of acquired samples per time) or information content, e.g., resolution and live cell imaging (*see* Table 2 for a small overview of screening microscopes).

Besides assay preparation and imaging, a central aspect is data mining, i.e., information workflows that not only provide analysis tools but also contain assay-specific information for a proper documentation and interpretation of the analysis results itself. Ideally, such an information pipeline covers the entire screening workflow containing library information, plate layouts resulting from assay preparation and dedicated image, statistics and bioinformatics results, as well as the visualization of the data.

Here, we give an introduction to high-throughput sample preparation for microscopy-based RNAi screens and considerations for the proper choice of screening microscopes for a certain resolution demand.

2 Materials

1. siRNA oligonucleotides (Ambion).
2. OptiMEM + Glutamax (Gibco).
3. Sucrose (USB).
4. Gelatin (Sigma-Aldrich).
5. Lipofectamin 2000 (Invitrogen).
6. Fibronectin, human (Sigma-Aldrich).
7. 384-Well low-volume plates (Nunc).
8. 384 Deep well plates (Eppendorf).
9. 384-Well image plates (BD Falcon).
10. Lab-Tek chambered cover glass (Nunc).
11. Sterile filter, 0.45 μm (Millipore).

3 Methods

For RNAi screening, "ready to use" solid-phase reverse transfection can be prepared in 96- and 384-well plates as well as on cell arrays [7]. The right choice depends on many factors (*see* Table 1).

3.1 Preparation of the Source siRNA Transfection Solution for Solid-Phase Transfection

1. Prepare an siRNA stock solution by dissolving lyophilized siRNAs with MilliQ water to a final concentration of 30 μM.
2. Transfer 3 μl of OptiMEM, containing 0.4 M sucrose, to each well of a 384-well low-volume plate.
3. Add 3.5 μl of Lipofectamin 2000 to each well of the 384-well low-volume plate and mix thoroughly.
4. Add 5 μl of the respective siRNA stock solution to each well of the 384-well low-volume plate and mix thoroughly.
5. Incubate for 20 min at room temperature.
6. Add 7.25 μl of a 0.2 % gelatin solution containing 1×10^{-2}% fibronectin to each well of the 384-well low-volume plate and mix thoroughly.

   See also **Note 1**.

3.2 Preparation of "Ready to Transfect" Plates

1. *Option 1:* Preparation of 96-well plates "ready to transfect":

   Dilute 18.75 μl of the source siRNA transfection solution with 468.75 μl MilliQ water and dispense 25 μl per well of a 96-well plate.

   Option 2: Preparation of 384-well plates "ready to transfect":

   Dilute 18.75 μl of the source siRNA transfection solution with 187.5 μl MilliQ water and dispense 5 μl per well of a 384-well plate.

   Option 3: Preparation of high-density cell arrays "ready to transfect":

Table 1

Advantages and drawbacks of different plate types

Plate type	Advantage	Drawback	Proposed application
96-Well plate	Large number of cells per well, area ~30 mm^2	Low number of wells	Validation screen with preselected low number of targets
384-Well plate	Medium number of wells	–	Genome-wide screen
Cell arrays	Full assay on a single plate. No need for plate handling. Cell seeding and antibody staining simultaneously on whole plate	Relatively small area (~0.13 mm) per spot, ~50–300 cells	Genome-wide screen with expensive reagents or rare patient cells

The siRNA transfection solution is not further diluted and printed directly onto the cell array by a full contact printer (*see* **Note 2**). No further steps are needed!

2. Dry the 384-well plates for 2.5 h at medium drying force in the Speed Vac (*see* **Note 3**).

3.3 Comparison of Different Screening Microscopes

Various types of microscopes can be used for screening approaches. Crucial factors for the choice of the right system are the imaging speed and the quality of the readout. First we want to give a comparison between three different fluorescence-based screening systems, a wide-field (Olympus, IX81), a spinning disc confocal (PerkinElmer, Opera), and a confocal (Leica, SP5) microscope. On each system, the same screen was performed. A 96-well plate (ibidi) was used on which a layout with 12 wells (*see* Fig. 1) was repeated 3 times, one repetition for each microscope screen. In each well, multiple subpositions were acquired until the total recorded area per well covered about 1,240 × 930 μm^2. At each subposition a z-stack with 24 steps (z-step width 2 μm) was recorded for three different color channels. The imaging parameters of the different microscopes are compared in Table 2.

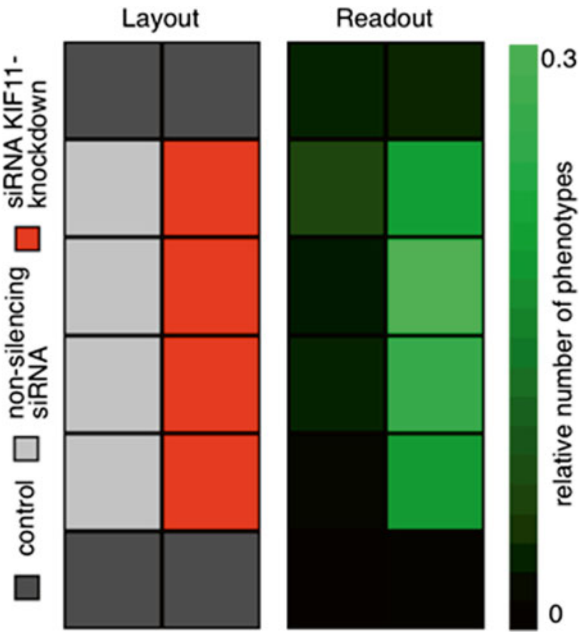

Fig. 1 Layout of the plate and readout example. Four wells are used as controls where no siRNA was applied (*dark gray*, *top* and *bottom row*), in four wells a non-silencing siRNA was applied (*light gray*, *left column*), and in four wells siRNA for Kif11 knockdown was transfected (*red*, *right column*), which resulted in prometaphase arrest of the cells. The relative number of cells in prometaphase is counted and the relative amount compared to all imaged cells is determined

Table 2
Imaging parameter for three different microscope systems

Imaging parameter	Wide field (Olympus IX81)	Spinning disc confocal (PerkinElmer Opera)	Confocal (Leica TCS SP5)
Objective	20× air, NA = 0.75	20× water, NA = 0.7	40× oil, NA = 1.25
Pixel size	322.5 nm	330 nm	331 nm
Z-step	2 μm	2 μm	2 μm
Number of planes	24	24	24
Field of view	433 × 330 μm^2	439 × 330 μm^2	338 × 338 μm^2
Number of fields	3 × 3	3 × 3	4 × 3
Acquired area	1,233 × 930 μm^2	1,239 × 930 μm^2	1,238 × 938 μm^2
Channel acquisition	Sequential	Sequential	Sequential
Acquisition time per frame (RGB, in ms)	300, 100, 100	1,000, 40, 40	293, 293, 293
Total acquisition time	51 min	59 min	8 h 13 min

Possible readouts can be manifold; some examples would be the siRNA knockdown-induced up-/downregulation of a certain protein which can be measured via fluorescence labeling and intensity analyses, morphological changes of fluorescently labeled cellular compartments (phenotype detection), or increase/decrease of cellular density. In Fig. 1, a phenotype readout example for the sample screen is shown. Here the phenotypes were determined by a workflow setup using the workflow and data mining manager KNIME (www.knime.org) with additional image processing (KNIP, tech.knime.org/community/image-processing) and WEKA [8] plug-ins, which performed three steps: image segmentation for cell detection, feature extraction for the individual cells, and feature clustering by an x-means algorithm [9]. Further details concerning data analysis using KNIME can be found on our webpage (http://www.bioquant.uni-heidelberg.de/technology-platforms/viroquant-cellnetworks-rnai-screening-facility/data-analysis.html).

Further possible imaging methods spanning low-resolution (high-throughput) to high-resolution (low-throughput) screening are listed in Table 3. The numbers (based on a reference sample with 384 imaging positions) reflect only a small subset of possible screening applications. The choice of the screening microscope to be used depends strongly on the assay and the information content which is needed. For instance, in the case that cell-based intensity expression profiles have to be analyzed, very fast 2D wide-field

Table 3

Overview of different screening microscopes in terms of speed and applicability

Imaging type	Data	Resolution	Speed	Example approach
Wide field, e.g., Olympus IX81	2D	10×, NA = 0.4	~3 h	Intensity profiles Phenotypic penetration
Confocal (spinning disc), e.g., PerkinElmer Opera	3D	60×, NA = 1.4	~10 h	Colocalization Structural information
Confocal (laser scanning), e.g., Leica SP5	3D	63×, NA = 1.4	~20 h	Colocalization Structural information

imaging with low resolution is sufficient. In contrast, if 3D (structural) information of small objects is targeted, confocal imaging is the method of choice.

3.4 Information Workflow for Screening Microscopy

A clear information workflow is mandatory in microscopy-based screening approaches. Here we will describe a typical information workflow for RNAi screening.

On the one hand, a typical data mining workflow contains assay-specific metadata like siRNA library and plate layouts including dedicated transformation protocols which are needed in order to translate the siRNA library plate layout (as given by the manufacturer) to the assay-specific plate layout. On the other hand, the information workflow contains data processing tools and provides analysis results that are based on the plate layout as integrated into the data pipeline upstream of the information workflow: The results from image processing are correlated with the corresponding siRNA approach during statistical data processing. Based on this, bioinformatics tools gain information by network and pathway reconstruction which finally leads to a siRNA correlated interpretation of the entire assay. For that purpose, advanced information workflows consist of different analysis tools and a dynamic database featuring continuous interaction with analysis results and corresponding update of the database, respectively (*see* Fig. 2).

4 Notes

1. The preparation can be done manually or by an automated liquid handler (e.g., "MICROLAB STAR" by Hamilton).
2. In our case either a 96 pin spotter "ChipWriter Pro" by Bio-Rad or a 384 pin spotter developed by Graffinity Pharmaceuticals.
3. The drying time depends on the amount of plates and the number of filled wells. (e.g., drying 4 384 plates takes approximately 20 min).

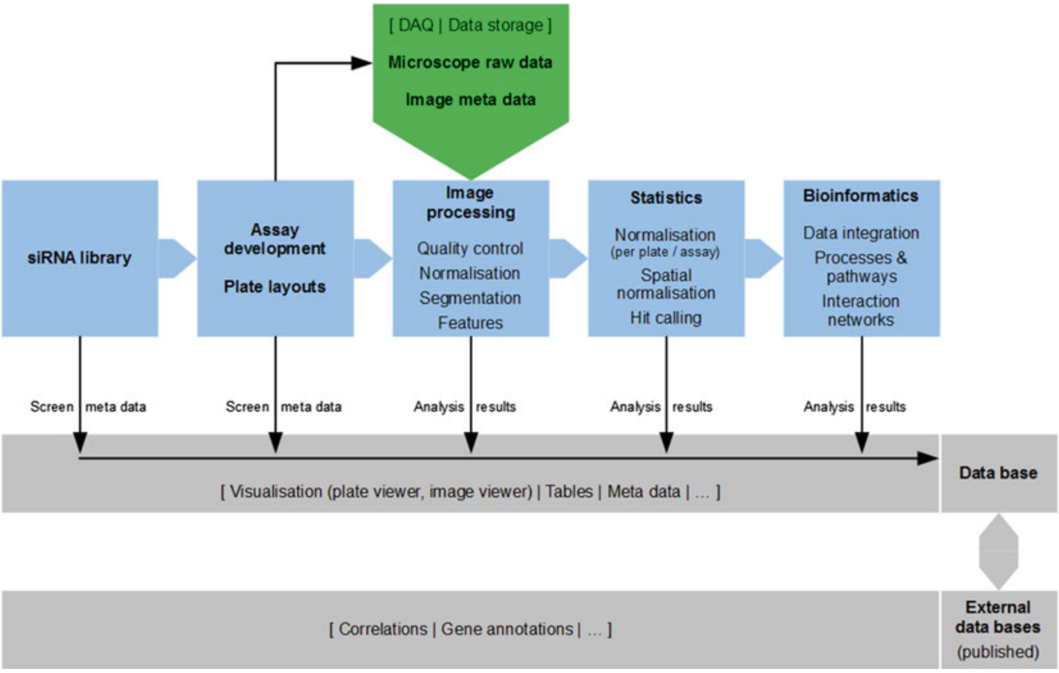

Fig. 2 Illustration of a screening microscopy information workflow. Ideally, the integrated database which finally contains the overall results of the screen is synchronized in a further step with external screening databases in order to search for correlations and overlaps

Acknowledgment

We like to thank Michael Berthold, FB Informatik und Informationswissenschaften, Uni Konstanz, and the whole KNIP-Team for image analysis support. The ViroQuant-CellNetworks RNAi screening facility is supported by the Federal Ministry of Education and Research (BMBF) and funded by the FORSYS program ViroQuant (Project 0313923) and by CellNetworks-Cluster of Excellence (EXC81).

References

1. Neumann B, Walter T, Hériché J-K et al (2010) Phenotypic profiling of the human genome by time-lapse microscopy reveals cell division genes. Nature 464:721–727
2. Liebel U, Starkuviene V, Erfle H et al (2003) A microscope-based screening platform for large-scale functional protein analysis in intact cells. FEBS Lett 20:394–398
3. Hamecher J, Rieß T, Bertini E (2011) A versatile framework for the analysis of high-throughput screening data. In: Koeppl H, Aćimović J, Kesseli J, Mäki-Marttunen T, Larjo A, Yli-Harja O (eds) Eighth international workshop on computational systems biology (WCSB). Tampere University of Technology, Tampere, pp 57–60

4. Carpenter AE, Jones TR, Lamprecht MR et al (2006) Cell profiler: image analysis software for identifying and quantifying cell phenotypes. Genome Biol 7:R100
5. Knapp B, Rebhan I, Kumar A, Matula P et al (2011) Normalizing for individual cell population context in the analysis of high-content cellular screens. BMC Bioinformatics 12:485
6. Sacher R, Stergiou L, Pelkmans L (2008) Lessons from genetics: interpreting complex phenotypes in RNAi screens. Cur Opin Cell Biol 20:483–489
7. Erfle H, Neumann B, Liebel U et al (2007) Reverse transfection on cell arrays for high content screening microscopy. Nat Protoc 2:392–399
8. Pelleg D, Moore A (2000) X-means: extending k-means with efficient estimation of the number of clusters. In: ICML '00 proceedings of the seventeenth international conference on machine learning. Morgan Kaufmann Publishers Inc. 727–734
9. Hall M, Frank E, Holmes G et al (2009) The WEKA data mining software. ACM SIGKDD Explor Newslett 11:10

Chapter 5

Fluorescence Resonance Energy Transfer Microscopy (FRET)

Katarzyna M. Kedziora and Kees Jalink

Abstract

FRET (*Förster* Resonance Energy Transfer) microscopy breaks the resolution limit of light to let us investigate the conformation and function of proteins within living cells. Intensity-based methods are the most popular and direct approach to detect FRET. Among them, detection of sensitized emission signals and ratio imaging of specially designed FRET sensors are routinely used in modern cell biology laboratories. In this chapter, we provide protocols for both these techniques. We guide the reader through the mathematical corrections necessary to calculate the sensitized emission image. We illustrate this approach with an example of studying the interaction of nexin (SNX1) proteins. In the ratio FRET protocol, we focus on monitoring changes in cellular concentration of cAMP with an EPAC-based FRET sensor.

Key words FRET, FilterFRET, Ratio imaging, Nexin, cAMP, EPAC

1 Introduction

Functional imaging allows us to look at protein-protein interactions and protein conformational changes within living cells. One of the most powerful functional imaging techniques is FRET microscopy [1, 2]. Specially designed FRET probes can spy on the activity of proteins (e.g., caspase cleavage assays [3]) or the concentration of small second messengers within a cell—Ca^{2+} [4], cAMP [5], PIP2 [6], etc. FRET microscopy provides answers to an exponentially increasing number of biological questions [7], as it gives insight into details two orders of magnitude smaller (1–10 nm) than the resolution available in classical fluorescence microscopy (~250 nm).

FRET (*Förster* Resonance Energy Transfer) is the physical phenomenon of radiationless transfer of energy between two molecules—the energy donor and acceptor [8]. When two fluorophores are engaged in energy transfer, excitation of the donor molecules results in emission of fluorescence characteristic of the acceptor, rather than the donor (sensitized emission).

Peter J. Verveer (ed.), *Advanced Fluorescence Microscopy: Methods and Protocols*, Methods in Molecular Biology, vol. 1251, DOI 10.1007/978-1-4939-2080-8_5, © Springer Science+Business Media New York 2015

The FRET efficiency (E) is defined as the fraction of the energy absorbed by the donor molecules that is transferred to acceptor molecules. For a given pair of fluorophores, this efficiency depends on their distance but also on their orientation and environment. Changes in FRET efficiency are usually greatest when fluorophores are within a distance 1–10nm from each other (spatial resolution available for FRET). Yet distance and orientation are often impossible to uncouple. Therefore, FRET efficiency responds to the spatial distribution of fluorophores, but it is not a simple “molecular ruler” in the complex settings of a living cell.

Several techniques were developed to study FRET efficiency. Perhaps the most intuitive approaches are based on studying changes in the intensity of fluorescence emission of the donor and acceptor, including simple ratio imaging, detection of sensitized emission, and “filter FRET” [9–11]. Ratio imaging suffices in many cases to detect FRET. This is very convenient as we can draw biologically valid conclusions from this kind of FRET experiment without applying the correction procedures necessary to quantitatively detect sensitized emission. Both of these techniques are described in the current chapter.

To understand the idea of such experiments, consider an experiment in which two molecules of interest are fused to donor and acceptor fluorophores, respectively. In this experiment, fluorescent signal can be collected in three different channels, defined by excitation and detection parameters optimized for donor or acceptor molecules (Fig. 1b, c):

- **d**—donor excitation (λ^{d}_{exc}) and donor emission (λ^{d}_{em}).
- **s**—donor excitation (λ^{d}_{exc}) and acceptor emission (λ^{a}_{em}).
- **a**—acceptor excitation (λ^{a}_{exc}) and acceptor emission (λ^{a}_{em}).

The fluorophores in this thought experiment are designed to be perfect for FRET experiments (Fig. 1a). A huge overlap between the emission spectrum of the donor and the absorption spectrum of the acceptor maximizes the possible efficiency of FRET. Yet there is neither cross-excitation between the fluorophores nor leak-through of fluorescence emission of one of them into the channel optimum for its partner.

The signal of the non-interacting molecules in this experiment can be detected directly in channel **d** (Fig. 1b continuous line) and

Fig. 1 (continued) (**c**, perfect FRETpair; **f**, real-world fluorophores). (**g**) Table summarizing signals present in the channels of a FRET experiment. Note that in case of a perfect FRET pair only diagonal elements are nonzero. Non-diagonal signals are present only in case of leak-through (signals marked with *), cross-excitation (signals marked with $_{**}$), or both (signals marked with $^{*}_{**}$). Donor molecules are essentially not cross-excited at acceptor excitation wavelength (I^{a}_{D-S} and I^{a}_{S} signals are grayed out). Equations to the right of the table introduce parameters linking the signals, originating from the same population of molecules but detected in different channels

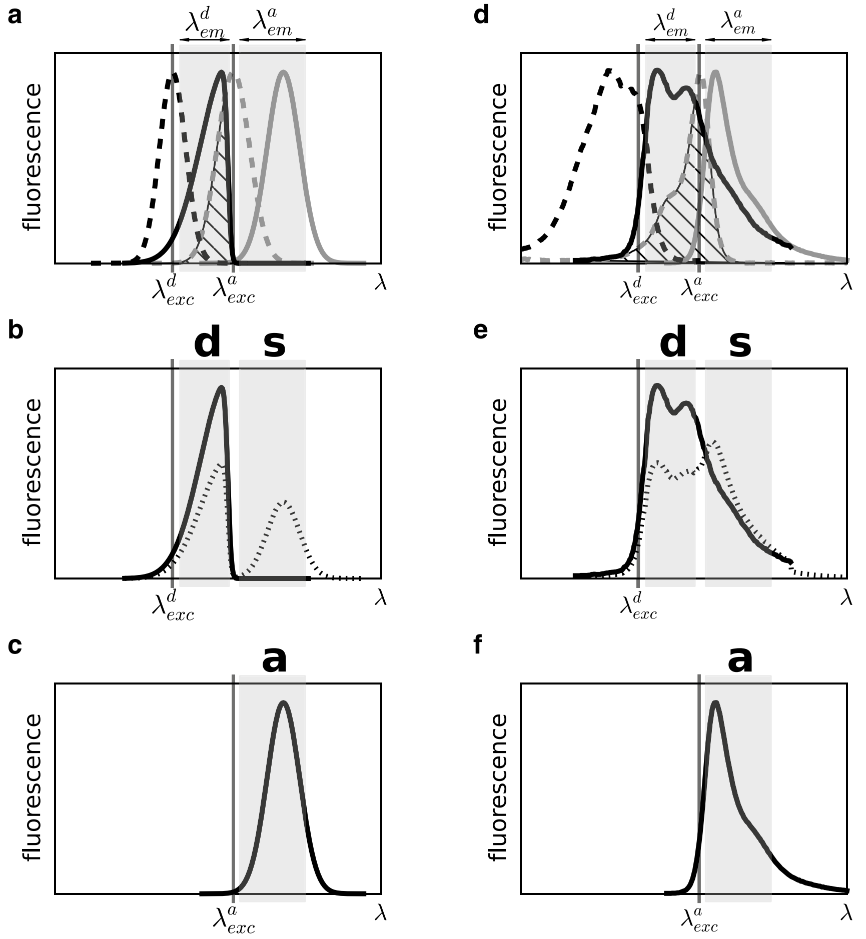

g

detection channels / populations of molecules	**d**	**s**	**a**			
I_{D-S}	$\boldsymbol{I_{D-S}^{d}}$	I_{D-S}^{s} *	I_{D-S}^{a} * **	$\longrightarrow$	$I_{D-S}^{s} = \beta I_{D-S}^{d}$	
I_S	I_S^d *	$\boldsymbol{I_S^s}$	I_S^a **	$\longrightarrow$	$I_S^d = \delta I_S^s$	
I_A	I_A^d * **	I_A^s **	$\boldsymbol{I_A^a}$	$\longrightarrow$	$I_A^d = \alpha I_A^a$	$I_A^s = \gamma I_A^a$

Fig. 1 Signals detected by ratio imaging and FilterFRET. (**a**–**c**) Spectra of a perfect FRET pair, i.e., there is no leak-through and cross-excitation between the fluorophores. (**d**–**f**) Spectra of real-world fluorophores—the CFP and YFP pair. Note that there is considerable leak-through of the emission of each fluorophore into the detection range of its partner. Acceptor molecules can be cross-excited at the donor excitation wavelength, but the excitation of donor molecules with an acceptor excitation wavelength is always negligible. (**a**, **d**) Excitation and emission spectra of a FRET pair with optimized excitation wavelengths (λ^{d}_{exc} and λ^{a}_{exc}) and detection ranges (λ^{d}_{em} and λ^{a}_{em}) indicated (**a**, perfect FRET pair; **b**, real-world fluorophores). (**b**, **e**) Signal detected in **d** and **s** channels with FRET (*dotted line*) or without (*continuous line*). Note that signals in **d** and **s** channels are detected after exciting with donor excitation wavelength (λ^{d}_{exc}), (**b**, perfect FRET pair; **e**, real-world fluorophores). (**c**, **f**) Signal detected in channel **a** (with an excitation optimized for acceptor molecules—λ^{a}_{exc}) is not affected by FRET

channel **a** (Fig. 1c). If molecules of interest can interact with each other, we expect FRET between their fluorophores. The signal in channel **d** is diminished (I_{D-S}) as now the donors that are in a complex transfer part of their absorbed energy to the acceptor molecule, rather than emitting it directly as photons. Signal of acceptors excited by FRET (sensitized emission, I_S) appears in channel **s**. The signal detected in channel **a** does not change as the presence of FRET does not interfere with the signal of (directly) excited acceptor molecules—I_A (Fig. 1c). Thus, we have introduced three detection channels as well as three populations of molecules. This setup is summarized in the table (Fig. 1g). In case of a perfect FRET pair, only diagonal elements of the table are nonzero—i.e., the signal from different populations of molecules can be detected only in the channels optimized for them. It is the signal of sensitized emission detected in channel **s** that provides the information on the presence and magnitude of sensitized emission and as a consequence about the presence of interaction between the studied molecules.

Unfortunately, in the experiments performed with real-world fluorophores, cross-excitation and leak-through usually complicate matters (Fig. 1d). The signal in channel **s** is no longer a measurement of pure sensitized emission. With (Fig. 1e dotted line) or without FRET (Fig. 1e continuous line), it always contains a leak-through signal from donor molecules and a signal from cross-excited acceptor molecules. In this situation, some signal from any of the three populations of molecules can be detected in all three detection channels (Fig. 1g). For example, Hence the signal in channel **d** (first column in the table Fig. 1g) is the sum of the signal from excited non-fretting donor molecules ($I_{D-S}{}^{d}$), signal of sensitized emission leaking back into the donor channel ($I_S{}^{d}$), and signal of cross-excited acceptor molecules also leaking back into the donor channel ($I_A{}^{d}$).

In most experiments, cross-excitation of donor molecules is very small and can be neglected. Hence the signal in channel **a** originates only from the population of acceptor molecules—$I_A{}^{a}$ ($I_{D-S}{}^{a}$ and $I_S{}^{a}$ appear gray in the table in Fig. 1g). Nevertheless, the measurements obtained from the channels **d**, **s**, and **a** do not suffice to calculate the value of the sensitized emission signal ($I_S{}^{s}$) because we have to determine seven different intensities (non-gray in the table) from just three measurements. Note however that in any specific row in the table (Fig. 1g), all the intensities originate from a single population of molecules. Therefore, a set of parameters (α, β, γ, and δ) that relate them to each other can be introduced (see equations to the right of the table in Fig. 1g). These parameters depend solely on the specific settings of the microscope (filters, spectral sensitivity, etc.) and on the spectral characteristics of donor (β) or acceptor (α, γ, and δ) molecules. Therefore, they can be calculated based on measurements of pure populations of donors or acceptors. For example, β just represents the fraction of leak-through of donors in the **s** channel.

On wide-field fluorescence microscopes, these factors are fixed for a given fluorophore. However, the parameters of the excitation and detection pathways in a confocal microscope can be tuned independently. Moreover, the intrinsic instability of laser intensities may easily amount to 5 %, even in modern instruments, making it often impossible to recreate exactly identical settings between the experiments. As a consequence, it is best to collect the data on the magnitude of the correction factors at the same time as performing the FRET experiment.

Based on the measurement of three channels together with four introduced parameters, it is finally possible to solve the system of seven equations to calculate the value of sensitized emission, I_S^s:

$$I_S^s = \frac{\mathbf{s} - \beta\mathbf{d} - (\gamma - \alpha\beta)\mathbf{a}}{1 - \beta\delta}$$

It is crucial to understand what kind of information is provided by the sensitized emission signal. By definition, this signal is a measurement of the amount of energy being transferred. It follows the spatial distribution of interactions between proteins or their activity and depends on the number of fluorophores available to interact with each other. Note that because sensitized emission is sensitive to the parameters of both excitation and emission, it is not possible to quantitatively compare two experiments as long as they are not acquired in exactly the same conditions.

FRET efficiency, on the other hand, is fully quantitative and can thus be compared between different experiments. Whether it is necessary to calculate FRET efficiency depends on the nature of the biological question that underlies the experiments. To calculate FRET efficiency, the measured sensitized emission has to be normalized, e.g., by dividing it by the intensity of the (unquenched) donor signal (E_d), signal of acceptors (E_a), or a combination of the two of them (*see* **Note 1**). Such normalizations are never straightforward. For example, to determine E_d, channels **d** and **s** are used that share the same excitation parameters but differ in sensitivity to donors and acceptors, respectively. On the other hand, the channels **a** and **s** that are needed to calculate E_a may have the same detections settings but do not share the same excitation intensities. Thus, quantitative determination of FRET efficiency requires an additional calibration, the details of which are beyond the scope of this chapter but may be found in literature [11].

The first protocol in the method section of this chapter describes a confocal experiment designed to study the interactions between nexin proteins (SNX1) by measuring FRET. Overexpression of a fusion construct (SNX with fluorescent proteins) enables the detection of signal mainly from tubulovesicular endosomal membranes and from the cytoplasm [12]. Therefore, confocal microscopy was chosen to visualize the fine tubular structures by optical sectioning. In this experiment, we make use of reference cells, expressing only one fluorophore, to calculate the values of the correction parameters.

The second protocol in the method section shows how to measure the intracellular concentration of cAMP with an EPAC-based sensor. For this single-polypeptide FRET sensor, ratio imaging is the method of choice. Ratio imaging, i.e., simply recording the ratio of the **d** and **s** images, is the easiest and most popular technique of FRET microscopy. The ratio image is insensitive to fluctuations in excitation light intensity and it normalizes signal differences caused by cell morphology (e.g., differences in cell height) and in expression level. If the stoichiometry of donor and acceptor fluorophores is fixed, quantitative data can be obtained simply by performing an end-point calibration. This can, for example, be the addition of forskolin together with IBMX which drives cAMP levels so high that they saturate the response of the FRET sensor.

2 Materials

2.1 Cell Culture

1. Cell culture media.
   (a) HEK293 (Embryonal Kidney Cells, American Type Culture Collection), N1E-115 (mouse neuroblastoma), and HeLa (cervical cancer) were cultured in DMEM (Gibco) supplemented with 8 % FCS (Sigma) and 1 % antibiotics (penicillin and streptomycin), in a 5 % CO_2, 37 °C, humidified incubator.
   (b) Cells were imaged in DMEM-F12 medium (Gibco).
   (c) Transfection reagent—PEI (Polyethylenimine, Polysciences) was dissolved in ethanol to the concentration of 1.5 mg/ml and stored in a glass container in −20 °C.
2. Agonists were added from 1,000-fold concentrated stocks:
   (a) Adrenalin (Sigma).
   (b) Forskolin (Santa Cruz Biotechnology).
   (c) IBMX (Sigma).
3. Coverslips (Thermo Scientific, 24 mm, #1) were sterilized in 70 % ethanol. Each coverslip was put in a separate well of a 6-well plate and left in a laminar flow to dry.
4. Plasmids.
   (a) SNX1-CFP and SNX1-YFP constructs were a kind gift of Professor Peter Cullen, University of Bristol, England.
   (b) ^{T}EPAC^{VV} construct was described previously [13].

2.2 Microscopy and Image Analysis

2.2.1 Sensitized Emission

1. A confocal microscope capable of exciting CFP (e.g., with a 442 nm HeCd laser line or a 458 nm Argon laser line) and YFP (e.g., a 514 nm Argon laser line). Readout of the signal should be simultaneous with two PMT detectors in the ranges 470–510 and 520–600 nm (slight deviations from these ranges work too). A high-NA immersion objective chromatically corrected for CFP/YFP detection should be used.
2. Image analysis software that can calculate images represented with floating point numbers (e.g., the freeware package ImageJ [14] or Fiji [15]).

2.2.2 Ratiometric FRET

1. Any inverted fluorescent microscope that can excite CFP (in a range 430–470 nm) and collect donor (470–510 nm) and acceptor (520–600 nm) emission. If a wide-field system is used, it would be beneficial to use an image-splitting device to acquire the images of donor and acceptor simultaneously.
2. Image acquisition software capable of calculating and plotting the ratio between CFP and YFP emission in a selected region of interest (ROI) during an experiment.

2.2.3 Temperature Control

The imaging systems were equipped with a thermostated chamber for live cell imaging (37 °C) with controlled atmosphere of 5 % CO_2 and elevated humidity. If not available, a HEPES-buffered system should be used.

3 Methods

Below we provide two protocols for preparing and performing intensity-based FRET experiments. The first protocol gives detailed information about the use of sensitized emission (FilterFRET) to study interactions of proteins. The second one deals with ratio FRET imaging of dynamic changes of small molecules inside the cells.

3.1 Sensitized Emission/FilterFRET

3.1.1 Planning of the Experiment

1. Select a pair of fluorescent proteins that constitute a good FRET pair. Their spectral properties have to be compatible with the sample to be studied and the image acquisition system (*see* **Notes 2** and **3**).

   To perform the example experiment, the classical FRET pair CFP (Cyan Fluorescent Protein) and YFP (Yellow Fluorescent Protein) has been chosen.
2. Prepare fusion constructs of the proteins of interest with fluorescent proteins. Test extensively whether tagging with fluorescent protein may affect the localization or function of the proteins (*see* **Note 4**).

   For this example two constructs SNX1-CFP and SNX1-YFP have been prepared.

3. Prepare reference cells, i.e., cells that express either donor or acceptor fluorophores alone. Make sure that their signal matches the signal from the cells of interest (*see* **Note 5**). It is convenient to choose the reference constructs so that the reference cells can be easily discriminated from the FRET cells (*see* **Note 6**).

   Reference cells used to perform the example experiment were HEK cells stably expressing CFP or YFP (HEK-CFP and HEK-YFP cell lines).

4. Make sure that the imaging setup is prepared for live cell imaging (*see* **Note 7**).
5. Optimize the image acquisition: optimal alignment (*see* **Note 8**), minimized chromatic aberration (*see* **Note 9**), and flatness of field (*see* **Note 10**) are extremely important in a FRET experiment.

3.1.2 Preparation of a FilterFRET Experiment

1. Day1: Plate cells of interest on glass coverslips (*see* **Note 11**).

   In the example, experiment N115 cells were seeded at 30,000 cells/well in 6-well plates containing sterilized 24 mm coverslips.

2. Day 2: Transfect the cells with the FRET constructs. Transfection protocol is cell-type specific. It may be necessary to refresh the cell culture medium ~12 h after transfection.

   N115 cells were transfected with SNX1-CFP and SNX1-YFP constructs using PEI transfection reagent (1 μg of each DNA + 4.5 μg of PEI for each well).

3. Day 3 (morning): Seed reference cells on the coverslips with the cells of interest (*see* **Note 12**).

   HEK-CFP and HEK-YFP cells growing in a culture flask were trypsinized and seeded onto the coverslips in the 6-well plate at 200,000 cells/well. Allow them minimally 2 h to attach and spread on the surface.

4. Day 3 (afternoon)/day 4: Transfer a coverslip with cells to a chamber suitable for live cell imaging (*see* **Note 13**). Check that the imaging chamber does not leak (*see* **Note 14**) and place it on the microscope. Allow the temperature to equilibrate before starting measurements to avoid focus drift.

3.1.3 FilterFRET Experiment

1. Find a healthy FRET cell that expresses both constructs. The image must also contain at least one donor and one acceptor reference cell.
2. Focus and zoom to optimize the visibility of details in the FRET cell.
3. Acquire three images in channels **d** (donor excitation and donor emission), **s** (donor excitation and acceptor emission),

and **a** (acceptor excitation and acceptor emission)—see introduction. Take care that the acquired images are of high quality (*see* **Notes 15** and **16**) and make sure no motion artifacts are present (*see* **Note 17**).

Images of N115 cells expressing SNX1-CFP and SNX1-YFP constructs together with reference cells are presented in Fig. 2a–c.

If time-lapse imaging is required, repeat the acquisition of **d**, **s,** and **a** images with the desired frequency.

3.1.4 Image Processing of FilterFRET Data

1. Calculate and subtract the value of background in the **d**, **s,** and **a** images. Background should be calculated as the mean value of the signal within a ROI that contains no cells (*see* **Note 18**).
2. Optionally, apply preprocessing procedures. It depends on the biological question and the quality of the acquired images what kind of procedures will be beneficial (*see* **Note 19**).

   In the example experiment, **d**, **s,** and **a** images were subjected to smoothing using a 3 × 3 averaging filter.
3. Calculate the values of the correction parameters:
   (a) Measure the values of the signal of an acceptor reference cell (HEK-YFP) in three channels **d**, **s**, and **a** (d_a, s_a, and a_a).
   (b) Calculate the values of the α, γ, and δ correction parameters:

   $$\alpha = \frac{d_a}{a_a}$$

   $$\delta = \frac{d_a}{s_a}$$

   $$\gamma = \frac{s_a}{a_a}$$

   (c) Measure the values of the signal of a donor reference cell (HEK-CFP) in two channels **d** and **s** (d_d, s_d).
   (d) Calculate the value of the β correction parameter:

   $$\beta = \frac{s_d}{d_d}$$

   (e) Calculate the value of sensitized emission signal according to

   $$I_S^s = \frac{\mathbf{s} - \beta\mathbf{d} - (\gamma - \alpha\beta)\mathbf{a}}{1 - \beta\delta},$$

   as derived in the introduction.

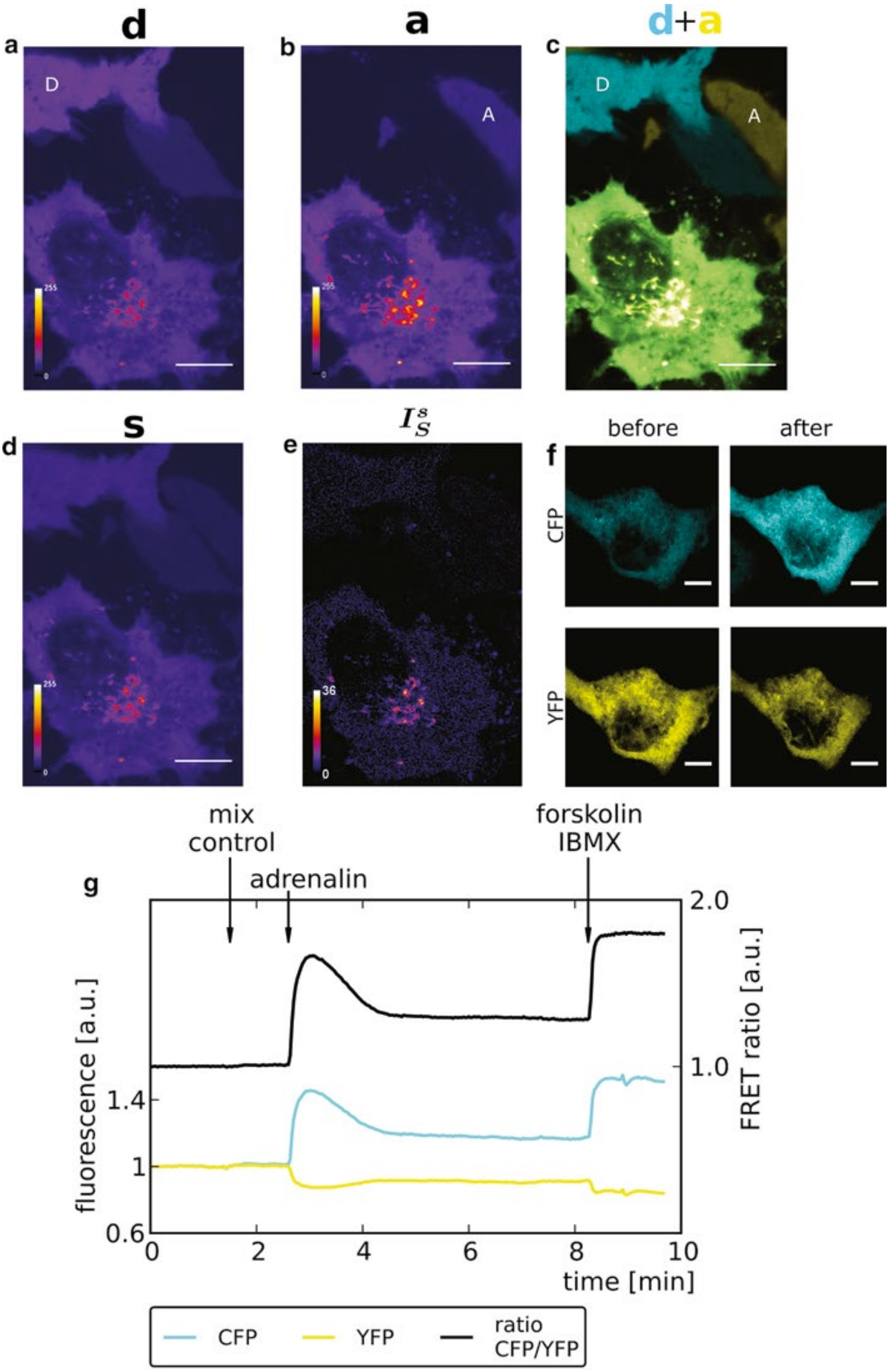

Fig. 2 Sensitized emission and ratio FRET. (**a**–**f**) Sensitized emission. N1E-115 cells expressing SNX1-CFP and SNX1-YFP were seeded together with reference cells (HEK-CFP and HEK-YFP). Images were collected in three channels (**d**, **s,** and **a**). Based on these data, the values of correction parameters were $\alpha = 0.01$, $\beta = 0.56$, $\gamma = 0.23$, $\delta = 0.04$, and sensitized emission (I_S^s) was calculated. Scale bar represents 10 μm. (**a**) Image collected in **d** channel. (**b**) Image collected in **a** channel. (**c**) Overlay of **d** and **a** channels showing FRET cell as well

3.2 Ratio FRET

3.2.1 Planning of a Ratio FRET Experiment

1. Select a FRET sensor to visualize changes in the concentration of a molecule of interest. The ^{T}EPAC^{VV} sensor is used in this example to follow the dynamic behavior of the cytosolic cAMP concentration [13].
2. Select an imaging setup (confocal or wide field—*see* **Notes 20** and **21**) and make sure that it is prepared for live cell imaging (*see* **Note 7**).
3. Find acquisition software that enables simple image analysis during the experiment. In fast dynamic experiments, it is beneficial to have immediate feedback on the result, enabling us to adapt the experiment accordingly.

3.2.2 Preparation of a Ratio FRET Experiment

1. Day 1: Plate cells of interest on glass coverslips.

   In the example experiment, HeLa cells were seeded at 50,000 cells/well in 6-well plates containing sterile coverslips.
2. Day 2: Transfect the cells with the FRET sensor constructs according to common laboratory practice.

   HeLa cells were transfected with the ^{T}EPAC^{VV} construct using PEI transfection reagent (1 μg of DNA + 3 μg of PEI for each well).
3. Day 3: Transfer a coverslip with cells to a chamber suitable for live cell imaging (*see* **Note 13**). Check carefully for fluid leaks (*see* **Note 14**) and place it on the microscope. Allow the temperature of the sample to equilibrate before starting measurements to avoid the main source of drift.

3.2.3 Experiment

1. Find a healthy cell expressing the sensor construct at moderate level (*see* **Note 22**).
2. Focus, zoom in, and set the parameters for the acquisition. Often, the signal from an entire cell is averaged in this kind of experiments. Find a compromise between spatial resolution, signal-to-noise ratio, and bleaching/phototoxic effects.
3. Acquire **d** (donor excitation and donor emission) and **s** (donor excitation and acceptor emission) images.
4. Using proper acquisition software, draw a region of interest around the cell or group of cells. This region is used during the experiment to calculate **d** over **s** ratio (Fig. 2g).

Fig. 2 (continued) as donor only and acceptor only cell. (**d**) Image collected in **s** channel. (**e**) Calculated signal of sensitized emission (I^{s}_{S}), showing that resonance energy transfer only takes place in tubular structures. (**f**, **g**) Ratio FRET. (**f**) Example images of HeLa cells expressing ^{T}EPAC^{VV} construct before and after stimulation with forskolin and IBMX. (**g**) Graph shows changes in signal in (**d**) CFP and (**s**) YFP channels during the experiment. The ratio CFP/YFP follows the changes in cAMP concentration after stimulation of the cells

5. Set a proper sampling rate and duration of the experiment (*see* **Note 23**), and start acquisition of a baseline (*see* **Note 24**).
6. Perform a mock stimulation (negative control) with vehicle (*see* **Note 25**).
7. Add a proper stimulus to the cells (*see* **Note 26**).

   In the example, cells were stimulated with 60 nM of adrenalin (Fig. 2f, g).
8. When the response to the stimulus is complete, add additional stimuli or perform an end-point calibration. This calibration doubles as a positive control for the experiment.

   In the example, cells were stimulated with a mixture of forskolin (5 μM) and IBMX (5 μM) to raise cytosolic cAMP levels maximally (Fig. 2g).

4 Notes

1. The different normalizations E_d and E_a provide fully quantitative yet different information on FRET efficiency. To understand this idea, imagine an experiment in which the acceptors highly outnumber the donor molecules. If in this experiment all the available donor molecules are in complex with acceptors and the efficiency of energy transfer within a pair is 100 %, the calculated value of E_d will be 100 %, but the value of E_a will be very low.
2. The choice of a proper FRET pair may play a significant role in the success or failure of the experiment. Obviously, it has to match the available imaging system. One should also take into account fluorophore brightness and resistance to bleaching, maturation time, possible photochromic changes, and propensity to create dimers. A full discussion on choosing proper fluorophores can be found in a range of excellent publications [16, 17].
3. If possible, the fluorophores should be the only source of signal during the FRET experiment. Therefore, it is important that the level of autofluorescence of the cells is negligible within that spectral range.
4. All considerations of fusion proteins, like N or C terminal tagging or proper folding, apply to the FRET constructs. Moreover, the interaction of the studied proteins should bring the fluorophores in close proximity. Therefore, proper design of the linker region is very important [18, 19].
5. Reference cells are to be imaged simultaneously with the cells of interest. Due to the limited dynamic range of microscopic images, it is important that fluorescence intensity of both cell types is approximately similar.

6. Reference cells serve only as a source of pure signal from donors or acceptors. These can be transiently transfected cells (select cells that can be easily and efficiently transfected—such as HEK293T cells) or stable cell lines. For convenience, the distribution of fluorophores should allow easy distinction between reference cells and the cells of interest. Moreover, the reference signal should be present exactly in the plane of interest in confocal imaging—for example, if the experiment is designed to study the FRET signal within a cell nucleus, a reference signal localized on the ventral membrane is of little use.
7. Depending on the duration of the experiment (time lapse versus single measurement), it is important to keep cells healthy and avoid stressing them during imaging. Discussion on proper imaging media can be found in literature [20].
8. Proper alignment of the optical system is very important because misalignment may cause spatial shift between the images, as well as necessitate very high excitation power in order to acquire images of good S/N ratio.
9. Chromatic aberration of the setup should be minimized as much as possible. The use of objectives specially designed to decrease the chromatic shift in the spectral range of choice is highly recommended.
10. It is important to ensure highly homogenous illumination within the field of view. If the flatness of the field is not satisfactory, shading correction procedures should be applied to the acquired images [21].
11. Plating density depends on the specific cell type and on the selected protocol for transfection. However, care should be taken that on the day of experiment there is enough space on the coverslip for the reference cells to adhere.
12. The number of reference cells of each type should exceed the number of cells of interest 3–5 times. This abundance of reference cells ensures that most FRET cells are accompanied by at least one of each reference cell types. The specific number of reference cells needed is cell-type specific, but in our hands, seeding at ~20 % density gives good results.
13. Transfer of a coverslip should be fast to prevent cells from drying. Sharpened forceps make it easy to pick up the coverslip from the 6-well plate. Add imaging medium immediately after transfer.
14. Any leakage of an imaging medium will deteriorate image quality and may be harmful to the microscope. Clean the bottom of the coverslip in the imaging chamber and dry it with a paper tissue. Any leakage can be easily found by checking for moist spots (which will appear dark) on a dry tissue pressed to the bottom.

15. For imaging, use the full dynamic range available to maximize the amount of collected information. However, overexposed pixels should definitely be avoided as they introduce bias in the calculated results.
16. It is critical to acquire images with maximum signal-to-noise ratio. To introduce necessary corrections, several calculations have to be performed with the images. This inevitably leads to the propagation of noise. If the quality of acquired images is not satisfactory, the calculated results may become very noisy and difficult to interpret. Acquisition of good quality images may require averaging and/or accumulating individual images. For time lapse, balance between the quality of the images and the well-being of the cells.
17. **d** and **s** images can easily be acquired simultaneously on a confocal setup, but to acquire the **a** image, a change in excitation light is necessary. To avoid possible movement artifacts (e.g., when imaging fast-moving vesicles), it is highly advisable to acquire **d**, **s,** and **a** images by changing the excitation light between lines and not frames on a confocal system.
18. Make sure that the region of interest selected to calculate the value of the background does not contain any very dim cells. This may be easier to check by using a LUT (look-up table) that emphasizes differences in dim regions.
19. Standard procedures include smoothing (to reduce noise) and thresholding (to exclude some regions from analysis). Exclusion of some regions may help in the interpretation of calculated results; for example, in background regions noise may be pronounced. Overexposed pixels must also be excluded from the analysis, as they do not provide useful information. However, one has to check whether such operations introduce bias in the results.
20. Confocal microscopy is of course preferred if small spatial details are to be resolved (e.g., if a FRET sensor localizes to some small structures within a cell). Wide-field microscopes are usually faster and may be less detrimental to the cells. In case very fast readout (ms or sub-ms temporal resolution) is required, consider using a microscope that does not create an image but rather collects all photons together on two PMTs.
21. On a confocal microscope, it is straightforward to acquire **d** and **s** images simultaneously. On a wide-field microscope, one has to change emission filters and acquire these two images sequentially. Besides the danger of introducing motion artifacts, this also necessitates double exposure and thus more photobleaching. Therefore, it is advisable to use a beam splitter device that enables simultaneous detection of both channels side by side on a single CCD [11].

22. Very high expression levels of fluorescent constructs may affect cell morphology and deteriorate the FRET response as well as cause saturation. On the other hand, a low signal-to-noise ratio may become a problem in low expressing cells.
23. Optimize the timing of the experiment as needed: the faster the biological process, the higher the necessary time resolution, but this will also affect bleaching and phototoxic effects.
24. Make sure that the baseline is long enough to give you a good indication of the variability and drift in the signal. This depends on the signal-to-noise ratio, stability of the system, and biological fluctuations.
25. Make sure to properly mix the medium after addition of stimuli to avoid gradients of concentration (pipetting up and down ~5 times with a P200 pipet in a 2 ml imaging dish should provide proper mixing). Mix the medium slowly and never point the pipet tip directly at the imaged cells in order not to squirt them away.
26. Stimulants are most often added from concentrated stocks. Take up the required volume of stimulus solution in a P20 pipet. Next, gently remove the yellow tip with the stimulus solution from the P20 and attach it to a P200 pipet. Make sure that the stimulus is not ejected in this step by keeping the P200 pipet piston slightly pressed; release it slowly while attaching the tip. The underpressure created in this way will prevent stimulus from spilling from the tip. Add the stimulus by mixing the sample medium several times with the P200 pipet (*see* **Note 25**).

References

1. Ciruela F, Vilardaga JP, Fernandez-Dueñas F (2010) Lighting up multiprotein complexes: lessons from GPCR oligomerization. Trends Biotechnol 2:138–147
2. Brunger AT, Strop P, Vrljic V et al (2011) Three dimensional molecular modeling with single molecule FRET. J Struct Biol 173:497–505
3. Xu X, Gerard ALV, Huang BCB et al (1998) Detection of programmed cell death using fluorescence energy transfer. Nucleic Acids Res 26:2034–2035
4. Nagai T, Sawano A, Park ES et al (2001) Circularly permuted green fluorescent proteins engineered to sense Ca2+. Proc Natl Acad Sci U S A 98:3197–3202
5. Ponsioen B, Zhao J, Riedl J et al (2004) Detecting cAMP-induced Epac activation by fluorescence resonance energy transfer: Epac as a novel cAMP indicator. EMBO Rep 5: 1176–1180
6. Hertel F, Switalski A, Mintert-Jancke E et al (2011) A genetically encoded tool kit for manipulating and monitoring membrane phosphatidylinositol 4,5-bisphosphate in intact cells. PLOS One 6:e20855
7. Sun Y, Wallrabe H, Seo S et al (2011) FRET microscopy in 2010: the legacy of Theodor Forster on the 100th anniversary of his birth. Chem Phys Chem 12:462–474
8. Forster T (1946) Energiewanderung und Fluoreszenz. Naturwissenschaften 6:166–175
9. Gordon G, Berry G, Liang XH et al (1998) Quantitative fluorescence resonance energy transfer measurements using fluorescence microscopy. Biophys J 74:2702–2713

10. Wouters FS, Verveer PJ, Bastiaens PIH (2001) Imaging biochemistry inside cells. Trends Cell Biol 11:203–211
11. Jalink K, van Rheenen J (2009) FilterFRET: quantitative imaging of sensitized emission. Fret and Flim Techniques, vol. 33, 1st edn. Elsevier B.V., pp. 289–349
12. Zhong Q, Lazar CS, Tronchere H et al (2002) Endosomal localization and function of sorting nexin 1. Proc Natl Acad Sci USA 99: 6767–6772
13. Klarenbeek JB, Goedhart J, Hink MA (2011) A mTurquoise-based cAMP sensor for both FLIM and ratiometric read-out has improved dynamic range. PLOS One 6:e19170
14. Schneider CA, Rasband WS, Eliceiri KW (2012) NIH Image to ImageJ: 25 years of image analysis. Nat Methods 9:671–675
15. Schindelin J, Arganda-Carreras I, Frise E et al (2012) Fiji: an open-source platform for biological-image analysis. Nat Methods 9: 676–682
16. Shaner NC, Lin MZ, McKeown MR et al (2008) Improving the photostability of bright monomeric orange and red fluorescent proteins. Nat Methods 5:545–551
17. Stepanenko OV, Stepanenko OV, Shcherbakova DM et al (2011) Modern fluorescent proteins: from chromophore formation to novel intracellular applications. BioTechniques 51:313–318
18. Komatsu N, Aoki K, Yamada M et al (2011) Development of an optimized backbone of FRET biosensors for kinases and GTPases. Mol Biol Cell 22:4647–4656
19. Chen H, Puhl HL, Koushik SV et al (2006) Measurement of FRET efficiency and ratio of donor to acceptor concentration in living cells. Biophys J 91:39–41
20. Goldman RD, Spector DL (2005) Live cell imaging: a laboratory manual. Cold Spring Harbor Laboratory, Cold Spring Harbor, NY
21. Tomazevic D, Likar B (2002) Comparative evaluation of retrospective shading correction methods. J Microsc 208:212–223

Chapter 6

Localizing Protein–Protein Interactions in Living Cells Using Fluorescence Lifetime Imaging Microscopy

Yuansheng Sun and Ammasi Periasamy

Abstract

In the past decade, advances in fluorescence lifetime imaging have extensively applied in the life sciences, from fundamental biological investigations to advanced clinical diagnosis. Fluorescence lifetime imaging microscopy (FLIM) is now routinely used in the biological sciences to monitor dynamic signaling events inside living cells, e.g., Protein–Protein interactions. In this chapter, we describe the calibration of both time-correlated single-photon counting (TCSPC) and frequency domain (FD) FLIM systems and the acquisition and analysis of FLIM-FRET data for investigating Protein–Protein interactions in living cells.

Key words Fluorescence lifetime imaging microscopy (FLIM), Förster resonance energy transfer (FRET), FLIM-FRET, Time-domain FLIM, Time-correlated single-photon counting (TCSPC) FLIM, Frequency-domain FLIM, Protein–protein interactions

1 Introduction

1.1 Overview of FLIM and Its Applications in the Biological Sciences

Fluorescence lifetime is the average time a molecule spends in the excited state before returning to the ground state, typically with the emission of a photon. The natural fluorescence lifetime of a fluorophore (in the absence of non-radiative processes) is an intrinsic property of the fluorophore. The natural fluorescence lifetimes of widely used fluorescent probes in cellular imaging such as fluorescent proteins and organic dyes are typically within 10 ns. The first nanosecond lifetime measurements using optical microscopy were made in 1959 [1, 2]. Since then, numerous FLIM methodologies have evolved for various biological and clinical applications [3, 4]. Although FLIM techniques can be challenging for biologists without a physics background, they provide an unprecedented level of information about the functions, dynamics, and interactions of proteins in living cells under physiological conditions at high temporal and spatial resolutions.

The fluorescence lifetime of a fluorescent molecule carries information about its local microenvironment and can be very

Peter J. Verveer (ed.), *Advanced Fluorescence Microscopy: Methods and Protocols*, Methods in Molecular Biology, vol. 1251, DOI 10.1007/978-1-4939-2080-8_6, © Springer Science+Business Media New York 2015

sensitive to certain environmental changes. Therefore, cellular responses to events such as changes in temperature, pH, and ion concentrations (e.g., calcium) can be measured accurately using FLIM. For example, high-speed widefield FLIM was employed to measure the change in calcium concentration in live cells using calcium sensitive probes (e.g., Oregon Green) [5–7]. Two-photon excitation (TPE) FLIM was used to map the response of rigor cross-bridges to stretching of the myosin essential light chain in skeletal muscle fibers by probing the microenvironment of the interface region of the myosin lever arm domain with Coumarin [8]. FLIM was implemented to investigate different conformational changes of the presenilin 1 (PS1) protein that is associated with Alzheimer's disease (AD) providing further understanding of the AD diagnosis [9]. FLIM techniques were also applied in plant biology. Eckert et al. [10] used the widefield single-photon counting FLIM technique to investigate the fluorescence dynamics of the chlorophyll d-containing cyanobacteria *Acaryochloris marina*.

FLIM has been employed to investigate a number of human diseases using endogenous autofluorescent molecules in human cells and tissues and shows great promise in several clinical applications. Nicotinamide adenine dinucleotide (NAD^+) is a coenzyme found in all living cells and carries electrons from one reaction to another through redox reactions in metabolism. When NAD^+ accepts electrons from other molecules, it forms NADH which is highly fluorescent with peak absorption and emission maxima at 340 and 460 nm, respectively [11]. NADH can be imaged with TPE microscopy [12], serving as a convenient noninvasive fluorescent probe of the cellular metabolic state. A new window for cancer diagnosis was opened up using TPE FLIM to detect the free (shorter lifetime) to bound (longer lifetime) NADH ratio to monitor cellular metabolic states [13, 14]. Monitoring the autofluorescence from human skin, the FLIM methodology was applied to distinguish between basal cell carcinomas and surrounding uninvolved skin [15].

1.2 FLIM and Förster Resonance Energy Transfer (FRET)

One of the major FLIM applications is to measure FRET, which is the non-radiative energy transfer from an excited molecule (the donor) to another nearby molecule (the acceptor), via a long-range dipole–dipole coupling mechanism. The most basic concepts of FRET are described by [16–19]:

$$E = R_0^6 / \left(R_0^6 + r^6 \right) \tag{1}$$

$$R_0^6 = 0.211 \times \left\{ \kappa^2 \times n^{-4} \times \mathrm{QY}_\mathrm{D} \times J \right\}^{1/6}, \quad J = \varepsilon_\mathrm{A} \frac{\int_0^\infty f_\mathrm{D}(\lambda) f_\mathrm{A}(\lambda) \lambda^4 d\lambda}{\int_0^\infty f_\mathrm{D}(\lambda) d\lambda} \tag{2}$$

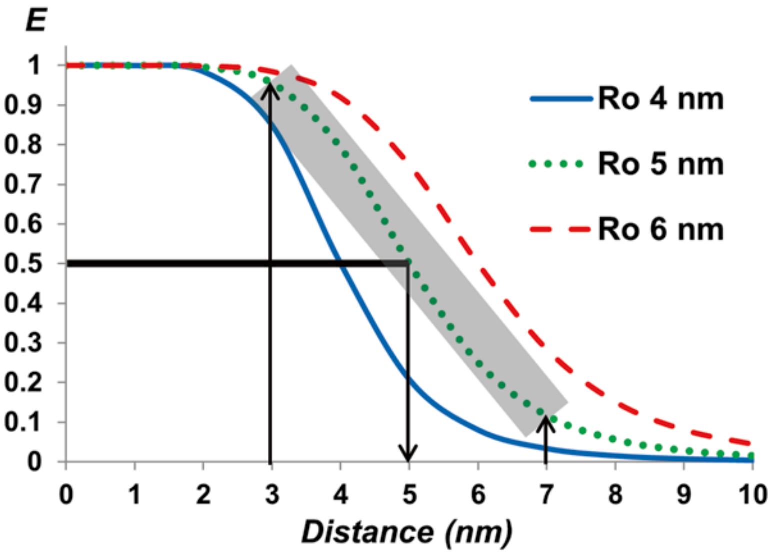

Fig. 1 FRET efficiencies (*E*) versus the separation distance between the donor and the acceptor (*r*), based on Eq. 1, for a Förster distance (R_0) of 4, 5, or 6 nm, at which E is 50 %. Due to the dependence on the sixth power of the donor-acceptor distance, *E* is very sensitive to the distance change around R_0—as an example highlighted for the R_0 of 5 nm, the E values fall sharply for the distance increase from 3 nm to 7 nm

As shown in Eq. 1, the efficiency of energy transfer (E) from the donor to the acceptor is dependent on the inverse of the sixth power of the distance (r) separating them, subject to the Förster distance "R_0," at which half of the excited-stated energy of the donor is transferred to the acceptor ($E = 50$ %). Determination of R_0 (in Ångstrom) for a FRET pair is given by Eq. 2, where κ^2 is the orientation factor between the donor emission and acceptor absorption dipoles, ranging from 0 to 4; n is the medium refractive index; QY_D is the donor quantum yield; J is the degree of the donor emission-acceptor absorption spectral overlap; ε_A is the extinction coefficient of the acceptor at its peak absorption wavelength; and $f_D(\lambda)$ and $f_A(\lambda)$ are the normalized donor emission and acceptor absorption spectra, respectively. For the majority of FRET pairs, the R_0 values are on the scale of a few nanometers. Thus, FRET is usually limited to distances less than about 10 nm. Due to the dependence on the sixth power of the donor-acceptor distance, E is very sensitive to the distance change around R_0 at the sub-nanometer scale (Fig. 1). Therefore, measuring FRET provides a sensitive tool for investigating a variety of phenomena that produce changes in molecular proximity [20–24].

Using FLIM, FRET events can be identified by measuring the reduction in the donor lifetime that results from quenching in the presence of an acceptor, and E can be estimated from the donor lifetimes determined in the absence (τ_D—unquenched lifetime) and the presence (τ_{DA}—quenched lifetime) of the acceptor, as shown by Eq. 3 [11].

$$E = 1 - \frac{\tau_{DA}}{\tau_D} \tag{3}$$

Since only donor signals are measured for determining E in FLIM-FRET, the method does not usually require the corrections for spectral bleedthrough that are necessary for intensity-based FRET measurements of the sensitized emission from the acceptor [20–24]. The fluorescence lifetime is insensitive to changes in fluorophore concentration, excitation light intensity, or light scattering but sensitive to environmental changes—these facts make FLIM-FRET an accurate method for FRET measurements. The FLIM-FRET method has been routinely applied in many laboratories including ours for studying Protein–Protein interactions and investigation of signaling events in a variety of biological systems [9, 25–46].

1.3 Overview of FLIM Techniques

FLIM techniques are generally subdivided into time-domain (TD) and frequency-domain (FD) methods. The basic physics that underlie the two methods is essentially identical, since they are finite Fourier transforms of each other. In TD FLIM, a fluorophore is excited by a pulsed light source, which is synchronized to high-speed detectors and electronics; its fluorescence decay profile is directly measured in a number of (at least two) sequential time bins after (and relative to) the excitation pulse (time zero); its fluorescence lifetime can be estimated by analyzing the recorded decay profile (Fig. 2a). In FD FLIM, a modulated light source is used to

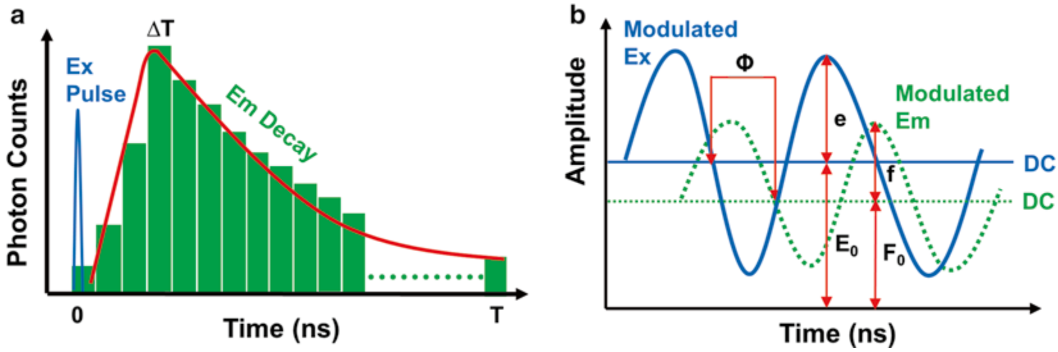

Fig. 2 The fundamental principles of time-domain (TD) and frequency-domain (FD) FLIM measurements. (**a**) TD FLIM usually employs a pulsed light source that is synchronized to high-speed detectors and electronics to measure the emission (Em) signals at different time bins relative to the excitation (Ex) pulse (time zero), directly producing a fluorescence decay profile; the fluorescence lifetime is estimated by analyzing the recorded decay profile. (**b**) FD FLIM typically uses modulated light sources and detectors and measures the phase shift Φ and the amplitude attenuation M {$M = (f/F_0)/(e/E_0)$} of the emission relative to the excitation, which are then analyzed to estimate the fluorescence lifetime

excite a fluorophore, whose emission signals are measured by a detector modulated either at the same modulation frequency of the excitation (homodyne) or at a slightly (a few hundred to thousand hertz) different frequency (heterodyne); analyzing the phase shift(s) and amplitude attenuation(s) of the emission relative to the excitation makes it possible to extract the fluorescence lifetime of the fluorophore (Fig. 2b). The repetition rate of the excitation source used in TD FLIM or the fundamental modulation frequency of the excitation source used in FD FLIM needs to be chosen according to the fluorescence lifetime to be measured. The rate or frequency for measuring nanosecond lifetimes in most biological applications should be on the megahertz scale, e.g., 10–100 MHz.

Many TD and FD FLIM techniques were developed and demonstrated for various biological applications. Fortunately, most of them are now commercially available, e.g., from Becker and Hickl (BH, www.becker-hickl.de), Picoquant (www.picoquant.com), ISS (www.iss.com), Lambert Instruments (www.lambert-instruments.com), and Intelligent Imaging Innovations (www.intelligent-imaging.com). These systems can be stand alone or integrated with existing widefield or confocal or multiphoton (MP) microscopy systems. Each FLIM technique has its own strengths and limitations and choosing the most suitable one is really dependent upon the biological investigation at hand. Several FLIM techniques are compared in Table 1.

1.4 Overview of FLIM Data Analysis

1.4.1 The General Fluorescent Decay Kinetics Model

In the majority of FLIM measurements, a fluorescent decay is measured from a population of fluorescent molecules. The intrinsic decay kinetics $f(t)$, represented by the numbers of emitted photons as a function of time relative to the excitation, can be modeled by Eq. 4:

$$f(t) = f_0 \sum_{n=1}^{N} \left\{ a_n \exp\left(-t/\tau_n\right) \right\} \tag{4}$$

where f_0 is the number of emitted photons at time zero and N $(N \geq 1)$ is the number of different fluorescent species—each one is associated with a distinct fluorescence lifetime (τ_n), and its percentage over the number of total fluorescent molecules is often termed as the pre-exponential factor (a_n). For a multi-exponential case $(N > 1)$, the apparent lifetime (τ_a) calculated by Eq. 5 is often used to indicate the mean lifetime of all fluorescent species.

$$\tau_a = \sum_{n=1}^{N} \left(a_n \tau_n \right), \quad \sum_{n=1}^{N} a_n = 1 \tag{5}$$

A variety of computer algorithms have been developed for FLIM data analysis [3, 4, 11]. Some are associated with specific FLIM data acquisition methods. For example, the rapid lifetime

Table 1
Comparison of several commonly used FLIM techniques

FLIM detection	Typical implementation
Time-correlated single-photon counting (TCSPC) TD FLIM	TCPSC [47] is typically implemented on laser scanning microscopes using a pulsed single- or multiphoton laser, a fast PMT or APD detector (timing jitter <300 ps), and TCSPC electronics [5, 30, 48, 49]. The TCSPC device synchronizes the detector and the scanning clock to the excitation pulse and records the arrival time and spatial information for each detected photon. Accumulating photons for thousands or millions of excitation pulses, a “photon counts” histogram (fluorescence decay profile) for estimating the fluorescence lifetime can be built at each pixel (or voxel) of a 2D (or 3D) image. A multichannel PMT module has also been employed in TCSPC FLIM to obtain spectrally resolved lifetimes [34, 50]
Gated image-intensified camera TD FLIM	The gating-camera FLIM is typically implemented on widefield and spinning-disk confocal microscopes using a single-photon pulsed laser, a gated image-intensified camera, and gating-control electronics. The gating-camera can be operated at a superfast speed to detect photons within a time (gating) window for a few hundred picoseconds to a few milliseconds relative to the excitation pulse [5, 27]. A number of images are acquired in sequential gating windows to estimate the lifetimes. Extracting single-component lifetimes requires collecting two gated images at minimum, which may only take a few seconds [6, 51]. Due to the fast data acquisition speed, the gating-camera FLIM was implemented in a high-content screening platform [45, 52]
Streak camera TD FLIM	A streak-camera system, consisting of a streak scope and a fast CCD camera, can be operated to transform the temporal profile of a light pulse into a spatial profile on a detector by causing a time-varying deflection of the light across the width of the detector [53]. In streak-camera FLIM, each line of an image consists of the time resolved information for a pixel location along the X-axis and a series of images are acquired for the Y-axis. The streak-camera FLIM uses a pulsed laser that is synchronized to a streak-camera system and was implemented on MP laser scanning microscopes [29, 31, 53]. Using a spectrograph device, the streak-camera FLIM was also demonstrated to obtain spectrally resolved lifetimes [31]
Heterodyne digital FD FLIM	In traditional heterodyne FD FLIM, both the light source and the detector are modulated, but at a slightly different frequency, e.g., a few hundred hertz. The recently developed digital FD FLIM employs a modulated pulsed excitation source (one- or multiphoton laser), but does not modulate the detector at all, making the technique much more simpler to implement in laser scanning confocal microscopes [54]. In digital FD FLIM, the detector (PMT or APD) is working in a manner like photon counting, and all operations including the generation of the light modulation frequency, the generation of the cross-correlation sampling frequency, and the assignment of the time of arrival of a photon to a bin are digital, allowing multifrequency measurements (for extracting multicomponent lifetimes) done simultaneously and thus greatly improving photon efficiency and data acquisition speed [46, 54]
Homodyne FD FLIM using an image-intensified camera	The camera-based FD FLIM is typically implemented in widefield or spinning-disk confocal microscopes, using an LED or diode laser excitation light source and an image-intensified camera, both modulated at the same frequency (homodyne) [55–57]. This FLIM method is very fast since only several images need to be acquired to obtain one lifetime image and this may only take only a few seconds [58]

determination (RLD) algorithm was developed to analyze time-resolved images acquired by a gated image-intensified camera [5, 27, 59]. Some FLIM data analysis strategies vary depending upon the particular biological models. For example, global analysis [60–63] can significantly improve the signal-to-noise ratio (SNR) of fluorescence lifetime images, but the method requires the assumption that identical fluorescence relaxation parameters pertain to the pixels grouped together for analysis, which may not be valid in many experimental systems.

1.4.2 Fitting Analysis of TCSPC FLIM Data

Fitting analysis is commonly used in both TD and FD FLIM data analyses [11, 64]. In TCSPC FLIM, a measured decay $g(t)$ is typically represented as the convolution of the intrinsic decay $f(t)$ (Eq. 4) and the instrument response function (IRF) of the FLIM system plus noise $n(t)$, as shown in Eq. 6:

$$g(t) = \mathrm{IRF} \times f(t) + n(t) \tag{6}$$

Given the IRF and some a priori parameters of the intrinsic decay, e.g., the number of exponential components (N in Eq. 4), an iterative fitting (deconvolution) procedure is usually applied to estimate the values of each lifetime component (τ_n in Eq. 4) and the corresponding pre-exponential factor (a_n in Eq. 4). At each iterative step k, an estimated $g_k(t)$ is calculated from the convolution of the IRF and the intrinsic decay modeled by the estimated lifetimes and pre-exponential factors; the estimated $g_k(t)$ is then compared to the measured $g(t)$ to produce the standard weighted least squares (χ^2), which will be used as a criterion to evaluate the fitting significance and to determine whether or not to stop the iterative fitting procedure. The value of χ^2, indicating a good fit for an appropriate model and a random noise distribution, should be close to 1 predicted by Poisson statistics with enough data points for fitting [11, 64].

1.4.3 Model-Free Phasor Plot Analysis of FD FLIM Data

In FD FLIM, the measured data at each pixel is usually composed of both phase delay (Φ) and amplitude modulation ratio (M), as shown in Fig. 2. The lifetime of a single fluorescent species ($N = 1$ in Eq. 4) can be directly calculated from either the phase ($\tau\Phi$—the phase lifetime) or the modulation by Eq. 8 (τ_M—the modulation lifetime).

$$\tau_\Phi = \tan\Phi / \omega \tag{7}$$

$$\tau_M = \sqrt{1 - M^2} / (M\omega) \tag{8}$$

where ω is the modulation frequency. A difference between $\tau\Phi$ and τ_M is an indication that the data does not follow a mono-exponential time course. For a multi-exponential case ($N > 1$ in Eq. 4), the phase and modulation values are often measured at several modulation frequencies. From low to high frequencies, the phase delays increase from 0 to 90°, while the modulation ratios decrease from 1 to 0. To estimate the values of each lifetime component (τ_n in Eq. 4) and the associated pre-exponential factor (α_n in Eq. 4), the weighted least squares numerical approach can be used to fit both phase and modulation values measured at different frequencies, given some priori parameters of the exponential model, e.g., the number of exponential components (N in Eq. 4). Similar to TCSPC FLIM data fitting analysis, the calculated χ^2 and residuals provide an evaluation for the fitted results.

Other than the fitting analysis, a graphical method for FLIM data presentation and analysis was developed. This method, named as polar plot [65], AB plot [66, 67], or phasor plot [68, 69] by different groups, is essentially based on the transformation of FD FLIM data defined by Eq. 9.

$$G_\omega = M_\omega \cos(\Phi_\omega),\ S_\omega = M_\omega \sin(\Phi_\omega) \tag{9}$$

Given a modulation frequency ω, each measured FD FLIM data point (Φ_ω and M_ω) can be directly located in a 2D plot using G_ω as the horizontal axis and S_ω as the vertical axis (Eq. 9). For a single-lifetime species, the phase (Eq. 7) and modulation (Eq. 8) lifetimes are equal, from which a relationship between the G_ω and S_ω coordinates shown in Eq. 10 can be derived.

$$S_\omega{}^2 + (G_\omega - 0.5)^2 = 0.25 \tag{10}$$

This $G_\omega - S_\omega$ relationship is represented as a semicircle curve centering at ($G_\omega = 0.5$, $S_\omega = 0$) with a radius of 0.5 in the phasor plot. The semicircle curve indicates the lifetime trajectory with decreasing lifetime from left to right, where (1, 0) indicates lifetimes near zero to (0, 0) being infinite lifetime. A point falling on the semicircle will have only a single lifetime, while a point that falls inside the semicircle will have multiple lifetime components.

Since no fitting is involved, the phasor plot approach is independent of any underlying physical model. By plotting raw data in the phasor plot, one can distinguish between single- and multicomponent lifetimes, identify the lifetime value of a single-lifetime species on the semicircle, and also visualize the relative lifetime changes between complex lifetime distributions. More conveniently, many data distributions measured from different samples can be directly compared in a same phasor plot. In FLIM-FRET measurements, FRET can be identified by comparing the phasor plot distributions of the donor fluorophores in the donor-alone versus the "donor + acceptor" specimens. Several analytical tools were developed based on the polar, AB, or phasor plot approach for multicomponent analysis without nonlinear fitting [66, 67] and determining the FRET efficiency [57, 68], e.g., the "FRET Trajectory" functions in the SimFCS software (www.lfd.uci.edu/globals) [68]. It should be noted that these methods can be also employed to analyze raw TCSPC FLIM data after being transformed into the frequency domain through the digital Fourier transform—such a function is provided by the SimFCS software [68].

1.5 Outline of a FLIM-FRET Protocol

A typical FLIM-FRET experiment involves three steps:

1. Calibrate the FLIM system with fluorescence lifetime standards.
2. Acquire FLIM data from biological specimens, typically including specimens that only have the donor and from specimens that contain both the donor and the acceptor.
3. Analyze the data to extract the lifetime information and interpret the analyzed data to illustrate the biological activity or other experimental objectives.

Here, we describe the procedures that are necessary to use both a TCSPC FLIM method and a FD FLIM method to monitor Protein–Protein interactions in live specimens based on FRET. Both synthetic and real biological models are used for FLIM-FRET demonstrations in live cells.

2 Materials

2.1 TPE TCSPC FLIM System

The basic principle of TCSPC FLIM is described in Fig. 2a and Table 1.

1. The TPE TCSPC FLIM system is implemented on a Bio-Rad Radiance 2100 confocal/MP microscope system using the MP system configuration, which is operated by the Bio-Rad LaserSharp 2000 software (www.zeiss.com/micro). The Bio-Rad scanning unit is attached to a Nikon TE300 inverted microscope.
2. The TCSPC module is a BH SPC-150 computer board (www.becker-hickl.de).
3. The FLIM detector is a BH PMC-100-0 PMT, which has a response time of approximately 150 ps [30, 46] and is attached to the non-descanning side port of the microscope.
4. The TPE laser is a Coherent 10 W Verdi pumped tunable (700–1,000 nm) mode-locked ultrafast (pulse width <150 fs) pulsed (repetition rate of 78 MHz) laser (www.coherent.com).
5. A remotely controlled filter wheel containing several emission filters is placed before the FLIM detector. The 480/40 nm (for Coumarin 6 and Cerulean) and 525/50 nm (for Fluorescein) emission filters (www.chroma.com) were used.
6. A Nikon 60X/1.2NA water objective was used for all TCSPC FLIM measurements.

7. The TCSPC module and FLIM detector are controlled by the BH SPCM software.
8. The acquired TCSPC FLIM data is analyzed using the BH SPCImage software.

2.2 Measurement of the TCSPC FLIM Instrument Response Function (IRF)

The IRF can be estimated from the acquired decay data itself. However, it is preferable to directly measure the IRF experimentally, e.g., by recording scattered excitation light. For visible light excitation, a strongly scattering specimen such as nondairy coffee creamer is conventionally used to record the IRF [5]. For infrared light excitation, the IRF can be measured using a sample (such as urea crystal) that yields second-harmonic generation (SHG) signals [70]. SHG is a nonlinear process that delivers a signal at one-half of the excitation wavelength.

1. A thin layer of urea crystal sandwiched between a glass coverslip and a glass slide was used to measure the IRF of the TPE TCPSC FLIM system.

2.3 Confocal FD FLIM System

The basic principle of digital FD FLIM is described in Fig. 2b and Table 1. We use the ISS ALBA confocal digital FD FLIM/FCS system (www.iss.com).

1. The ISS ALBA FastFLIM system is attached to a Nikon TiE300 inverted microscope.
2. The excitation source is a Fianium SC450-6 pulsed supercontinuum laser module (www.fianium.com), which covers the excitation wavelengths ranging from 460 to 2,200 nm and has a repetition rate of 60 MHz and a pulse width of 6 ps.
3. The system is equipped with two identical PerkinElmer SPCM-AQRH-15 avalanche photodiode (APD) detectors (www.perkinelmer.com).
4. Various combinations of excitation, emission filters, and dichroic mirrors can be configured through the system software. The 445/20 nm (for Coumarin 6, Fluorescein and Cerulean) and 560/25 nm (for Rose Bengal) excitation filters and the 480/40 nm (for Coumarin 6 and Cerulean), 531/40 nm (for Coumarin 6 and Fluorescein), and 630/92 nm (for Rose Bengal) emission filters (www.semrock.com) were used.
5. A Nikon 60X/1.2NA water objective was used for all FD FLIM measurements.
6. The phase shifts and modulation attenuations of the emission relative to the excitation at three frequencies (60, 180, 300 MHz) are simultaneously measured at each pixel of a fluorescence lifetime image.
7. The ISS VistaVision software is used for data acquisition and analysis.

Table 2
List of several commonly used fluorescence lifetime standard fluorophores

Fluorophore	Absorption peak [a]	Emission peak[a]	Solvent	Lifetime[b]	Reference
Coumarin 6	~460 nm	~505 nm	Ethanol	~2.5 ns	[46]
HPTS	~454 nm	~511 nm	Phosphate buffer (pH 7.5)	~5.3 ns	[46]
Fluorescein	~494 nm	~521 nm	Phosphate or Tris buffer (pH > 7)	4–4.1 ns	[54, 71]
Rhodamine B	~542 nm	~565 nm	Water Methanol Ethanol	~1.7 ns ~2.5 ns ~3.1 ns	[54] [72] [5, 55, 73]
Rose Bengal	~560 nm	~571 nm	Water Methanol Ethanol 2-propanol Acetonitrile Acetone	~0.12 ns ~0.54 ns ~0.74 ns ~0.98 ns ~2.38 ns ~2.57 ns	[5, 53, 73]

[a] The absorption and emission peaks may vary upon the solvent

[b] All lifetimes given were measured at room temperature (~22 °C)

2.4 Fluorescence Lifetime Standards for FLIM System Calibration

Prior to any scientific investigation, a FLIM system must be calibrated with standard fluorophores of known lifetimes. Many of them have been used for calibrating FLIM systems, and a few commonly used ones are given in Table 2. The following standards were used for calibrating our FLIM systems at room temperature (~22 °C).

1. Coumarin 6 dissolved in ethanol (~2.5 ns).
2. Fluorescein dissolved in Tris buffer at pH 7.5 (~4.05 ns).
3. Rose Bengal dissolved in water (~0.12 ns).
4. Rose Bengal dissolved in methanol (~0.54 ns).
5. Rose Bengal dissolved in 2-proponal (~0.98 ns).
6. Rose Bengal dissolved in methanol (~2.57 ns).

2.5 FRET Standards for Verification of a FLIM-FRET Approach

It is desirable to employ FRET reference standards in addition to positive and negative controls to verify the FLIM-FRET results. A comparative method to determine the accuracy of FRET measurements was developed by the Vogel laboratory (NIH/NIAAA) [74, 75]. The approach uses "standards" in the form of genetic constructs encoding fusions between donor and acceptor fluorescent proteins separated by defined amino acid (aa) linker sequences. A series of FRET-standard constructs were generated through encoding Cerulean [76] and Venus [77], directly coupled by either a 5, 17, or 32 aa linker—named as C5V, C17V, and C32V, correspondingly [75]. In addition, a construct of a low FRET efficiency as a negative control was also made using a 229 aa linker and is named CTV, where Cerulean and Venus are separated by a TRAF domain [74]. These plasmids are now available at www.addgene.org/Steven_Vogel. Here, three FRET-standard constructs expressed in live mouse pituitary GHFT1 cells (transfected by FuGENE 6) are used to verify both TCSPC and FD FLIM-FRET approaches.

1. Cells alone without any transfection.
2. Cells transfected with Venus alone.
3. Cells transfected with Cerulean alone (donor-alone control).
4. Cells transfected with the C5V construct.
5. Cells transfected with the C32V construct.
6. Cells transfected with the CTV construct.

2.6 A FRET Model in Living Cells: Homo-dimerization of the CCAAT/Enhancer Binding Protein Alpha (C/EBPα) Transcription Factor

The example biological model for demonstration is the basic region-leucine zipper (bZip) domain of the CCAAT/enhancer binding protein alpha (C/EBPα) transcription factor. The bZip family proteins form obligate dimers through their leucine zipper domains, which position the basic region residues for binding to specific DNA elements. Immunocytochemical staining of differentiated mouse adipocyte cells showed that endogenous C/EBPα was preferentially bound to satellite DNA-repeat sequences located in regions of centromeric heterochromatin [78, 79]. When the C/EBPα bZip domain is expressed as a fusion to a fluorescent protein in cells of mouse origin, such as the pituitary GHFT1 cells used here, it is localized to the well-defined regions of centromeric heterochromatin in the cell nucleus [80]. FRET microscopy has been demonstrated to be a perfect tool for detecting the homo-dimerization of C/EBPα in living cells [24, 32, 33, 38, 46]. A FRET system for this biological model can be built by fusing the C/EBPα bZip domain to two fluorescent proteins of a good FRET pair separately, e.g., Cerulean (FRET donor) and Venus (FRET acceptor) as used here. In FLIM, the donor fluorescence lifetimes are measured from cells co-expressing the donor (Cerulean-bZip) and the acceptor (Venus-bZip) as well as cells that only express the donor (Cerulean-bZip). Here, the Cerulean lifetimes in live GHFT1 cells expressing only Cerulean-bZip or both Cerulean-bZip and Venus-bZip (transfected by FuGENE 6) are measured by the TPE TCSPC FLIM approach, to demonstrate the quenching of Cerulean in doubly expressed cells due to FRET between Cerulean-bZip and Venus-bZip.

1. Cells transfected with Cerulean-bZip (donor-alone control).
2. Cells transfected with both Cerulean-b Zip and Venus-bZip.

3 Methods

3.1 System Calibration with Fluorescence Lifetime Standards

See **Note 1** for the selection of fluorescence lifetime standards for FLIM system calibration.

3.1.1 Calibration of the TPE TCSPC FLIM System with the Measured IRF

1. Excite the Urea Crystal sample at the 940 nm wavelength and collect its SHG signals using the 480/40 nm emission filter. The recorded SHG decay can then be imported into the BH SPCImage software as the IRF for data analysis (*see* more details in [46] and **Note 2**).
2. Acquire at least three fluorescence lifetime images from the Coumarin 6 standard solution at different fields of the solution, using the 870 nm excitation wavelength and the 480/40 nm emission filter.
3. Acquire at least three fluorescence lifetime images from the Fluorescein standard solution at different fields of solution, using the 870 nm excitation wavelength and the 525/50 nm emission filter.
4. In the BH SPCImage software, fit the Coumarin 6 and Fluorescein lifetime images using the single-exponential model and the measured IRF. As shown in Fig. 3, both of their fluo-

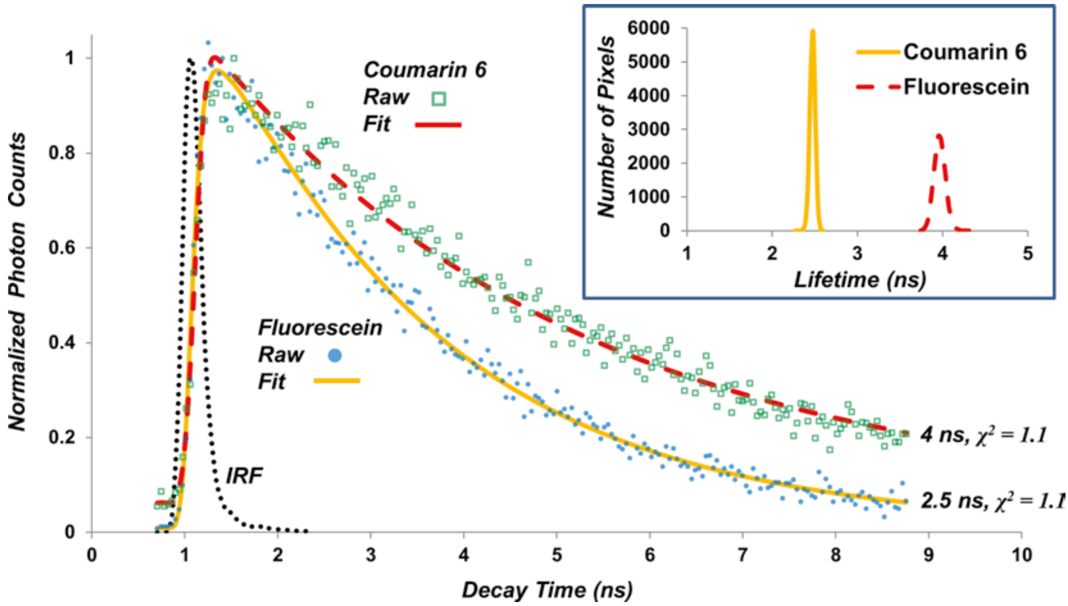

Fig. 3 Calibration of the TPE TCSPC FLIM system with Coumarin 6 in ethanol and Fluorescein in Tris buffer at pH 7.5. For both, the mono-exponential fitting of the raw decay data with the measured instrument response function (IRF) appears to be sufficient with a good χ^2 of 1.1 and yields the correct lifetimes of Coumarin 6 (2.5 ns) and Fluorescein (4 ns). As expected for these homogeneous solutions, each histogram of the representative Coumarin 6 and Fluorescein fluorescence lifetime images (given in the inset) shows a very narrow Gaussian distribution—the small variation is mainly due to noise

rescence lifetimes should be accurately resolved with small variations (Fig. 3 inset), as expected from these homogeneous solutions.

3.1.2 Calibration of the Confocal Digital FD FLIM System

In FD FLIM measurements, the system needs to be first calibrated using a standard fluorophore solution of known lifetime. In the calibration procedure, the software will adjust and set the initial DC, phase, and modulation values at each measured frequency for each detector, based on the data acquired from the standard fluorophore solution and its lifetime given to the software (*see* **Note 3**). Therefore, it is important to use a second fluorescence lifetime standard to verify the calibration procedure.

1. Run the system calibration with the Coumarin 6 standard solution, using the 445/20 nm excitation and the 531/40 nm emission filters, given its lifetime of 2.5 ns to the ISS VistaVision software. Using the same setup, acquire at least three fluorescence lifetime images at different fields of the Coumarin 6 solution; then switch to the Fluorescein standard solution and acquire at least three fluorescence lifetime images at different fields of the Fluorescein solution.
2. Run the system calibration with the Rose Bengal acetone standard solution, using the 560/25 nm excitation and the 630/92 nm emission filters, given its lifetime of 2.57 ns to the ISS VistaVision software. Using the same setup, acquire at least three fluorescence lifetime images at different fields of the Rose Bengal acetone solution; then switch to other Rose Bengal (water, methanol and 2-propanol) standard solutions one by one and acquire at least three fluorescence lifetime images at different fields of each solution.
3. In the ISS VistaVision software, plot the acquired fluorescence lifetime images using the phasor plot approach (*see* **Note 4**). As shown in Fig. 4, the phasor distribution of each standard solution should almost center on the semicircle, demonstrating its mono-exponential decay nature, as expected from these homogeneous solutions. Placing the cursor at the center of a distribution gives both its phase and modulation lifetimes, which should be nearly identical.

3.2 Verification of a FLIM System for FRET Studies with FRET Standards

3.2.1 Measure FRET Standards Using the TPE TCSPC FLIM Method

1. Use untransfected cells to check if there is autofluorescence from the specimen in the donor (480/40 nm) channel for the donor excitation (820 nm) wavelength (*see* **Note 5**).
2. Use cells transfected with Venus to check if there is back bleedthrough to the donor (480/40 nm) channel for the donor excitation (820 nm) wavelength and (*see* **Note 6**).
3. Use cells expressing Cerulean alone and acquire fluorescence lifetime images from at least 10 cells using the 820 nm excitation

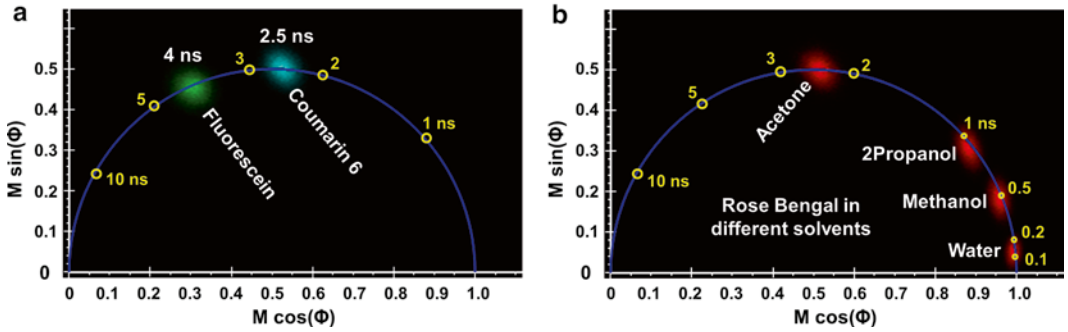

Fig. 4 Calibration of the confocal digital FD FLIM system with Coumarin 6 in ethanol, Fluorescein in Tris buffer pH 7.5, and Rose Bengal in acetone, 2-propano, methanol, or water. (**a**) The FD FLIM system was calibrated with Coumarin 6, given its lifetime of 2.5 ns to the system software, and then used to measure the Fluorescein lifetime, showing the correct value of 4.0 ns. (**b**) The FD FLIM system was calibrated with Rose Bengal in acetone and the input lifetime of 2.57 ns and then used to measure the lifetimes of Rose Bengal in other solvents—water, methanol, and 2-propanol, which are clearly resolved to be 0.14, 0.5, and 0.92 ns, respectively. For each standard solution, the raw FD FLIM data is presented by the phasor plot at the fundamental frequency of 60 MHz. Each point in the phasor plot represents a pixel in a fluorescence lifetime image, and its *x*, *y-coordinates* and intensity are determined by the phase (Φ), modulation (*M*), and DC values of the corresponding pixel

wavelength and the 480/40 emission filter, which were also used for the FRET-standard constructs.

4. Use cells expressing the C5V construct and acquire the donor (Cerulean) fluorescence lifetime images from at least 10 cells.
5. Use cells expressing the C32V construct and acquire the donor (Cerulean) fluorescence lifetime images from at least 10 cells.
6. Use cells expressing the CTV construct and acquire the donor (Cerulean) fluorescence lifetime images from at least 10 cells.
7. In the BH SPCImage software, fit the Cerulean-alone lifetime images using the single-exponential model and the measured IRF to estimate the unquenched donor lifetime; for the FRET-standard constructs, both single- and double-exponential fittings were applied with the measured IRF and the results were then compared to determine the quenched donor lifetimes—the CTV lifetime images were sufficiently fitted with the single-exponential model, while the C32V and C5V lifetime images were better fitted using the double-exponential model (*see* **Note 7**). The representative raw decays and fitting results are shown in Fig. 5, clearly demonstrating that the TPE TCSPC FLIM technique can distinguish subtle changes in FRET in the CTV, C32V, and C5V FRET-standard constructs by resolving the different lifetimes of Cerulean (FRET donor) in the absence of Venus (FRET acceptor) versus in the presence of Venus at different proximity in these FRET-standard constructs (*see* **Note 8**).

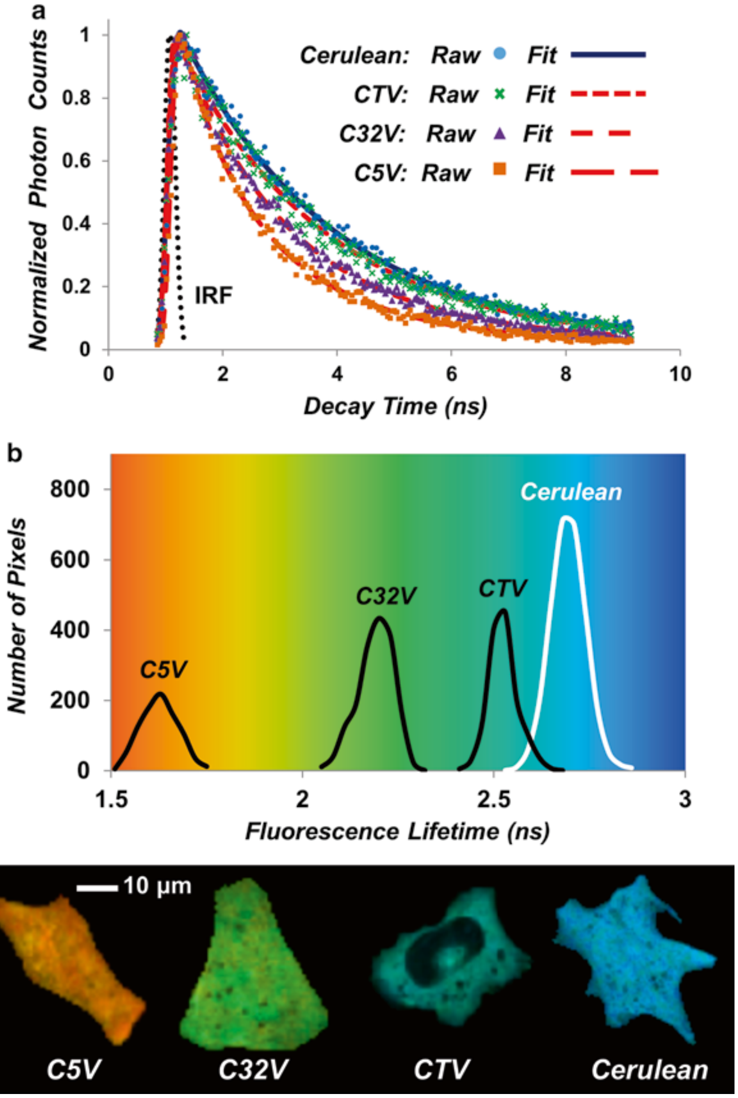

Fig. 5 Verification of the TPE TCSPC FLIM-FRET method using FRET-standard constructs—C5V, C32V, and CTV (adapted from [24]). The Cerulean fluorescence lifetimes in live cells expressing Cerulean alone (Cerulean) or a FRET-standard construct (CTV, C32V, or C5V) were measured using the TPE TCSCP FLIM system. (**a**) For each, the raw decay data points along with the corresponding fitted decay curve at a representative pixel are plotted—the comparison clearly shows a faster decay from Cerulean to CTV to C32V to C5V. Both Cerulean-alone and CTV data were analyzed by single-exponential fitting. However, C32V and C5V data were better fitted with two lifetime components, and their mean lifetimes are used for comparison. (**b**) The lifetime distributions and color-coded lifetime images of the representative cells are also compared, confirming that lifetimes get shorter from Cerulean to CTV to C32V to C5V

3.2.2 Measure FRET Standards Using the Confocal FD FLIM Method

1. Run the system calibration with the Coumarin 6 standard solution, using the 445/20 nm excitation and the 480/40 nm emission filters, given its lifetime of 2.5 ns to the ISS VistaVision software. Using the same setup, acquire at least three fluorescence lifetime images at different fields of the Coumarin 6 solution and then plot the acquired Coumarin 6 fluorescence lifetime images in the phasor plot to make sure to obtain a single lifetime of 2.5 ns for Coumarin 6 (Fig. 4a).
2. Use untransfected cells to check if there is autofluorescence from the specimen in the donor (480/40 nm) channel for the donor excitation (445/20 nm) wavelength (*see* **Note 5**).
3. Use cells transfected with Venus to check if there is back bleedthrough to the donor (480/40 nm) channel for the donor excitation (445/20 nm) wavelength (*see* **Note 6**).
4. Use cells expressing Cerulean alone and acquire fluorescence lifetime images from at least 10 cells using the 445/20 nm excitation and the 480/40 emission filters, which were also used for the FRET-standard constructs.
5. Use cells expressing the C5V construct and acquire Cerulean (donor) fluorescence lifetime images from at least 10 cells.
6. Use cells expressing the C32V construct and acquire Cerulean (donor) fluorescence lifetime images from at least 10 cells.
7. Use cells expressing the CTV construct and acquire Cerulean (donor) fluorescence lifetime images from at least 10 cells.
8. In the ISS VistaVision software, plot the Cerulean-alone, CTV, C32V, and C5V fluorescence lifetime images using the phasor plot approach. As shown Fig. 6, the FD FLIM technique clearly resolved the Cerulean-alone, CTV, C32V, and C5V fluorescence lifetime data distributions in the phasor plot, demonstrating that the lifetimes of Cerulean decrease from Cerulean-alone to CTV to C32V to C5V.

3.3 Localization of Homo-dimerization of C/EBPα in Living Cells Using the TPE TCSPC FLIM-FRET Method

1. Use cells expressing Cerulean-bZip and acquire fluorescence lifetime images from at least 10 cells using the 820 nm excitation wavelength and the 480/40 emission filter.
2. Use cells expressing both Cerulean-bZip and Venus-bZip and acquire Cerulean (donor) fluorescence lifetime images from at least 10 cells using the 820 nm excitation wavelength and the 480/40 emission filter.
3. In the BH SPCImage software, fit the Cerulean-bZip lifetime images using the single-exponential model and the measured IRF to estimate the unquenched donor lifetime; by comparing both single- and double-exponential fittings, the "Cerulean-

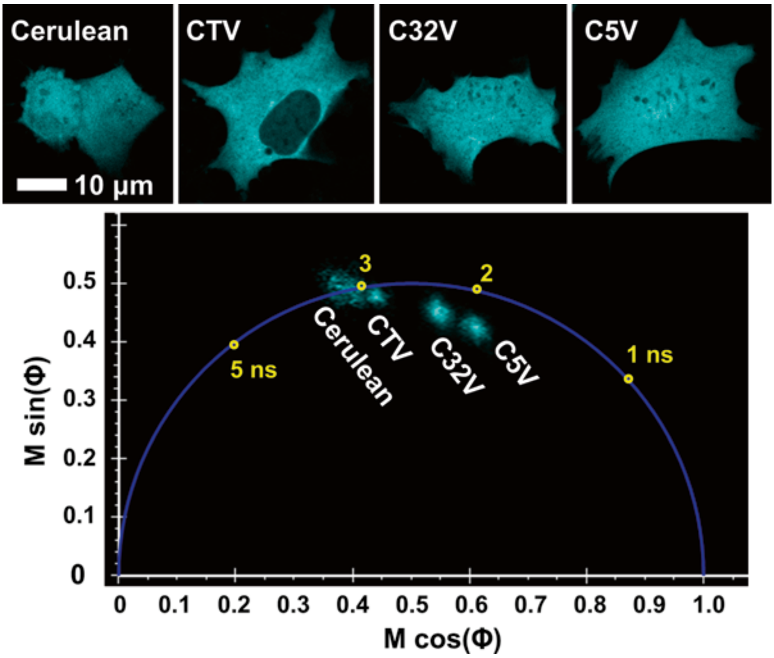

Fig. 6 Verification of the confocal digital FD FLIM-FRET method using FRET-standard constructs—C5V, C32V, and CTV. The Cerulean fluorescence lifetimes in live cells expressing Cerulean alone (Cerulean) or a FRET-standard construct (CTV, C32V or C5V) were measured using the confocal digital FD FLIM system. The representative images and the corresponding phasor plot distributions are shown. It is clearly demonstrated by the phasor plot (without any fitting) that the Cerulean lifetimes decrease from Cerulean alone to CTV to C32V to C5V. The phasor distribution of Cerulean alone is centered on the universal semicircle of the phasor plot, indicating that it has a single lifetime component. However, the C32V and C5V phasor distributions are completely located inside the universal semicircle of the phasor plot, indicating that they have more than one lifetime component. The CTV phasor distribution is close to that of Cerulean alone, as expected from the linker system

bZip + Venus-bZip" fluorescence lifetime images were better fitted using the double-exponential model with the measured IRF. The representative raw decays and fitting results are shown in Fig. 7, where comparing the lifetimes of Cerulean in singly versus doubly expressed cells, measured by the TPE TCSPC FLIM method, clearly shows the quenching of Cerulean-bZip by Venus-bZip due to FRET between them, demonstrating homo-dimerization of C/EBPα-bZip in living cells (*see* **Notes 9** and **10**).

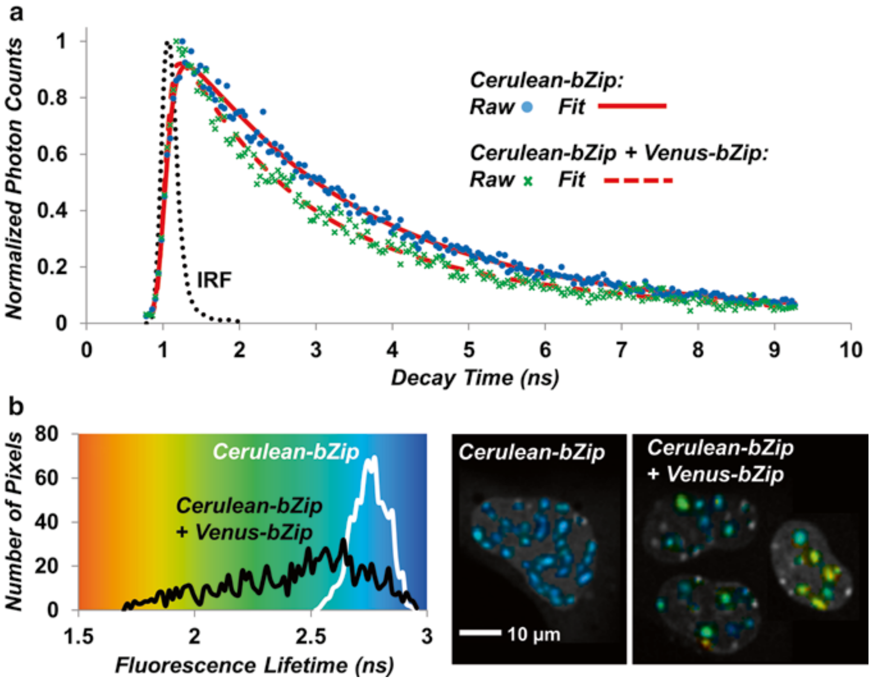

Fig. 7 Localization of dimerized C/EBPα-bZip in living cell nuclei using the TPE TCSPC FLIM-FRET method (adapted from [46]). C/EBPα-bZip was tagged with either Cerulean (Cerulean-bZip: FRET donor) or Venus (Venus-bZip: FRET acceptor). The unquenched Cerulean lifetimes were measured from the donor-alone control cells that only express Cerulean-bZip and were determined by single-exponential fitting. The lifetimes of quenched Cerulean in cells co-expressing Cerulean-bZip and Venus-bZip were analyzed by double-exponential fitting, and the mean lifetime of the two lifetime components is used for comparison. (**a**) Comparing their representative raw decay data points along with the corresponding fitted curves shows a faster decay of Cerulean-bZip in the presence of Venus-bZip than in the absence of Venus-bZip, demonstrating FRET between the two and indicating the homo-dimerization of C/EBPα-bZip. (**b**) By applying suitable thresholds, fittings were only applied to the pixels in regions of centromeric heterochromatin of the cell nucleus. The representative intensity-overlaid lifetime images and the corresponding lifetime distributions are compared, showing the shorter Cerulean lifetimes in doubly expressed cells than singly expressed cells and demonstrating that the quenching of Cerulean-bZip by Venus-bZip in dimerized C/EBPα-bZip

4 Notes

1. It is preferable to choose standard fluorophores whose excitation, emission, and fluorescence lifetime properties are close to those of the fluorophores in the intended samples, so that the same imaging setup used for biological samples can be applied for the system calibration. Importantly, the standard should be carefully prepared according to the reference, such as solvent, pH, temperature, molar concentration, etc, because these factors may influence its fluorescence lifetime. Typically, the concentration of a dye would not influence its fluorescence lifetime. However, most of these standard dyes cannot be prepared in

100 % purity and the impurity at a high dye concentration may quench the dye, resulting in a decrease in its fluorescence lifetime. Thus, one should carefully prepare the dye concentration upon the dye and the system sensitivity.

2. It is important to apply the same optics and TCPSC settings used for experimental samples, since the IRF may vary depending upon both the optical path (such as the objective lens and the thickness of the emission filter) and the TCSPC configuration (such as the constant fraction discriminator parameters). More importantly, the IRF of a TPE TCSPC FLIM system should be periodically checked, since it can change due to reflections in the optical path, poor mode locking of the TPE laser, or instability of the TCPSC electronics.
3. To ensure the accuracy and reproducibility of the lifetime measurements, the FD FLIM system calibration needs to be done in every experiment and repeated periodically (every a few hours) for a long experimental course.
4. Since in most of biological applications the nanosecond-scale lifetimes are measured with high frequencies, it is important to apply a de-noising technique such as Gaussian or wavelet smoothing or median filtering to facilitate the phasor plot analysis [68, 81]. The phasor plot data shown in Figs. 4 and 6 are applied with Gaussian smoothing.
5. Autofluorescence from specimens should be carefully checked. If the donor fluorescence signals are contaminated with the sample autofluorescence, the autofluorescence lifetime needs to be first determined using unlabeled specimens and then considered in the data analysis of labeled samples. In our case, no noticeable autofluorescence was observed from the unlabeled specimens in either the TPE TCSPC FLIM setup or the confocal FD FLIM setup.
6. It is important to check if there is back bleedthrough from the acceptor fluorophore to the donor channel under the donor excitation wavelength. If there is back bleedthrough, it would be better to choose another acceptor fluorophore since the back bleedthrough could significantly complicate FLIM data analysis. In our case, no noticeable back bleedthrough from the acceptor-alone specimens was observed in either the TPE TCSPC FLIM setup or the confocal FD FLIM setup.
7. The goodness-of-fit is considered an important factor for making the decision on whether or not to accept fitted FLIM results and is usually assessed by the calculated χ^2 and residuals, as well as by visually comparing the fitting curve versus the measured data points. An example of evaluating the fit of TCSPC FLIM data is shown in Fig. 8. One should

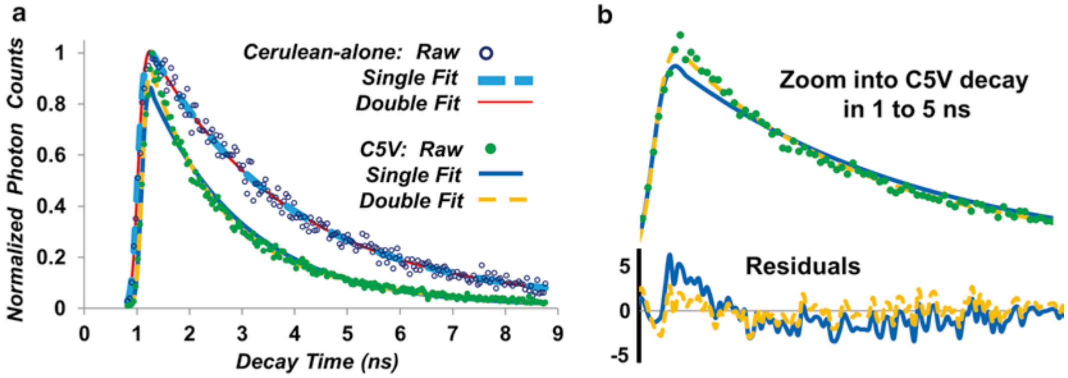

Fig. 8 Evaluation of fitting of TCSPC FLIM data. Fitting the Cerulean decay data acquired from Cerulean-alone (Cerulean) or C5V cells is used as an example—each was analyzed by both single- and double-exponential fittings. (**a**) For the Cerulean-alone decay, the single-exponential (Single) fit is nearly identical to the double-exponential (Double) fit, and the obtained weighted least squares (χ^2) values of the two fits are almost the same (Single: 1.12 vs. Double: 1.13), indicating that the Cerulean-alone decay is mono-exponential. However, a difference is seen from comparing the single- versus double-exponential fits of the C5V decay data. (**b**) A zoom view into the C5V decay of 1–5 ns clearly shows a better fit of using the double-exponential model than the single-exponential model, especially at the beginning (1–2 ns) of the decay. This is also confirmed by the calculated χ^2 values (Single: 2.47 vs. Double: 1.18) and residuals. Therefore, the C5V decay should be analyzed for two lifetime components

always be careful when accepting a more complicated model for data analysis, since it is the reproducibility of data for a particular data processing model that is critical. Most importantly, more photon counts are required to obtain an accurate statistical fit of the lifetime data when resolving more lifetime components.

8. The FLIM *E*% can be calculated using Eq. 3, where the unquenched donor lifetimes (τ_D) are measured from the donor-alone specimens, e.g., cells expressing Cerulean-alone; the quenched donor lifetimes (τ_{DA}) are estimated from the "donor + acceptor" specimens, e.g., cells expressing a CTV, C32V, or C5V FRET-standard construct. The average of Cerulean lifetimes obtained from all donor-alone lifetime images is used as τ_D for the E% calculation. For doubly expressed cells, the mean Cerulean lifetime (Eq. 5) at each pixel is used as τ_{DA} for the E% calculation to produce an E% image [46]. The average FLIM E%s of CTV, C32V, and C5V were determined to be 6, 20, and 40 %, respectively [82].
9. For accurate FLIM-FRET measurements, a few cautions need to be taken into consideration to rule out the lifetime changes caused by the factors other than FRET. Photobleaching is a common problem in fluorescence microscopy imaging and can induce false information in quantitative analysis. Although

FLIM techniques are generally more tolerant to some extent of photobleaching compared to intensity-based techniques for FRET measurements, photobleaching could influence the measured lifetime [46]. Prior to FLIM measurements, the significance of photobleaching should be monitored for the time course of acquiring a FLIM data set, to establish an imaging condition where the measured donor-alone lifetimes are not affected [46]. The fluorescence lifetime of a fluorophore can be influenced by its microenvironment. Thus, it is important to make sure that the donor fluorophores reside in the same microenvironment in both donor-alone control specimens and specimens containing both donor and acceptor fluorophores. For example, suitable thresholds were applied for both donor-alone and doubly expressed cells to only analyze the donor lifetimes in the regions of centromeric heterochromatin of the cell nucleus (Fig. 7).

10. The unquenched Cerulean lifetimes have a narrow distribution with an average of about 2.75 ns (Fig. 7b) [46]. However, the quenched Cerulean lifetimes measured from cells co-expressing Cerulean-bZip and Venus-bZip vary substantially (2.0–2.6 ns) from one centromeric region to another (Fig. 7b), resulting in an E% range of 5–27 % [46]. Since the donor and acceptor fusion proteins in the C/EBPα-bZip model are expressed independently and there are also donor-donor and acceptor-acceptor dimers other than donor-acceptor dimers, the stoichiometry between the acceptor and the donor (the "acceptor/donor" ratio) varies from one region of interest (ROI) to another. The donor will more likely be quenched when it is surrounded by many more acceptors. Quantifying the "acceptor/donor" ratio in addition to the quenched lifetime of Cerulean in each ROI will help to understand the changes of those quenched lifetimes in different ROIs [46].

Acknowledgments

The authors acknowledge funding from the University of Virginia, National Heart, Lung, and Blood Institute (NHLBI) PO1HL101871 and National Center for Research Resources NCRR-NIH RR027409. The authors thank Ms. Kay Christopher (Biology, University of Virginia) for preparing the samples, Dr. Steven Vogel (NIH/NIAAA) for providing the FRET-standard constructs, and Dr. Richard Day (Indiana University School of Medicine) for providing the C/EBPα-bZip constructs.

References

1. Venetta BD (1959) Microscope phase fluorometer for determining the fluorescence lifetimes of fluorochromes. Rev Sci Instrum 30: 450–457
2. Biener E, Charlier M, Ramanujan VK et al (2005) Quantitative FRET imaging of leptin receptor oligomerization kinetics in single cells. Biol Cell 97:905–919
3. Gadella TWJ (2009) FRET and FLIM techniques. In: Pillai S, van der Vliet PC (eds) Laboratory techniques in biochemistry and molecular biology. Elsevier, Oxford, UK, p 534
4. Periasamy A, Clegg RM (2009) FLIM microscopy in biology and medicine. CRC Press, London
5. Periasamy A, Wodnicki P, Wang XF et al (1996) Time-resolved fluorescence lifetime imaging microscopy using a picosecond pulsed tunable dye laser system. Rev Sci Instrum 67:3722–3731
6. Agronskaia AV, Tertoolen L, Gerritsen HC (2003) High frame rate fluorescence lifetime imaging. J Phys D 36:1655–1662
7. Agronskaia AV, Tertoolen L, Gerritsen HC (2004) Fast fluorescence lifetime imaging of calcium in living cells. J Biomed Opt 9:1230–1237
8. Ushakov DS, Caorsi V, Ibanez-Garcia D et al (2011) Response of rigor cross-bridges to stretch detected by fluorescence lifetime imaging microscopy of myosin essential light chain in skeletal muscle fibers. J Biol Chem 286:842–850
9. Berezovska O, Lleo A, Herl LD et al (2005) Familial alzheimer's disease presenilin 1 mutations cause alterations in the conformation of presenilin and interactions with amyloid precursor protein. J Neurosci 25:3009–3017
10. Petrasek Z, Eckert HJ, Kemnitz K (2009) Wide-field photon counting fluorescence lifetime imaging microscopy: application to photosynthesizing systems. Photosynth Res 102:157–168
11. Lakowicz JR (2006) Principles of fluorescence spectroscopy. Springer, New York
12. Huang S, Heikal AA, Webb WW (2002) Two-photon fluorescence spectroscopy and microscopy of NAD(P)H and flavoprotein. Biophys J 82:2811–2825
13. Bird DK, Yan L, Vrotsos KM et al (2005) Metabolic mapping of MCF10A human breast cells via multiphoton fluorescence lifetime imaging of the coenzyme NADH. Cancer Res 65:8766–8773
14. Skala MC, Riching KM, Gendron-Fitzpatrick A et al (2007) In vivo multiphoton microscopy of NADH and FAD redox states, fluorescence lifetimes, and cellular morphology in precancerous epithelia. Proc Natl Acad Sci U S A 104:19494–19499
15. Galletly NP, McGinty J, Dunsby C et al (2008) Fluorescence lifetime imaging distinguishes basal cell carcinoma from surrounding uninvolved skin. Br J Dermatol 159:152–161
16. Förster T (1946) Energy transport and fluorescence [in German]. Naturwissenschaften 6:166–175
17. Förster T (1948) Zwischenmolekulare energiewanderung und fluoreszenz. Annalen Der Physik 437:55–75
18. Förster T (1965) Delocalized excitation and excitation transfer. In: Sinanoglu O (ed) Modern quantum chemistry. Academic Press Inc., New York, pp 93–137
19. Clegg RM (1996) Fluorescence resonance energy transfer. In: Wang XF, Herman B (eds) Fluorescence imaging spectroscopy and microscopy. Wiley, New York, pp 179–251
20. Jares-Erijman EA, Jovin TM (2003) FRET imaging. Nat Biotechnol 21:1387–1395
21. Sekar RB, Periasamy A (2003) Fluorescence resonance energy transfer (FRET) microscopy imaging of live cell protein localizations. J Cell Biol 160:629–633
22. Vogel SS, Thaler C, Koushik SV (2006) Fanciful FRET. Sci STKE re2
23. Piston DW, Kremers GJ (2007) Fluorescent protein FRET: the good, the bad and the ugly. Trends Biochem Sci 32:407–414
24. Sun Y, Wallrabe H, Seo SA et al (2011) FRET microscopy in 2010: the legacy of theodor forster on the 100th anniversary of his birth. Chem Phys Chem 12:462–474
25. Wouters FS, Bastiaens PIH (1999) Fluorescence lifetime imaging of receptor tyrosine kinase activity in cells. Curr Biol 9:1127–1130
26. Verveer PJ, Wouters FS, Reynolds AR et al (2000) Quantitative imaging of lateral ErbB1 receptor signal propagation in the plasma membrane. Science 290:1567–1570
27. Elangovan M, Day RN, Periasamy A (2002) Nanosecond fluorescence resonance energy transfer-fluorescence lifetime imaging microscopy to localize the protein interactions in a single living cell. J Microsc 205:3–14
28. Chen Y, Mills JD, Periasamy A (2003) Protein localization in living cells and tissues using FRET and FLIM. Differentiation 71:528–541
29. Krishnan RV, Masuda A, Centonze VE et al (2003) Quantitative imaging of protein–protein interactions by multiphoton fluores-

cence lifetime imaging microscopy using a streak camera. J Biomed Opt 8:362–367

30. Chen Y, Periasamy A (2004) Characterization of two-photon excitation fluorescence lifetime imaging microscopy for protein localization. Microsc Res Tech 63:72–80
31. Biskup C, Zimmer T, Benndorf K (2004) FRET between cardiac na + channel subunits measured with a confocal microscope and a streak camera. Nat Biotechnol 22:220–224
32. Wallrabe H, Periasamy A (2005) Imaging protein molecules using FRET and FLIM microscopy. Curr Opin Biotechnol 16:19–27
33. Demarco IA, Periasamy A, Booker CF et al (2006) Monitoring dynamic protein interactions with photoquenching FRET. Nat Methods 3:519–524
34. Biskup C, Zimmer L, Kelbauskas T et al (2007) Multi-dimensional fluorescence lifetime and FRET measurements. Microsc Res Tech 70:442–451
35. Li Q, Seeger S (2007) Label-free detection of protein interactions using deep UV fluorescence lifetime microscopy. Anal Biochem 367:104–110
36. Li H, Li HF, Felder RA et al (2008) Rab4 and Rab11 coordinately regulate the recycling of angiotensin II type I receptor as demonstrated by fluorescence resonance energy transfer microscopy. J Biomed Opt 13:031206
37. Murakoshi H, Lee SJ, Yasuda R (2008) Highly sensitive and quantitative FRET-FLIM imaging in single dendritic spines using improved non-radiative YFP. Brain Cell Biol 36:31–42
38. Sun Y, Wallrabe H, Booker CF et al (2010) Three-color spectral FRET microscopy localizes three interacting proteins in living cells. Biophys J 99:1274–1283
39. Li H, Yu P, Sun Y et al (2010) Actin cytoskeleton-dependent rab GTPase-regulated angiotensin type I receptor lysosomal degradation studied by fluorescence lifetime imaging microscopy. J Biomed Opt 15:056003
40. Boutant E, Didier P, Niehl A et al (2010) Fluorescent protein recruitment assay for demonstration and analysis of in vivo protein interactions in plant cells and its application to tobacco mosaic virus movement protein. Plant J 62:171–177
41. Bu W, Lim KB, Yu YH et al (2010) Cdc42 interaction with N-WASP and toca-1 regulates membrane tubulation, vesicle formation and vesicle motility: Implications for endocytosis. PLoS One 5:e12153
42. Martin-Villar E, Fernandez-Munoz B, Parsons M et al (2010) Podoplanin associates with CD44 to promote directional cell migration. Mol Biol Cell 21:4387–4399
43. Jones PB, Adams KW, Rozkalne A et al (2011) Apolipoprotein E: isoform specific differences in tertiary structure and interaction with amyloid-beta in human alzheimer brain. PLoS One 6:e14586
44. Timpson P, McGhee EJ, Morton JP et al (2011) Spatial regulation of RhoA activity during pancreatic cancer cell invasion driven by mutant p53. Cancer Res 71:747–757
45. Kumar S, Alibhai D, Margineanu A et al (2011) FLIM FRET technology for drug discovery: automated multiwell-plate high-content analysis, multiplexed readouts and application in situ. Chem Phys Chem 12:609–626
46. Sun Y, Day RN, Periasamy A (2011) Investigating protein–protein interactions in living cells using fluorescence lifetime imaging microscopy. Nat Protoc 6:1324–1340
47. Becker W (2005) Advanced time-correlated single photon counting techniques. Springer, Berlin
48. Gerritsen HC, Asselbergs MA, Agronskaia AV et al (2002) Fluorescence lifetime imaging in scanning microscopes: acquisition speed, photon economy and lifetime resolution. J Microsc 206:218–224
49. Becker W, Bergmann A, Hink MA et al (2004) Fluorescence lifetime imaging by time-correlated single-photon counting. Microsc Res Tech 63:58–66
50. Becker W, Bergmann A, Biskup C (2007) Multispectral fluorescence lifetime imaging by TCSPC. Microsc Res Tech 70:403–409
51. Elangovan M, Wallrabe H, Chen Y et al (2003) Characterization of one- and two-photon excitation fluorescence resonance energy transfer microscopy. Methods 29:58–73
52. Talbot CB, McGinty J, Grant DM et al (2008) High speed unsupervised fluorescence lifetime imaging confocal multiwell plate reader for high content analysis. J Biophotonics 1: 514–521
53. Krishnan RV, Saitoh H, Terada H et al (2003) Development of a multiphoton fluorescence lifetime imaging microscopy system using a streak camera. Rev Sci Instrum 74:2714–2721
54. Colyer RA, Lee C, Gratton E (2008) A novel fluorescence lifetime imaging system that optimizes photon efficiency. Microsc Res Tech 71:201–213
55. Gadella TWJ Jr, Jovin TM, Clegg RM (1993) Fluorescence lifetime imaging microscopy (FLIM): Spatial resolution of microstructures on the nanosecond time scale. Biophys Chem 48:221–239
56. Buranachai C, Kamiyama D, Chiba A et al (2008) Rapid frequency-domain FLIM spinning disk confocal microscope: lifetime resolu-

tion, image improvement and wavelet analysis. J Fluoresc 18:929–942

57. Chen YC, Clegg RM (2011) Spectral resolution in conjunction with polar plots improves the accuracy and reliability of FLIM measurements and estimates of FRET efficiency. J Microsc 244:21–37
58. Goedhart J, van Weeren L, Hink MA et al (2010) Bright cyan fluorescent protein variants identified by fluorescence lifetime screening. Nat Methods 7:137–139
59. Periasamy A, Skoglund P, Noakes C et al (1999) An evaluation of two-photon excitation versus confocal and digital deconvolution fluorescence microscopy imaging in xenopus morphogenesis. Microsc Res Tech 47:172–181
60. Verveer PJ, Squire A, Bastiaens PIH (2000) Global analysis of fluorescence lifetime imaging microscopy data. Biophys J 78: 2127–2137
61. Verveer PJ, Bastiaens PIH (2003) Evaluation of global analysis algorithms for single frequency fluorescence lifetime imaging microscopy data. J Microsc 209:1–7
62. Pelet S, Previte MJ, Laiho LH et al (2004) A fast global fitting algorithm for fluorescence lifetime imaging microscopy based on image segmentation. Biophys J 87:2807–2817
63. Grecco HE, Roda-Navarro P, Verveer PJ (2009) Global analysis of time correlated single photon counting FRET-FLIM data. Opt Express 17:6493–6508
64. Gryczynski I, Bharill S, Luchowski R et al (2009) Nonlinear curve-fitting methods for time-resolved data analysis. In: Periasamy A, Clegg RM (eds) FLIM microscopy in biology and medicine. Chapman and Hall/CRC, Boca Raton, pp 341–369
65. Redford GI, Clegg RM (2005) Polar plot representation for frequency-domain analysis of fluorescence lifetimes. J Fluoresc 15:805–815
66. Clayton AH, Hanley QS, Verveer PJ (2004) Graphical representation and multicomponent analysis of single-frequency fluorescence lifetime imaging microscopy data. J Microsc 213:1–5
67. Hanley QS, Clayton AH (2005) AB-plot assisted determination of fluorophore mixtures in a fluorescence lifetime microscope using spectra or quenchers. J Microsc 218:62–67
68. Digman MA, Caiolfa VRM, Zamai VR et al (2008) The phasor approach to fluorescence lifetime imaging analysis. Biophys J 94: L14–L16
69. Stringari C, Cinquin A, Cinquin O et al (2011) Phasor approach to fluorescence lifetime microscopy distinguishes different metabolic states of germ cells in a live tissue. Proc Natl Acad Sci U S A 108:13582–13587
70. Sun Y, Booker CF, Kumari S et al (2009) Characterization of an orange acceptor fluorescent protein for sensitized spectral fluorescence resonance energy transfer microscopy using a white-light laser. J Biomed Opt 14: 054009
71. Koushik SV, Blank PS, Vogel SS (2009) Anomalous surplus energy transfer observed with multiple FRET acceptors. PLoS One 4:e8031
72. Boens N, Qin W, Basaric N et al (2007) Fluorescence lifetime standards for time and frequency domain fluorescence spectroscopy. Anal Chem 79:2137–2149
73. Cramer LE, Spears KG (1978) Hydrogen bond strengths from solvent-dependent lifetimes of rose bengal dye. J Am Chem Soc 100:221–227
74. Thaler C, Koushik SV, Blank PS et al (2005) Quantitative multiphoton spectral imaging and its use for measuring resonance energy transfer. Biophys J 89:2736–2749
75. Koushik SV, Chen H, Thaler C et al (2006) Cerulean, venus, and VenusY67C FRET reference standards. Biophys J 91:L99–L101
76. Rizzo MA, Springer GH, Granada B et al (2004) An improved cyan fluorescent protein variant useful for FRET. Nat Biotechnol 22:445–449
77. Nagai T, Ibata K, Park ES et al (2002) A variant of yellow fluorescent protein with fast and efficient maturation for cell-biological applications. Nat Biotechnol 20:87–90
78. Tang QQ, Lane MD (2000) Role of C/EBP homologous protein (CHOP-10) in the programmed activation of CCAAT/enhancer-binding protein-beta during adipogenesis. Proc Natl Acad Sci U S A 97:12446–12450
79. Tang QQ, Lane MD (1999) Activation and centromeric localization of CCAAT/enhancer-binding proteins during the mitotic clonal expansion of adipocyte differentiation. Genes Dev 13:2231–2241
80. Day RN, Voss TC, Enwright JF 3rd et al (2003) Imaging the localized protein interactions between pit-1 and the CCAAT/enhancer binding protein alpha in the living pituitary cell nucleus. Mol Endocrinol 17:333–345
81. Buranachai C, Tong B, Clegg R et al (2009) General concerns of FLIM data representation and analysis. In: Periasamy A, Clegg RM (eds) FLIM microscopy in biology and medicine. Chapman and Hall/CRC, Boca Raton, pp 323–340
82. Sun Y, Periasamy A (2010) Additional correction for energy transfer efficiency calculation in filter-based forster resonance energy transfer microscopy for more accurate results. J Biomed Opt 15:020513

Chapter 7

Analysis of Biomolecular Dynamics by FRAP and Computer Simulation

Bart Geverts, Martin E. van Royen, and Adriaan B. Houtsmuller

Abstract

We present a Monte Carlo simulation environment for modelling complex biological molecular interaction networks and for the design, validation, and quantitative analysis of FRAP assays to study these. The program is straightforward in its implementation and can be instructed through an intuitive script language. The simulation tool fits very well in a systems biology research setting that aims to maintain an interactive cycle of experiment-driven modelling and model-driven experimentation: the model and the experiment are in the same simulation. The full program can be obtained by request to the authors.

Key words FRAP, FRET, Modelling, Simulation, Dynamics, Quantitative fluorescence assay

1 Introduction

Cell function can be largely, if not fully, described by a set of well-orchestrated and highly compartmentalized biomolecular transformations [1]. Such transformations may be covalent modifications (e.g., enzymatic addition or removal of phosphates), intermolecular associations (e.g., heterodimerization or homodimerization, complex formation), intracellular (re)localizations (e.g., nucleocytoplasmic shuttling, formation of DNA damage-induced foci), or synthesis from small compounds (e.g., DNA replication, protein synthesis), all together acting in a highly regulated manner to perform their simple or complex tasks in the cell. Importantly, in the context of this chapter, photobleaching of a fluorescent tag is also a molecular transformation. Although it is not relevant for cell function, it can be used to extract information on protein mobility, which is highly relevant in cell biological or biophysical research (e.g., [2, 3]).

Mathematical or "physicochemical" modelling of cellular function aims to describe these transformations in terms of "equations derived from established physical and chemical theory" [1], usually culminating in extensive sets of partial or ordinary

Peter J. Verveer (ed.), *Advanced Fluorescence Microscopy: Methods and Protocols*, Methods in Molecular Biology, vol. 1251, DOI 10.1007/978-1-4939-2080-8_7, © Springer Science+Business Media New York 2015

differential equations (PDEs and ODEs) [4]. These approaches have substantially contributed and are still contributing to increasing biological knowledge at the systems level [5]. Similarly, ODE- and/or PDE-modelling approaches have enabled quantitative analysis of fluorescence recovery after photobleaching (FRAP) data [6–9]. In general, a high level of mathematical skill is needed to design, validate, calibrate, and finally solve these sets of interdependent equations, which in highly complex scenarios are not solvable at all. Moreover, modifying or expanding models, or introducing spatial confinements like compartmentalization in irregular structures, prompts revision of the entire set, which, if still possible at all, is in general time consuming and requires expert mathematicians to be permanently involved in the project. Therefore, in many biology labs, where it is difficult to maintain a team of mathematicians or physicists on a stable basis, it is hard to create a sustainable modelling environment that can be used on a permanent and routine basis.

Monte Carlo simulation provides an alternative approach to model complex systems involved in cellular function (or methods like FRAP to study them) that circumvents the intensive use of PDEs and ODEs. In the straightforward MC simulation approach we present here, it is assumed that (molecular) events in a living cell have a certain probability to occur within a specific short period of time. Examples of such events are binding of two molecules or molecule complexes, release of a molecule from a complex, movement of a molecule by random diffusion, degradation of a molecule, or bleaching of a fluorescent dye in an intense laser beam. In MC simulation, these events occur or do not occur during small simulated time steps dependent on the result of generating a random number and the probability distribution related to the nature of the event. The implementation is therefore relatively simple. All the program has to do is go through cycles representing small periods of time, in which for each molecule, a couple of random numbers are generated on the basis of which is decided whether the molecule, for instance, binds, unbinds, moves, or is photobleached. Similar to the straightforward implementation of the simulation program, the required input is fully intuitive. The user defines molecules and assigns properties like, “it moves by diffusion,” “it is able to bind to this or that other molecule,” “it is accumulating in nuclear foci,” or “it is tagged with a fluorescent dye.” The only mathematical or rather statistical input required are the probabilities that molecules actually effectuate these properties, i.e., the probability that they bind, unbind, move, or bleach during the time span simulated in each cycle of the program.

In this chapter, we present a straightforward Monte Carlo (MC)-based simulation tool to model biomolecular interactions and to subject those to FRAP assays to generate simulated FRAP curves and use the output to fit experimental data.

The program can be instructed through a simple and intuitive script language and can therefore be used by anyone with basic knowledge of biomolecular processes. The initial motivation to develop the program was the limited availability of solutions to accurately quantitate FRAP curves using formulas or equations amenable in a biology setting. In addition, the simple modelling environment appeared to be a surprisingly strong educational tool in that it provides the possibility to understand FRAP curves and how they are influenced by specific experimental conditions like, for instance, cell size and shape. In addition, the tool is well suited to design and optimize FRAP experiments and also its combination with fluorescence resonance energy transfer (FRET) [10], in relation to the specific properties of the biological system under surveillance.

In the following, we will first provide a brief description of the FRAP method and an overview of published quantitative FRAP analysis methods. Second, the implementation and use of the simulation tool in understanding and quantitatively analyzing FRAP and FRET experiments will be described. We then will present results of studying important properties of FRAP and combined acceptor photobleaching FRET and FRAP using the simulation tool.

2 Materials

2.1 Monte Carlo FRAP Simulation Tool

The Java-based Monte Carlo FRAP simulation tool can be obtained by request to the authors.

3 Methods

3.1 FRAP Analysis

FRAP is based on the property of fluorescent molecules that they are photobleached, i.e., irreversibly made nonfluorescent, when exposed to high-intensity excitation light. This often undesired property can be put to use when a small volume within a larger volume is photobleached, and the recovery of fluorescence due to movement of unbleached mobile molecules into the bleached region is followed in time. The recovery velocity and final level then represent their average displacement per unit time and the fractions of mobile and immobile molecules. FRAP is especially powerful in a situation where the system under surveillance is studied in active ("wild type") state and compared with passive or modified state, so that a difference in mobility can be attributed to protein function. For instance, in DNA repair, one can compare protein mobilities in unchallenged cells with those in cells exposed to a DNA damage-inducing agent. In transcriptional regulatory systems, like the nuclear hormone receptors, one can compare mobilities of ligand-induced and inactive receptors such as either non-liganded receptors, receptors inhibited by antagonistic ligands, or receptor mutants lacking DNA-binding properties [11].

There are two straightforward ways to perform FRAP analysis, i.e., visual inspection of the curves or semiquantitative analysis, by calculating the half-life of fluorescence recovery. In addition, a permanently immobilized fraction can be readily estimated from the incomplete recovery of fluorescence. Although this straightforward approach is by itself useful, as can be seen from the wealth of mechanistic insight that has been gained from many studies, half-lives provide information on overall mobility but do not allow detailed quantitative analysis. For example, when relatively small fractions of proteins are engaged in immobilizing DNA-binding events, half-life will be only slightly increased compared to fully free protein. Therefore, half-life is not easily translated into quantitative estimates of bound fractions or residence times in immobile DNA–protein complexes. To obtain more quantitative information from FRAP analysis, sophisticated analytical models have been established. The parameters that one aims to quantitatively assess are effective on- and off-rates to and from immobile DNA–protein complexes, which can be used to calculate the DNA-associated fraction and residence time in that state. When on-rates increase at constant off-rate, the immobile fraction also increases. When off-rates increase, the immobile fraction becomes smaller at constant on-rate, and, in addition, the residence time becomes shorter.

Apart from the parameters to be extracted from FRAP curves, mathematical models should include a number of fixed parameters representing microscopic properties, like shape, size, and intensity profile of the laser beam focused by the objective lens. In addition, FRAP curves may be influenced by properties like cell shape and size or heterogeneous distribution of the factors under surveillance. Although most of these can be obtained experimentally, incorporating them in mathematical models often complicates the situation to an extent where solving differential equations involved is hard or even impossible [12]. Therefore, a number of simplifications have been applied.

One complicating factor in FRAP modelling is the conical shape of high aperture lenses that are in general used for single-cell imaging. Initially, the photobleached region was modelled as a cylindrical uniform profile [13] or a cylindrical region with a radial Gaussian distribution [14–17]. However, although a cylindrical profile is justified when a low numerical aperture (NA) lens is used, a double-cone profile may be more accurate, even for low NA lenses [3, 18, 19]. Furthermore, unlike a cylindrical bleaching profile, the double-cone profile also implies a significant dependency of the three-dimensional situation, because of the axial Gaussian distribution of the laser beam [19–21]. These and other experimental conditions, like photophysical properties of the fluorophores in use (e.g., blinking) and also like the duration of bleaching and the consequences of diffusion during bleaching, should be carefully considered in the development of a kinetic model [7, 12, 22, 23].

Another potential complication in the development of mathematical models is a heterogeneous distribution of target sites of the labelled proteins. Most models assume a homogeneous distribution of binding sites, ignoring the typical spatial organization of nuclear processes like gene transcription or DNA replication [15, 23]. A more accurate binding model would then be one which takes the actual inhomogeneous distribution of binding sites into account by using the acquired imaging data [6].

Because of the complications described above, which in some instances demand simplification to an unwanted extent, we decided to develop a Monte Carlo-based simulation environment that avoids the necessity of designing and solving differential equations.

3.2 Monte Carlo Simulation Tool

The simulation program we developed consists of three parts: (1) a core program which runs the simulation using basic algorithms for diffusion, binding, and bleaching (Figs. 1 and 2); (2) a user interface which visualizes the simulation, allows the user to modify input parameters, and provides output (Fig. 3); and (3) a script language which allows to design models, both of molecular interactions and of FRAP and FRET assays to study those.

The core program is implemented in a straightforward and easily maintainable manner. It translates the user-defined scripts imported through the user interface and sends output to that interface. The program goes through cycles representing small time steps, usually in the order of 10–100 ms. In each cycle, the behavior of each molecule present at that time is simulated by generating random numbers on the basis of which a decision is taken whether the molecule performs specific actions. These decisions are based on probability distributions related to the events happening to the molecule or the actions taken by it. The underlying algorithms dealing with this are described in detail below, where we present the script language, in which compartments, molecules, labels, and their properties are defined. In the user interface, the simulations are visualized, graph and text output relevant for the simulated system is provided, and a number of model-related parameters can be modified by the user (Fig. 3).

3.2.1 Script Language

In order to provide a versatile modelling environment that can be used without the need to write new or modify existing program code, an intuitive script language was developed. The script language consists of a list of *definitions* of PARTICLES (e.g., proteins, phosphates, DNA), LABELS (gfp, yfp, cfp), COMPLEXES (combinations of particles), and COMPARTMENTS (e.g., nucleus, cytoplasm, laser cone), as well as a series of *rules* by which specific properties are assigned to the defined complexes. Rules like BIND

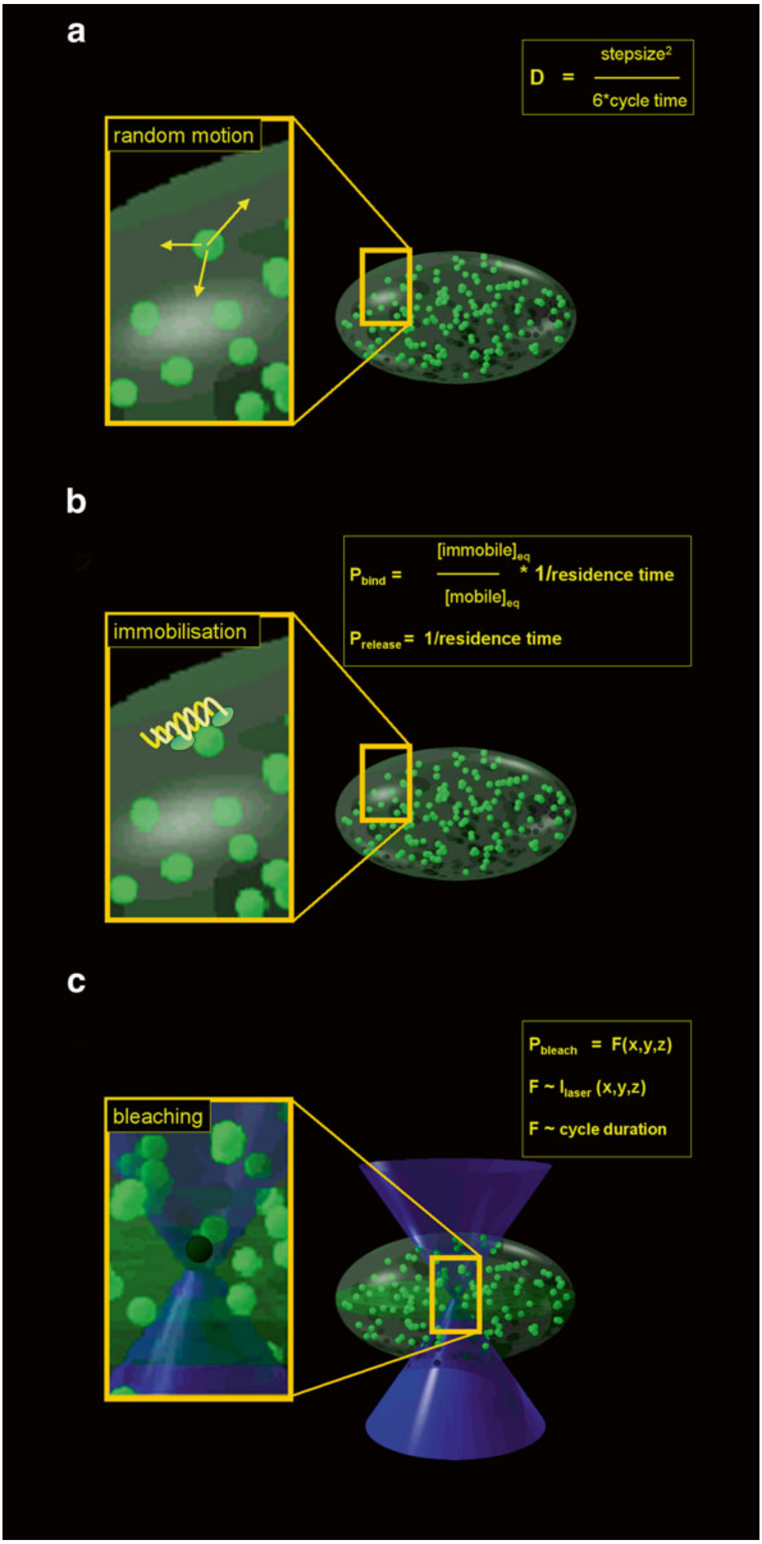

Fig. 1 General scheme for Monte Carlo simulation of FRAP on nuclear proteins. Overview of th e COMPARTMENTS that can be defined in the script language.

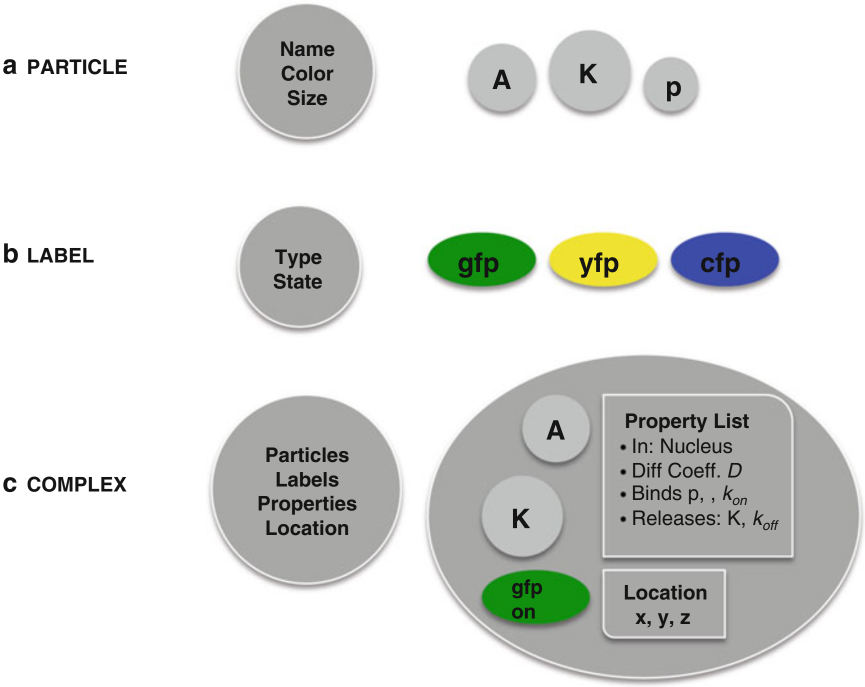

Fig. 2 Overview of the different components in the simulation. (**a**) PARTICLES are the basic building blocks from which complexes are created. They represent, for instance, proteins, phosphates, or DNA but only acquire properties when added to a complex. (**b**) LABELS are similar to particles in that they have to be added in a complex. Labels have a reserved name (gfp, yfp, or cfp) and have one property, representing the state of their fluorescent behavior: on, dark, or bleached. (**c**) COMPLEXES are composed of particles and (optional) labels. When formed, they acquire a property list from a blueprint composed on the basis of the user-defined rules in the script language (*see* text). They also have *x*-, *y*-, and *z*-coordinates representing their location

Fig. 1 (continued) The nucleus is represented as an *ellipsoid*; the laser *double cone* is a dedicated compartment that also contains values representing local laser intensities which are stored in a text file that is translated by the program into a 3-D array. (**a**) Schematic drawing of a cell nucleus (*ellipsoid*) containing randomly distributed COMPLEXES (*spheres*). Random Brownian motion (*inset*) is simulated on the basis of the Einstein–Smoluchowski equation (*see* text). (**b**) Simulation of binding to randomly distributed immobile target sites in the DNA (*inset*) is simulated by evaluating a chance to bind or to release based on simple binding kinetics, where the ratio between on- and off-rate constants (k_{on} and k_{off}) equals the ratio between the number of immobile and mobile molecules. (**c**) Photobleaching is simulated by evaluating a chance to get bleached based on the intensity profile of the laser beam. (Figure adapted from [3])

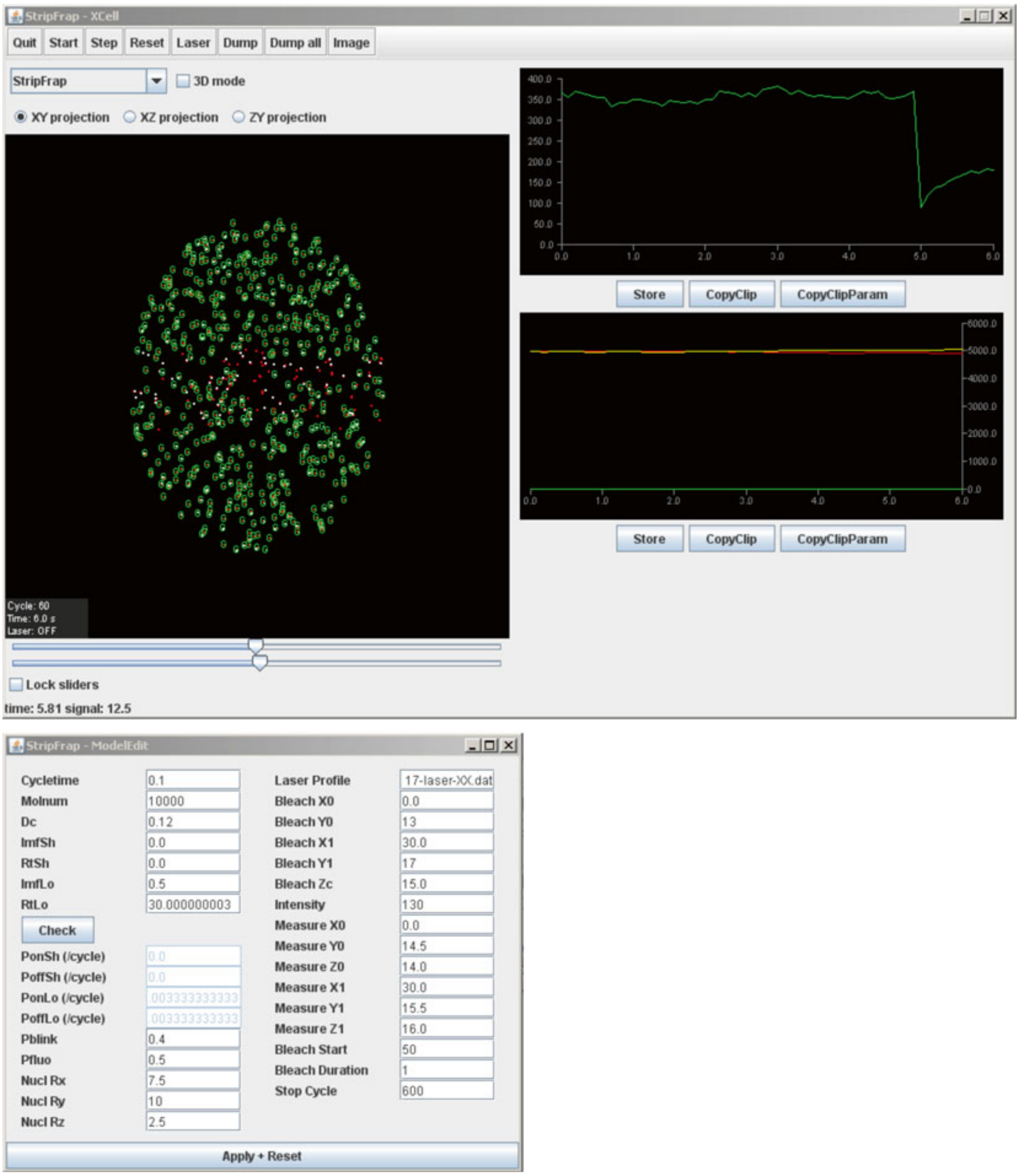

StripFrap ▾ ☐ 3D mode

● XY projection ○ XZ projection ○ ZY projection

Cycle: 60
Time: 6.0 s
Laser: OFF

☐ Lock sliders

time: 5.81 signal: 12.5

Cycletime	0.1
Molnum	10000
Dc	0.12
ImfSh	0.0
RtSh	0.0
ImfLo	0.5
RtLo	30.000000003
PonSh (/cycle)	0.0
PoffSh (/cycle)	0.0
PonLo (/cycle)	.003333333333
PoffLo (/cycle)	.003333333333
Pblink	0.4
Pfluo	0.5
Nucl Rx	7.5
Nucl Ry	10
Nucl Rz	2.5

Laser Profile	17-laser-XX.dat
Bleach X0	0.0
Bleach Y0	13
Bleach X1	30.0
Bleach Y1	17
Bleach Zc	15.0
Intensity	130
Measure X0	0.0
Measure Y0	14.5
Measure Z0	14.0
Measure X1	30.0
Measure Y1	15.5
Measure Z1	16.0
Bleach Start	50
Bleach Duration	1
Stop Cycle	600

Fig. 3 Graphical interface of the Monte Carlo simulation. The user interface contains two windows; the top window contains the visualization of the COMPLEXES, either fluorescent (*red dot with green G*) or nonfluorescent (*red dot only*) and bound (*red dot with white dot*) or freely mobile (*red dot*). The two graphs show the number of fluorescent COMPLEXES in the measured strip (FRAP curve) (*top*) and the sizes of the mobile (*red curve*), shortly bound (*green curve*), and long-bound (*yellow curve*) population in time. The buttons enable export of numerical data in text files. The lower window is used to modify the parameters of the model using indicated variables, including diffusion coefficient (*Dc*) and binding properties (both short (Sh) and long (Lo) immobile fractions) of the molecules. The binding parameters are set as immobile fractions (Imf) with corresponding residence times (Rt). The software automatically calculates the corresponding probabilities of binding (P_{on}) or release (P_{off}). Depending on the fluorophore used in FRAP analysis, the blinking parameters (P_{blink} and P_{fluo}) should be adjusted. Furthermore, general parameters like nuclear position and size (Nucl), the laser profile for FRAP analysis, and the position and size of the bleached (Bleach) and measured (Measure) areas, in addition to the bleach intensity and duration in cycles, the length of the prebleach period, and the total length of the FRAP curve can be adjusted

and RELEASE or ADD and REMOVE define which molecules interact, including corresponding rate constants (k_{on} and k_{off}), which are translated in the program to probabilities that are evaluated on the basis of numbers generated by a random generator. When the script is translated, the program adds all rules assigned to a specific complex in a property list which serves as a blueprint that is read when the specific complex is actually formed at the start or during the simulation (Fig. 2).

Below, the script language will be explained together with the most important algorithms used in the simulation in the context of the script definition or rule being discussed.

3.2.2 Script Definitions

COMPARTMENT(<NAME>, Compartment type, Fill-file.txt, Parameter list).

Compartments are predefined volumes, which are specified by their reserved-type name followed by a number of parameters that depend on the compartment type. Simple volumes like rectangular boxes (Box) or ellipsoids (Ellipsoid) require the *x*-, *y*-, and *z-coordinates* of their centers and diameters. The laser cone and bleach area (Bleach area) are special volumes that in addition to center and size coordinates, require specification of a formalized text file which contains a table with laser intensities at different positions in the laser.

EXCLUDE(*compartment1*, *compartment2*);

Compartments like the cytoplasm that contains other compartments like the nucleus are defined by defining two ellipsoids and then exclude the smaller from the larger.

Examples:

COMPARTMENT(nucleus, Ellipsoid, 0,0,0,10,15,5).

COMPARTMENT(cytoplasm, Ellipsoid, 0,0,0,20,20,7).

EXCLUDE(nucleus, cytoplasm).

COMPARTMENT (stripbleach, Bleach area, Laserprofile40X--1.3.txt, 0,0,0,20,1).

PARTICLE (<name>, Colour, Shape, Size).

PARTICLES (Fig. 2a) are the basic building blocks representing units from which COMPLEXES (described below) can be constructed. Particles have a user-defined name, for reference in defining complexes, as well as drawing instructions for visualization in the user interface. The most basic complex contains one particle (*see* **Note 1**).

Examples:

PARTICLE(transcriptionfactorX, RED, 2).

PARTICLE(kinaseY, RED, 2).

PARTICLE(phosphate, BLUE, 1).

PARTICLE(promotersequence, WHITE, 1).

COMPLEX(particle*1*-particle*2*-…-particle*N*, Compartment).

COMPLEXES (Fig 2c) consist of user-defined combinations of particles, which are specified by the particle names (see above) separated by hyphens. All possible combinations of particles that exist at the start of the simulation or that may form during the simulation have to be defined. The simplest complex consists of a single particle. The compartment in which the complex is present is the only property defined here. Mobility and interaction properties are assigned by the rules explained in the next section.

Examples

Complexes formed during phosphorylation:

COMPLEX(factorX, nucleus).

COMPLEX(kinaseY, nucleus).

COMPLEX(factorX-kinaseY, nucleus).

COMPLEX(phosphate-factorX-kinaseY, nucleus).

COMPLEX(phosphate-factorX, nucleus).

ADDLABEL(Label, complex).

One or more LABELS (Fig. 2b) can be added to complexes. Currently, three fluorescent labels are supported in the program, gfp, yfp, and cfp. Labels are different from particles in that they have one property of their own (whereas particles have no properties when not in a complex), i.e., they can be in three states: on state, dark state, and bleached. Fluorescent labels are different from particles in that they do not alter the complex property list.

CREATECOMPLEXES (complex, copy number, compartment);

Here, the number of copies of a specific complex present at the start of the simulation is specified. Note that only after this definition, actual complexes are formed. When complexes are created, their property list is read from a blueprint that was composed from the rules specified for each complex type while the script was read.

Example:

CREATECOMPLEXES (A, 10,000, nucleus).

3.2.3 Script Rules

Rules assign properties to COMPLEXES. When the script is read, the blueprint property list of each defined complexes is (which after complex definition contains one property, the compartment it is in) built up from properties derived from the rules (*see* also Fig. 3).

MOVE(complex, Diffusion Coefficient, Compartment).

The MOVE rule adds a diffusion coefficient to the complex blueprint property list. In the simulation, diffusion is simulated on the basis of the Einstein–Smoluchowski equation which defines the mean square displacement MSD of a pool of particles as $\mathrm{MSD} = 2nDt$, where D is the diffusion coefficient, t is time, and n is the number of dimensions in which the particles diffuse. In the simulation core program, 3-D diffusion of individual complexes is simulated by moving each complex in x-, y-, and z-direction, over a distance obtained by generating a random number R from a uniform distribution, and subsequently computing G(R) where G is a cumulative inverse Gaussian distribution with $\mu = 0$ and $\sigma^2 = 2Dt$ (*see* **Note 2**).

Anomalous diffusion can be simulated by using the ADD and REMOVE rule described below, adding and removing a (virtual) particle, with high on- and off-rate constants. The definitions and rules needed are described in an example below, where the ADD and REMOVE rules are described.

BIND(complex*1*, complex*2*, Compartment, *rate constant*,).
RELEASE(complex*1*, complex1-complex*2*, *rate constant*, Compartment).

The BIND rule assigns the property that complexes may bind to each other when they collide, and in which compartment this property is valid. A rate constant, k_{on}, is specified in s^{-1}. The chance of binding upon collision between complexes is derived by the program dependent on the duration of the simulated time step. In a relatively simple binding algorithm, the user-specified rate constant and the distance between two molecules under consideration together determine the chance that the two actually bind. We applied two different strategies for calculating the binding chance. In the first simple approach, the binding chance derived from k_{on} is applied when the distance between two molecules is smaller than a user-defined threshold. In a second more complex approach, the chance of collision is retrieved from a 3-D look-up table that gives the chance that two molecules with diffusion coefficients D1 and D2 collide when they are at distance d. The chance in each table cell (*D1, D2, d*) was estimated by performing a large number of MC simulations at very small time steps of 0.1 ms, for each table cell, and counting the times the two molecules collide, i.e., come closer than 1 nm.

The RELEASE rule assigns the property to a complex that part of the complex may detach and in which compartment this property is valid. The rate constant, k_{off}, is specified here in s^{-1} and translated by the program to the actual chance per simulated time step.

Examples:

BIND (A, B, nucleus, 0.01).

RELEASE (A, A-B, nucleus, 0.01).

ADD (complex*1*, complex*2*, *rate constant,* compartment).
REMOVE (complex*1*, complex*2*, *rate constant,* compartment).

ADD and REMOVE are similar to BIND and RELEASE, with the very important difference that added or removed complexes do not exist independently in the simulation, but are created by ADD, and taken up in the complex, or destroyed by REMOVE. The rate constant is therefore in both cases in s^{-1}, that is, independent of concentration. ADD and REMOVE rules can and should be used only when variations in spatial distribution and concentration of the added or removed complex are negligible during the simulation, i.e., when its concentration is in excess compared to the complex it is added to or removed from, and no local depletion or accumulation occurs. This is, for instance, useful for abundant phosphates or other small compounds.

Examples

Addition of a phosphate by a kinase and removal by a phosphatase:

ADD (phosphate, txnfactorX-KinaseY, nucleus, 0.5).

REMOVE (phosphate, txnfactorX-phosphate-PhosphataseY, nucleus, 0.5).

Simulation of anomalous diffusion:

ADD (anomdiffparticle, A, nucleus, 0.9).

REMOVE (anomdiffparticle, A-anomdiffparticle, nucleus, 0.9).

MOVE (A, 5, nucleus).

MOVE (A-anomdiffparticle, 0.01, nucleus).

BLEACH (start time, stop time, label, bleach area).

If a molecule contains a fluorescent label, this label can be bleached by a laser. We have implemented two approaches to define the laser intensity profile of the laser. In a simple approach, a theoretical intensity distribution was used based on a Gaussian distribution of intensities. In a second approach, the laser profile was experimentally determined by photobleaching a homogeneous fluorescent test slide with a focused stationary laser beam and measuring the bleach intensities at different optical sections spaced 1 μm. These values were then translated to laser intensities. Bleaching will take place during the simulation between the specified start and stop times in the bleach area defined in the definition section. For example:

COMPARTMENT (spotbleach, Bleach area, Laserfile.txt, 0,0,0).

BLEACH (100,101, gfp, spotbleach).

bleaches a spot at (0, 0, 0), usually the center of an ellipsoid representing the nucleus, during two simulated time steps.

3.3 Simulation of FRAP and FRET Assays

The simulation software was originally developed to quantitatively analyze FRAP applied to proteins in the cell nucleus. In addition, it provides a useful tool to study the influence of experimental conditions like the shape and size of the volume in which the proteins under surveillance reside as well as of the shape, size, and position of the bleach area. These two applications will be studied in the next two sections. In a third section, we will demonstrate the combination of acceptor photobleaching FRET and FRAP, which generates highly complex data.

3.3.1 FRAP Simulation, Fitting Experimental Data

There are basically three ways to fit simulation-generated FRAP curves to a given experimental curve:

1. Trial-and-error interactive search (Fig. 4). This approach requires some experience with the specific FRAP method. For instance, in a strip-FRAP experiment applied to the cell nucleus, which we routinely apply, one can start comparing an inactive

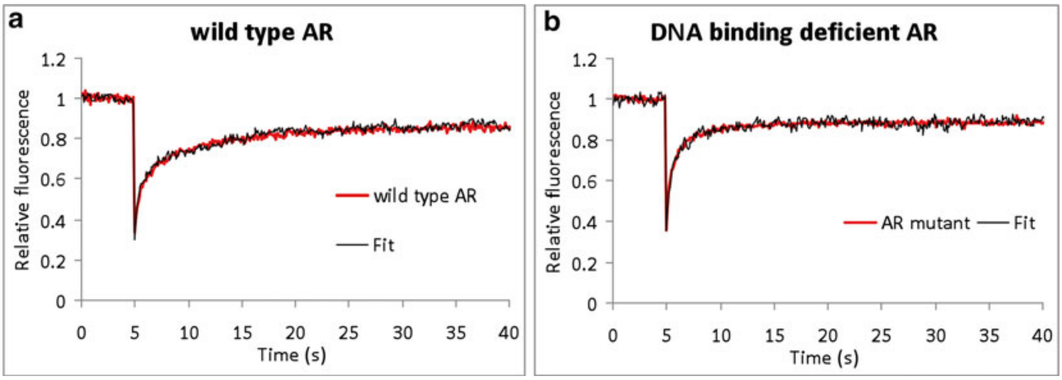

Fig. 4 Applications of FRAP in biological model systems. Two examples of the use of FRAP simulation of nuclear proteins (**a**, **b**), the androgen receptor (AR) (**a**) with its DNA-binding deficient mutant (**b**). (**a**) Like most nuclear proteins, the transcription factor AR shows a high mobility and in addition to transient immobilizations. The wild-type AR curve was best fitted to a curve representing a Dc of 1.9 μm^2/s and fraction of 35 % of the ARs immobilized for 8 s. This immobilization is due to DNA binding as is shown by a FRAP analysis of (**b**), a DNA-binding deficient AR, which fitted best to a scenario of freely mobile molecules (Dc = 1.9 μm^2/s). Experimental curves are *red*; simulated curves are *black*. The fit was performed by interactive trial-and-error modelling

situation, for instance, a non-DNA-binding mutant androgen receptor (AR) with an active situation, the activated wild-type AR. Then assume that the inactive molecules are freely mobile and try to fit with models of free diffusion (Fig. 4b). Then, when fitting the active situation, fix the best fitting diffusion coefficient and introduce an immobile fraction. This fraction can initially be estimated roughly, by checking how far recovery has proceeded at the time the freely mobile protein is fully recovered. The residence time can initially be estimated by checking time until full recovery (Fig. 4a).

2. Creating a large database in which all parameters to be fitted are systematically varied. We have extensively applied this approach in many studies investigating a variety of nuclear model systems [24–34]. Briefly, the experimenter first provides a number of fixed parameters, including the experimentally derived size of the nuclei, the FRAP approach, and the lens used for photobleaching and recording. Then a database is created where diffusion and DNA-binding properties (on- and off-rate constants) are systematically varied. Note that usually the rate constants are translated to intuitively better understandable immobile fraction and residence time (cf. Fig. 1b). In some cases, we also fitted a second pair of on- and off-rate constants representing short immobilization events [31, 33, 35]. When the database is created, a set of 20–50 simulated curves that fit best to the experimental curve are generated. In practice, there will be two or sometimes more different scenarios represented of which usually only one is realistic in the view of the system under surveillance. From the 5–10 best fitting curves, the diffusion and binding parameters are then averaged and considered best estimates.
3. Find the best curve automatically by search algorithms. Typically, these approaches start at a number of estimated or randomized solutions; abort simulation as soon as the generated curve deviates from the experimental; move to a solution nearby, in any direction of the parameter space; check if the fit is worse; if so, move back, step in another direction, and so on, until a (local) best fit is found. By starting at several points in parameter space, finding an erroneous local fit only is avoided. Although the latter undoubtedly will in the end be the method of choice, it is the least straightforward and will not give better results than generating databases and by brute force find the best fit.

3.3.2 FRAP Simulation, Studying FRAP Principles

As discussed above, issues like the conical shape of the laser beam or the confined space in which diffusion and immobilization take place may strongly influence FRAP curves, complicating analytical approaches to quantify them. Below, we present results of studying a number of experimental conditions that contribute to the shape of the curve, the recovery time, and/or the degree to which recovery takes place these aspects. The results of all simulation below are presented after two different types of normalization, i.e., expressed relatively to the average prebleach value (further indicated as "normalized to prebleach") and expressed relative to intensity immediately after the bleach (0) and at full recovery (1) (further referred to as "normalized as for bleach depth and final recovery"). To get an impression of the results of a standardized bleach experiment on nuclear proteins, we first generated FRAP curves of proteins in an ellipsoid volume representing the nucleus at increasing diffusion rates (Fig. 5a) and varying immobile fractions and various residence times in the immobile state (Fig. 5b).

In Fig. 5c, the results are shown of applying FRAP to a nucleus that has two large foci (for instance, nucleoli) in which a significant fraction of the protein is accumulating. The bleach area was chosen in between the accumulation, an experiment that is often applied to determine diffusion coefficient of the free pool. However, as can be seen, one has to be cautious when doing so, since a secondary recovery due to exchange of the free pool and the accumulation will occur. If this exchange is very slow, free diffusion can be separated from exchange by analyzing the first part of the curve. However, when exchange is fast, this will not be possible, and full modelling of the obtained curve including the exchange is required to determine diffusion coefficient of the free pool.

In many FRAP analyses, a straightforward "inert" DNA-binding model is chosen where the distribution of residence times is exponential, representing a scenario where immobile molecules have a constant chance to get mobilized. The characteristic residence time then is $1/k$, where k is the time constant of the exponential distribution of residence times e^{-kt} (Fig. 5e, left panel). However, it is conceivable that residence times are variable over time, especially when initial binding factors like androgen receptors or DNA damage sensors are studied. Initially, these factors may have a fair chance to release after DNA binding, but after binding of additional factors, the complex may be stabilized, lowering the off-rate constant. While the growing complex becomes more stable, it may after completion rapidly achieve its goal, i.e., launching transcription or repairing DNA damage, and the complex likely rapidly falls apart (Fig. 5d). This more complex scenario has a completely different distribution of binding times but can hardly be distinguished using FRAP (Fig. 5e) (*see* **Note 3**).

The initially most popular way to perform photobleaching experiments was to bleach a spot using a stationary laser to bleach the spot [36, 37]. Simulation of FRAP curves from differing spot locations shows that recoveries are much slower when a spot close to the edge of the nucleus is bleached compared to when the spot is approximately in the center (Fig. 6a). Interestingly, this differ-

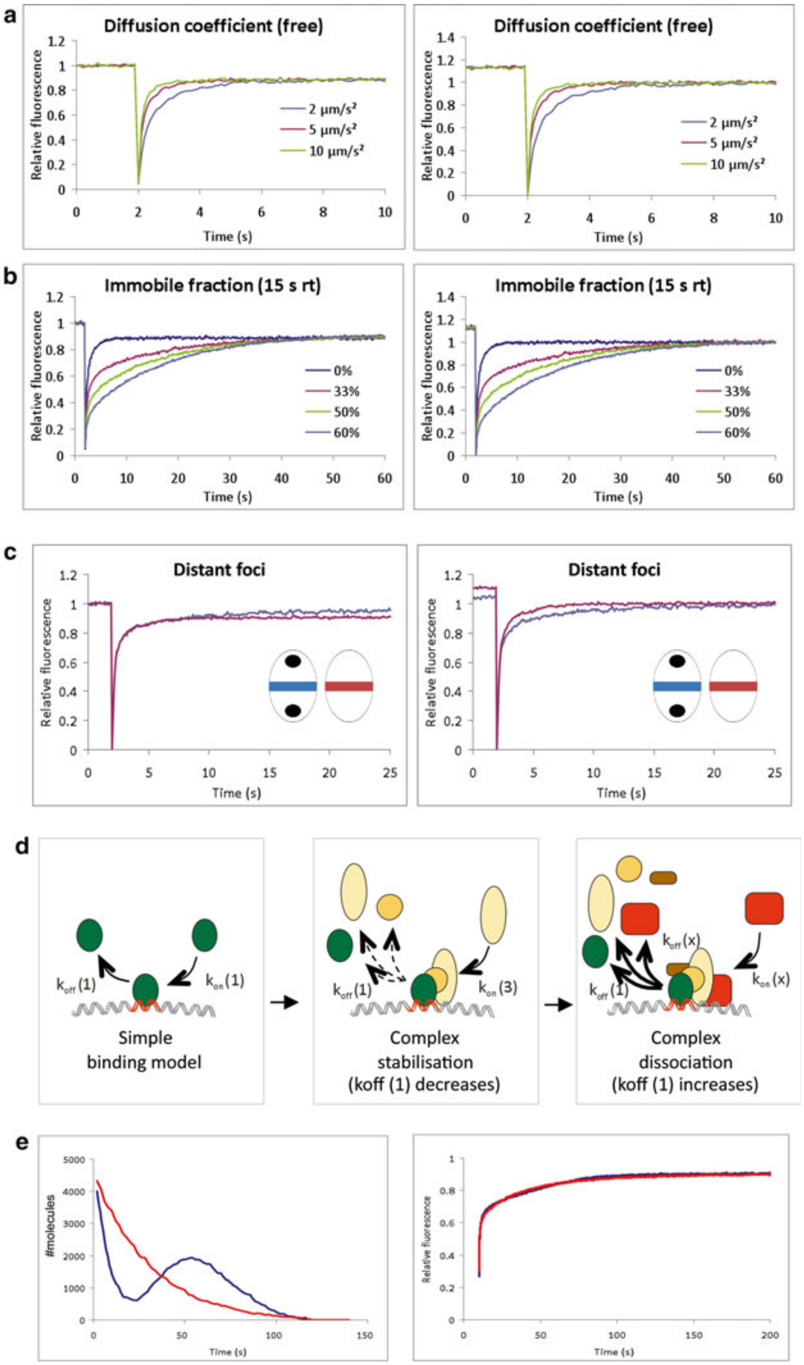

Fig. 5 Computer simulation aided analysis of diffusion and binding kinetics. Simulated spot-FRAP curves generated with (**a**) variable diffusion (2, 5, and 10 $\mu m^2/s$) and (**b**) variable immobile fraction (0, 33, 50, and 60 %) with fixed 15 s residence time ($D = 5\ \mu m^2/s$). (**c**) Curves representing a scenario where accumulations of the investigated protein exist at a distance from the bleached area compared to free diffusion in a homogeneously distributed scenario. (**d**) Complex DNA-binding scenario where the stability of the complex changes over time (*see* text). (**e**) *Left panel*: distribution of binding times for two scenarios; *red curve*, simple binding model with constant k_{off} ($e^{-k_{off}t}$); *blue curve*, complex binding model with varying k_{off}. *Right panel*: FRAP curves corresponding to the simple (*red*) and complex (*blue*) binding models. Curves were normalized to prebleach only (*left column*) and normalized for bleach depth and full recovery (*right column*, see text)

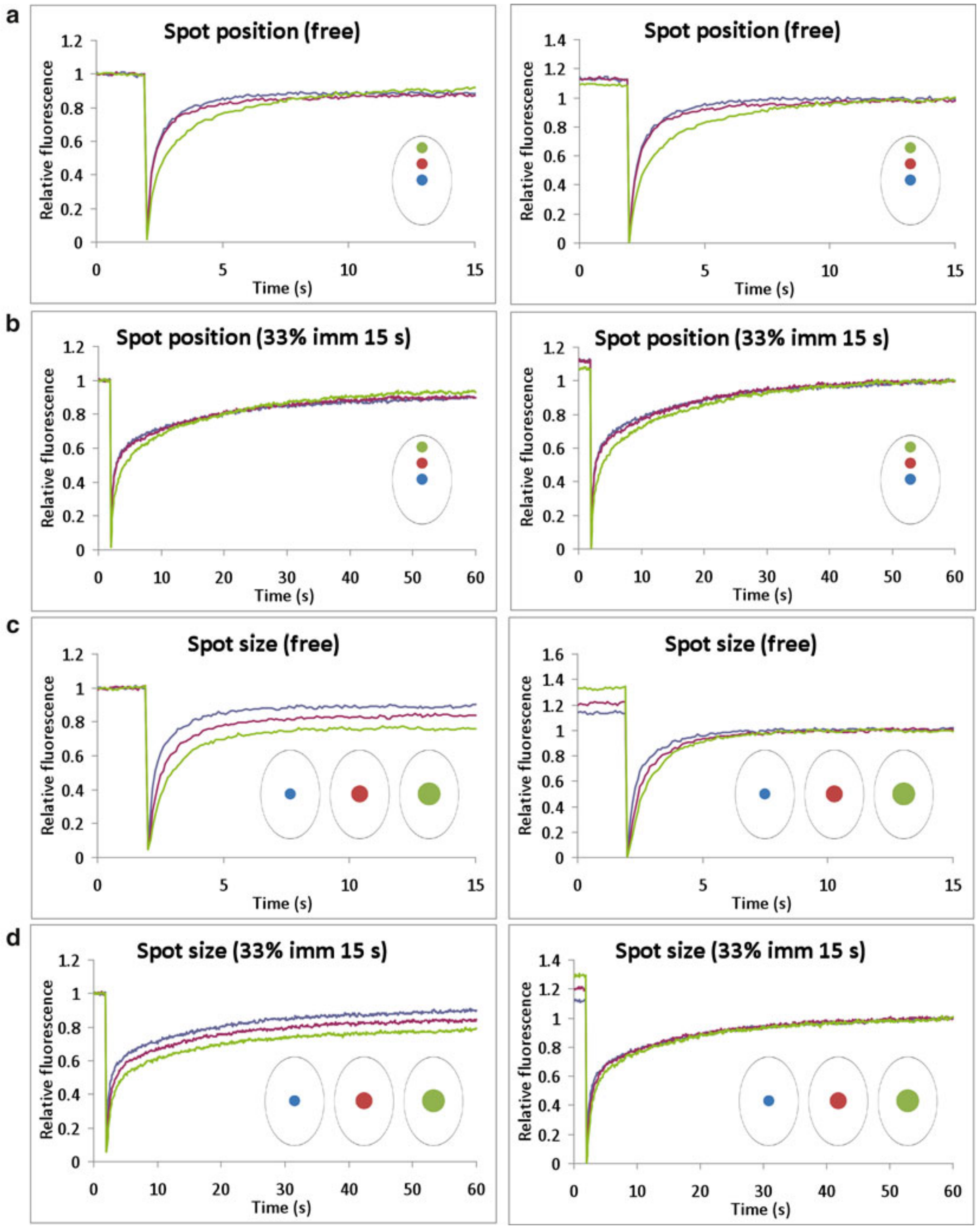

Fig. 6 Spot position and size variation affects FRAP curves. (**a** and **b**) Variable spot positions affect the FRAP curves of free diffusion ($D = 2\ \mu m^2/s$) (**a**) and a scenario with 33 % immobile fraction with a 15 s residence time (**b**). More polar positioned spots along the longitudinal axis result in a slower recovery of fluorescence predominantly in the first part of the FRAP curve suggesting a slower diffusion (**a**) rather than more or longer immobilization (**b**). (**c**, **d**) In contrast, variable spot sizes result predominantly in an increased permanently bleached fraction which can mistakenly be interpreted as an incomplete recovery suggesting a long immobile fraction in scenarios of free diffusion ($D = 2\ \mu m^2/s$) with (**d**, *left column*) or without (**c**, *left column*) and a 33 % immobile fraction with 15 s residence time. In addition to the increased permanently bleached fraction, increased spot sizes introduce a delayed recovery in the first part of a FRAP curve, suggesting a slower diffusion coefficient (**c**, *right column*). Curves were normalized both prebleach only (*left column*) and a combination of the intensity immediately after bleaching and after compete recovery (*right column*)

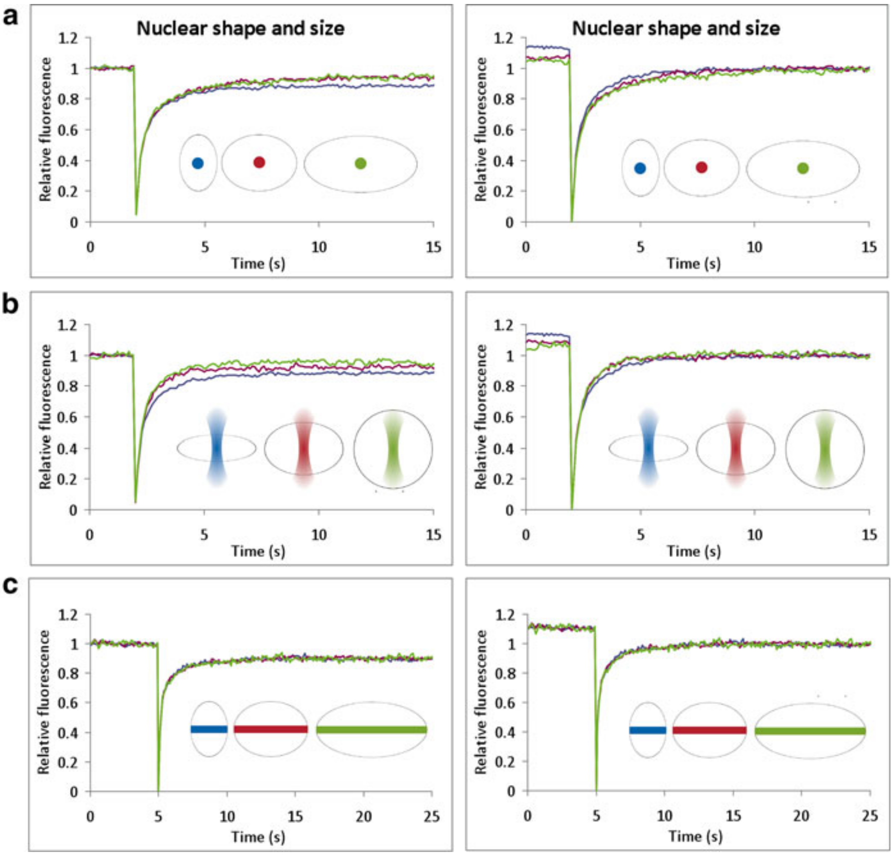

Fig. 7 The role of nuclear size and shape in spot- and strip-FRAP analysis. (**a**, **b**) Variation in nuclear size on the lateral ($r=5$, 10 and 15 μm) (**a**) and longitudinal ($r=5$, 7.5 and 15 μm) (**b**) axes all result in an incomplete recovery in spot-FRAP in a scenario of free diffusion ($D=2$ μm^2/s). Similarly to variation in spot size, variation in nuclear size introduces an additional but limited delay of recovery in the first part of the curve. (**c**–**e**) In contrast, variation in nuclear size only on the longitudinal (**d**) and vertical axes (**e**), and, importantly, not the lateral (**c**) axis, affects recovery of fluorescence. Furthermore, the delay in recovery in the first part of the curves found in spot-FRAP (**a**, **b**; *right column*) is absent in strip-FRAP (**c**–**e**; *right column*). (**f**) Similar effect of incomplete recovery by nuclear size variation along the longitudinal axis is found in a scenario of 33 % immobile fraction, 15 s residence time ($D=2$ μm^2/s). Curves were normalized like in Fig. 5

ence is smaller when an immobile fraction is present (Fig. 6b). Increasing spot size has a considerable effect on FRAP curves, obviously on the fraction bleached (Fig. 6c, left panel), but also on the shape of the recovery curve (Fig. 6c, right panel). The latter is fully abolished when a (large) transiently immobile fraction is present, showing that changing bleach area is a method to distinguish freely mobile proteins from transiently immobilized (Fig. 6d).

The size and shape of the cell nucleus may also affect the shape of FRAP curves, dependent on which FRAP approach is used (Fig. 7). Nuclei with increasing length and constant width and height as well as nuclei of varying thickness showed a small but

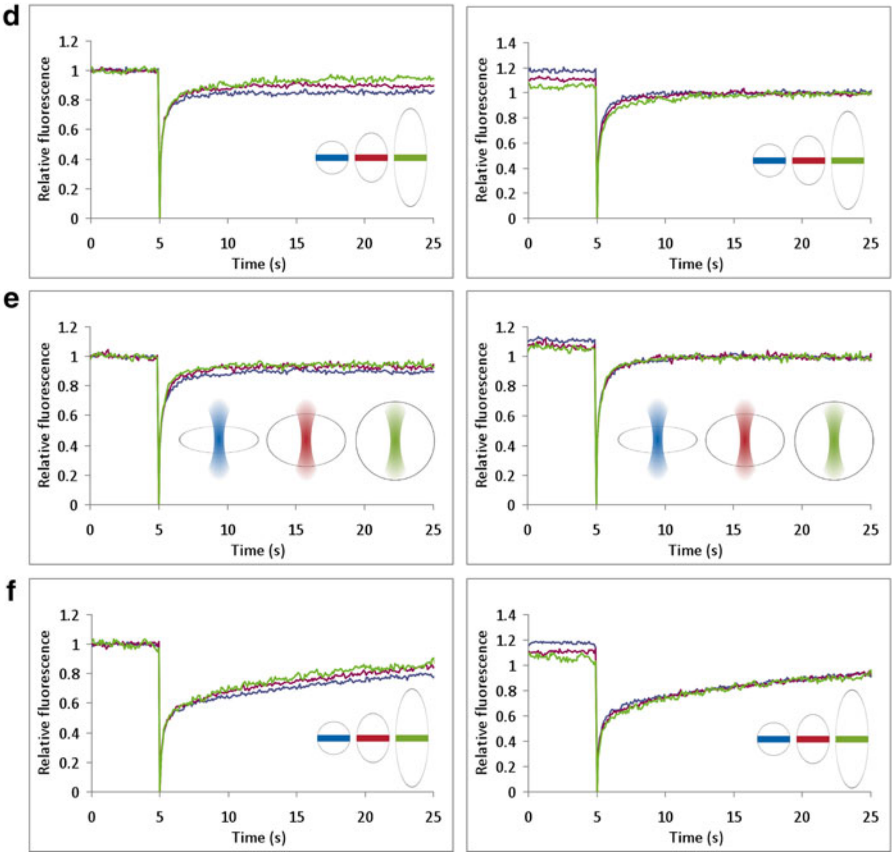

Fig. 7 (continued)

significant difference in a spot-FRAP experiment that could easily be confused with differences in mobility (Figs. 7a, b; left panels). If unnoticed, this is specifically a threat when a protein is studied under different conditions that influence the size of the cell or the cell nucleus. Especially when curves are normalized for bleach depth and final recovery, where the difference may be interpreted as the existence of a small transiently immobilized fraction, this leads to erroneous interpretation of the FRAP-curve. Interestingly, although bleaching a strip spanning the short axis of ellipsoid with different length results in different FRAP curves (Fig. 7d), no difference is observed when a strip is bleached spanning the longest axis of the ellipsoid nuclei (Fig. 7c), showing that the strip-FRAP method is less sensitive to nuclear size when applied in this way and therefore probably is a better method for these type of studies.

3.3.3 FRAP Simulation, Combined FRET and FRAP

Fluorescence resonance energy transfer (FRET) is a method to study interactions. One of the ways to quantitatively analyze FRET is acceptor photobleaching. Briefly, images are recorded before and after photobleaching the acceptor, leading to an increased donor signal in interacting molecules in which FRET occurred. The degree to which the donor signal is increased is a measure for the fraction of interacting molecules [38]. Interestingly, acceptor photobleaching can be combined with FRAP, the acceptor signal in a bleached area within a larger area being a conventional FRAP curve. If all molecules interact, the donor signal will be the opposite of the acceptor signal, since all bleached acceptors are accompanied by an unquenched donor. The curves can be compared by inverting the donor signal and normalizing both curves [10]. When not all molecules are interacting and the interaction takes place in a pool that is different from the pool of noninteracting molecules, e.g., if interaction only takes place in a DNA-bound, immobile fraction, the donor curve will be different from the acceptor curve (Fig. 8).

We first applied this method to investigate the N/C interaction of androgen receptors (AR, *see* glossary). We studied this N/C interaction using combined FRET and FRAP applied to AR double tagged with CFP and YFP. We observed that the donor signal represented a completely mobile molecule, whereas the acceptor curve (the conventional FRAP curve) showed an additional transiently immobilized fraction (cf. Fig. 4b; [10]).

The analysis of FRET–FRAP applied to double-tagged proteins is relatively easy. The analysis of FRET–FRAP on interaction of two single-tagged molecules is complicated by the fact that interacting molecules may be constantly releasing and rebinding again, which also contributes to the donor signal. In this case, the donor signal is constituted by three different phenomena, diffusion, and immobilization, like in the example with double-tagged AR, but also by exchange of interacting molecules. To interpret FRET–FRAP results, the simulation tool is very powerful (Fig. 8). We simulated different scenarios where a DNA-binding factor and a cofactor interact with each other, either in the nucleoplasm

Fig. 8 (continued) can be created that, e.g., represent a cofactor-binding receptor (e.g., androgen receptor (AR)) that transiently binds DNA, as is shown in the first column. Three general scenarios of cofactor ($n = 10{,}000$) binding to the receptor ($n = 10{,}000$) are simulated; cofactor interaction with either mobile (**a**, **b**) or immobile (**c**, **d**) DNA-binding factor only and with DNA-binding factors irrespective of their mobility (**e**, **f**). All three scenarios are simulated both with (**b**, **d** and **f**—$p_{on} = 0.4$, $p_{off} = 0.2$) and without (**a**, **c** and **e**—$p_{on} = 1$, $p_{off} = 0$) cofactor turnover on the DNA-binding factors (indicated by *black arrows* with corresponding probabilities) resulting in shifts in the fraction sizes (*second column*). DNA-binding behavior of the DNA-binding factor ($D = 1$ μm^2/s) is simulated with fixed probabilities (*gray arrows*—$p_{on} = 0.0025$, $p_{off} = 0.01$), and direct cofactor binding to DNA is excluded ($D_{cofactor} = 10$ μm^2/s). Quantitative analysis of dynamic behavior of the YFP-labelled cofactor (*third column*) and YFP labelled (*fourth column*) both in combination with their interacting subpopulation of their counterpart. To reverse the FRET–FRAP curve and enable comparison FRAP and FRET–FRAP data, curves were normalized by calculating $I_{norm} = (I_{raw} - I_0)/(I_{final} - I_0)$, where I_0 and I_{final} are fluorescence intensities after the bleach and after complete recovery, respectively. A more elaborated analysis of reciprocal labelled proteins enables distinction between models that show initially very similar curves (e.g., model in (**a**) and model in (**f**))

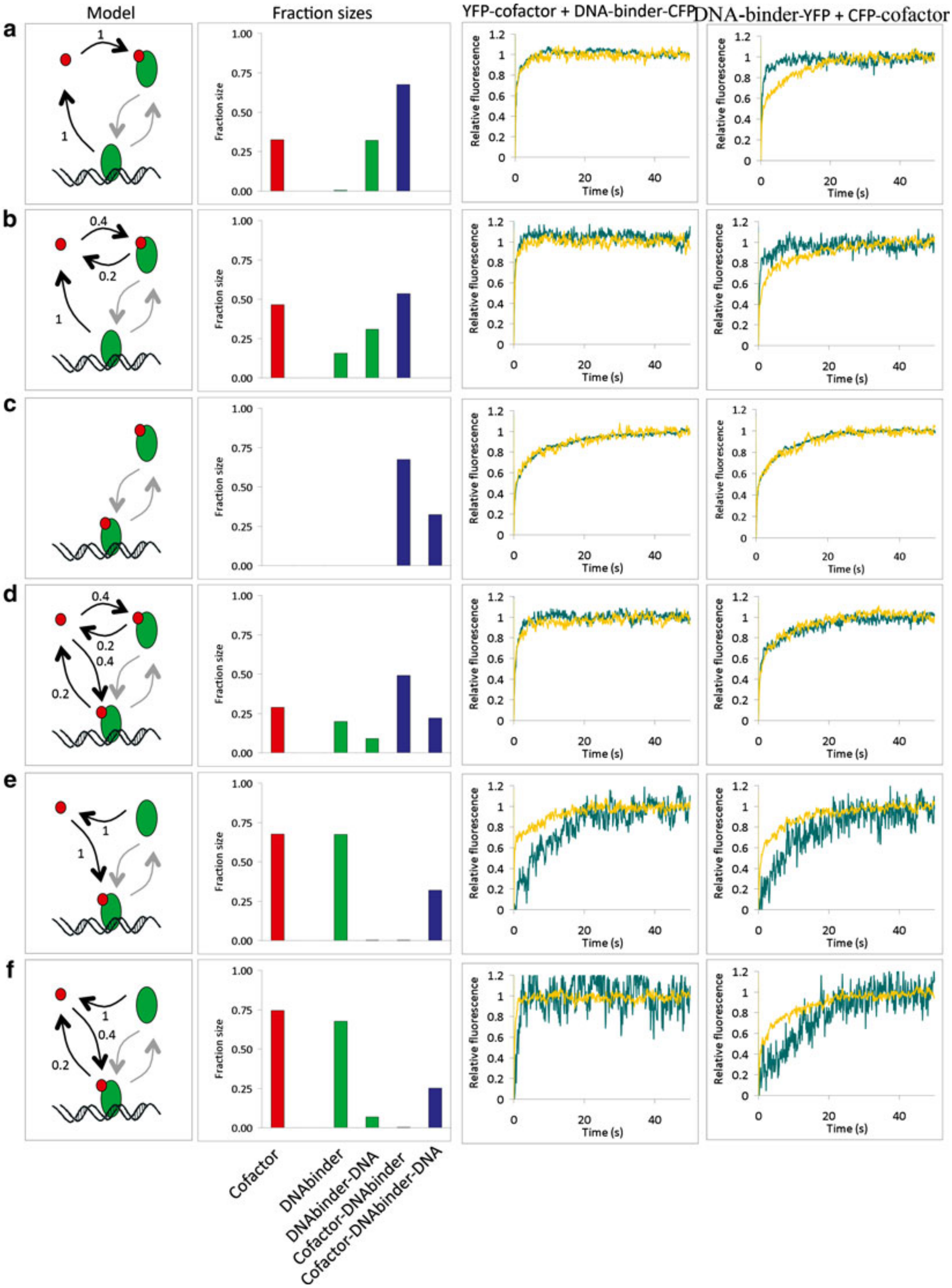

Fig. 8 Computer simulations of combined FRET and FRAP analysis. FRAP simulations can be extended with a combination of FRAP with acceptor-bleaching FRET (abFRET) to quantitatively analyze the relation between protein–protein interactions and the mobility of these proteins. By assigning probabilities not only to the DNA-binding properties of molecules but also to their ability to interact either in mobility or immobile state, models

(Fig. 8a, b), on DNA (Fig. 8e, f), or both (Fig. 8c, d). In order to distinguish between these scenarios, which would definitively contribute to insight in the molecular mechanisms by which these factors act, it is necessary to perform FRET–FRAP experiments with cofactors bound to donor (e.g., CFP) and DNA-binding factors tagged with acceptor (e.g., YFP) and vice versa.

3.4 Conclusions

In their intensive correspondence almost two centuries ago, Michael Faraday concluded a letter to James Maxwell raising an important issue: "there is one thing that I would be glad to ask you. When a mathematician engaged in investigating physical actions and results, has arrived at his own conclusions, may they not be expressed in common language, as fully, clearly and definitely as in mathematical formulae? (…) If so, would it not be a great boon to such as we to express them so — translating them out of their hieroglyphics that we might work upon them by experiment?" [39]. It may seem to many experimental biologists today dealing with analysis of complicated results from experiments like FRAP or FRET that these questions remain valid and urgent (for an in-depth discussion of the topic, *see* [40]). Nowadays, however, computers with their ever-increasing computational power may well be able to help solving the issue—not by translating the hieroglyphics, but by offering the possibility to shed light on complicated phenomena by intuitively instructable numerical simulations rather than by complex "mathematical formulae."

In order to contribute to opening up the analysis of complicated systems for a broad community, we aimed to develop a simulation tool that is straightforward in its implementation, maintenance, and expansion and can be used in a routine way without the need to design, validate, and solve sets of differential equations each time a new model is created or an existing one is modified. In addition, we aimed to provide the possibility to design models through an intuitive, easy-to-learn script language. Since our prior need was to be able to quantitate FRAP experiments, the presented modelling tool can be used not only to model complex systems but also to simulate any FRAP (or FRET) experiment applied to the modelled biological system. Therefore, the simulation environment fits very well into a systems biology research setting where one aims to achieve an iterative cycle of experiment-driven modelling and model-driven experiments: the model and the method are united in one simulation. Apart from the advantage that models can be created in a simple intuitive script language, the complexity of the designed models with respect to molecular interactions and transformations is only limited by computer speed. In addition, and in sharp contrast with mathematical modelling strategies, compartmentalization in multiple (irregular shaped) volumes of specific interactions poses no problem to our approach and also does not significantly reduce the speed of the program.

In conclusion, we have shown that Monte Carlo simulation of FRAP (1) can be used for automatically or interactively fitting FRAP data using a large set of fixed parameters reflecting influential experimental conditions that are hard to include in other approaches; (2) is well suited to understand, demonstrate, and teach FRAP principles; and (3) can be used to design, validate, and quantify more complex approaches such as the combination of FRAP and acceptor-bleaching FRET. Finally, since not only microscope procedures but also the investigated molecular behavior and molecular interactions are simulated, the program provides a versatile educational tool to model and study complex molecular interaction schemes which contribute to understanding important molecular aspects of cell function.

4 Notes

1. Small molecules like, for instance, phosphates, which modify complex properties and which are in general highly abundant, like phosphates, are usually not defined as a single molecule that actually exists during the simulation when not bound, but are added to complexes, which means that they are not present before addition.
2. For simulation of collision with the boundaries of the compartment in which the complex is diffusing, we considered the implementation of fully elastic or dampened collision. However, such algorithms require time-consuming calculation of the normal plane to an ellipsoid. Second, it is likely that the inside membrane of, for instance, the nucleus or cytoplasm is highly roughled. In addition, the nuclear membrane is covered with lamins, lamin receptors, and other macromolecules to which most likely also chromatin is attached, and the cytoplasm membrane harbors high amounts of transmembrane proteins. In other words, it is currently not at all known what type of collision behavior we can expect at membranes. Therefore, in the current simulation, we use the simple solution where each time the random-generated new position of the complex is outside the compartment, a new random step is generated until the new position is inside. This leads to a certain degree of stickiness of the membrane, which does not significantly contribute to FRAP simulations and, moreover, is not unlikely to reflect the actual situation.
3. Interestingly, novel methods to track single molecules may be applied to shed light on this, since the additional information obtained when tracking individual molecules is the distribution of binding times, whereas bulk methods only provide averages.

References

1. Aldridge BB, Burke JM, Lauffenburger DA et al (2006) Physicochemical modelling of cell signalling pathways. Nat Cell Biol 8: 1195–1203
2. van Royen ME, Dinant C, Farla P et al (2009) FRAP and FRET methods to study nuclear receptors in living cells. In: McEwan IJ (ed) Nuclear receptor superfamily, vol 505, Methods Mol Biol. Springer, Totowa, pp 69–96
3. van Royen ME, Farla P, Mattern KA et al (2009) Fluorescence recovery after photobleaching (FRAP) to study nuclear protein dynamics in living cells. In: Hancock R (ed) The nucleus, vol 464, Methods Mol Biol. Springer, Totowa, pp 363–385
4. Chen WW, Niepel M, Sorger PK (2010) Classic and contemporary approaches to modeling biochemical reactions. Genes Dev 24: 1861–1875
5. Alves R, Antunes F, Salvador A (2006) Tools for kinetic modeling of biochemical networks. Nat Biotechnol 24:667–672
6. Beaudouin J, Mora-Bermudez F, Klee T et al (2006) Dissecting the contribution of diffusion and interactions to the mobility of nuclear proteins. Biophys J 90:1878–1894
7. Braga J, Desterro JM, Carmo-Fonseca M (2004) Intracellular macromolecular mobility measured by fluorescence recovery after photobleaching with confocal laser scanning microscopes. Mol Biol Cell 15:4749–4760
8. McNally JG (2008) Quantitative FRAP in analysis of molecular binding dynamics in vivo. Methods Cell Biol 85:329–351
9. Phair RD, Scaffidi P, Elbi C et al (2004) Global nature of dynamic protein-chromatin interactions in vivo: three-dimensional genome scanning and dynamic interaction networks of chromatin proteins. Mol Cell Biol 24: 6393–6402
10. van Royen ME, Cunha SM, Brink MC et al (2007) Compartmentalization of androgen receptor protein-protein interactions in living cells. J Cell Biol 177:63–72
11. Farla P, Hersmus R, Trapman J et al (2005) Antiandrogens prevent stable DNA-binding of the androgen receptor. J Cell Sci 118: 4187–4198
12. Mueller F, Mazza D, Stasevich TJ et al (2010) FRAP and kinetic modeling in the analysis of nuclear protein dynamics: what do we really know? Curr Opin Cell Biol 22:403–411
13. Carrero G, McDonald D, Crawford E et al (2003) Using FRAP and mathematical modeling to determine the in vivo kinetics of nuclear proteins. Methods 29:14–28
14. Braeckmans K, Peeters L, Sanders NN et al (2003) Three-dimensional fluorescence recovery after photobleaching with the confocal scanning laser microscope. Biophys J 85:2240–2252
15. Kang M, Kenworthy AK (2008) A closed-form analytic expression for FRAP formula for the binding diffusion model. Biophys J 95: L13–L15
16. Tsibidis GD (2009) Quantitative interpretation of binding reactions of rapidly diffusing species using fluorescence recovery after photobleaching. J Microsc 233:384–390
17. Tsibidis GD, Ripoll J (2008) Investigation of binding mechanisms of nuclear proteins using confocal scanning laser microscopy and FRAP. J Theor Biol 253:755–768
18. Braeckmans K, Remaut K, Vandenbroucke RE et al (2007) Line FRAP with the confocal laser scanning microscope for diffusion measurements in small regions of 3-D samples. Biophys J 92:2172–2183
19. Hallen MA, Layton AT (2010) Expanding the scope of quantitative FRAP analysis. J Theor Biol 262:295–305
20. Mazza D, Braeckmans K, Cella F et al (2008) A new FRAP/FRAPa method for three-dimensional diffusion measurements based on multiphoton excitation microscopy. Biophys J 95:3457–3469
21. Mazza D, Cella F, Vicidomini G et al (2007) Role of three-dimensional bleach distribution in confocal and two-photon fluorescence recovery after photobleaching experiments. Appl Opt 46:7401–7411
22. Kang M, Day CA, Drake K et al (2009) A generalization of theory for two-dimensional fluorescence recovery after photobleaching applicable to confocal laser scanning microscopes. Biophys J 97:1501–1511
23. Mueller F, Wach P, McNally JG (2008) Evidence for a common mode of transcription factor interaction with chromatin as revealed by improved quantitative fluorescence recovery after photobleaching. Biophys J 94: 3323–3339
24. Agarwal S, van Cappellen WA, Guenole A et al (2011) ATP-dependent and independent functions of Rad54 in genome maintenance. J Cell Biol 192:735–750
25. de Graaf P, Mousson F, Geverts B et al (2010) Chromatin interaction of TATA-binding protein is dynamically regulated in human cells. J Cell Sci 123:2663–2671

26. Farla P, Hersmus R, Geverts B et al (2004) The androgen receptor ligand-binding domain stabilizes DNA binding in living cells. J Struct Biol 147:50–61
27. Luijsterburg MS, Goedhart J, Moser J et al (2007) Dynamic in vivo interaction of DDB2 E3 ubiquitin ligase with UV-damaged DNA is independent of damage-recognition protein XPC. J Cell Sci 120:2706–2716
28. Nicassio F, Corrado N, Vissers JH et al (2007) Human USP3 is a chromatin modifier required for S phase progression and genome stability. Curr Biol 17:1972–1977
29. Nishi R, Alekseev S, Dinant C et al (2009) UV-DDB-dependent regulation of nucleotide excision repair kinetics in living cells. DNA Repair (Amst) 8:767–776
30. Sabbioneda S, Gourdin AM, Green CM et al (2008) Effect of proliferating cell nuclear antigen ubiquitination and chromatin structure on the dynamic properties of the Y-family DNA polymerases. Mol Biol Cell 19:5193–5202
31. Tanner TM, Denayer S, Geverts B et al (2010) A 629RKLKK633 motif in the hinge region controls the androgen receptor at multiple levels. Cell Mol Life Sci 67:1919–1927
32. van den Boom V, Kooistra SM, Boesjes M et al (2007) UTF1 is a chromatin-associated protein involved in ES cell differentiation. J Cell Biol 178:913–924
33. Xouri G, Squire A, Dimaki M et al (2007) Cdt1 associates dynamically with chromatin throughout G1 and recruits Geminin onto chromatin. EMBO J 26:1303–1314
34. Zotter A, Luijsterburg MS, Warmerdam DO et al (2006) Recruitment of the nucleotide excision repair endonuclease XPG to sites of UV-induced dna damage depends on functional TFIIH. Mol Cell Biol 26: 8868–8879
35. van Royen ME, van Cappellen WA, Geverts B et al (2014) Androgen receptor complexes probe DNA for recognition sequences by short random interactions. J Cell Sci 127(Pt 7):1406–1416
36. Houtsmuller AB, Rademakers S, Nigg AL et al (1999) Action of DNA repair endonuclease ERCC1/XPF in living cells. Science 284: 958–961
37. Phair RD, Misteli T (2000) High mobility of proteins in the mammalian cell nucleus. Nature 404:604–609
38. Dinant C, van Royen ME, Vermeulen W et al (2008) Fluorescence resonance energy transfer of GFP and YFP by spectral imaging and quantitative acceptor photobleaching. J Microsc 231:97–104
39. Faraday M (2008) The correspondence of Michael Faraday, Vol 5. Institution of Engineering and Technology, Stevenage, pp 1855–1860
40. Tweney RD (2009) Mathematical representations in science: a cognitive-historical case history. Top Cogn Sci 1:758–776, 2010

Chapter 8

Fluorescence Correlation Spectroscopy

Mark A. Hink

Abstract

Fluorescence fluctuation spectroscopy techniques allow the quantification of fluorescent molecules present at the nanomolar concentration level. After a brief introduction to the technique, this chapter presents a protocol including background information in order to measure and quantify the molecular interaction of two signaling proteins inside the living cell using fluorescence cross-correlation spectroscopy.

Key words Fluorescence correlation spectroscopy, Fluorescence cross-correlation spectroscopy, Living cells, Dimerization, Molecular interactions, PI3K signaling

1 Introduction

Fluorescence correlation spectroscopy (FCS) is the most well-known member of the family of fluorescence fluctuation spectroscopy (FFS) techniques that analyzes temporal changes of the fluorescence intensity and relates these fluctuations to physical parameters of the observed molecules. FCS was developed in the early 1970s of the last century, but it took until the early 1990s, after the introduction of the confocal microscope with the use of improved lasers and detectors, to increase significantly in popularity.

The high sensitivity of the technique allows the detection of single molecules and obtaining information about the concentration, diffusion rate, and interactions of the molecules [1]. FCS measurements are typically done with a standard confocal microscope equipped with highly sensitive detectors and an objective of high numerical aperture. The focused laser beam illuminates a sub-femtoliter volume element (ca. 1 μm^3). The fluorescence photons emitted in this element pass through a pinhole and are detected by a highly sensitive detector. The signal-to-noise ratio achieved by this method is very high, since signal interference from scattered laser light, background fluorescence, and Raman emission can be largely eliminated. This allows measurements at the single-molecule level typically in the nanomolar concentration range.

Peter J. Verveer (ed.), *Advanced Fluorescence Microscopy: Methods and Protocols*, Methods in Molecular Biology, vol. 1251, DOI 10.1007/978-1-4939-2080-8_8, © Springer Science+Business Media New York 2015

During the measurement, molecules will, due to their Brownian motion, move in and out of the volume element and emit photons in a burst-type manner. The observed fluctuations can be used to determine the average time required for the passage through the volume element of a fluorescent molecule. This is dependent on its diffusion coefficient, which, in turn, is related to the size of a molecule. Therefore, it is possible to examine if molecules are moving freely or are part of a large, slow moving complex. Meseth et al. [2] examined the resolving power of FCS to distinguish between different molecular sizes. In case of an unchanged fluorescence yield upon binding, the diffusion constants of the bound and unbound form have to differ at least 1.6 times, corresponding to a fourfold mass increase which is required to discriminate both species without prior knowledge of the system. To overcome these limitations of FCS, Schwille et al. [3] applied dual-color fluorescence cross-correlation spectroscopy (FCCS). In such studies, interacting molecules are tagged by spectrally different fluorescent groups, for example, a green and a red dye. The different fluorescent dyes can be either excited with different lasers or with the same laser. The emission light is split into two different detectors by which the two fluorophores can be monitored simultaneously. Now, molecular interactions can be studied by following the fluorescence fluctuations of both fluorophores. In this case, the discriminating factor is not the increase of the molecular mass upon complex formation but the simultaneous occurrence of fluctuations in both detection channels.

Fluorescence fluctuations can also be analyzed in different ways, for example, to study the oligomerization of molecules via photon counting histogram (PCH) [4] or number and brightness (N&B) analysis [5]. In order to combine temporal information with spatial information, the FFS approaches can be used to analyze images as well, which are therefore referred to as image correlation spectroscopy (ICS) techniques [6]. In addition, one could combine FCS with other spectroscopic parameters like fluorescence lifetime [7], anisotropy [8], or Förster resonance energy transfer (FRET) [9], thereby increasing the selectivity of the measurement. In this chapter however, the focus is on single-point FCS and FCCS and its use to determine concentrations and quantify molecular interactions of fluorescently labeled molecules in living cells.

2 Materials

2.1 Fluorescence Microscope

A standard FCS setup utilizes a confocal microscope, in order to reduce background and increase FCS sensitivity by limiting the size and therefore the number of molecules within the observation volume (Fig. 1). The standard photomultiplier tube detectors

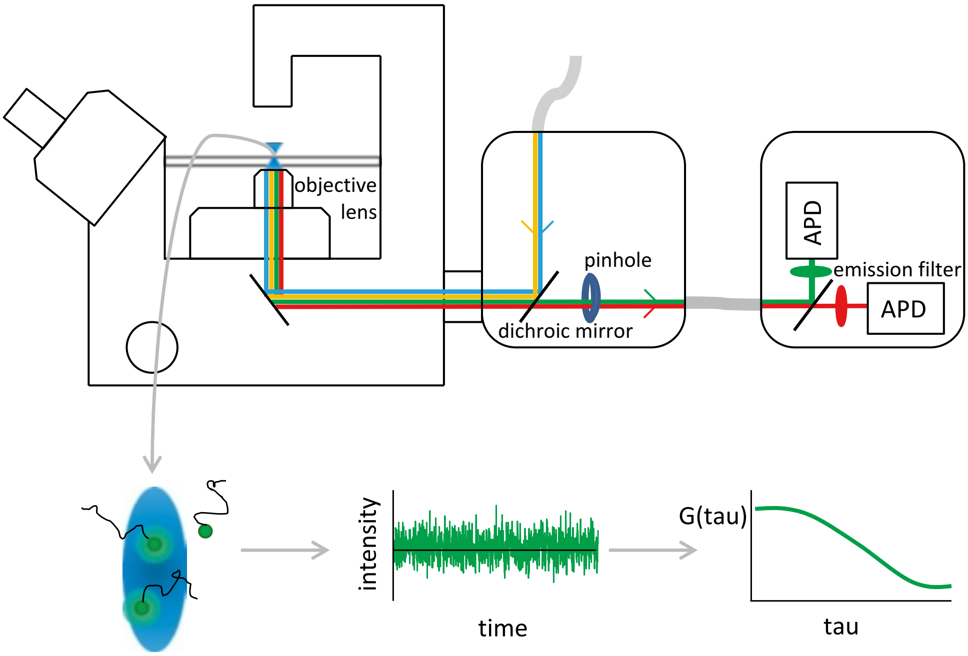

Fig. 1 FCCS setup. Light from two laser beams is focused into the sample using a highly corrected objective lens with a large numerical aperture. Fluorescence is guided via a pinhole into the detection unit where dichroic mirror and emission filters separate the light into two sensitive detectors. Diffusion of fluorescent molecules through the detection volume causes intensity fluctuations that can be analyzed by fitting the auto- and/or cross-correlation curves

(PMTs) delivered with confocal systems are not sensitive enough and should be replaced by avalanche photodiodes (APDs) or hybrid photodetectors (HPDs). Back-illuminated electron multiplying charge coupled device (EM-CCD) cameras have a higher sensitivity, but the current limitations in readout speed result in a low temporal resolution, often not sufficient to monitor the relative fast molecular diffusion in the cell cytoplasm or in vitro.

Although not discussed in this chapter, alternative excitation strategies like TIRF, SPIM, STED, or spinning disk illumination can be combined with FCS, allowing the differently shaped and/or smaller observation volume. Furthermore, some of these options open the possibility to use FCS at higher dye concentrations [10–13].

A critical part of the equipment is the objective lens, especially when multicolor analysis is being used. It is essential to utilize an objective with a high numerical aperture (NA) in order to collect as many of the emitted photons as possible, during the limited residence time of a molecule in the detection volume. Most FCS data fitting models require a 3D Gaussian or Gaussian-Lorentzian-shaped observation volume, and therefore, any mismatch between the refractive index of the objective immersion liquid and the sample should be minimized. An objective with the best chromatic corrections is needed to have the best overlap between the multicolor excitation and detection volumes. Apochromat objectives fulfill these requirements and have a collar ring to manually correct for mismatches. For biological samples, a water-immersed lens is preferred since oil-immersed objectives, despite their higher NA values, lead to shape distortions of the observation volume and therefore result in poor data fits. Recently, a silicon-immersed objective with high NA was introduced by Olympus which approaches the refractive index of the cellular environment closely, resulting in high-quality intracellular FCCS curves [14].

However, even when using these highly corrected objective lenses, the Gaussian approximation of the detection volume is not perfectly met. If diffusion coefficients with extreme high accuracy should be obtained, a two-focus-FCS setup can be used where the cross-correlation signal of molecules diffusing between two closely spaced observation volumes, generated by a Wollaston prism in the excitation path, is analyzed [15].

For two-color analysis, a common problem is the presence of cross talk: the fluorescence of one type of dye detected in the "other" detector (e.g., the emission of the "green" dye in the "red" detector). The large tail in the dye emission spectrum causing this cross talk could give rise to false-positive cross-correlation. One could correct the data for this artifact, as discussed later in this chapter, but this issue can be prevented by using pulsed interleaved excitation (PIE) [16]. Most absorbance spectra are relatively narrow, and therefore, it is possible to excite each dye selectively using two specific laser lines. When two pulsed laser units are emitting in an alternating mode and at a frequency much faster than the residence time of the molecule in the observation volume, one can obtain the fluorescence of both dyes in different time windows. By time-gating the detected fluorescence, one can omit the cross-talk photons in the calculation of the auto- and cross-correlation curves.

2.2 Fluorescent Dyes

Since FCS is a method that relies on the analysis of relative fluorescence fluctuations, the average concentration of fluorescent molecules should be kept low, typically between 1 nM and 1 μM. During the passage of the molecules through the detection volume, as many photons as possible should be detected. As shown by Koppel [17], the molecular brightness of the fluorophore is one of the most important parameters determining the quality of an FCS measurement. In order to select a high-quality FCS dye from the multitude of dyes commercially available, the product of extinction coefficient times fluorescence quantum yield gives a good indication. Therefore, fluorescent beads or quantum dots will result in FCS curves with a high signal-to-noise ratio (SNR), but due to the relative large size of these beads and limited coupling possibilities, their application to biological samples is still limited. In addition, one has to consider other dye-related parameters as well like the sensitivity to photobleaching, environmental conditions that alter the dye characteristics (e.g., pH or hydrophobicity effects), the probability to go into a temporal dark state (triplet-state kinetics and blinking), and its stickiness to other molecules or to the sample holder.

2.2.1 Autofluorescence

For intracellular FCS measurements, the spectral profile of cellular autofluorescence should be taken into account. In many animal cells, the autofluorescence background is the strongest in the blue spectral region, while in plant cells, also a strong fluorescence is observed in the red region (>640 nm) when chlorophyll is present. Since (intracellular) FCS experiments are typically performed with nanomolar concentrations of the fluorescent probe, the autofluorescence of the cell could become a significant fraction of the total detected fluorescence. When the autofluorescence is not giving rise to an autocorrelation curve, a constant correction factor will be added to the data fitting model. It should be prevented that autofluorescence generates an autocorrelation curve since it is difficult to (quantitatively) correct for this contribution. It might be worth to put some effort in reducing the autofluorescence by optimizing growth conditions like varying the composition of the growth medium, changing to 37 °C and CO_2 incubation of living animal cells, reducing the amount of light exposure in case of plant samples, or changing the experimental setup by shifting to another spectral detection region.

Common organic dyes used for FCS experiments are members of the Alexa (Invitrogen), Atto (ATTO-TEC), and CY (Amersham) families. When fluorescent proteins (FPs) are selected as the dye of choice (Table 1), one has to keep in mind that especially the red

Table 1
Recommended standard monomeric fluorescent proteins for FC(C)S experiments

Fluorescent protein	λ_{max} exc. (nm)	λ_{max} em. (nm)	Comment	Reference
TagBFP2	399	456	Check maturation, UV excitation	[32]
mTurquoise2	434	477	very bright	[33]
sGFP2 (or eGFP)	495	512	Photostable, bright	[34]
sYFP2 (or mVenus)	515	527	Significant photophysics	[35]
mCherry	587	610	Check maturation	[36]
TagRFP-T	555	584	Photostable, bright, low maturation	[37]
mKate2	588	635	Check maturation	[38]

variants often show reduced maturation. Due to the delay time in forming a fluorescent chromophore, the true number of proteins will be underestimated. For example, when observing fusion proteins involved in yeast pheromone signaling, roughly 50 % of the mCherry fusion proteins were not visible [18]. This maturation issue is highly cell-type dependent, for example, in HeLa cells, only ~5 % of the mCherry fusions are not visible. Maturation ratios can be estimated by determining the concentration of green and red proteins in an FCS experiment using a < red FP-spacer protein-eGFP > fusion construct, assuming the eGFP protein to mature instantaneously. The large spacer protein present should prevent (FRET) between the two, which would complicate the analysis [9]. In order to increase the molecular brightness, multiple copies of the FPs could be introduced in the fusion protein, although distortion of the biological functionality and heterogeneous maturation should be prevented [18].

2.2.2 Two-Color FCCS

For two-color FCCS studies, a critical point is the cross talk. Although one could correct for this artifact, it is desirable to diminish the spectral cross talk as much as possible. The popular FP pair CFP-YFP has a CFP bleed-through factor of 30 % in a typical setup. This will lead to significant false-positive cross-correlation, and therefore, corrections are required [18–20]. If the PIE excitation strategy is not possible, the quality of the measurements can be improved by choosing a pair that is spectrally more separated. However, when choosing such a pair, the overlap between the two detection volumes (which depends inversely on the spectral separation) will become less, and the maximum observable cross-correlation, and therefore the sensitivity, will decrease. Thus, a trade-off should be found between spectral separation and detection volume overlap. A good FCCS pair is eGFP-mCherry having high molecular brightness values, low photobleaching rates, and a reasonable spectral separation. Alternatively, one could use the more blue-shifted mTurquoise2-sYFP2 pair. When the fusion proteins give rise to FRET, the analysis is more complicated [21]. FRET will lower the molecular brightness of the donor molecule. Since the contribution of a molecule to the autocorrelation curve scales to the square of the molecular brightness [17], non-FRETting donor molecules that are brighter will dominate the correlation curve. Therefore, analysis can be simplified when a probe pair is chosen that will have a low FRET efficiency, e.g., due to a large spectral difference or spatial distance.

In order to minimize the importance of the correction factors and the uncertainty connected to it, the experimental conditions in two-color FCCS must be optimized. To lower the effect of cross talk, one should increase the signal of the red dye in the red detector. One could couple the red dye to the most abundant protein studied, lower the brightness of the green, and increase the brightness of the red dye by optimizing both laser powers or selecting a more red-shifted emission filter for the red detector [20]. To minimize the non-perfect overlap between the different observation volumes, dyes like the large Stokes shift fluorescent proteins [22] can be used. Here, multiple types of fluorescent proteins are excited using only a single laser line, while each FP fluoresces in a separate spectral window, due to their different Stokes shifts.

2.3 Data Analysis

Raw or correlated data can be fitted with dedicated analysis software. Many microscope manufacturers (e.g., Zeiss, ISS, Olympus, PicoQuant, and Becker & Hickl) distribute their own analysis software. In addition, commercial software packages can be purchased (e.g., SSTC FFS Data Processor and LFD SimFCS), and some user-written scripts for programs like Matlab, Igor, ImageJ, Origin, or Mathematica can be found on the Internet.

3 Methods

In the following section, a protocol is presented that can be used to measure dual-color fluorescence cross-correlation spectroscopy in living HeLa cells. Many issues discussed below will be similar in the case of single-color and/or in vitro FCS measurements. The idea behind this protocol is to study molecular interaction in the cell cytoplasm between sGFP2 and mCherry-labeled signaling proteins p110 and p85 [23] using an Olympus FV1000 microscope equipped with a PicoQuant PicoHarp detection unit. Although PIE excitation is possible with this setup, many FCS system do not have this feature and therefore is not employed in the protocols below.

3.1 Transfection of HeLa Cells

1. Grow HeLa cells in DMEM medium (Gibco) supplemented with GlutaMAX (Gibco) in a live cell incubator at 37 °C with 5 % CO_2.
2. One day before transfection, transfer the cells from the culture flask to sterile circular (ø 24 mm, size 1) coverslips (Menzel-Gläser), stored in a six-well container (Greiner), at a confluency of approximately 60 % (~5.0×10^5 cells).
3. Six hours after the cell transfer, replace the growth medium by phenol-free DMEM medium (Gibco), thereby lowering the autofluorescence.
4. Transfect the cells using Lipofectamine in Opti-MEM according to the manufacturers protocol (Invitrogen). An important point to consider, especially when using high expression promoters in the construct(s), is that FCS requires low expression levels (*see* **Note 1**).

3.2 Microscope Calibration

1. The microscope is placed in an air-conditioned room to ensure temperature stability and the calibration samples are stored in glass-bottomed 96-well plates (Whatman). In order to reduce the amount of detected background light, a protective blackened aluminum cover was placed on top of the sample during the measurements.
2. Turn the microscope and lasers on roughly 30 min before starting the measurements in order to stabilize.
3. Configure the FCS microscope filters: the sGFP2-labeled samples will be excited with the 488 nm laser line and the mCherry samples with the 561 nm diode laser (if available, use one or two pulsed lasers, suitable for the PIE excitation strategy, preventing cross talk). The fluorescence is separated from the excitation light by a dual-band dichroic filter, reflecting both the 488 and 561 nm excitation lines (Chroma). A secondary dichroic filter, LP562 (Chroma), separates the emission light into two different detection channels. Appropriate bandpass and longpass filters (e.g., BP500-550 (Semrock) for sGFP2 and LP572 (Chroma) for mCherry, respectively) are used for spectral selection and placed in front of the APD detectors (*see* **Note 2**).
4. Measure the fluorescence of a ~100 nM solution of Alexa 488 (Invitrogen) in phosphate buffered saline (PBS) at a laser power of approximately 10–50 $\mathrm{kW \cdot cm^{-2}}$. Adjust the correction collar of the objective to the position where the highest fluorescence count rate is observed in one of the two detection channels (*see* **Note 3**). In order to prevent that one optimizes scattered excitation light or adsorbed probe from the bottom of the sample holder, instead of observing the wished fluorescence signal, the focus should be set at least 20 μm into the solution.
5. Optimize the detected fluorescence to its highest value by moving the *X*-, *Y*-, and, if available, *Z*-position of the pinhole(s) in the confocal microscope and optimize the lens position in front of the APD, if possible.
6. Perform an FCS measurement of Alexa 488 and one of Atto 565 in PBS using their corresponding laser lines at 3.2 (488 nm) and 4.0 $\mathrm{kW \cdot cm^{-2}}$ (561 nm) (*see* **Note 4**). Adjust the measurement time such that the resulting correlation curves are smooth in the decaying part of the curve.
7. The intensity traces are imported into the FFS data processor 2.3 software, autocorrelated, and fitted to a model including terms for triplet-state kinetics and three-dimensional Brownian diffusion [24] (*see* **Note 5**):

$$G(\tau)=1+\frac{\gamma}{N}\cdot\left(\frac{1-T+Te^{\frac{-\tau}{\tau_{TRIP}}}}{(1-T)}\cdot\frac{1}{\left(1+\frac{\tau}{\tau_{dif}}\right)\sqrt{1+\frac{\tau}{\tau_{dif}}\cdot\left(\frac{\omega_{xy}}{\omega_z}\right)^2}}\right) \tag{1}$$

8. Validate if the obtained fitting parameters are within the expected range. For our system, the value for a $(=\omega_z/\omega_{xy})$ ranges from 4 to 15 and the values of τ_{dif} for Alexa 488 or Atto 565 are around 35 and 60 μs, respectively. The observed brightness values vary between 8 and 12 kHz per molecule. Note that these values will be different for other microscope systems. In general, the higher the brightness per particle, the better the quality of the obtained data will be. The system has to be calibrated until the highest possible brightness is reached without having photobleaching and/or saturation artifacts [25].
9. By solving Eqs. 2 and 3, using the translational diffusion coefficient (*D*) of 410 $\mu m^2 \cdot s^{-1}$ for Alexa 488 [26] and 360 $\mu m^2 . s^{-1}$ for Atto 565 in buffer, the dimensions of the "green" and "red" detection volumes, *V*, can be calculated by approximating these as cylinders (*see* **Note 6**).

$$\tau_{dif}=\frac{\omega_{xy}{}^2}{4D} \tag{2}$$

$$V=2\cdot\pi\cdot a\cdot\omega_{xy}{}^3 \tag{3}$$

The effective cross-correlation observation volume is estimated from the cross-correlation curve, measuring a sample of purified sGFP2 in PBS ($D=90\ \mu m^2 \cdot s^{-1}$). Here we make use of the cross talk of sGFP2 since some of its emission will be detected in the mCherry detection channel. The emission of mCherry in the GFP channel can be omitted.

3.3 Fluorescence Fluctuation Measurements

1. A coverslip with the transfected HeLa cells is sealed in an Attofluor cell chamber (Invitrogen) submerged in microscopy medium (20 mM HEPES (pH = 7.4), 137 mM NaCl, 5.4 mM KCl, 1.8 mM $CaCl_2$, 0.8 mM $MgCl_2$, and 20 mM glucose). Note that most growth media will acidify when incubated in the absence of 5 % CO_2 during the measurement.
2. Measure a positive cross-correlation sample, e.g., a fusion protein of sGFP2 linked to mCherry separated by a large protein. This control protein, like the negative control in step 3, should preferably be targeted to the same subcellular location as where the sample proteins will be localized. Here, we use

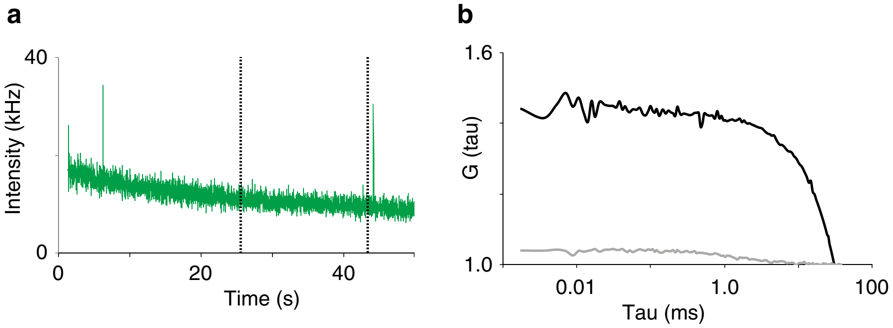

Fig. 2 Photobleaching and intensity spikes cause artifacts in the correlation curve (*black*) visible at the long tau values as a stepwise decay that might be erroneously assigned to slow moving molecules. By selecting only the stable part of the intensity trace (between markers) for calculation, a correct correlation curve (*gray*) is obtained although one has to validate that the observed decay is not biased to lower values due to photobleaching of mobile molecules (**Note 7**)

the cytoplasmic fusion protein mCherry-p63GEFT-sGFP2 [27]. To select the cells with FCS-compatible expression levels, the sample is scanned by the confocal microscope using standard imaging settings for the PMT detector sensitivity but with an open pinhole. Those cells that are more fluorescent than the mock-transfected control cells, but do not give rise to detector saturation in the image, are selected for FCS measurements. For cross-correlation measurements, only cells are selected that express both the eGFP and mCherry fusion proteins. The laser power is set not higher than 2.1 kW·cm^{-2} for the 488 nm laser line and 1.7 kW·cm^{-2} for the 561 nm laser line to prevent photobleaching, cellular damage, and photophysical effects. These excitation intensities are still sufficient to achieve reasonable SNRs [5–10] within measurement times of 60–180 seconds. Above these laser powers, photobleaching and probe saturation lead to significant distortions of the correlation curves (Fig. 2). Optimize the objective correction collar and the pinhole such that the amplitude of the cross-correlation curve is as high as possible. Sometimes this will lead to slightly worse structure parameter values a, but the overlap of the detection volumes is the most important parameter in these experiments.

3. Perform a measurement of a negative cross-correlation sample. The ideal sample would consist of mutants of the two sample proteins now lacking the possibility to interact with each other due to point mutations or domain deletions. When the amino acid residues responsible for binding are unknown, HeLa cells co-transfected with free sGFP2 and free mCherry could be used as an alternative.

4. Measure the samples. All raw fluorescence intensity files are saved for processing. Data sets containing large intensity spikes

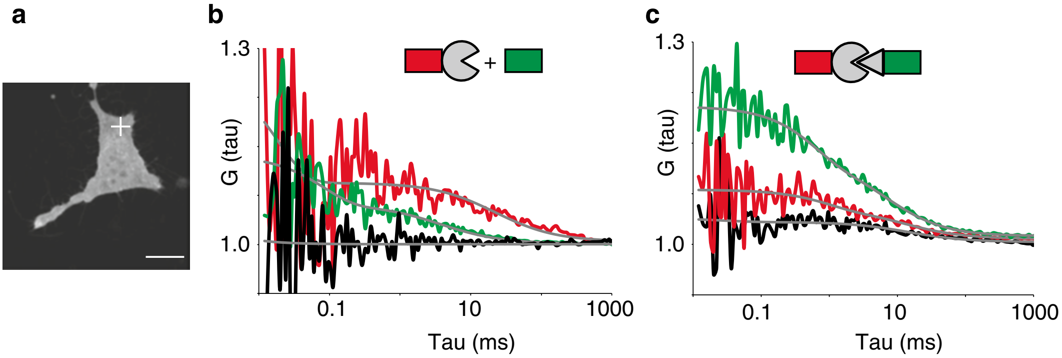

Fig. 3 Auto- (*green* and *red*) and cross-correlation (*black*) curves and their fits (*gray*) as measured (*cross*) in the cytoplasm of transfected HeLa cells (**a**). For the negative control (**b**), p85-mCherry plus sGFP2, no cross-correlation amplitude is observed after cross-talk correction, while the positive cross-correlation amplitude for the measurements of the p85-mCherry plus sGFP2-p110 constructs (**c**) indicates a large fraction of interacting molecules

(>10 times the intensity standard deviation around the mean intensity), significant signal drift, or photobleaching (>20 % intensity loss per minute) are discarded (*see* **Note 7**).

3.4 Auto- and Cross-Correlation Analysis

1. After loading the raw data into the FFS data processor software, a region that contains at least 50,000 photons in each channel is selected out of the two complete raw data traces. The selected intensity trace should be stable, so without an intensity drift, and the presence of (small) intensity spikes should be minimal in both channels. The selected intensity trace is auto- and cross-correlated resulting in the two autocorrelation curves $G_G(\tau)$ (for the GFP channel) and $G_C(\tau)$ (for the mCherry channel) and the cross-correlation curve $G_{GC}(\tau)$. Figure 3 shows some typical experimental curves.
2. The autocorrelation curves can be fitted according to

$$G(\tau)=1+\left(1-\frac{F_{background}}{F_{total}}\right)^2\cdot\left(\frac{1}{<N>}\cdot\frac{1-T+Te^{-\tau/\tau_T}}{(1-T)}\sum_m\Phi_m\cdot\frac{1}{\left(1+\frac{\tau}{\tau_{dif,m}}\right)\sqrt{1+\frac{\tau}{\tau_{dif}}\cdot\left(\frac{\omega_{xy}}{\omega_z}\right)^2}}\right)+\text{offset} \qquad (4)$$

$$\text{with } \Phi_m=\frac{\left(\eta_m^2Y_m\right)}{\left(\sum_m\eta_mY_m\right)^2}$$

where the first term between brackets corrects for the background fluorescence in the corresponding detection channel ($F_{background}$). The value of this parameter is determined by averaging the fluorescence intensity in the subcellular region of interest (e.g., cytoplasm or membrane) in mock-transfected cells. In order to correct for the noncorrelating cross-talk of sGFP2 in the mCherry channel, the background fluorescence in the mCherry channel was raised by 0.10 times the intensity observed in the GFP channel. This bleed-through factor of 10 % was determined by comparing the intensities in both detection channels using an sGFP2-only sample. Each molecular species, m, contributes to the autocorrelation curve function according to its fraction (Υ_m) and molecular brightness (η_m). The ratio ω_{xy}/ω_z is fixed to the value obtained from the calibration measurement for each channel. An offset can be included in the fit to correct for the effect of small intensity drifts in the selected data trace.

3. The amplitude of the cross-correlation curve $G_{GC}(\tau)$ contains the information of the number of doubly labeled particles, N_{GC}, observed in the cross-correlation observation volume, V_{GC}. Equations 5–7 contain corrections for cross talk and assume a 1:1 stoichiometry for the complex p110-p85; for more complex situations, modified equations can be found in [19]. In the case of higher order complexes, one could determine the brightness and distribution of those oligomers using PCH techniques [28] and include brightness corrections in Eqs. 5–7:

$$G_{GC}(0)=1+\frac{N_G\left(\frac{\eta_{GGC}}{\eta_{CCC}}\right)+N_{GC}\left(1+\frac{\eta_{GGC}}{\eta_{CCC}}\right)}{\left(N_G+N_{GC}\right)\left(N_C+N_{GC}\left(1+\frac{\eta_{GGC}}{\eta_{CCC}}\right)+N_G\left(\frac{\eta_{GGC}}{\eta_{CCC}}\right)\right)} \tag{5}$$

$$G_G(0)=1+\frac{1}{\left(N_G+N_{GC}\right)} \tag{6}$$

$$G_C(0)=1+\frac{1}{\left(N_C+N_{GC}+\left(N_G+N_{GC}\right)\left(\frac{\eta_{GGC}}{\eta_{CCC}}\right)^2\right)} \tag{7}$$

where N_G, N_C are the number of monomers labeled with sGFP2 or mCherry. N_{GC} is the heterodimer and no homodimers are being formed. The $\eta_{probe,excitation,emission}$ values correspond to the molecular brightness values for the probes as detected for the different excitation and emission wavelengths. For example, η_{GGC} should be read as the molecular brightness of sGFP2 as detected in the mCherry channel using the 488 nm "GFP" laser line. These values were obtained by the calibration measurements using the same laser settings as for the samples.

Table 2
FCCS results in HeLa cells transfected with mCherry-p110 and p85-sGFP2. The data was analyzed using Eqs. 4–7. Diffusion times are presented for the detection channel corresponding to the FP in the construct. *n.a.* not applicable

Construct(s)	Diffusion time (ms)	% Interaction (N_{GC}/N_{Xtotal})	Apparent K_D (nM)	n (–)
p85-sGFP2	1.1 ± 0.2	0 ± 0	n.a.	10
mCherry-p110	1.8 ± 0.4	0 ± 0	n.a.	10
mCherry-GEFT-sGFP2 (fusion)	1.9 ± 0.3 1.1. ± 0.2	99 ± 2 98 ± 1	n.a	10
p85-mCherry + sGFP2	1.7 ± 0.3 1.2 ± 0.3	1 ± 1 0 ± 0	2,560 ± 3,984	10
p85-mCherry sGFP2-p110	2.0 ± 0.4 1.4 ± 0.3	85 ± 4 82 ± 5	172 ± 36	12
p85-sGFP2 + mCherry-p110	1.2 ± 0.3 1.8 ± 0.4	83 ± 5 80 ± 4	230 ± 41	12

The relative brightness of sGFP2 to mCherry in the mCherry detection channel, η_{GGC}/η_{CCC}, is 9 % in our setup.

Equations 5–7 are linked and fitted globally including a weight factor to correct for the different detection volume sizes. An example of our experimental values is presented in Table 2. Due to the different expression levels among the cells, caused by the transient transfection procedure, the interaction values are presented as percentage complex and as apparent dissociation constant assuming the absence of nonfluorescent and endogenous p85 and p110 proteins.

4 Notes

1. Although suitable for fluorescence imaging experiments, standard overexpression promoters like cowpea mosaic virus (CMV) will result in too high expression levels. In order to prevent this, one could change promoter sequence, reduce the amount of DNA in the transfection procedure, or shorten the time between transfection and FCS measurement. Here, 1 nanogram of DNA constructs has been used containing a CMV promoter sequence in front of p110 and p85 coding sequences. The cells were transfected the evening before the FCCS measurements. To prevent the presence of unfinished protein product, like free FP, interfering with the measurement the FP should be located preferably at the C-terminal of the protein of interest.

2. For measurements at extreme low fluorophore concentrations, the Raman scattering signal of water molecules, present at roughly 55 M, could contaminate the fluorescence signal. The wavelength of the Raman peak can be calculated since the main peak is always red-shifted 3,382 cm^{-1} relative to the excitation, so proper bandpass filters can be selected blocking this signal.
3. The optimal setting of the ring, where the highest count rate is observed, corresponds very often *not* to the printed value on the ring that indicates the sample glass thickness.
4. Many fluorescent probes like the FPs are susceptible to photobleaching and show blinking behavior, due to continuous conversions between fluorescent and dark states [29–31]. Both processes become more pronounced at higher laser powers. In addition, at higher laser intensities, probe saturation might occur in the center of the focus [25]. This will change the effective shape of the detection volume, resulting in a deviation from the 3D-Gaussian-shaped detection volume that is assumed in the fitting models. Therefore, a trade-off should be found using a laser power where the brightness of the molecule (expressed as detected counts $\cdot s^{-1} \cdot$ molecule^{-1}) is as high as possible but where artifacts caused by the processes described above are minimized. To find this saturation level, one should plot the fluorescence intensity of the dye versus laser power.
5. The sizes of the green, red, and cross-correlation volumes are calculated from calibration measurements in vitro since a diffusion coefficient has to be known in order to solve Eqs. 2 and 3. Note that the biological samples measured in living cells will introduce small optical aberrations. The obtained observation volume sizes are therefore only approximations.
6. The autocorrelation function $G(\tau)$ contains a parameter N, which corresponds to the average number of fluorescent particles in the detection volume. τ_{dif} is the average diffusion time of the molecules, ω_{xy} is the equatorial radius, and ω_z is the axial radius of the observation volume. T is the fraction of molecules present in the dark state and τ_{TRIP} is the average time a molecule resides in the dark state. Take care that τ_{TRIP} is determined correctly, typically 10–200 μs dependent on dye and laser power, and is not mixing with τ_{dif}. Parameter γ describes the shape factor of the observation volume and equals 0.3535 for a 3D Gaussian or 1.0 for a cylindrical-shaped observation volume. From the autocorrelation fits the shape factor, a, describing the ratio between the axial and lateral e^{-2} radii of the green and red observation volumes ($a = \omega_z/\omega_{xy}$) and the τ_{dif} for Alexa 488 and Atto 565 are obtained. Although the shape of the detection volumes is close to a 3D Gaussian in "ideal conditions," the optical aberrations introduced by measuring inside the living cell make it possible to approximate the detection volumes by cylinders.

Then the amplitude of the autocorrelation function, *G(0)*, equals to γ/N. In all the equations used in this chapter, cylindrical detection volumes are assumed with $\gamma = 1$.

7. Typically one observes a significant intensity drop during the first few seconds of the measurement after which the signal stabilizes. Often this is caused by photobleaching of molecules that are immobile or present in protein synthesis or degradation organelles like the endoplasmic reticulum (ER) or lysosomes. In order to distinguish this effect from a continuous photobleaching of the mobile molecules being studied, one can block the excitation light for a few seconds after which the measurement is repeated. When a signal recovery is being observed, the bleaching of the mobile molecules should be lowered using less excitation power.

Acknowledgments

The author would like to thank Kevin Crosby, Max Tollenaere, Marten Postma, and Ronald Breedijk for their assistance during the experiments. This work was supported by Middelgroot and Echo investment grants from the Netherlands Organisation for Scientific Research (NWO).

References

1. Haustein E, Schwille P (2007) Fluorescence correlation spectroscopy: novel variations of an established technique. Annu Rev Biophys Biomol Struct 36:151–169
2. Meseth U, Wohland T, Rigler R et al (1999) Resolution of fluorescence correlation measurements. Biophys J 76:1619–1631
3. Schwille P, Meyer-Almes FJ, Rigler R (1997) Dual-color fluorescence cross-correlation spectroscopy for multicomponent diffusional analysis in solution. Biophys J 72:1878–1886
4. Chen Y, Müller JD, So PTC et al (1999) The photon counting histogram in fluorescence fluctuation spectroscopy. Biophys J 77:553–567
5. Digman MA, Wiseman PW, Choi C et al (2009) Stoichiometry of molecular complexes at adhesions in living cells. Proc Natl Acad Sci U S A 106:2170–2175
6. Kolin DL, Wiseman PW (2007) Advances in image correlation spectroscopy: measuring number densities, aggregation states, and dynamics of fluorescently labeled macromolecules in cells. Cell Biochem Biophys 49:141–164
7. Kapusta P, Wahl M, Benda A et al (2007) Fluorescence lifetime correlation spectroscopy. J Fluoresc 17:43–48
8. Barcellona ML, Gammon S, Hazlett T et al (2004) Polarized fluorescence correlation spectroscopy of DNA-DAPI complexes. Microsc Res Tech 65:205–217
9. Price ES, DeVore MS, Johnson CK et al (2010) Detecting intramolecular dynamics and multiple Förster resonance energy transfer states by fluorescence correlation spectroscopy. J Phys Chem B 114:5895–5902
10. Hassler K, Leutenegger M, Rigler P et al (2005) Total internal reflection fluorescence correlation spectroscopy (TIR-FCS) with low background and high count-rate per molecule. Opt Express 13:7415–7423
11. Wohland T, Shi X, Sankaran J et al (2010) Single plane illumination fluorescence correlation spectroscopy (SPIM-FCS) probes inhomogeneous three-dimensional environments. Opt Express 18:10627–10641
12. Leutenegger M, Ringemann C, Lasser T et al (2012) Fluorescence correlation spectroscopy with a total internal reflection fluorescence STED microscope (TIRF-STED-FCS). Opt Express 20:5243–5263
13. Needleman DJ, Xu Y, Mitchison TJ (2009) Pin-hole array correlation imaging: highly

parallel fluorescence correlation spectroscopy. Biophys J 96:5050–5059

14. Hink MA (2012) Single-molecule microscopy using silicone oil immersion objective lenses. Biomed Scientist 2012:83–85
15. Dertinger T, Pacheco V, von der Hocht I et al (2007) Two-focus fluorescence correlation spectroscopy: A new tool for accurate and absolute diffusion measurements. ChemPhys Chem 8:433–443
16. Müller BK, Zaychikov E, Bräuchle C et al (2005) Pulsed interleaved excitation. Biophys J 89:3508–3522
17. Koppel DE (1974) Statistical accuracy in fluorescence correlation spectroscopy. Phys Rev A 10:1938–1945
18. Maeder CI, Hink MA, Kinkhabwala A et al (2007) Spatial regulation of Fus3 MAP kinase activity through a reaction-diffusion mechanism in yeast pheromone signaling. Nat Cell Biol 9:1319–1326
19. Foo YH, Naredi-Rainer N, Lamb DC et al (2012) Factors affecting the quantification of biomolecular interactions by fluorescence cross-correlation spectroscopy. Biophys J 102:1174–1183
20. Bacia K, Petrášek Z, Schwille P (2012) Correcting for spectral cross-talk in dual-color fluorescence cross-correlation spectroscopy. ChemPhysChem 13:1221–1231
21. Eggeling C, Widengren J, Brand L et al (2006) Analysis of photobleaching in single-molecule multicolor excitation and Förster resonance energy transfer measurements. J Phys Chem A 110:2979–2995
22. Shcherbakova D, Hink MA, Joosen L et al (2012) An orange fluorescent protein with a large Stokes shift for single-excitation multicolor FCCS and FRET imaging. J Am Chem Soc 134:7913–7923
23. Yu J, Christina Wjasow C, Backer JM (1998) Regulation of the p85-p110a phosphatidylinositol 3′-kinase. J Biol Chem 273:30199–30203
24. Skakun VV, Hink MA, Digris AV et al (2005) Global analysis of fluorescence fluctuation data. Eur Biophys J 34:323–334
25. Gregor I, Patra D, Enderlein J (2005) Optical saturation in fluorescence correlation spectroscopy under continuous-wave and pulsed excitation. ChemPhysChem 6:164–170
26. Kaputsa P (2010) Absolute diffusion coefficients: compilation of reference data for FCS calibration. Picoquant application note: http://www.picoquant.com/technotes/appnote_diffusion_coefficients.pdf
27. Adjobo-Hermans MWJ, Goedhart J, van Weeren L et al (2011) Real-time visualization of heterotrimeric G protein Gq activation in living cells. BMC Biol 9:32
28. Chen Y, Johnson J, Macdonald P et al (2010) Observing protein interactions and their stoichiometry in living cells by brightness analysis of fluorescence fluctuation experiments. Methods Enzymol 472:345–363
29. Haupts U, Maiti S, Schwille P et al (1998) Dynamics of fluorescence fluctuations in green fluorescent protein observed by fluorescence correlation spectroscopy. Proc Natl Acad Sci U S A 95:13573–13578
30. Schwille P, Kummer S, Heikal AA et al (2000) Fluorescence correlation spectroscopy reveals fast optical excitation-driven intramolecular dynamics of yellow fluorescent proteins. Proc Natl Acad Sci U S A 97:151–156
31. Hendrix J, Flors C, Dedecker P et al (2008) Dark states in monomeric red fluorescent proteins studied by fluorescence correlation and single molecule spectroscopy. Biophys J 94:4103–4113
32. Subach OM, Cranfill PJ, Davidson MW et al (2011) An enhanced monomeric blue fluorescent protein with the high chemical stability of the chromophore. PLoS One 6:e28674
33. Goedhart J, von Stetten D, Noirclerc-Savoye M et al (2012) Structure-guided evolution of cyan fluorescent proteins towards a quantum yield of 93 %. Nat Commun 3:751
34. Kremers GJ, Goedhart J, van den Heuvel DJ et al (2007) Improved green and blue fluorescent proteins for expression in bacteria and mammalian cells. Biogeosciences 46:3775–3783
35. Kremers GJ, Goedhart J, van Munster EB et al (2006) Cyan and yellow super fluorescent proteins with improved brightness, protein folding, and FRET Förster radius. Biogeosciences 45:6570–6580
36. Shaner NC, Campbell RE, Steinbach PA et al (2004) Improved monomeric red, orange and yellow fluorescent proteins derived from Discosoma sp. red fluorescent protein. Nat Biotechnol 22:1567–1572
37. Shaner NC, Lin MZ, McKeown MR et al (2008) Improving the photostability of bright monomeric orange and red fluorescent proteins. Nat Methods 5:545–551
38. Shcherbo D, Murphy CS, Ermakova GV et al (2009) Far-red fluorescent tags for protein imaging in living tissues. Biochem J 418:567–574

Chapter 9

Homo-FRET Imaging Highlights the Nanoscale Organization of Cell Surface Molecules

Suvrajit Saha*, Riya Raghupathy*, and Satyajit Mayor

Abstract

Several models have been proposed to understand the structure and organization of the plasma membrane in living cells. Predicated on equilibrium thermodynamic principles, the fluid-mosaic model of Singer and Nicholson and the model of lipid domains (or membrane rafts) are dominant models, which account for a fluid bilayer and functional lateral heterogeneity of membrane components, respectively. However, the constituents of the membrane and its composition are not maintained by equilibrium mechanisms. Indeed, the living cell membrane is a steady state of a number of active processes, namely, exocytosis, lipid synthesis and transbilayer flip-flop, and endocytosis. In this active milieu, many lipid constituents of the cell membrane exhibit a nanoscale organization that is also at odds with passive models based on chemical equilibrium. Here we provide a detailed description of microscopy and cell biological methods that have served to provide valuable information regarding the nature of nanoscale organization of lipid components in a living cell.

Key words (Homo)-FRET, Fluorescence, Anisotropy, Microscopy, Membranes

1 Introduction

The living cell surface is a complex ensemble of diverse lipid and protein molecules, where specific lipid-protein and protein-protein interactions trigger signal transduction pathways controlling the cellular physiology. The molecular organization and such interactions occur at a length scale of few nanometers and pose a challenging question to study such processes in the living cells. Although light microscopy has allowed visualizing the cells in live, studying the nanoscale presents a physical problem for conventional diffraction limited optics, which cannot access the length scales below the optical resolution of ~200–300 nm. Two complementary approaches have evolved to circumvent this issue. Recent developments in super-resolution imaging modalities (like STED, STORM, PALM, NSOM, SIM) have pushed the limits of the

---

* Authors contributed equally.

Peter J. Verveer (ed.), *Advanced Fluorescence Microscopy: Methods and Protocols*, Methods in Molecular Biology, vol. 1251, DOI 10.1007/978-1-4939-2080-8_9, © Springer Science+Business Media New York 2015

resolution of light microscopy to as low as 20 nm [1]. On the other hand, several parallel fluorescence-based techniques have been developed in the past couple of decades that have been used to examine protein-protein interactions in living cells [2–4]. Here we will discuss a fluorescence resonance energy transfer (FRET)-based approach, homo-FRET, and how it can be used to understand the nanoscale organization of cell surface molecules.

1.1 Homo-FRET and Fluorescence Emission Anisotropy

FRET (fluorescence resonance energy transfer or Förster resonance energy transfer) is the process of non-radiative energy transfer between a donor fluorophore in excited state and an acceptor fluorophore in ground state. The theoretical description of FRET [5] was developed by Theodor Förster in the 1940s. Energy transfer between the donor and the acceptor species is a result of dipolar interaction between them and is governed by the extent of spectral overlap between the emission spectrum of the donor species and the absorption spectrum of the acceptor, the quantum yield of the donor, and the relative orientation of the donor and acceptor transition dipoles (Fig. 1a, b). Due to the dipolar nature of FRET, the efficiency of energy transfer is inversely proportional to the sixth power of distances between the fluorophores. The distance at which efficiency of energy transfer (E) is 50 % is referred to as Förster's distance (R_0), typically ranging from 1 to 10 nm depending on the molecular and spectral properties of the fluorophores and the local environment. This makes FRET a suitable tool to measure distances at the biomolecular scale [6]:

$$E = 1/\left[1 + \left(r/R_0\right)^6\right] \quad (1)$$

Here, r is the distance between the donor and acceptor fluorophores. While FRET is generally described as an energy transfer process between distinct donor and acceptor fluorophores (hetero-FRET), energy transfer can also occur between like fluorophores with low Stokes shift and hence a significant overlap between their absorption and emission spectra. Here we focus on the ways of monitoring FRET between like fluorophores, or homo-FRET, in live cells. Homo-FRET can be estimated by measuring the loss of the polarization of emitted fluorescence. Fluorescence emission polarization in turn may be monitored by determining fluorescence emission anisotropy. This is measured by exciting fluorophores by plane-polarized illumination and collecting the emitted fluorescence in two orthogonal planes [7].

Fluorescence anisotropy (r) is defined by

$$r = \frac{I_{\mathrm{pa}} - I_{\mathrm{pe}}}{I_{\mathrm{pa}} + 2I_{\mathrm{pe}}}, \quad (2)$$

where I_{pa} and I_{pe} are the emission intensities collected in the parallel and the perpendicular directions, respectively. Since

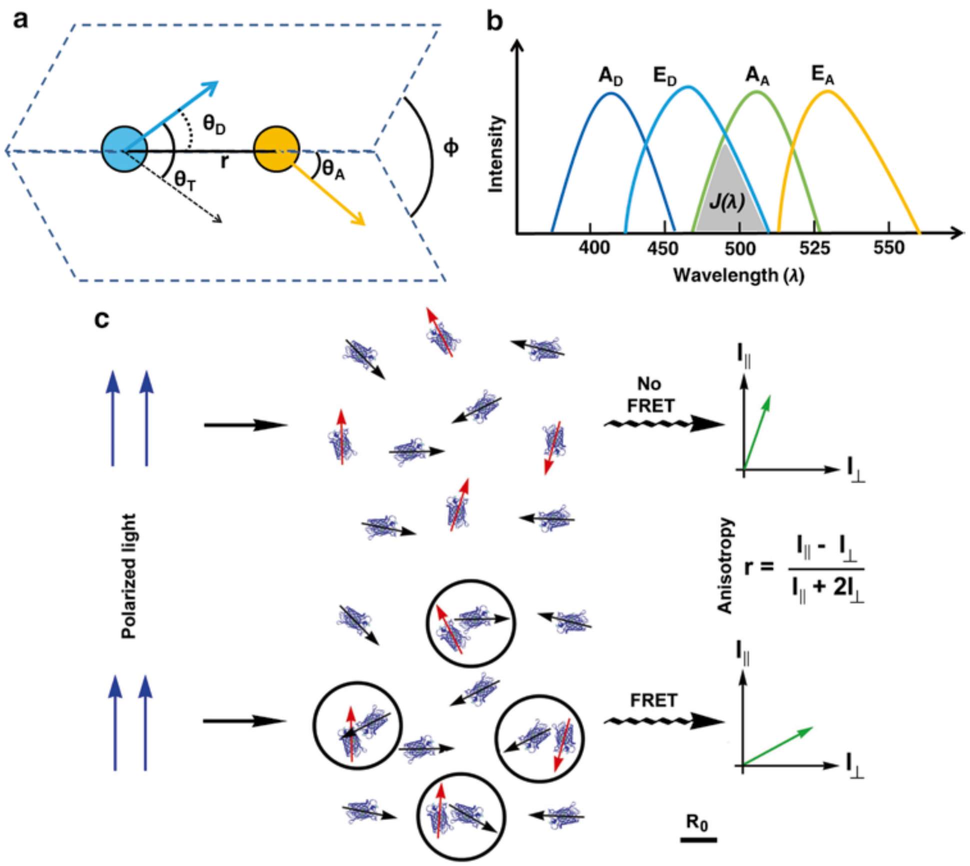

Fig. 1 Principle of homo-FRET process. (**a**) Angular orientation of donor (*cyan*) and acceptor (*yellow-orange*) transition dipoles are shown as θ_D and θ_A, respectively, where the intermolecular distance is shown as **r**. The extent of depolarization in the emission is dependent on the angle between the two transition dipoles, during the energy transfer process. (**b**) Spectral overlap integral J (λ) (shown in *gray*) between the donor emission (**E_D**) and acceptor absorption (**A_A**) is one of the factors determining the Förster distance, R_0. (**c**) A pool of isolated fluorophores when excited by polarized light (in the absence of significant rotational motions) results in fluorescence emission being relatively polarized (*top*). When fluorophores are relatively close together (in *circles below*), homo-FRET can take place between two like fluorophores, if the fluorophores have a significant overlap between their own excitation and emission spectrum, resulting in depolarized fluorescence emission and a lower value of anisotropy. Adapted with permission from Krishnan et al. [2] and Sharma et al. [18]

fluorescence anisotropy (r) is normalized to the total intensity (denominator term), its readout can be considered as a sum of intensity-weighted fluorescence anisotropies of individual fluorophores. The polarized illumination allows selective excitation (photoselection) of a pool of fluorophores with excitation dipoles aligned to the plane of illumination. The depolarization (or loss of anisotropy) of the fluorescence emission of a population of photoselected fluorophores can be dictated by two processes, rotational diffusion and homo-FRET. In a dilute solution of fluorophores (say 1–10 μM), the high intermolecular distances

($r \gg R_0$) between individual fluorophores preclude homo-transfer, and hence, the anisotropy of emission is depolarized only by rotational diffusion. The rotational diffusion rates of molecules are governed by their size and local viscosity. If the rotational diffusion time is smaller than the lifetime of the probe, the probe can tumble multiple times during its lifetime and thereby depolarize the emission. The same probe when placed in a considerably more viscous medium will have much higher rotational diffusion time than its lifetime, and hence, the emission retains polarization partially. The Perrin equation provides the relationship between rotational diffusion, viscosity and molecular size, and fluorescence anisotropy (r):

$$\frac{1}{r} = \frac{1}{r_0} + \frac{\tau RT}{r_0 \eta V} \tag{3}$$

where T is the temperature, V is the hydrodynamic volume, η is the viscosity, τ is the rotational correlation time, and R is the universal gas constant [7]. Here r_0 is the fundamental anisotropy of the fluorophore in the absence of any rotational diffusion and arising only from the photoselection and the angular displacement between its excitation and emission dipoles. Homo-FRET can further depolarize the fluorescence emission (and thereby reduce emission anisotropy) under conditions of low inter-fluorophore distances ($r < R_0$) and significant spectral overlap. This is because photoselected fluorophores can transfer energy to acceptors with different relative angular orientations of their transition dipoles. Moreover, the acceptors can also undergo rotational tumbling during its fluorescence lifetime, thereby reducing the emission anisotropy of the system considerably (Fig. 1c). Since both the acceptor and donor are spectrally similar in homo-FRET, a precise measurement of the extent of loss in fluorescence emission anisotropy is the only way to monitor homo-FRET.

In most experiments, a comparison of the fluorescence anisotropy of an experimental sample is made with situations where there is no FRET. Like hetero-FRET, an expression for homo-FRET efficiency can make quantitative comparisons across different measurements convenient. One can use an expression based on measuring anisotropies r_c and r_m of donor fluorescence in the presence or absence of FRET conditions, respectively, i.e.:

$$E = 1 - \frac{r_\mathrm{c}}{r_\mathrm{m}} \tag{4}$$

It must be noted that the above equation is valid only under simple assumptions that homo-FRET is the only agent for the change in anisotropy and where excitation after leaving the donor never returns to the same donor species and where there is no change in the donor lifetimes [5].

The spatiotemporal interaction of like fluorophores inside living cells can be imaged by implementing the measurement of fluorescence anisotropy in a microscope configuration. In subsequent sections we describe how homo-FRET imaging is carried out in living cells to look at the nanoscale organization of cell surface molecules.

2 Materials

2.1 Buffers and Media

All the buffers and media are prepared in autoclaved Milli-Q-filtered water and filter sterilized prior to storage:

1. Medium 1(M1) buffer: 150 mM NaCl, 20 mM HEPES, 5 mM KCl, 1 mM $CaCl_2$, 1 mM $MgCl_2$, pH 7.2–7.4.

   M1 can be used as the buffer system for washing, labeling, and imaging cells (both live and fixed) for fluorescence imaging. M1 should be supplemented with 2 mg/ml of glucose (M1-Glc) for live cell imaging.
2. Phosphate buffer saline (PBS): 137 mM NaCl, 2 mM KCl, 10 mM Na_2HPO_4, 2 mM KH_2PO_4, pH 7.4.

   PBS is widely used for passaging of cells and clearing coverslips and in immunofluorescence experiments with CHO cells.
3. Cell culture media: Chinese hamster ovary (CHO) is maintained in Ham's F12 medium (HiMedia). The cells expressing folate receptor are specifically maintained in a folate-free variant of HF-12, which also needs to be supplemented by dialyzed serum (free of folate) when labeling the receptor with folate analogs.

2.2 Cell Lines

1. CHO cell line stably expressing folate receptor (FR-GPI), also referred to as IA2.2F, is used to study the native nanoscale organization of FR-GPI. They are also used for labeling the cells with different lipid probes to look at their specific organization.
2. CHO cell line stably expressing EGFP-GPI, also referred to as GG8. These cells do not need any exogenous labeling as they are expressing GPI-anchored fluorescent protein. Instead, they need to be treated with cycloheximide (50–75 μg/ml) for 3 h prior to imaging to clear the pool of the protein residing in internal organelles like the Golgi and the endoplasmic reticulum.

2.3 Reagents for Cleaning Coverslips

1. Hellmanex III (Hellma Analytics): An alkaline cleaning agent for glass surfaces.
2. Piranha solution: Conc. H_2SO_4, 30 % H_2O_2 (Merck).
3. Phosphate buffer saline (PBS).

2.4 Reagents for Replating Method

1. Ham's F12 media without phenol red (HiMedia, India) are reconstituted in water with $NaHCO_3$ (Merck, India) as per manufacturer's instructions (*see* **Note 1**).
2. Cell de-adhering buffer: 5 mM EDTA (Na^+ salt, Merck) in Ca^{2+}- and Mg^{2+}-free M1 (150 mM NaCl, 20 mM HEPES, 5 mM KCl, pH 7.4).
3. Human/bovine fibronectin (Sigma-Aldrich), used at 1 mg/ml, maintained as 10 μl aliquots at −20 °C or 4 °C as per manufacturer's instructions.

2.5 Solvents for Lipid Storage

HPLC grade chloroform, methanol, ethyl acetate, acetone, water (SD-Fine Chemicals, India).

Lipids are dissolved in chloroform/methanol (9:1) or ethyl acetate/acetone /methanol/water (7:1:1:1) based on their hydrophilicity, aliquoted into glass vials or Eppendorf centrifuge tubes (*see* **Note 2**), dried under nitrogen (*see* **Note 3**), and stored under nitrogen/argon at −80 °C.

2.6 Reagents for Lipid Incorporation

1. Lipofectamine (Invitrogen).
2. Fatty acid-free BSA (Sigma-Aldrich).
3. γ-Cyclodextrin (Sigma-Aldrich).

2.7 Reagents to Label the Cell Membrane

1. Folate analogs: Folate analog (pteroyl lysine) is synthesized in the laboratory and conjugated to commercially available organic fluorophores like FITC, BODIPY-TMR, or BODIPY-FL (Molecular Probes) to generate the analogs of varying spectral ranges. These analogs can be used for the cell surface labeling of FR-GPI.
2. Lipid analogs: The fluorescent analogs (Molecular Probes, Avanti Polar Lipids) of sphingomyelin (C5-BODIPY-FL SM, chain labeled) and phosphatidylethanolamine (BODIPY-FL-DHPE, head labeled) have been used to study the nanoscale organization of incorporated probes.

2.8 Reagents to Mark Intracellular Compartments

1. Transferrin (Tf): Apo-transferrin (Sigma-Aldrich) is iron loaded, purified, and stored at 4 °C [8]. 1 mg of iron loaded transferrin is conjugated to Alexa 647 (Molecular Probes) such that it gives a dye to protein ratio of 1:1, followed by purification by size exclusion chromatography, and stored at 4 °C. Conjugated Tf was pulsed at 10 μg/ml concentration.
2. 10 kDa dextran (Invitrogen) conjugated to FITC as reported in [9] is stored at 4 °C and pulsed at 1 mg/ml.

3 Methods

Here we will highlight in a stepwise manner the different stages of making a homo-FRET measurement, from preparing the cells, setting up the microscope, followed by the analysis and interpretation of the data.

3.1 Cleaning Coverslips to Minimize Background Noise Due to Sticking of Probes

Homo-FRET is a sensitive technique, and hence, it is very important to minimize the background signals emanating due to nonspecific sticking of fluorescent probes on glass coverslips. For this purpose, prior to plating cells, we resort to one of the following methods to clean the coverslips.

3.1.1 Piranha Solution

This is a 3:1 mixture of concentrated sulfuric acid (conc. H_2SO_4) and hydrogen peroxide (H_2O_2), which forms a strong oxidizing agent to remove organic residues from the coverslip. This solution is prepared fresh each time by adding conc. H_2SO_4 drop by drop (! caution: exothermic reaction!) into cold H_2O_2 solution in a beaker and with frequent mixing. To this piranha solution, coverslips are added and incubated for 30 min followed by thorough cleaning with double-distilled water five times and then once with PBS. The treated coverslips are air-dried and UV exposed prior to plating cells for experiment.

3.1.2 Hellmanex III

This is a strong alkaline reagent used to clean glass surfaces of coverslips and cuvettes. Coverslips are incubated with 1 % Hellmanex III solution (in ion-free water, double-distilled water) at room temperature for 45 min and then washed thoroughly with copious amounts of double-distilled water five times and then one final wash with PBS. The coverslips are air-dried and UV exposed prior to plating cells for experiment (*see* **Note 10**).

3.2 Methods to Get Rid of Lipid Sticking on Coverslips

In case of certain lipids especially BODIPY-tagged lipids, cleaning the coverslips by the above mentioned methods might not be enough to minimize nonspecific sticking, and in such cases, we resorted to replating method. In this method, post-lipid incorporation, the cells were de-adhered and replated on to fresh coverslips coated with fibronectin for the cells to adhere faster.

1. Fibronectin plating on coverslip dishes: Coverslips were incubated with fibronectin (10 μg/ml) at 37 °C for 1 h or 4 °C overnight. Excess fibronectin was gently removed and the coverslips were rinsed once with PBS before use.

2. Protocol: Cells grown on coverslip for 24 h and at 80 % confluence are incubated in 5 mM EDTA solution (in Ca^{2+}- and Mg^{2+}-free M1 or PBS, pH 7.2–7.4) for 10 min at 37 °C. During this time the cells will round up and float in the buffer, failing which it is advisable to tap gently on the sides of the coverslip (*see* **Note 8**). The cells floating in the buffer are then transferred to a 1.5 mL Eppendorf tube (*see* **Note 9**) and centrifuged at room temperature or 4 °C (as per requirement) at 82 × *g* for 10 min. The supernatant is carefully removed and the pellet containing cells are resuspended in Ham's F12 media. These cells are then transferred on to fibronectin-coated dishes, followed by incubation at 37 °C for 30 min. During this time the cells will re-adhere to the coverslip completely, ready to be used for microscopic imaging.

One can use a combination of methods described in Subheadings 3.1 and 3.2 to get rid of the background sticking (Fig. 2).

3.3 Preparing Cells for Microscopy

3.3.1 Exogenous Labeling of Cells with Folate Analogs

CHO cells expressing folate receptor are plated in HF-12 (with dialyzed serum) at a density such that they become semi-confluent (70–80 %) in 36–42 h. The media are removed from the dishes, and the cells are washed 2–3 times gently with cold 1× M1-Glc buffer. Cells can be labeled with folate analog resuspended in M1 at saturating concentrations (~100–500 nM) on ice for 45 min [10]. Following this, the labeling mix is removed, and the cells are washed gently two times with cold M1-Glc and further imaged live in the same buffer at the desired temperatures (Figs. 2 and 3).

3.3.2 Preparing Cells Expressing Fluorescent Protein Constructs

The power of the homo-FRET technique also lies in the fact that it can be easily extended to making measurements on fluorescent protein-based chimeric constructs, like EGFP-GPI, which is a lipid-tethered protein we have extensively studied. Since most of the GFP-tagged proteins in cells are fluorescent, there is considerable fluorescence from the biosynthetic pool of GFP-tagged proteins present in ER, Golgi, and secretory vesicles. This is undesirable when measurements are made on GFP-tagged proteins (GFP-GPI in our case) present on cell surface. Cycloheximide treatment is used to deplete GFP-tagged proteins from its biosynthetic pool. For GPI-APs, conditions required for depletion of proteins from biosynthetic pool was found to be highly cell type specific. In CHO cells, 50–75 μg/ml of cycloheximide reconstituted into plating medium for 3 h could remove Golgi-localized GPI-APs from >90 % of the cells [9]. Post-cycloheximide treatment, the media from the dishes are removed, and the dishes are washed 2–3 times gently with cold M1-Glc buffer. The experiments are done using M1-Glc as the imaging buffer at the desired temperature.

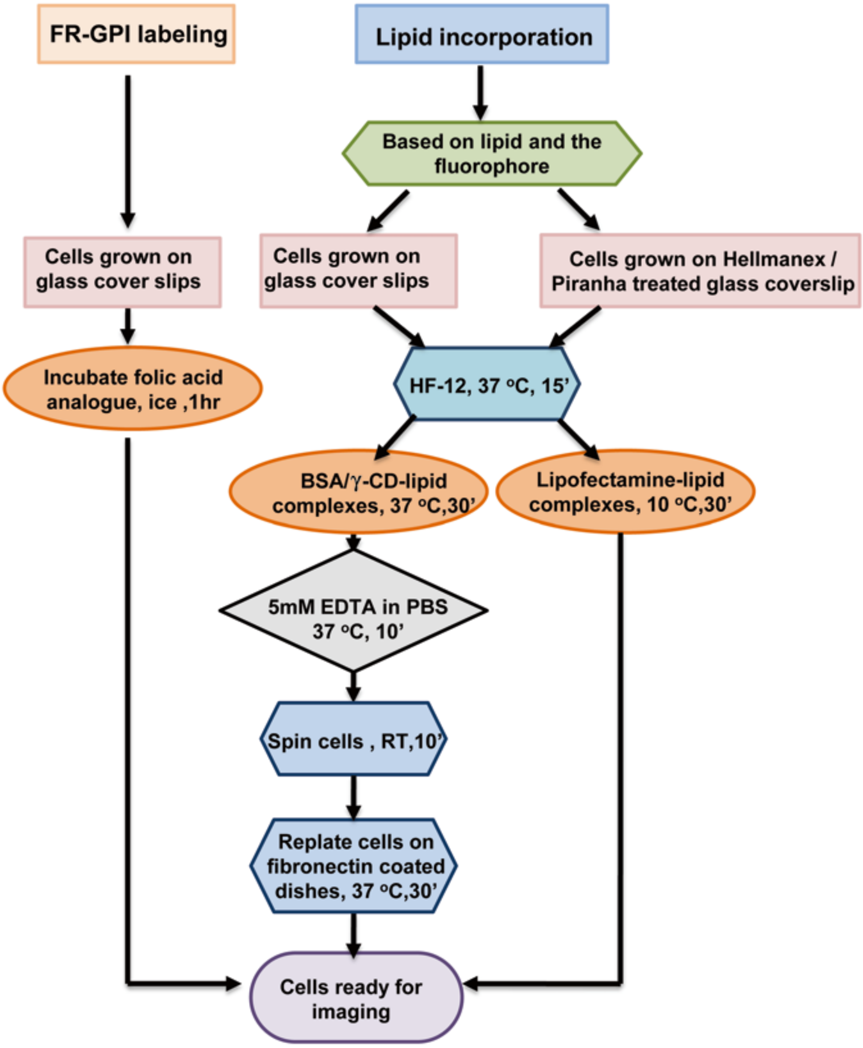

Fig. 2 Flowchart of cell surface labeling strategies. Protocols for exogenous labeling of FR-GPI (with fluorescent folate analogs) and incorporation of fluorescent lipid probes via three different methods, using γ-CD, defatted BSA, and lipofectamine

3.3.3 Exogenous Incorporation of Lipids into Cells

Lipid molecules are amphipathic in nature due to the presence of hydrophilic head group and hydrophobic lipid tails. This property of lipid molecules poses a problem for exogenous incorporation into native cell membrane. This problem can be solved by using a vehicle to transfer lipids into the cell membrane, which can be lipids that help in the formation of micelles, lipid transfer proteins or lipid trapping organic molecules. Based on this, lipids are incorporated into the cell membrane by three different methods. In particular, we introduce lipofectamine-based lipid incorporation as a novel method: (1) BSA method, (2) **γ**-CD method, and

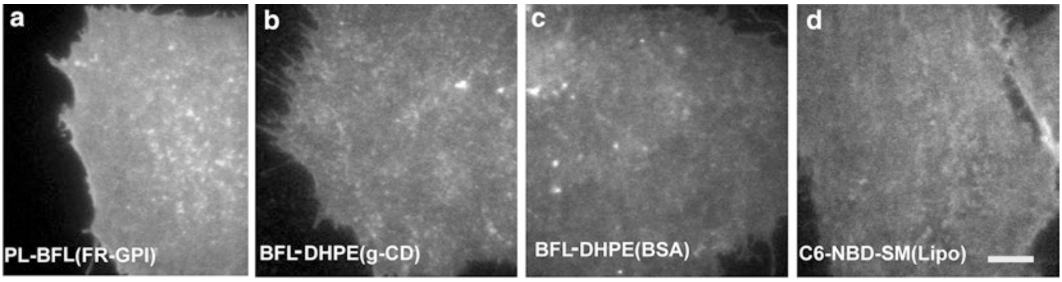

Fig. 3 Cell surface labeling of lipid probes and lipid-tethered proteins. Representative images of CHO cells labeled exogenously with fluorescent folate analog (PL-BFL) to mark the surface expressed folate receptor (FR-GPI) (**a**) or incorporated with lipid probes like BODIPY-FL-DHPE (BFL-DHPE) by either γ-CD method (**b**) or defatted BSA (**c**) method and C6-NBD-SM by lipofectamine method (**d**) and imaged on a custom-built TIRF-anisotropy platform. Scale bar 5 μm

(3) lipofectamine method. In each of these methods, prior to incubation of lipid complexes with cells, it is important to get rid of the serum components which itself are capable of trapping lipids. For this purpose the cells are incubated in Ham's F12 media for 15 min at 37 °C prior to incorporation of lipids.

1. BSA method: Bovine serum albumin (BSA) contains lipid pockets that can stably incorporate lipid molecules. The BSA-lipid complexes are incubated on cells to exchange the lipids from BSA to that of the cell membrane [11] and hence act like lipid transfer proteins. However, the BSA-lipid complex formation is dependent on the fatty acid chain length. The longer the chain length, the higher the affinity to BSA and the lower the efficiency of lipid transfer to the membrane [12, 13] (*see* **Note 4**). This method works efficiently for lipids with short fatty acid tails:
   (a) Preparation of BSA-lipid complexes: Fatty acid-free BSA, dissolved in Ham's F12 media (20 μM), is added to dried lipids such that final BSA-lipid complex attains BSA to lipid ratio 1:x ($x > 1$ for short lipid tails C8–C12 and $x < 1$ for long lipid tails). The mix was vortexed vigorously or probe sonicated (3 × 2 s) for three times (*see* **Note 5**).
   (b) Protocol for lipid incorporation as BSA-lipid complexes: Firstly to get rid of serum components, the cells are incubated in Ham's F12 media for 15 min at 37 °C followed by incubation with BSA-lipid complexes for 30 min either on ice for short-chain lipids or at 37 °C for long-chain lipids (*see* **Note 11**, Fig. 3b)
2. **γ**-Cyclodextrin (γ-CD) method: γ-Cyclodextrin is a cyclic oligosaccharide made up of 8 **γ**-D-glucopyranoside units. The glucose units are linked to each other by means of 1–4 linkages such that it becomes hydrophobic within and hydrophilic

outside the cyclic ring. The hydrophobic cavity of the ring is thus suitable to carry hydrophobic fatty acid moieties. Thus, **γ**-CD acts as an efficient transfer reagent for lipid molecules into the cell membrane. This method works well for lipids with long fatty acid tails [14]:

(a) Preparation of γ-CD-lipid complexes: **γ**-CD is dissolved in Ham's F12 media at millimolar concentrations and mixed with lipids at micromolar concentrations such that the final **γ**-CD to specific lipid molar ratio (*see* **Note 6**) [14]. This mixture is further probe sonicated for 3×2 s for three times.

(b) Protocol for lipid incorporation as γ-CD-lipid complexes: Incubate **γ**-CD-lipid complexes with cells at 37 °C for 30 min (*see* **Note 12**, Fig. 3a).

3. Lipofectamine method: Lipofectamine consists of a mixture of cationic and neutral co-lipids to assist nucleic acid molecules in bypassing the cell membrane. We have developed this new method to deliver fluorescent lipid analogs using Lipofectamine:

   (a) Preparation of lipofectamine-lipid complexes: 2 μl of lipofectamine reagent was added to 98 μl Ham's F12 media to obtain 100 μl of labeling complex (*see* **Note 7**). 20 μl of this solution was added to dried lipid (0.2 mM, 10 μl) and incubated at room temperature for 30 min to form lipofectamine-lipid complexes (18 μg/ml of lipofectamine lipids). After the incubation, this solution is made up to 100 μl to give 20 μM lipofectamine-lipid complex solution. This lipid solution is further diluted to desired lipid concentrations prior to use.

   (b) Protocol for lipid incorporation as lipofectamine-lipid complexes: The cells are incubated with lipofectamine-lipid complexes at 10 °C for 10–30 min, lower incubation time required to incorporate short-chain lipids and higher incubation time for long-chain lipids (*see* **Note 13**, Fig. 3d).

The final concentration of lipofectamine used on cells is 18 μg/ml and does not change the membrane composition/fluidity, as measured from folate receptor membrane organization and trafficking. We find that neither the cell surface organization and diffusion nor the trafficking of GPI-AP is perturbed at this concentration of lipofectamine reagent and hence can be used as a suitable reagent for lipid incorporation into plasma membrane of live cells.

3.4 Microscopy Setup for Homo-FRET Imaging

Fluorescence anisotropy measurements (homo-FRET imaging) have been implemented on a wide range of available fluorescence microscopy platforms. To be specific, wide-field, single-photon confocal (point scanning, line scanning, and spinning disk), multiphoton, and evanescent field (TIRF)-based imaging modalities have been successfully customized for high-resolution fluorescence anisotropy measurements [15]. Anisotropy measurements involve exciting the sample with a polarized illumination and detecting the emitted fluorescence in the planes parallel and perpendicular to the axis of polarized excitation. Here, we outline the basic requirements for setting up any fluorescence microscope (wide-field or confocal) for real-time simultaneous detection of both the polarized components of emission.

3.4.1 Polarized Illumination Source

A key requirement of anisotropy measurement setups is a stable excitation source with a defined polarization output. This can be met by the following illumination options:

1. Mercury arc lamp: A very bright and broad-spectrum (UV-visible) output makes mercury arc lamps a suitable candidate for wide-field fluorescence microscopy. However, the emission from this source is not intrinsically polarized. Hence, the light produced by the lamp is collimated and selected for a specific wavelength using an excitation filter before it passes through a sheet excitation polarizer (of high extinction ratio of 10^{-3} for visible white light) and the p-polarized component of the excitation is selected. An important issue with the arc lamps is their intrinsic temporal variability (~2–3 %) in output. This is detrimental to the anisotropy measurements by sequential detection of the polarization [16]. The real-time two-camera detection of both the orthogonal polarization components, which we discuss here, circumvents the problem, as these fluctuations affect both parallel and perpendicular image similarly, without significantly affecting the anisotropy measurements.
2. Lasers: Lasers are often preferred sources of illumination for confocal microscopy-based anisotropy imaging setups and in TIRF microscope. Lasers are monochromatic coherent light sources which are often intrinsically polarized [17]. The light produced by many lasers is linearly polarized, making them ideal for fluorescence polarization anisotropy measurements. The output at the laser combiner is coupled directly onto a polarization preserving optical fiber. An essential requirement for fluorescence anisotropy measurement is to ensure polarized excitation at the sample plane with extinction coefficient 500–1,000:1, which is the ratio of the intensities of the two orthogonal polarized components of the excitation (as measured by a power meter on the sample plane). This is a direct measure of preservation of polarized excitation through the light path and should be carefully monitored regularly as a change in the value of this ratio can affect the anisotropy measurements. A wide range of laser sources have been used, e.g., gas lasers and solid-state diode lasers for single-photon microscopy.

3.4.2 Real-Time Detection of the Two Orthogonal Planes of Emission

In an epifluorescence setup, the excitation light (from sources described above) is delivered to the sample via the objective, and the fluorescence emission is being collected by the same objective and is selected for a specific spectral band comprising of the specific emission. This is done by a dichroic mirror (DM) followed by an appropriate emission filter (EM). To detect emission anisotropy, the fluorescence is then passed through a polarizing beam splitter (PBS) splitting it into its two orthogonal components I_{pa} and I_{pe} which may be then imaged simultaneously using suitable detectors, allowing real-time measurement of anisotropy. In this section, we present a brief description of the key optical elements specifically used for anisotropy imaging:

1. Polarizing beam splitter (PBS): A polarizing beam splitter (PBS) separates the incident emission light into two principal orthogonal components; while the p-plane is transmitted, the s-plane is reflected (Fig. 4a). Hence, the PBS makes possible the simultaneous detection of both the polarizations using two detectors, allowing real-time anisotropy imaging. The PBS should be placed after the microscope-detection port, as close to the microscope as possible to avoid light losses. Moreover, focusing light rays must be avoided since they will give rise to major aberrations in polarization at different parts of the image leading to artifacts. Light should be incident on the beam splitter coating at the Brewster's angle of $45 \pm 2°$. Hence, only a collimated beam should be incident on the PBS. There are broadly two designs of PBS used for anisotropy imaging, the broadband polarizing cube beam splitter (CVI Melles Griot, USA) and the nanowire-based sheet polarizing beam splitter (Proflux$^{\mathrm{TM}}$ Beam Splitter, MOXTEK Inc., USA).
2. Detectors for imaging: The fluorescence emission split into the p- and s-plane-polarized components at the PBS travels onward as a collimated beam, which needs to be focused at the detector to generate the image. Hence, two tube lenses of similar focal lengths are fitted equidistant from the beam splitter in the path of the two orthogonally polarized components of the emission (Fig. 4b). The two detectors are placed at a distance, equivalent to the focal length of the tube lenses. Simultaneous detection of both the polarizations is done by a wide range of detectors, chiefly depending on the anisotropy measurement modality in use. On imaging setups for measuring steady-state anisotropy such as the wide-field, TIRF, spinning disk, or the line-scanning confocal system, a cooled CCD or EM-CCD is used. Two key requirements in implementing real-time dual detector imaging are the synchronization of acquisition between the two detectors to minimize time delay in simultaneous real-time imaging and a high degree of spatial image registration between both the detectors. Cameras used for

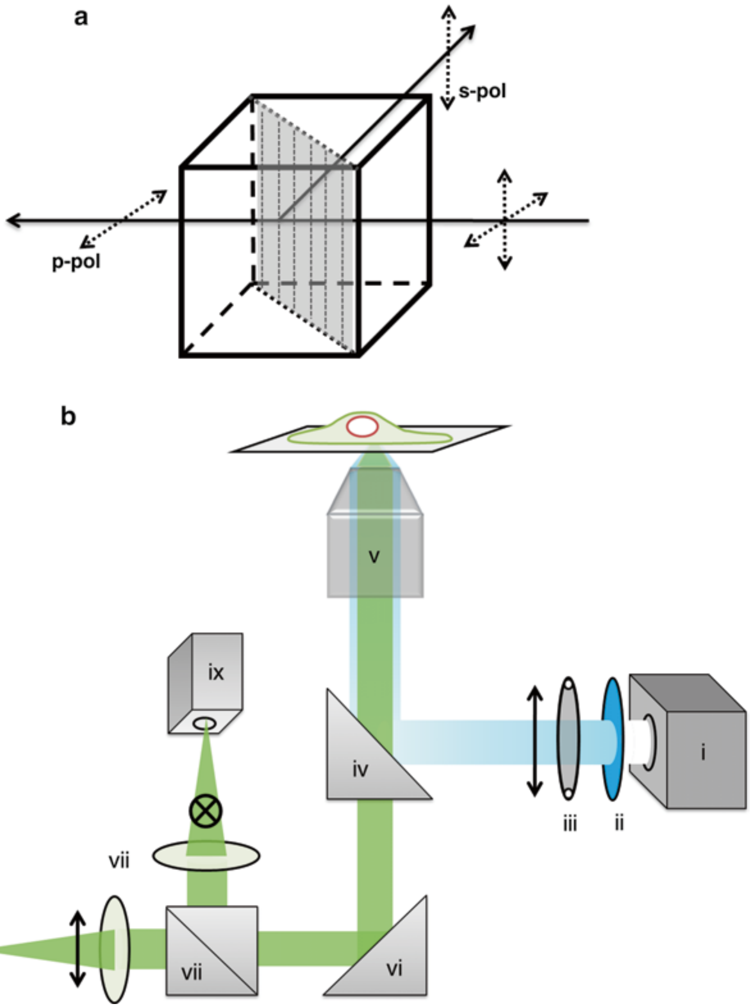

Fig. 4 Basics of homo-FRET microscopy. The key component of a real-time homo-FRET microscopy platform is a polarizing beam splitter (PBS) cube (**a**), which divides the non-polarized collimated light into two orthogonal polarized beams at the diagonal interface (*gray* with stripes, **a**) facing the incoming fluorescence emission. Generally the p-polarized light is transmitted, while the s-polarized light is reflected. Schematic representation (**b**) of wide-field fluorescence anisotropy measurement setup showing the individual components: (i) mercury arc lamp, (ii) excitation filter, (iii) sheet polarizer oriented to select p-polarized light, (iv) dichroic mirror with the emission filter (in detection side), (v) objective, (vi) side port prism, (vii) PBS, (viii) tube lens pair, (ix) cameras—EMCCDs. Although this is a very simple representation, the fundamental layout of components is conserved among the different microscopy modalities like confocal and TIRFM, which have been adapted for homo-FRET imaging

image acquisition play an important role in determining the signal to noise obtained in anisotropy measurements and have to be chosen for the highest possible quantum yield and lowest possible system noise. High-performance camera systems utilize design enhancements that dramatically reduce read noise.

3.4.3 Microscope Calibration and Characterization

Here we list some of the basic calibrations and measurements, which are necessary for interpretable anisotropy measurements. Their calibration also allows one to assess the suitability of the microscope for such measurements:

1. *G*-factor: The intrinsic differences between the dichroics, filters, and other optical elements in terms of their ability to transmit s- and p-plane-polarized light result in the biased sensitivity of detection of one of the polarized component of the emission. Moreover, there can be differences in the relative sensitivities of the two detectors for real-time simultaneous imaging configurations. These can introduce potential artifacts, if not accounted for by a correction factor which estimates this bias correctly. This correction factor, referred to as the *G*-factor, should be introduced for quantitative analysis of such images [7]. The *G*-factor is defined as the bias in detection of parallel I_{pa} and perpendicular I_{pe} intensities:

$$G_{\mathrm{fac}} = I_{\mathrm{pa}} / I_{\mathrm{pe}}$$

   Typically, aqueous solution (1–10 μM) of fluorescein (at pH 11) can be used to estimate the *G*-factor. In water, the fluorescein molecules are isotropically distributed and have a rotational correlation timescale of ~120 ps and tumble rapidly many times within the fluorophore lifetime (~4 ns) to give emission anisotropy values close to zero at room temperature. During image analysis, the *G*-factor correction is performed on images by multiplying the perpendicular (I_{pe}) image (after background correction) to the *G*-factor image or value. The value of the *G*-factor varies between different setups and largely depends on the nature of optical elements and detectors used.

2. Flat-fielding of the illumination: Most of the quantitative imaging tools assume uniform illumination or flat-fielding across the field of view. Illumination gradients are quite common and can arise from the illumination source or the optical components in the detection and sometimes from both. This must be checked and corrected before any intensity measurements are made. This can be easily checked by imaging a solution of fluorophores, which is homogenous, and hence, the probe is uniformly distributed. Generally, the same sample used for *G*-factor measurement meets this requirement and both flat-fielding and *G*-factor can be assessed from the same image.

3. Extinction ratio of the emission path: The extinction ratio of the PBS is calculated as the efficiency in transmitting p-polarized light or that of reflecting s-polarized light (Fig. 4a). To determine the extinction ratio of the entire setup, a polarizer is placed on the microscope stage aligned to select p- or s-polarized light from the bright field source. Alternatively, the laser light can be reflected back into the microscope and sent out to the PBS. Light intensities collected by a low NA objective

(typically less than 0.7) would be nearly perfectly polarized. The net extinction of the setup should be above 95 %.

4. Alignment of the imaging setup: System alignment is done by accurate placement of the different optical component and the detector in the light path. The PBS should be set up to face the emitted light beam at exactly 45°, the two tube lenses are placed equidistant from the PBS, and the detector is placed exactly at their focus. Alignment of the two orthogonal orientations is an important requirement for imaging and determines the overall resolution of the imaging setup. The initial alignment is a time-consuming process, where each optical component as well as the detectors is moved manually, one at a time, and each of the alignment parameters such as the G-factor, extinction ratio, flat-fielding, and coincidence of sub-resolution beads is checked iteratively to obtain a best possible alignment (Fig. 5a). Since the real-time anisotropy setups have different light path for the two detectors, one might encounter more complicated distortions arising from chromatic or spherical aberrations as well as due to imprecise placement of optical components in the light path leading to a variety of defects such as skewness, shearing, tilt, rotation, translation, or a combination of these in different parts of the image. This is done by simultaneously imaging sub-resolution beads and assessing their spatial overlap to determine the nature of defects. Accordingly, the PBS and the detectors are moved to attain maximal alignment.
5. Steady-state anisotropy setup characterization: It is essential to finally characterize the setup for its sensitivity in detecting changes in anisotropy. A standard set of anisotropy measurements are made which should yield expected results based on theoretical calculations. A good test is to monitor the change in emission anisotropy of Rhodamine 6G in a glycerol-water solution as a function of increasing molar concentration of Rhodamine 6G (Fig. 5c). This will directly read out the extent of homo-FRET due to the decrease in average intermolecular distances at higher concentrations. Alternatively, one can also measure the anisotropy of a solution of fluorophore such as Rhodamine 6G dissolved in a glycerol-water mixture with varying concentrations of glycerol, to estimate the effect of solvent viscosity (Fig. 5d). Soluble EGFP in phosphate-buffered saline (pH 7.4), with a mass of 27 kDa and high rotational correlation timescale (~17 ns at room temperature), has a polarized emission. It can also be used as an anisotropy standard for checking the setup on a day-to-day basis after instrument calibration. These simple checks are robust indicators of the sensitivity of the real-time anisotropy setup to measure small changes in the anisotropy, which can typically be attributed to homo-FRET.

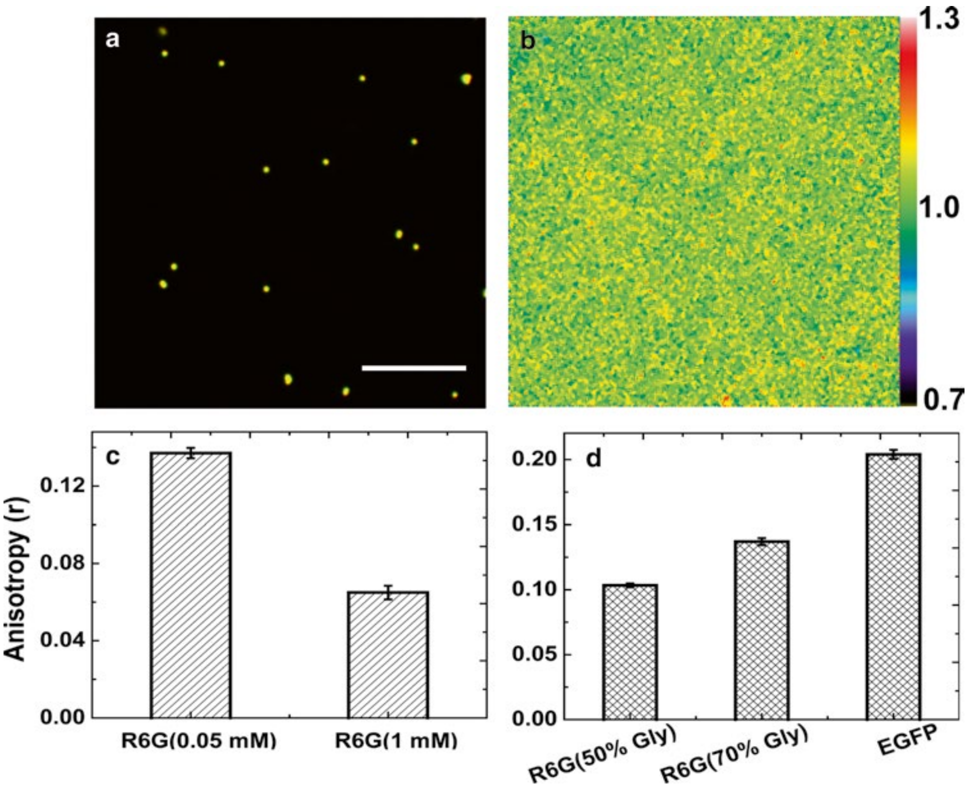

Fig. 5 Microscope alignment and calibration. Sub-resolution bead samples are used to check the system alignment and the image registration between the two cameras. On a well-aligned setup, it is possible to attain sub-pixel overlap precision, as shown (**a**). A dilute solution of fluorophores (like FITC in water, pH 11) should be used to check the flat-fielding and calculate the *G*-factor which should be uniform across the field of view (**b**); scale bar is 10 μm for both (**a**) and (**b**). The setup can be characterized by measuring anisotropy changes observed between solutions of varying concentrations of Rhodamine 6G (R6G) in 70 % glycerol-water mixtures (**c**). A highly concentrated solution of R6G (1 mM) undergoes random collisional homo-FRET, which leads to decrease in the ensemble anisotropy values. Similarly the effect of solvent viscosity on the emission anisotropy (**d**) can be monitored using solutions of same concentration of R6G in varying glycerol-water mixtures, thereby changing the viscosity (say 50 and 70 % glycerol-water as shown here). In solution of lower viscosity (50 % glycerol-water), the tumbling of the dye molecule is fast, and hence, the anisotropy is lower; increasing glycerol concentrations (to 70 % glycerol-water) increase the overall fluorescence anisotropy. Moreover, soluble EGFP in PBS has a higher rotational correlation timescale and hence has a polarized emission, as reported by a high value of fluorescence anisotropy (**d**), compared to R6G solutions (bar represents mean ± s.d.). These measurements were all made using a custom-built spinning disk anisotropy platform

3.5 Image Acquisition, Processing, and Analysis

3.5.1 Image and Data Acquisition

A typical homo-FRET experiment can be divided into the following steps:

1. The illumination source, microscope, and the cameras are switched on, and the individual components of the light path are set up for the anisotropy measurement.
2. Sub-resolution bead sample is placed on the microscope, and images are acquired using the two detectors along the orthogonal

polarization axis. The quality of alignment and image registration is judged by the extent of pixel overlap, and if required the optical components are moved to attain the best possible alignment (ideally sub-pixel precision) (*see* **Note14**).

3. Flat-fielding of the illumination is checked using a homogenously mixed solution of fluorophores (say fluorescein), and the *G*-factor is estimated. The extinction ratio is also monitored as described earlier (*see* **Notes 15** and **16**).
4. Fluorescence anisotropy standards like Rhodamine 6G in varying glycerol concentrations or EGFP solution are imaged, and the anisotropy is measured to check the system performance (*see* **Note 17**).
5. Cells are prepared for imaging (as described in Subheading 3.1) and shifted to the microscope stage, which is pre-maintained at the desired temperature for the imaging. The imaging medium should have minimal autofluorescence to keep the background counts low (*see* **Note 18**). The cells are randomly chosen for imaging by a quick survey of the dish using a weak-illumination and low-exposure setting (*see* **Note 19**). The chosen cells are placed suitably in the field and focused at the membrane plane using the fine-focus knob. The detector gain, illumination power, and the camera exposure are optimized to obtain images at the highest possible signal/noise.
6. The sample background is estimated correctly at the same acquisition settings as used for imaging the cell samples. Finally, a *G*-factor is also re-estimated at the similar gain settings as the rest of the experiment.

3.5.2 Image Processing and Analysis

The images of the two orthogonal polarizations obtained from the two detectors should be perfectly aligned for anisotropy measurements. However, most often they are not completely aligned for a variety of reasons as discussed earlier. The residual misalignment between the two channels can be corrected by using 2D spatial transformation algorithms. Sub-resolution beads imaged in both polarization channels are used to identify reference points (Fig. 5). A mathematically defined affine transform can be generated to correct one channel image with respect to the other [15]. Such corrections can be done using routine algorithms available in MATLAB (MathWorks, USA) or ImageJ (NIH, USA). Post alignment an appropriate background image is subtracted from both channels and the perpendicular image is corrected with the G-factor image. To obtain reliable spatial anisotropy maps, a spatial averaging filter may be used on both parallel and perpendicular images to reduce the noise levels, where the average intensity of a rolling 3×3 pixel box is calculated and replaced at the center pixel of the box. The smoothened images are used to generate the pixel-by-pixel anisotropy map (Fig. 6a, c). These images can be further

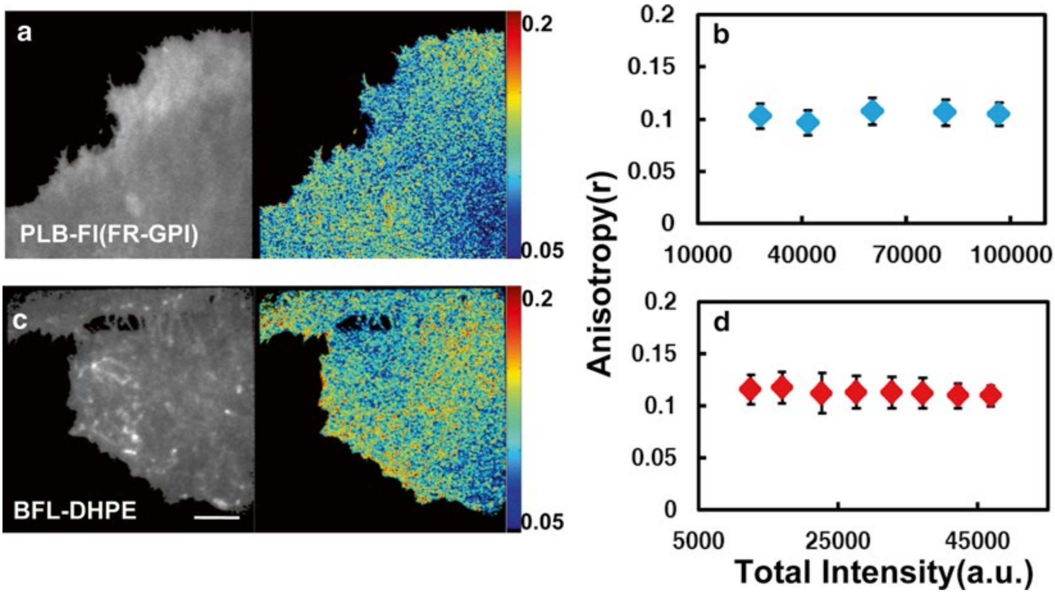

Fig. 6 Representative homo-FRET images and measurements on cells. CHO cells expressing folate receptor (FR-GPI) were either labeled with folate analog PL-BFL (**a**, **b**) or incorporated with BODIPY-FL-DHPE (BFL-DHPE in **c**, **d**) as shown in the concatenated images of grayscale intensities and color-coded spatial anisotropy map. The anisotropy values (mean ± s.d.) measured from such cells are plotted against the total average pixel intensities for both FR-GPI (**b**) and BFL-DHPE (**d**). These images were acquired on a TIRF microscope capable of homo-FRET imaging. Scale bar 5 μm

quantified to obtain average anisotropy values of region of interest selected from the cells (Fig. 6b, d).

3.6 Homo-FRET Imaging of Nanoscale Organization of Cell Surface Molecules

Homo-FRET imaging has been employed to look at the nanoscale organization of different membrane proteins like the GPI-anchored proteins and transmembrane EGF receptor [18–20]. Homo-FRET applications can be broadly divided into two modalities, the steady-state and the time-resolved modalities. Both the modalities have been used to develop a sensitive assay to study the nanoscale organization and its dynamics. Since we have discussed only the steady-state anisotropy modality here, we will only discuss applications of the same.

GPI-anchored proteins (GPI-APs) are outer-leaflet lipid-tethered membrane molecules, which have been implicated, in myriad roles like cell signaling and adhesion [21]. Based on the classical assay of lipid raft association, like the detergent resistance, these proteins were thought to be a putative raft marker, but the detection and the scale of their organization on living cells remained elusive [22]. Using homo-FRET microscopy and steady-state anisotropy as a readout, folate receptor (FR-GPI) was shown to undergo homo-FRET and form submicron domains sensitive to the cholesterol levels on the membrane [10]. The steady-state anisotropy was measured for cells of varying surface expression or density, and it was found that the anisotropy remains fairly constant for a large range of surface density [10]. Cholesterol depletion resulted in an increase in the anisotropy values suggesting that there is a significant loss of homo-FRET. Although these measurements were made at lower resolution scale of whole cells, which precluded direct observation of domains, it was convincingly demonstrated that the GPI-APs clusters were nonrandomly distributed and exhibit a peculiar density-independent clustering over a huge range of densities [10, 22]. One way to assess whether reduced values of anisotropy or depolarized fluorescence arises from FRET is to utilize methods to reduce the density fluorophores in situ. This should predictably increase distances between fluorophores thereby reducing FRET efficiencies and lead to a systematic increase in anisotropy [18]. Fluorophore densities can be reduced by photobleaching and/or chemical quenching. It was shown that photobleaching results in predictably increasing fluorescence anisotropy of FR-GPI. This is due to the increase in distances between fluorophores and also allows the estimation of anisotropy at infinite dilution ($A\infty$) for FR-GPI [18]. The anisotropy changes upon photobleaching can be analyzed by complementary theoretical models of nanoscale clustering which can explain the experimental data, as detailed in Sharma et al. [18]. Based on the modeling of the homo-FRET changes upon photobleaching, Sharma et.al. showed that 20–40 % of the cell surface FR-GPI make nanoclusters of 2–4 molecules [18]. These results have now been confirmed independently by super-resolution imaging modalities like near-field scanning microscopy (NSOM) and photo-activated localization microscopy (PALM) [23, 24]. More recently, it has been possible to implement homo-FRET imaging on multiple microscopy modalities and platforms, which offer superior spatiotemporal resolutions, as detailed elsewhere [15]. Such modalities include the spinning disk, TIRF, line-scanning confocal, and the point-scanning multiphoton microscopes. Homo-FRET imaging at a higher spatial resolution has shown GPI-APs are patterned into a highly nonrandom and hierarchical organization in which nanoscale clusters come together to form submicron cluster-rich domains [25]. The dynamics of this clustering behavior has been studied by two homo-FRET-based photobleaching recovery assays, as elaborated in Goswami et al. [25]. These two assays are complementary in the sense that they report on two different length scales of cluster remodeling. It was elegantly demonstrated that the GPI-AP clusters, though immobile, turn over more frequently at 37 °C than 20 °C, suggesting that the cluster remodeling is an activity-dependent process. It was also shown that both the steady-state organization and the dynamics of GPI-AP clusters depend on elements of actin cytoskeleton and cholesterol [25]. Recently, similar tools have also been extended to look at the nanoclustering of transmembrane molecules interacting directly with actin [26], the ligand-induced oligomerization of EGF receptor [19, 20], and the organization of myosin motors on endosomes [27]. These are a few examples which clearly bring out the potential of homo-FRET microscopy and how it has helped break new grounds in exploring the nanoscale organization of cell surface molecules.

4 Notes

1. Phenol red will fluoresce and hence increases background fluorescence and interferes with the measurements.
2. Always use glass vials when chloroform is used for dissolving lipids.
3. While handling lipids it is important to wear gloves to prevent contamination of lipids from our hand to the sample.
4. The BSA to lipid ratio is 1:2 for lipids with short-chain (8–12) fatty acid and 2:1 for that with long-chain fatty acids (14–18).
5. Excess lipid or non-lipid impurity in the BSA-lipid complex is removed by dialysis.
6. The γ-CD to lipid ratio we commonly use is 1,000:1 but the reader should try a range to determine the optimum ratio for the lipid species being incorporated.
7. Always add the lipofectamine reagent to the Ham's F12 media and not vice versa.
8. Do not tap too hard, because this will cause the cells to tear if not properly de-adhered from the coverslip. This will lead to leakage of the probe into the solution and defeats the purpose of replating.
9. Be careful not to scrape the coverslip with pipette as this will tear the adhered cells, which will lead to the same problem as described in **Note 8**.
10. Lipid sticking on the coverslip is specific to the fluorophore used to tag the lipids. BODIPY lipids stick more than the fluorescein- or NBD-tagged lipids. In the former case we resort to cell replating method, and in the latter case we resort to Hellmanex^{TM} treatment of coverslips.
11. In case of long tail lipids, 10–50 μM lipid concentration is used and for small chain lipids it is 1–10 μM.
12. In case of long-chain lipids low concentration (1–5 μM) is used, and for short-chain lipids, high concentration (10–20 μM).
13. Lipofectamine is sensitive to the polarity of the dye tagged to the lipids. This labeling protocol works well with fluorescein- and NBD-labeled lipids but not with BODIPY-TMR-labeled lipids.
14. The image on both the cameras should retain the same sample plane in focus across the entire image. This maximizes the chances of a good alignment between the two detectors.

15. Excitation light should illuminate the entire field of view uniformly and maintains uniform polarization over the entire field. The extinction coefficient of the laser should be monitored on a regular basis.
16. *G*-factor should be uniform across the whole field of view, and extinction coefficient should be constant and uniform across the entire field of view.
17. Anisotropy standards should be measured on a day-to-day basis to ensure the system performance.
18. The excess label should be carefully washed away after the labeling while preparing the samples for imaging. This reduces the background contributed by the label and can reduce the chances of potential artifacts. For cells expressing fluorescent protein chimeras, transient protein synthesis inhibition is a must to reduce the signals coming from the internal pools.
19. The cells should be well adhered to the glass coverslips prior to homo-FRET imaging of the cell membrane. Moreover, high-resolution FRET imaging should be done on cells, which have been freshly labeled, and imaging should be completed before significant endocytic pools develop inside the cells. This will maximize signals specific only to the membrane pool of the probes hence adding reliability to the results.

Acknowledgments

This work was supported by grants from HFSP(RGP0027/2012) and J.C. Bose Fellowship(Department of Science and Technology, India) to SM. We acknowledge support from the Wellcome Trust, the Nanoscience Mission (Department of Science and Technology, India) for the imaging stations built in the laboratory and the Central Imaging and Flow Facility (NCBS) in NCBS. S.S. would like to acknowledge fellowship support from the NCBS-TIFR Graduate programme.

References

1. Schermelleh L, Heintzmann R, Leonhardt H (2010) A guide to super-resolution fluorescence microscopy. J Cell Biol 190:165–175
2. Krishnan RV, Varma R, Mayor S (2001) Fluorescence methods to probe nanometer-scale organization of molecules in living cell membranes. J Fluoresc 11:211–226
3. Jares-Erijman EA, Jovin TM (2003) FRET imaging. Nat Biotechnol 21:1387–1395
4. Rao M, Mayor S (2005) Use of Forster's resonance energy transfer microscopy to study lipid rafts. Biochim Biophys Acta 1746:221–233
5. Agranovich V, Galanin M (1982) Electronic excitation energy transfer in condensed matter. North-Holland Publishing, Amsterdam
6. Stryer L (1978) Fluorescence energy transfer as a spectroscopic ruler. Annu Rev Biochem 47:819–846
7. Lakowicz JR (2006) Principles of fluorescence spectroscopy, 3rd edn. Springer, New York
8. Mukherjee S, Soe TT, Maxfield FR (1999) Endocytic sorting of lipid analogues differing solely in the chemistry of their hydrophobic tails. J Cell Biol 144:1271–1284

9. Sabharanjak S, Sharma P, Parton RG et al (2002) GPI-anchored proteins are delivered to recycling endosomes via a distinct cdc42-regulated, clathrin-independent pinocytic pathway. Dev Cell 2:411–423
10. Varma R, Mayor S (1998) GPI-anchored proteins are organized in submicron domains at the cell surface. Nature 394:798–801
11. Martin OC, Pagano RE (1994) Internalization and sorting of a fluorescent analogue of glucosylceramide to the Golgi apparatus of human skin fibroblasts: utilization of endocytic and nonendocytic transport mechanisms. J Cell Biol 125:769–781
12. Spector AA, John K, Fletcher JE (1969) Binding of long-chain fatty acids to bovine serum albumin. J Lipid Res 10:56–67
13. Eggeling C, Ringemann C, Medda R et al (2009) Direct observation of the nanoscale dynamics of membrane lipids in a living cell. Nature 457:1159–1162
14. Koivusalo M, Jansen M, Somerharju P et al (2007) Endocytic trafficking of sphingomyelin depends on its acyl chain length. Mol Biol Cell 18:5113–5123
15. Ghosh S, Saha S, Goswami D et al (2012) Dynamic imaging of homo-FRET in live cells by fluorescence anisotropy microscopy. Methods Enzymol 505:291–327
16. Varma R, Mayor S (2006) Homo-FRET measurements to investigate molecular-scale organization of proteins in living cells. In: Stephens D (ed) Cell imaging: methods express. Scion Publishing Limited, UK, pp 247–268
17. Pawley JB (2006) Handbook of biological confocal microscopy, 3rd edn. Springer, New York
18. Sharma P, Varma R, Sarasij RC et al (2004) Nanoscale organization of multiple GPI-anchored proteins in living cell membranes. Cell 116:577–589
19. Bader AN, Hofman EG, Voortman J et al (2009) Homo-FRET imaging enables quantification of protein cluster sizes with subcellular resolution. Biophys J 97:2613–2622
20. Hofman EG, Bader AN, Voortman J et al (2010) Ligand-induced EGF receptor oligomerization is kinase-dependent and enhances internalization. J Biol Chem 285:39481–39489
21. Fujita M, Kinoshita T (2012) GPI-anchor remodeling: potential functions of GPI-anchors in intracellular trafficking and membrane dynamics. Biochim Biophys Acta 1821:1050–1058
22. Mayor S, Rao M (2004) Rafts: scale-dependent, active lipid organization at the cell surface. Traffic 5:231–240
23. van Zanten TS, Cambi A, Koopman M et al (2009) Hotspots of GPI-anchored proteins and integrin nanoclusters function as nucleation sites for cell adhesion. Proc Natl Acad Sci U S A 106:18557–18562
24. Sengupta P, Jovanovic-Talisman T, Skoko D et al (2011) Probing protein heterogeneity in the plasma membrane using PALM and pair correlation analysis. Nat Methods 8:969–975
25. Goswami D, Gowrishankar K, Bilgrami S et al (2008) Nanoclusters of GPI-anchored proteins are formed by cortical actin-driven activity. Cell 135:1085–1097
26. Gowrishankar K, Ghosh S, Saha S et al (2012) Active remodeling of cortical actin regulates spatiotemporal organization of cell surface molecules. Cell 149:1353–1367
27. Altman D, Goswami D, Hasson T et al (2007) Precise positioning of myosin VI on endocytic vesicles in vivo. PLoS Biol 5:e210

Chapter 10

Practical Structured Illumination Microscopy

E. Hesper Rego and Lin Shao

Abstract

Structured illumination microscopy (SIM) is a method that can double the spatial resolution of wide-field fluorescence microscopy in three dimensions by using spatially structured illumination light. In this chapter, we introduce the basic principles of SIM and describe in detail several different implementations based on either a diffraction grating or liquid crystal spatial light modulators. We also describe nonlinear SIM, a method that in theory can achieve unlimited resolution. In addition, we discuss a number of key points important for high-resolution imaging.

Key words Fluorescence microscopy, Spatial resolution, Structured illumination microscopy, Diffraction grating, Reciprocal space, Image reconstruction

1 Introduction

In fluorescence microscopy, light emitted by the sample is blurred by diffraction, often resulting in an image of insufficient resolution for the question being asked. However, we, as biologists or microscopists, are not necessarily interested in the structure of the emitted light, $E(r)$. Rather, we are interested in the distribution of fluorescence molecules that make up the underlying sample $S(r)$. $S(r)$ is not identical to $E(r)$, but it is related as a local product with the excitation light intensity distribution: $E(r) = S(r) \cdot I(r)$. This relationship has led to the development of a number of techniques—so-called structured illumination microscopy—that structure the incoming illumination, $I(r)$, in order to gain more information about the sample.

Broadly speaking, any microscope that uses a spatially varying pattern of light as the source of fluorescence excitation can be considered a structured illumination microscope. Perhaps the most successful of these techniques is confocal microscopy, which relies on a tightly focused "point of light" for excitation and a pinhole in a conjugate image plane to discard out-of-focus light. Superb in its ability to optically section, the confocal microscope is in theory also capable of up to 2-time resolution enhancement.

Peter J. Verveer (ed.), *Advanced Fluorescence Microscopy: Methods and Protocols*, Methods in Molecular Biology, vol. 1251, DOI 10.1007/978-1-4939-2080-8_10,

However, in practice, confocal microscopy rarely achieves greater than diffraction-limited resolution since, to do so, would require using a very small pinhole and thus discarding valuable in-focus photons. For optical sectioning, a wide-field structured illumination technique has also been developed [1] and commercialized, although, like the confocal, it does little for resolution enhancement.

For the purposes of this chapter, we narrowly define structured illumination microscopy (SIM) as a wide-field fluorescence microscopy technique designed to extend the resolution of a microscope beyond the classical Abbe diffraction limit, both axially (or along the optical axis) and laterally (or perpendicular to the optical axis), by using sinusoidal illumination patterns. For references, we refer readers to [2, 3]. We will briefly discuss the theory of SIM in the rest of this section and then in the following sections, the practical considerations of its optical implementation in different configurations and image reconstruction algorithms. It is our hope to offer useful information for both users of the commercial SIM systems and scientists who wish to develop their own SIM setups.

1.1 Lateral Resolution Enhancement

The key concept behind SIM is the well-known moiré pattern. If two patterns are superposed multiplicatively, a beat pattern—moiré fringes—will appear in their product (Fig. 1). In the case of fluorescence microscopy, one of the patterns is the unknown spatial distribution of fluorescent dye (the sample) and the other pattern is a purposely structured excitation light intensity. Since the amount of light emitted from a point is proportional to both the dye density and excitation intensity of that point, the observed image is the product of the two patterns and will thus contain moiré fringes. Such moiré fringes can be much coarser (Fig. 1c) than either of the original patterns (Fig. 1a, b) and, by consequence, are easily observable in the microscope even if the original patterns are too fine to resolve. In other words, the observed microscope images contain the normally unobservable fine details encoded in the form of moiré fringes. Such images can then be "decoded" to recover the information beyond the normal resolution limit, provided that

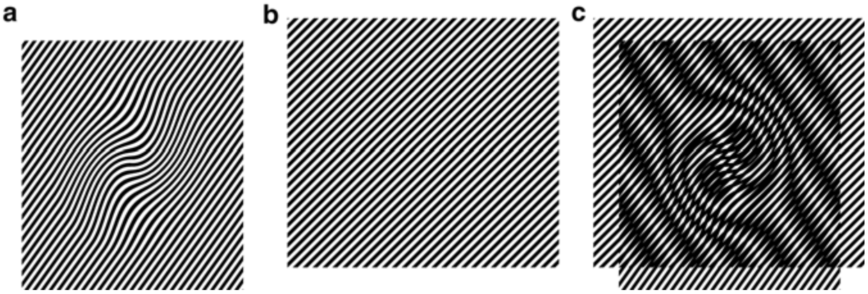

Fig. 1 Moiré fringes. (**a**) and (**b**) are two examples of fine patterns. When one is superimposed onto the other, a coarser beat pattern—moiré fringes—appears (**c**)

a simple illumination structure is used, such as sinusoidal stripes of known line spacing and orientations.

In optics, reciprocal space (also known as spatial-frequency space or Fourier space) is often a more informative representation of the physical reality, especially when spatial resolution is concerned [4]. In reciprocal space, low- and high-resolution information occupies locations close to and far away from the origin, respectively. The lateral resolution limit of a microscope can be conveniently represented by a circle whose radius is proportional to the numerical aperture and the inverse of the wavelength (Fig. 2a). All high-resolution sample information outside of the

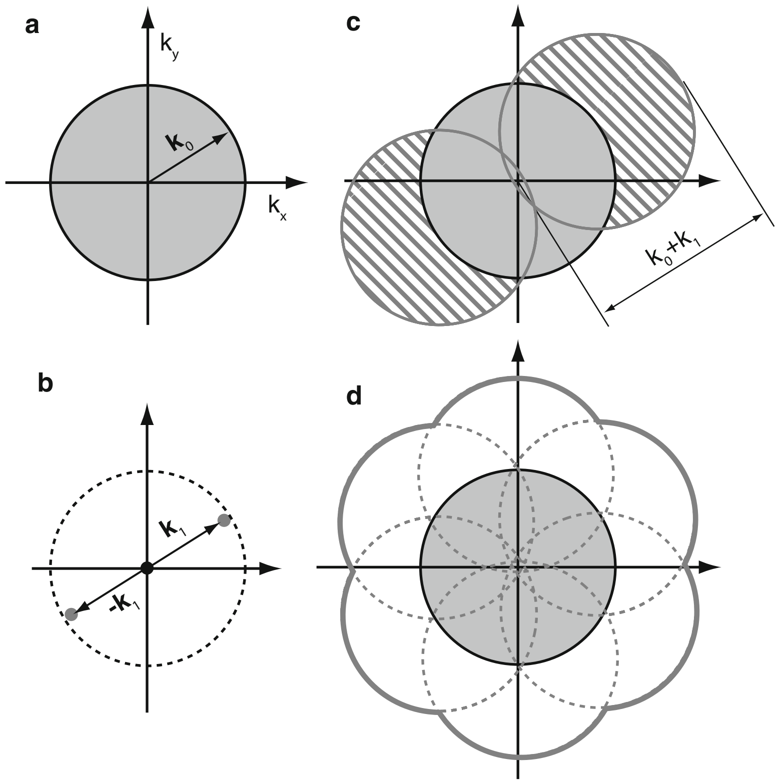

Fig. 2 Principle of structured illumination—lateral resolution enhancement. (**a**) A microscope's observable region of frequencies in reciprocal space; the resolution limit is represented by the radius of the *shaded circle*, $|\mathbf{k}_0|$. (**b**) The frequencies of a simple sinusoidal intensity pattern, represented by the *three dots* in reciprocal space. When the pattern is formed by an objective lens, the highest frequencies cannot exceed the *dashed circle* because the pattern formation is also resolution limited. (**c**) Illuminated under the pattern shown in (**b**), the frequencies in the *hatched areas* are translated into the normal observable region and hence become effectively observable. Resolution limit is now represented by $|\mathbf{k}_0| + |\mathbf{k}_1|$. (**d**) Excitation patterns of the same period but of different orientations are applied to extend the lateral resolution isotropically

circle is lost through imaging; only the region inside the circle is *observable* to the microscope. A sinusoidal laterally structured excitation pattern corresponds to three frequency points (Fig. 2b). The product of this pattern and the dye distribution amounts to the translation of sample information in reciprocal space along the arrows drawn from the origin to those points (Fig. 2c); in particular, information normally outside of the circle can be shifted into the circle and become effectively observable as moiré fringes (Fig. 2c). However, the extra information is mixed together additively with the normal resolution information and therefore needs to be separated. The only way to do so is by acquiring enough images (three in this case) to be able to solve a set of linear equations. Each image is taken with a different phase of the same excitation pattern. As a result, lateral resolution enhancement happens only along the line perpendicular to the excitation pattern stripes (Fig. 2c). To obtain nearly isotropic resolution, the pattern needs to be rotated to two other angles equally spaced by 60°, and additional data needs to be acquired for all pattern orientations. With all the components available from all pattern orientations, represented by the seven circles in Fig. 2d, they are then "stitched" back together according to their original positions in frequency space, forming a final reconstructed image with extended resolution (Fig. 2d).

1.2 Axial Resolution Enhancement

The axial resolution in 3D wide-field microscopy is much lower than the lateral resolution, especially for low-resolution features. This is reflected in reciprocal space by the shape of the observable region in 3D (Fig. 3a, b): its variable axial depth is about 1/3 of its lateral diameter at most and approaches 0 near the origin. Although the same idea of lateral resolution enhancement by structured illumination can be applied for the axial case, the same excitation pattern would not work (Fig. 3c, d) since it is structured only in the lateral direction; instead, what is needed is an axially structured illumination pattern. One such illumination pattern, as seen in reciprocal space, has frequency components above and below the k_x–k_y plane (Fig. 3e), translating sample information axially and making information above and below the normal observable region effectively observable (Fig. 3f–h). Compared to lateral-only structured illumination, two more lateral information components are present in the raw data, and therefore, five in total need to be separated. This means that five raw images within each pattern orientation and at each 3D defocus, acquired at five different lateral pattern phases, are needed in order to solve the five unknowns.

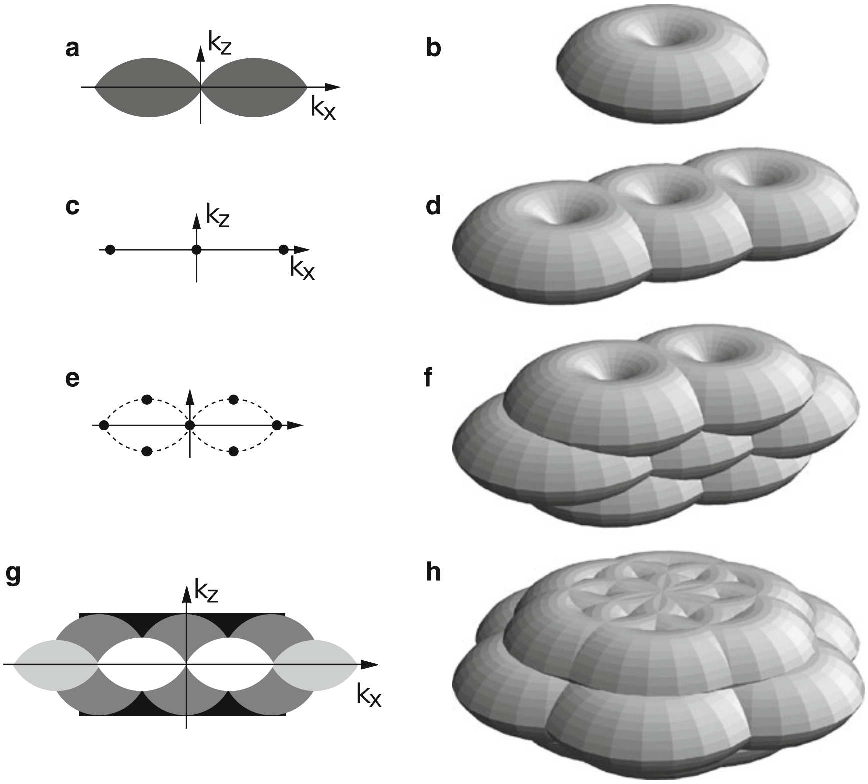

Fig. 3 Principle of 3D SIM. Observable regions for the conventional microscope (**a** and **b**), for structured illumination microscopy using two illumination beams (**d**), and three illumination beams in one (**f**) or three (**g**, **h**) sequential orientations. (**a**) and (**g**) are the k_x–k_z cross section of the 3D observable regions shown in (**b**) and (**h**), respectively. The spatial-frequency components of the structured illumination intensity for the two-beam (**c**) and three-beam (**e**) case. The *dotted outline* in panel (**e**) indicates the set of the highest spatial frequencies that are possible to generate by illumination through the objective lens; compare with the observable region in panel (**a**)

2 Materials

2.1 SIM Hardware

2.1.1 3D or TIRF Wide-Field Microscope, Either Commercial Body or Home-Built

A SIM microscope can be constructed around a commercial inverted microscope body; alternatively, it can be built on a damped optical table without requiring a microscope body. All SIM implementations to date take the form of a wide-field fluorescence microscope with inserted optical components in the excitation path for generating the illumination pattern (with the exception that some setups use more than one objective, as briefly discussed in **Notes 2** and **3**). One consideration is that of thermal drift. This is especially a problem for setups that cannot quickly switch between different phases and orientations of the pattern, as is the case in the grating-based SIM discussed below. While modest drift between different orientations of the pattern can be corrected for in the post-processing algorithm, drift within a phase series is more challenging to correct. As might be expected, thermal drift is negligible for setups that are designed to capture the movement of living cells and therefore must quickly switch between illumination patterns.

2.1.2 Diffraction Grating or Spatial Light Modulator

In Subheading 3, we will discuss two diffraction-based methods to generate the sinusoidally varying excitation pattern for SIM. One method uses a transmission phase grating that is mechanically manipulated to produce all the phases and orientations of the pattern. While simple, this method is inherently slower than an alternative we discuss, which relies on a spatial light modulator (SLM) to electronically generate the pattern. Non-diffraction-based ways of generating an illumination pattern are also possible as discussed in **Note 4**.

2.1.3 Lasers

An important factor to consider when designing a structured illumination microscope is the coherency properties of the illumination source (Fig. 4a). Fully incoherent sources, like lamp illumination, can be used but will do little for resolution improvement. On the other hand, laser light can be tightly focused at the edge of the back pupil, generating the finest illumination pattern and thus the highest resolution improvement. However, the ultra-long coherence lengths of lasers can create stray interference patterns that are problematic for the reconstruction software. To alleviate this problem, it is possible to spatially scramble laser light (*see* **Note 5**), creating a partially incoherent source. In this case, every point in a source beam is *incoherent* with every other point in that same source beam, but is *coherent* with its corresponding point in the other source beams (Fig. 4b, c). This is especially attractive in 3D SIM imaging because it helps to confine the excitation light in the axial direction. However, this partial incoherence can lead to degradation in the zeros of the pattern especially at high angles of incidence that are used in TIRF or near TIRF (Fig. 4d). For this reason and also because of the stringent requirement on the placement of illumination beam at the rear pupil (Fig. 4e, f), in all the SIM–TIRF setups described [5, 9], a fully coherent source was used. In this case, the microscope should be searched for causes of any stray interference patterns (*see* **Note 6**).

2.1.4 Linear Polarizer or Liquid Crystal-Based Polarization-Rotating Device

It is important to note that only light of the same polarization state may interfere. Therefore, to maximize the peak-to-trough contrast in the sinusoidal excitation patterns, all interfering illumination beams must be *s*-polarized relative to each other; i.e., they must be linearly polarized perpendicularly to the plane of diffraction. To achieve this at all orientations of the pattern, a polarizer that can rotate with the diffraction angle is needed. Below, we will discuss two different options depending on acquisition speed requirements.

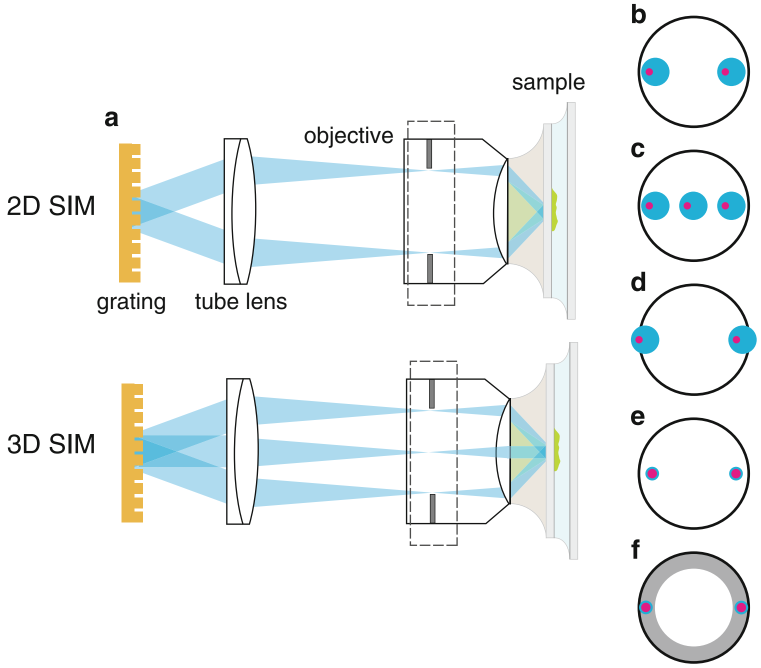

Fig. 4 (**a**) A simplified schematic of a 2D or 3D structured illumination excitation path. Beams diffracted from a grating (diffraction orders) are focused to the edges of the objective back focal plane (pupil). In 3D SIM, three beams are used to create a pattern with both lateral and axial components. (**b**) Spatially scrambled laser light generates a "partially incoherent source"; that is, the points within one diffraction beam are all incoherent with each other (*blue*), but corresponding points (*pink*) in the other diffraction orders are coherent with each other. (**c**) In 3D structured illumination microscopy, this had the advantage that the axial excitation light is more confined than with a completely coherent source. (**d**) One disadvantage of this setup is that at high N.A., the beams may be clipped in the pupil, leading to imperfect zeros of the pattern. (**e**) A completely coherent illumination source can be used, which produces diffraction-limited spots in the pupil of the objective, but can create unwanted stray interference patterns. (**f**) In TIRF microscopy, small focal spots of the beams are required so that they are confined to the "TIRF zone" (*gray*), i.e., the region of the pupil that the produces total-internal reflection

2.1.5 Polychromatic Mirror and Emission Filters

We recommend using a custom-made polychromatic mirror instead of the filter cube switching mechanism that usually comes with a modern inverted microscope. One reason for doing so is speed: with such a setup, there would be no need to switch filter cube for multicolor SIM, especially in live-cell imaging. Another reason is that the polychromatic mirror used in SIM should transmit shorter wavelength (i.e., excitation wavelength) and reflect longer wavelength; this is because a reflective optical device tends to introduce ellipticity in polarization and thus reduces the excitation pattern contrast. In addition, the mirror and the optical axis can be made closer to being perpendicular (22.5° as opposed to 45° incident angle) to minimize aberration due to the difference in optical path length because the excitation beams are generally not collimated where they pass the polychromatic mirror.

2.1.6 Mirrors

There is often a need to use a mirror or two to direct the excitation beams toward the objective lens. A mirror generally has different phase retardance along the *s*- and *p*-polarization axes and therefore would make linearly polarized excitation beams elliptically polarized. To avoid this, two mirrors of the same type of coating can be used to compensate each other's retardance effect with one angled around the *s*-polarization and the other around the *p*-polarization axis. For an inverted microscope that often uses an upward turning mirror or prism directly underneath the objective, it is therefore almost necessary to have another mirror or prism before the up-turning one and after the point where the desired linear polarization state has been achieved for the excitation beams. This second mirror needs to reflect strictly within the horizontal plane.

2.1.7 Camera

Since SIM is a wide-field technique, it is possible to image large fields of view without sacrificing acquisition speed. Of course, the read-out rate of CCD cameras does depend on pixel area. However, the latest scientific CMOS cameras can read out large number of pixels on millisecond timescales. Nevertheless, at extremely low light levels, a back-illuminated EMCCD may be preferred.

3 Methods

3.1 Grating-Based SIM Microscope

3.1.1 Microscope

One way to generate the SIM excitation patterns is by using a diffraction grating and letting 2 (for 2D SIM) or 3 central diffraction orders (for 3D SIM) interfere at the sample plane. We have outlined such a possible setup in Fig. 5. A transmission phase grating is placed at a conjugate image plane in the illumination path. Laser light comes out of the end face of an optical fiber, is collimated by a lens (L1), and then diffracted by the grating. The diffracted beams are focused onto a secondary pupil plane by a relay lens (L2) and after passing through a dichromatic (or polychromatic) mirror are refocused onto the objective's back focal plane by another relay lens (L3) and the tube lens (assuming an infinite conjugate objective lens is used). The spacing of the grating and focal lengths of the relay lenses are chosen such that the ±1 diffraction orders are located on the edge of the objective's back focal plane. If TIRF is desired, care should be taken to place the beams in the region of the back focal plane that produces total internal reflection. The interference of 0 and ±1 diffraction orders (or only the ±1 orders in the case of 2D or TIRF SIM) at the sample space generates the sinusoidal excitation pattern used in SIM.

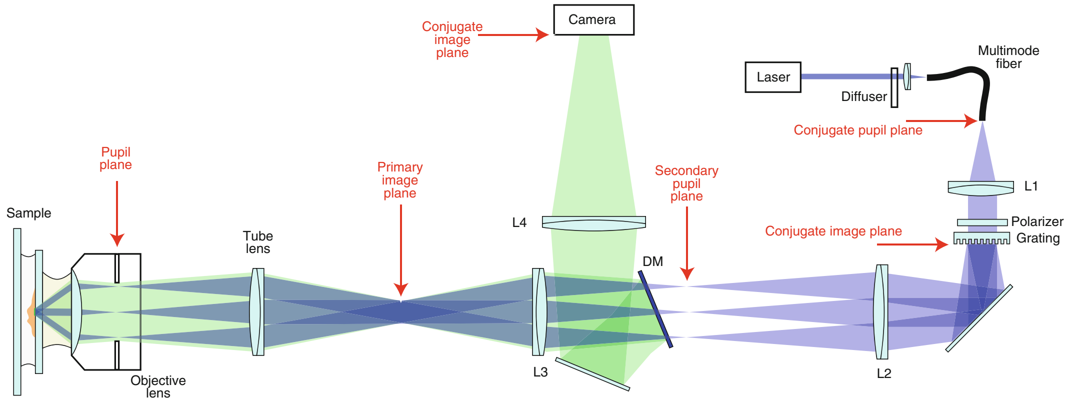

Fig. 5 Simplified diagram of 3D structured illumination apparatus. Scrambled laser light from a multimode fiber is collimated onto a linear phase grating. Diffraction orders −1, 0, and +1 are refocused into the back focal plane of an objective lens. The beams, re-collimated by the objective lens, intersect at the focal plane in the sample, where they interfere and generate an intensity pattern with both lateral and axial structure. Emission light from the sample is observed by a camera via a dichromatic mirror (DM)

To change the phase of the excitation pattern, the grating can be mounted on a piezoelectric translator, which in turn can be mounted on a motorized rotation stage. We have successfully used a piezoelectric translator which is controlled in closed loop using a capacitive distance sensor consisting of one convex electrode on one side of the grating holder and one hollow cylindrical counter electrode that surrounds the grating holder, each flanked by a guard electrode [3]. The counter electrode is rigidly attached to the optical table and serves as a fixed reference, so that any drift in the rotation stage would not affect the translation precision. To maintain *s*-polarization at all orientations of the pattern, a linear polarizer can be corotated with the grating by mounting it on the same stage as the grating.

To achieve the highest quality in SIM images, there are a number of key implementation issues that need to be addressed. These include axial positioning of lens L3 (*see* **Note 7**), lens L4, the camera (*see* **Note 8**) and the grating (*see* **Note 9**), locating of the secondary pupil plane (*see* **Note 10**), and lateral centering and axial focusing of the fiber end (*see* **Note 11**).

3.1.2 2D SIM Acquisition

2D SIM acquisition is straightforward. Nine images are taken: three phases at three orientations of the pattern. As mentioned earlier, a motorized rotation stage and a piezoelectric translator are responsible for changing the orientation and phase of the excitation pattern, respectively. Since all mechanical stages need time to change position and settle, it is important to ensure that camera exposure happens only when all mechanical parts involved are completely static.

3.1.3 3D SIM Acquisition

Image acquisition in 3D SIM is carried out in a way similar to that in regular 3D wide-field microscopy, with the following differences: (1) three 3D stacks are acquired in sequence, one for each lateral excitation pattern orientation; (2) at every defocus position within each orientation, five images are acquired with five different lateral excitation patterns of different phases evenly spaced by 2π; and (3) it is important that the Nyquist sampling criteria is satisfied. With that in mind, each defocus step should be ½ the conventional defocus step.

3.2 SLM-Based SIM Microscope

The speed of data acquisition in a grating-based SIM system is limited by the rotational and the translational stages that switch excitation patterns. The time for the piezoelectric translator and the motorized rotator to settle is on the order of milliseconds and 100 ms, respectively, making it nearly impossible to use such a microscope for live-cell imaging. Speed can be improved by replacing the grating with a liquid crystal-based spatial light modulator (SLM) as the means of generating the excitation patterns (Fig. 6a), because an SLM can be programmed to display any desired pattern with sub-millisecond switching rate. It has been shown that an SLM-based SIM microscope can be effectively used for live 3D imaging of whole cells [6, 7].

For the highest speed achievable, a ferroelectric liquid crystal (FLC) SLM should be used, and preferably, it needs to be at least of SVGA resolution (i.e., more than 1,280 × 1,024 pixels). Each pixel of a FLC SLM behaves as a half-wave plate with its fast axis' orientation changeable to either 0° or 45° (Fig. 6b). Working together with a polarizing beam splitter and a half-wave plate, the SLM can function essentially as a phase grating by phase modulating the parts of the incident plane wave front that is reflected off the SLM's ON pixels to be π phase different than the parts reflected off the OFF pixels. To act as a phase grating for SIM, the SLM needs to be programmed into pixel patterns that resemble a regular grating. Regardless of the SLM pixel pattern, however, the output wave fronts would share the same linear polarization. To maintain the *s*-polarization as discussed earlier, one can use a variable wave plate together with a quarter-wave plate to rapidly rotate the polarization angle. Such a variable wave plate needs to operate at about 1 ms retardance switching rate in order to not slow down the overall acquisition speed.

3.3 Image Reconstruction

A thorough description of SIM reconstruction was published [3]. We briefly review the main steps here.

1. Preprocessing: the original images are smoothed at the edges and flat-field corrected (i.e., correction of the pixel-to-pixel variation in the response of the camera to light intensity).
2. Information unmixing: for each pattern orientation, the raw data is a mixture of three or five different information

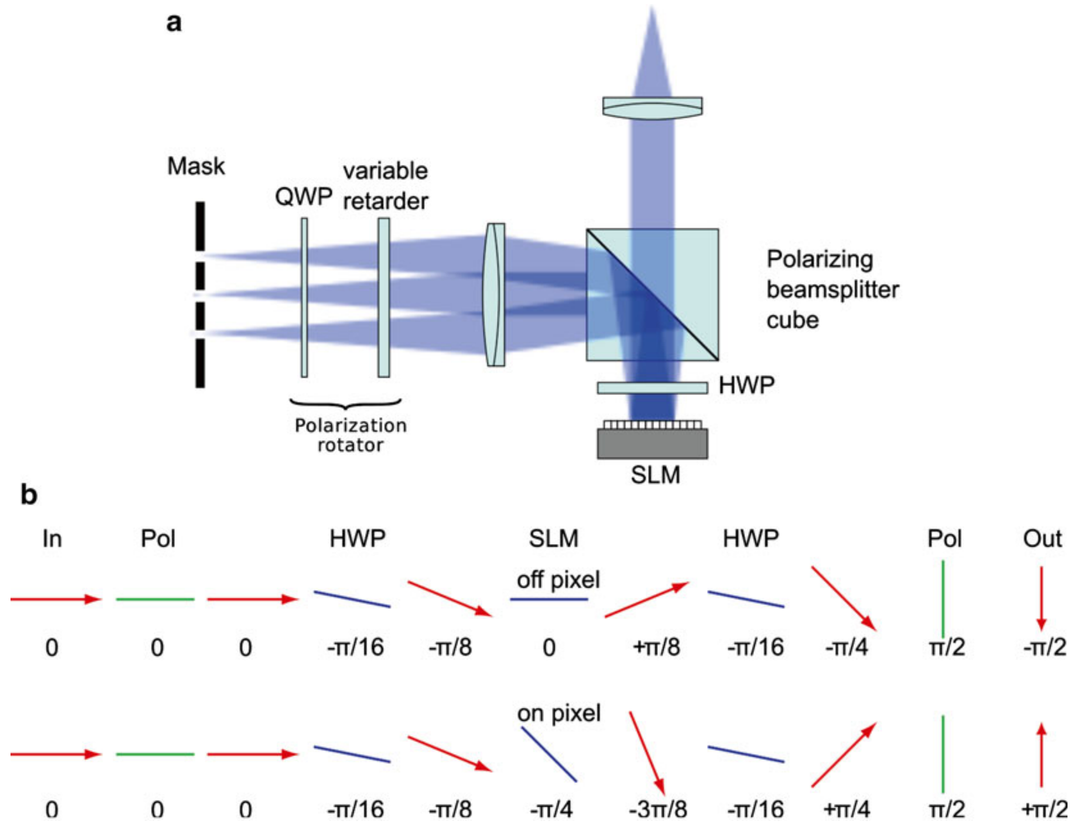

Fig. 6 Using a spatial light modulator (SLM) as a diffraction grating. The parts shown in (**a**) replace the transmission grating and rotating linear polarizer shown in Fig. 5. Each pixel of the SLM behaves as a half-wave plate with the fast axis either vertical or at 45° (**b**) depending on the state with which each pixel is programmed. As a result, a plane wave front reflected off the SLM is phase modulated by π between the pixels in two different states (**b**). Furthermore, a liquid crystal-based variable retarder together with a quarter wave plate (**a**) act as a rapidly programmable polarization rotator to maintain *s*-polarization for all pattern orientations

components that are originally centered around different frequency–space points, which need to be separated first. This is done by a simple pixel-by-pixel matrix–vector multiplication using a decomposition matrix simulating a Fourier transform and a three- or five-element vector composed of the images acquired with different pattern phases.

3. Parameter fitting: for each pattern orientation, the spacing and the angle of the pattern is accurately estimated by maximizing the cross-correlation between each higher-resolution component and the conventional component in the frequency–space region where they overlap (Figs. 2d and 3g); between these same overlaps, a complex numbered ratio is obtained. This ratio's amplitude represents how close to the ideal scenario the actual pattern contrast is, and its phase indicates the phase of the first of the three or five patterns.

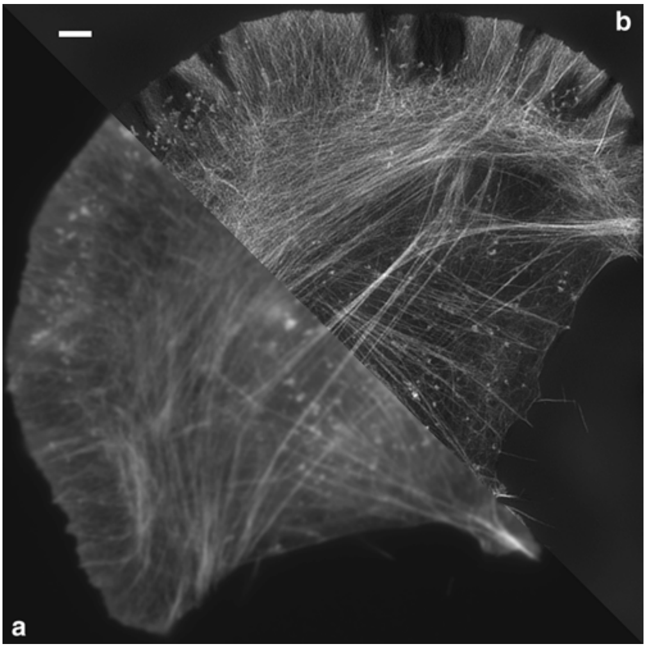

Fig. 7 A comparison of images acquired with conventional wide-field microscopy (**a**) and SIM (**b**). The sample is a fixed mouse embryo fibroblast cell stained with phalloidin–TRITC. One plane out of a 3D stack is shown. The voids seen at the leading edge of the cell in panel (**b**) demonstrate the axial resolution of SIM: the lamellipodium is not flat and there is little actin visible where it ruffles away from the plane shown. Scale bar: 2 μm

4. Inverse filtering and reassembly: each information component is a low-pass filtered version of the part of the sample structure originating from various frequency–space locations; they are assigned back to where they are from and the low-pass filtering is reversed.
5. System calibration: to be able to perform **step 4**, i.e., to reverse the low-pass filtering by the imaging system, the filter itself needs to be calibrated first. This can be done by acquiring a SIM dataset of a single fluorescent bead (usually only one pattern orientation is sufficient), and the dataset is unmixed into several components as explained in **step 2**. To improve the signal-to-noise ratio, it is possible to rotationally average around the optical axis (i.e., z-axis).

One example of reconstructed 3D SIM image is shown in Fig. 7 in comparison with the image acquired with conventional wide-field microscopy.

3.4 Nonlinear SIM

So far in this chapter, we have discussed SIM under conditions of conventional fluorescence, which can double the resolution of a fluorescence microscope. However, it is possible to achieve even greater resolution by exploiting a nonlinear fluorescence phenomenon in combination with structured illumination. This idea has been realized by saturating the fluorophore excited state [8] or the “off state” of a photoswitchable protein [9]. In principle, any nonlinear fluorescence phenomenon can be used to extend the resolution by introducing higher order harmonics into the effective illumination pattern. While saturation and other nonlinear phenomena like stimulated emission or ground state depletion have the distinct advantage of being compatible with conventional fluorescence probes, photoswitchable molecules tend to switch at lower illumination intensity, making them more suitable for biological imaging. Here, we will briefly discuss nonlinear SIM (NL-SIM) in the context of the photoswitching.

NL-SIM does not require special hardware or reconstruction software. It does, however, require a slightly more complicated acquisition sequence. First, the molecules are switched to their on state. Second, using a sinusoidal pattern of light that drives the molecules to their off state, the molecules are turned *off* leaving only the molecules in the trough of the pattern *on*. The width of the region containing the on-state molecules can be smaller than the diffraction limit and will depend on the line spacing of the pattern and the saturation of the off state. For a more complete description, we refer readers to ref. 9. Third, the light from the on-state molecules is collected. This process is repeated for a predetermined number of phases and orientations of the pattern. Compared to linear SIM, more phases and orientations of the pattern are needed to successfully separate the information around the higher-order harmonics and obtain isotopic resolution, respectively.

Since each acquisition sequence is a switching cycle, the resolution of NL-SIM is inherently linked to the photophysical properties of the photoswitchable molecule. For optimal imaging and maximum resolution by NL-SIM using photoswitching, probes should exhibit the following characteristics:

1. Complete turnoff. Incomplete turnoff results in molecules being *on* in the zeros of the pattern, which lowers the signal-to-noise of the higher order harmonics. Patterned excitation with optically clean zeros can alleviate this issue however, since that will lead to cleaner zeros of the emission distribution.
2. Complete turn-on. While it is not an absolute requirement that every molecule be switched *on* during an imaging cycle, incomplete turn-on does cause potential problems: (a) it will contribute to overall noise in the system in the form of shot noise since light coming from subsequent cycles could be coming from different molecules and (b) the fewer molecules being turned *on* inherently means less fluorescent signal. However,

for dense labeling, it might make sense to only excite a few molecules per cycle, since this may lead to a slower photobleaching rate.

3. Photobleaching. During the course of an imaging experiment, the molecules should not bleach "significantly." The exact definition of significantly is determined experimentally; for example, molecules that emit more photons may decay to a greater extent than molecules that emit less photons but still have an acceptable SNR in the images acquired last. Consequently, molecules that emit more photons are more desirable than those that are less bright.

4 Notes

1. Notation notes: f_{XX} denotes the focal length of lens XX (e.g., f_{L2} stands for the focal length of lens L2).
2. While SIM as discussed above can double both lateral and axial resolution, the axial and lateral resolution limit ratio remains identical to normal wide-field microscopy, i.e., about one third in both cases. To make the ratio closer to 1, two opposing objective lenses can be used in techniques such as I^5S [10]. The two objectives and a beam splitter/combiner in such configuration form an interferometer such that emission light collected by the two objectives interferes. In addition, structured illumination beams are split into halves, incident on the sample from both objectives, and interfere to form a more complicated 3D excitation pattern than single-objective SIM. As a result of the interference in both emission detection and excitation, the axial resolution of I^5S is extended to just below 100 nm [10]. Interferometry-based microscopy techniques such as I^5S have stringent requirement on the optical homogeneity of the samples, which is usually difficult to meet. In addition, because of the higher axial resolution than regular SIM, Nyquist sampling rate means shorter focal step (~40 nm) and thus more total exposures.
3. Another configuration of multiple-objective SIM is to use two objective lenses placed at a right angle to each other with one for excitation and the other detection [11]. Instead of scanning the excitation beams to form a light sheet, the beams can be spaced by a certain distance and simulate a sinusoidal excitation pattern. All the SIM principles discussed above apply to the so-called Bessel-beam SIM, except that lateral resolution is only extended along the beam scanning direction. Due to the geometric limit imposed by the right-angle configuration, the numerical aperture of either objective cannot exceed 1.1

usually, and therefore the achievable lateral resolution is not as high as regular SIM. The main advantage of Bessel-beam SIM is its capability to image samples thicker than a single layer of cells, due to the narrowness of the illuminated layer and therefore reduced out-of-focus background compared to a conventional wide-field microscope.

4. In addition to using a grating-like device to generate structured illumination (diffractive beam splitting), one can also use reflective beam splitting, in which a beam is split, one arm phase shifted, and then recombined to generate interference. Reflective beam splitting has an advantage for multicolor applications in that the positions of the illumination beams in the pupil plane can be made independent of their wavelength, whereas with diffractive beam splitting, the distance of a beam from the pupil center is typically proportional to its wavelength and can therefore be strictly optimized only for one wavelength at a time. If diffractive beam splitting is used, simultaneous multiwavelength datasets can still be taken by optimizing for the longest wavelength, with only minor performance penalties at the shorter wavelength channels. On the other hand, reflective beam splitting has a severe disadvantage in that it typically causes the beams to be separated spatially and handled by separate optical components (mainly lenses); any nanometer-scale drift of any such component translates directly into a phase error in the data. With diffractive beam splitting, by contrast, all beams typically traverse the same optical components in an essentially common-path geometry, which decreases the sensitivity to component drift by several orders of magnitude. In addition, reflective beam splitting typically requires separate mirror sets for each pattern orientation, which becomes increasingly bulky as the number of pattern orientations increases.
5. To remove the spatial coherence and speckle pattern in the light transmitted by a multimode optical fiber, it is possible to use a fast rotating holographic diffuser before the laser beam enters the fiber and a focusing lens to couple the diffused light into the fiber. The diffusing angle is chosen to approximately fill the mode space of the fiber. Another more light-efficient way of laser scrambling is to mechanically shake a segment of the fiber. To maximize the scrambling effect, at least 10 m of the fiber should be involved in the shaking and the protective fiber jacket should not be used. The fiber can be wound into a figure-8 loop to increase the length being shaken and the cross-junction can be used as the point of attachment to a vibrator. Caution needs to be taken when working with the extremely fragile unprotected optical fiber.

6. To check for stray interference patterns in the illumination light distribution, one can use as a sample a cover glass coated thinly (<300 nm) with fluorescence dye. Allow only one of the SIM illumination beams to reach the sample at a time. In images taken under such illumination, look for any interference fringes and the causes for them because only uniform images should be observed. Usual causes for stray interference patterns include the beam intersecting the edge of the objective's rear aperture, dust on lenses and mirrors along the illumination path, and back reflections.
7. To achieve optimal aberration correction, relay lens L3 (Fig. 5) should be placed a focal length f_{L3} away from the primary image plane. This can be done by directing a collimated beam from the objective lens side of the tube lens toward the tube lens and L3. When L3 is positioned precisely at f_{L3} away from the primary image plane, the beam should be collimated again after L3. A shear plate placed after L3 can assist in judging whether a beam is truly collimated.
8. Once L3 is correctly positioned, the same collimated beam can be further utilized to precisely position the camera axially. For this purpose, the camera should work in video mode while its axial position is being adjusted; the desired position is when the beam's focal spot formed by lens L4 is the sharpest. One needs to make sure enough attenuation is applied to the beam to avoid camera damage. In general, L4's position is not critical as long as the distance between L3 and L4 is not so large that the diameter of L4 is not sufficiently big to catch all the rays originating from the periphery of the field of view.
9. For ideal imaging, the grating face should be perfectly conjugate to the image plane. To optimize this parameter, one should prepare a sample composed of a single layer of fluorescent beads and acquire a 3D SIM dataset using only one pattern orientation and with focal steps much smaller than the Nyquist sampling rate (25–50 nm). The acquired dataset is first unmixed into five information components. The amplitudes of the ±1 and ±2 order components at each z section are summed, resulting in two plots of the axial variation of the illumination intensity. These two plots are referenced against a through-focus intensity plot of a selected bead. If the grating is perfectly conjugate to the image plane, the peak of the three curves should all coincide. If they do not coincide, the axial distance between the first-order peak and the focus peak can be then converted into the distance by which the grating needs to be moved axially based on the overall axial magnification from the sample plane to the grating.
10. Since the axial positioning of all optical components from L2 up to the optical fiber entirely depends on the position of the

secondary pupil plane (SPP), it is crucial to locate it precisely. The SPP is usually not focal length f_{L3} from relay lens L3 because the distance between the objective and the tube lens is usually not strictly $f_{\mathrm{obj}}+f_{\mathrm{tube}}$ and unknown to the users (unless a custom-designed microscope is used). It is thus often best to locate the SPP experimentally. This can be achieved by shining a point-like light source, such as a laser diode or laser light coming out of a single-mode fiber, from near the SPP toward the objective with the tube lens and L3 in place. At far field above the objective, an Airy pattern should be visible if the point source is well centered and near the secondary pupil plane. One can then adjust the light source's axial position until the Airy pattern looks the sharpest and note down that position as the SPP. With the SPP precisely located, lens L2 should be positioned f_{L2} away from the SPP, grating or SLM f_{L2} away from L2, and finally the fiber end f_{L1} away from the grating.

11. The fiber end surface ideally needs to be positioned laterally on the optical axis and axially conjugate to the SPP. Severe lateral misalignment leads to either of the ±1 diffraction order beams being partially or completely stopped by the back pupil when it is severe, resulting in inefficient interference and thus low contrast in the excitation patterns. Minor lateral misalignment causes the configuration of 3D SIM information components in reciprocal space (the ideal case of which is shown in Fig. 3) asymmetric with respect to the k_x–k_y plane, which can lead to reconstruction artifacts because such asymmetry cannot be accounted for by the ideal imaging model assumed in the reconstruction algorithm. One can precisely center and focus the fiber end by checking the illumination spot formed by the objective lens at the ceiling (or any far-field location): the spot needs to be round with distinct edge and centered around the point where the extension of the optical axis intersects the ceiling.

References

1. Neil MA, Juskaitis R, Wilson T (1997) Method of obtaining optical sectioning by using structured light in a conventional microscope. Opt Lett 22:1905–1907
2. Gustafsson MG (2000) Surpassing the lateral resolution limit by a factor of two using structured illumination microscopy. J Microsc 198: 82–87
3. Gustafsson MG, Shao L, Carlton PM et al (2008) Three-dimensional resolution doubling in wide-field fluorescence microscopy by structured illumination. Biophys J 94:4957–4970
4. Goodman JW (2005) Introduction to Fourier optics. Roberts & Co., Englewood
5. Kner P, Chhun BB, Griffis ER et al (2009) Super-resolution video microscopy of live cells by structured illumination. Nat Methods 6:339–342
6. Fiolka R, Shao L, Rego EH et al (2012) Time-lapse two-color 3D imaging of live cells with doubled resolution using structured illumination. Proc Natl Acad Sci U S A 109:5311–5315
7. Shao L, Kner P, Rego EH et al (2011) Super-resolution 3D microscopy of live whole cells using structured illumination. Nat Methods 8:1044–1046
8. Gustafsson MG (2005) Nonlinear structured-illumination microscopy: wide-field fluorescence

imaging with theoretically unlimited resolution. Proc Natl Acad Sci U S A 102: 13081–13086

9. Rego EH, Shao L, Macklin JJ et al (2012) Nonlinear structured-illumination microscopy with a photoswitchable protein reveals cellular structures at 50-nm resolution. Proc Natl Acad Sci U S A 109:E135–E143

10. Shao L, Isaac B, Uzawa S et al (2008) I^5S: wide-field light microscopy with 100-nm-scale resolution in three dimensions. Biophys J 94:4971–4983

11. Planchon TA, Gao L, Milkie DE et al (2011) Rapid three-dimensional isotropic imaging of living cells using Bessel beam plane illumination. Nat Methods 8:417–423

Chapter 11

4Pi Microscopy of the Nuclear Pore Complex

Martin Kahms, Jana Hüve, and Reiner Peters

Abstract

4Pi microscopy is a far-field fluorescence microscopy technique, in which the wave fronts of two opposing illuminating beams are adjusted to constructively interfere in a common focus. This yields a diffraction pattern in the direction of the optical axis, which essentially consists of a main focal spot accompanied by two smaller side lobes. At optimal conditions, the main peak of this so-called point spread function has a full width at half maximum: fixed phrase of 100 nm in the direction of the optical axis, and thus is 6–7-fold smaller than that of a confocal microscope. In this chapter, we describe the basic features of 4Pi microscopy and its application to cell biology using the example of the nuclear pore complex, a large protein assembly spanning the nuclear envelope.

Key words 4Pi microscopy, Nuclear pore complex, Topographic analysis, Nuclear transport receptors, Binding site distribution

1 Introduction

Among the currently available methods for the analysis of protein complexes in living cells, fluorescence microscopy is a promising candidate as it allows for live cell imaging, molecular specificity, high time resolution and spectral multiplexing, and at the same time can be regarded as minimally invasive [1]. However, an obvious shortcoming of conventional fluorescence microscopy is spatial resolution. But recently, several concepts emerged to overcome the classical resolution limit in light microscopy opening a highly attractive perspective to analyze single protein complexes in living cells and tissues. Among these concepts are, e.g., stochastic detection of individual switchable fluorophores (photoactivated localization microscopy, PALM [2, 3]; stochastic optical reconstruction microscopy, STORM [4]); nonlinear de-excitation of fluorescent dyes (stimulated emission depletion, STED [5]); and superposition of coherent wave fronts, constituting the basic principle of 4Pi microscopy [6].

Peter J. Verveer (ed.), *Advanced Fluorescence Microscopy: Methods and Protocols*, Methods in Molecular Biology, vol. 1251, DOI 10.1007/978-1-4939-2080-8_11, © Springer Science+Business Media New York 2015

In 4Pi microscopy, a classical point-scanning confocal microscope is combined with an interferometer, i.e., a laser beam is split into two beams that are focused by two opposing objectives onto a common focal point. This arrangement leads to a doubled total aperture angle, and though the ideal case of covering the complete solid angle of 4Pi is not possible, the acronym 4Pi is used as an approximation. When the phases of the two counter-propagating beams are carefully adjusted, this optical configuration results in a characteristic and peculiar 4Pi point spread function (PSF), consisting of a sharp main peak accompanied by two weaker side lobes in the direction of the optical axis [6], while in the focal plane, the 4Pi PSF consists of a single peak that has virtually the same dimensions as the confocal PSF. At optimal conditions, the main peak of the PSF has a full width at half maximum (FWHM) of ~100 nm in axial direction and thus is 6–7-fold smaller compared to a confocal PSF. When employing one-photon excitation, the intensity of the side lobes is frequently larger than half of the intensity of the main peak. However, the relative size of the side lobes can be decreased by two-photon excitation [7], and with a relative intensity <50 %, ghost images present in 4Pi raw data can be removed by mathematical procedures [8].

Different optical configurations for 4Pi microscopy have been described in which either interference of the excitation light (type A), interference of the emitted fluorescence light (type B), or interference of both, excitation and fluorescence light (type C), is used for resolution improvement. While type A 4Pi microscopy usually requires two-photon excitation for achieving side lobe reduction [7], type C 4Pi microscopy can be performed with one-photon excitation [9]. 4Pi microscopy of type B, in contrast, is only of conceptual interest [10].

One of the largest protein complexes in the cell is the nuclear pore complex (NPC) (for review see [11, 12]). In vertebrates, the NPC is composed of several hundreds of proteins with a total mass of 125 MDa. The NPC spans the nuclear envelope (NE), and one of its major function is to mediate transport of matter, energy, and information between the cell nucleus and cytoplasm. Being the only gate between the cytoplasm and nucleus, the NPC is involved in almost all basic cellular functions like chromatin organization, gene activation, and cell cycle regulation (for review see [13, 14]).

The structure of the NPC has emerged from electron microscopy studies, providing currently three-dimensional models at a resolution of 6–10 nm [15–17]. According to these models, the vertebrate NPC consists of an approximately cylindrical scaffold of ~125 nm diameter and ~70 nm height containing a large channel of ~50 nm in diameter. The central scaffold is composed of three connected rings, the cytoplasmic ring, the spoke ring, and the nuclear ring, exhibiting on a gross level eightfold symmetry with regard to the central axis of the NPC and twofold symmetry with regard to the plane of the NE. Eight filaments of ~50 nm in length are attached to the cytoplasmic ring, while the nuclear ring is decorated with eight filaments which distally conjoin to form a basket-like structure.

NPCs are composed of about 30 different protein species, known as nucleoporins (Nups). Each Nup occurs in eight copies or multiples of eight per NPC [18, 19]. Several Nups have been crystallized and their structures solved at atomic resolution. These studies indicate that Nups are composed of only a few different folds, which somewhat reduces the complexity of Nup structures and NPC architecture [20, 21].

Although intensively studied, the detailed mechanism of cargo transport mediated by the NPC is still vividly debated. Several transport models have been proposed to explain the remarkable features of cargo transport through the NPC in terms of speed and selectivity (for review see [22, 23]). In this context, structure and arrangement of Nups in the most inner layer of the NPC, forming the walls of the central channel, are of particular interest [24]. These Nups, comprising about one third of all proteins in the NPC, contain domains with multiple repeats of phenylalanine and glycine and are therefore termed FG-Nups. FG domains serve as interaction sites for nuclear transport receptors (NTRs) and their cargo complexes, and therefore it is essential to analyze the arrangement of these FG domains and the interaction with NTRs in great detail to further elucidate the mechanism of cargo translocation.

Here, we describe the application of 4Pi microscopy for the analysis of topographic features of single NPCs as well as determination of binding site distributions of transport factors along the central axis of the NPC. This work demonstrates that super-resolution fluorescence microscopy is a promising method for analyzing single protein complexes and the cellular nanomachinery in general.

2 Materials

2.1 4Pi Microscope

The basic parts of the commercially available 4Pi setup used in our studies (TCS 4Pi microscope, type A, Leica Microsystems, Mannheim, Germany) are depicted in Fig. 1a and comprise a confocal laser scanning microscope of type TCS SP2, laser systems for one- and two-photon excitation, and photon counting by avalanche photodiodes. The standard objective turret of the SP2 microscope is replaced by a 4Pi attachment which operates comparable to a classical Michelson interferometer. In the attachment, the excitation laser light is split into two illumination beams. The two beams are deflected by mirrors into the entrance pupil of two opposing objective lenses which focus

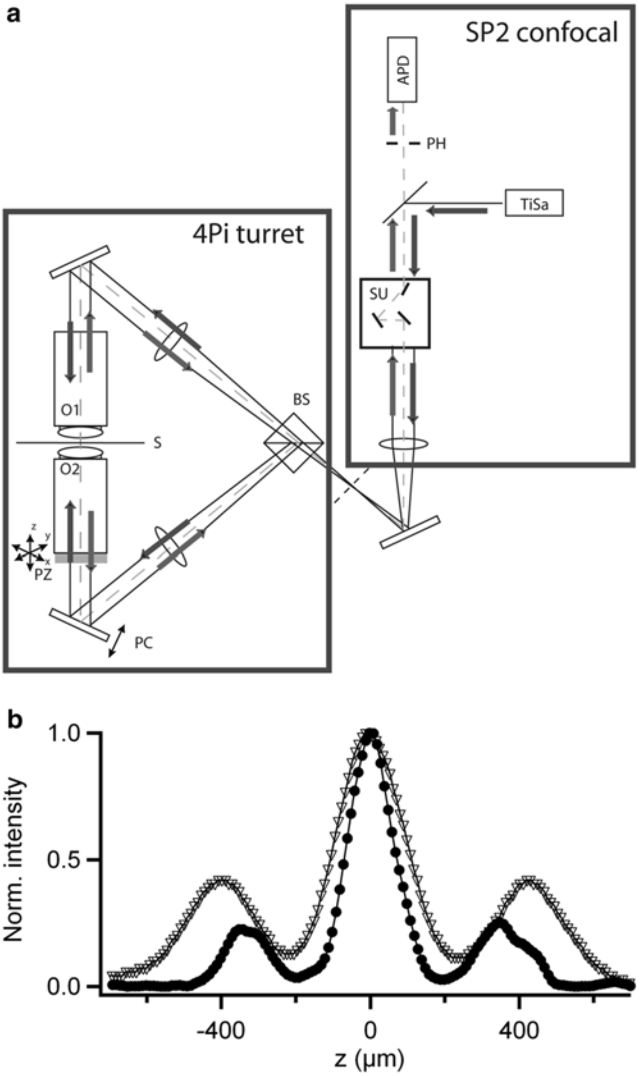

Fig. 1 4Pi setup. (**a**) Scheme of the commercially available 4Pi setup (TCS 4Pi microscope, type A, Leica Microsystems, Mannheim, Germany). O1 and O2: objective lenses; S: sample; BS: beamsplitter; PC: phase control; PZ: piezo-element; SU: scan unit; PH: pinhole; APD: avalanche photodiode; TiSa: Ti:sapphire laser. (**b**) 4Pi PSF profiles along the optical axis for glycerol immersion lenses (100×, NA = 1.35, *circles*) and water immersion lenses (63×, NA = 1.2, *triangles*) in a two-photon 4Pi microscope type A determined at immobilized beads of sub-resolution size

the counter-propagating wavefronts in a common focal point. Lateral scanning is performed by the scan unit of the SP2 system, while axial scanning is accomplished by a piezo-scanning stage. The position of the lower objective relative to the upper one can be adjusted in all three dimensions by means of piezo-elements.

The correct adjustment of the whole system, i.e., the achievement of a common focus, is visualized and checked by imaging the entrance pupils of both objective lenses by a CCD camera located at the beam splitter. Additionally, the relative phase of the two beams can be changed by moving the lower deflecting mirror to achieve constructive interference in the focal point. Especially for analyzing live specimens, in which the refractive index step between the cover glass and immersion medium induces a phase change which increases linearly with penetration depth, an active external compensation can be additionally implemented to ensure the same relative phase of the counter-propagating beams while scanning in z-direction.

The two interferometer arms can be independently blocked by shutters. Thus, the microscope can be used in the confocal mode with the upright or inverted beam path and single- or two-photon excitation or as a two-photon excitation 4Pi microscope. Unlike in a classical type A setup, where detection of the emission light is blocked in one interferometer arm, emission light is collected through both objectives and detected in a noncoherent fashion. For two-photon excitation, a mode-locked Ti:sapphire laser (MaiTai, Spectra Physics, Mountain View, USA) with a pulse length stretched to >1 ps is employed. Its wavelength can be tuned in the range of 710–990 nm. Fluorescence originating from the sample is imaged onto the confocal pinhole of the SP2 system, then passed a filter cube (SP700, BS560, BP500–550, and BP607–683; Chroma Technology Corporation, Bellow Falls, USA), and fluorescence intensity was measured by photon-counting avalanche photodiodes (PerkinElmer, Foster City, USA).

2.2 Objectives

As mentioned above, in 4Pi microscopy constructive interference of two opposing wave fronts yields a main diffraction maximum that is 3–7 times narrower than that of a single lens. But the drawback of this optical configuration is the appearance of elevated side lobes along the optical axis. To obtain the highest possible image resolution, the height of the side lobes has to be <50 % of that of the main maximum [25]. Otherwise spatial information is partially lost, as indicated by a frequency gap in the corresponding optical transfer function (OTF). The relative height of the side lobes sharply decreases with increasing semi-aperture angle α of the objectives, and hence, the best performance is reached with the highest possible α. Oil immersion lenses such as the HCX PL APO CS 100/1.46 Oil (Leica Microsystems, Mannheim) provide a semi-aperture angle of $\alpha = 74°$ and, in combination with a high refractive index embedding medium (97 % thiodiethanol, TDE [26]), yield a resolution along the optical axis of ~100 nm [27]. In addition, it has been reported that these lenses enable 4Pi confocal fluorescence microscopy of type C and even type A employing one-photon excitation [9, 28]. However, the application of oil immersion lenses requires embedding media with a refractive index close to 1.52.

Glycerol immersion lenses such as the HCX PL APO 100/1.35 Gly Corr (Leica Microsystems, Mannheim) provide a semi-aperture angle of 68.5° [29]. Calculations suggested that at $\alpha > 68°$ 4Pi microscopy of type A should be feasible employing one-photon excitation, but experiments showed insufficient side lobe suppression [28]. Hence, two-photon excitation has to be employed. Typically, a FWHM of ~110 nm for the main peak can be achieved accompanied by side lobes of ~30 % relative height. Although this resolution is slightly smaller than that achieved with oil immersion lenses and that two-photon excitation is required, glycerol immersion objectives appear advantageous for imaging fixed specimens. The correction collar of these objectives tolerates refractive indices ranging from ~1.44 to ~1.46, corresponding to glycerol concentrations between 72 and 88 %. In combination with quartz coverslips, an isotropic refractive index of 1.46 throughout the optical path is generated, and proper interference of the opposing beams can be optimized. In our hands glycerol immersion yielded the most reliable 4Pi measurements and was least sensitive to sample preparation.

For live cell imaging or analysis of cellular preparations under physiological conditions, water immersion objectives are required (e.g., HCX PL APO 63/1.2W Corr, Leica Microsystems, Mannheim). The reduced NA of 1.2 results in a decreased FWHM of 150–180 nm for the main maximum [30, 31], and due to the discontinuity of the refractive index at the glass/water interface, this configuration is highly sensitive to any inaccuracy along the optical path like poorly adjusted correction collars with respect to coverslip thickness or even slight tilting of the probe. 4Pi PSF profiles along the optical axis for glycerol immersion lenses (100×, NA = 1.35) and water immersion lenses (63×, NA = 1.2) are shown in Fig. 1b (for a specialized configuration *see* **Note 1**).

3 Methods

3.1 General Aspects

3.1.1 Sample Preparation

For 4Pi microscopy, the sample is sandwiched between two coverslips. This configuration permits focusing the coaxial but antiparallel laser beams into a common point within the sample. Because the working distance of high NA objectives is very small, the layer thickness between the two coverslips should not exceed 30 μm. Furthermore, great care has to be taken to avoid a deformation of the 4Pi point spread function (PSF), which can be induced by any refractive index mismatch. It is therefore essential to use the highest-quality coverslips of well-defined thickness (*see* **Note 2**) and to adjust the correction collar of the objectives properly (*see*

Note 3). Additionally, the sample has to contain a reference which can be used to align the focus and phase of the counter-propagating waves. This reference can consist of either fluorescently labeled endogenous point- or rodlike structures of sub-diffraction dimensions or of artificial immobilized fluorescent beads (*see* **Note 4**). To prepare such samples use the following protocol:

1. Chose coverslips (30 mm in diameter) depending on the objective configuration of the 4Pi microscope (quartz coverslips for glycerol immersion lenses, BK7 coverslips for water immersion lenses, *see* **Note 2**).
2. Coat a coverslip with poly-(L)-lysine (0.01 %) by distributing a drop of solution on the coverslip surface. Wait for 10 min, wash with ddH_2O, and let dry.
3. Add 10 μl of bead solution (*see* **Note 4**). After evaporation of ddH_2O most of the beads are immobilized on the glass surface.
4. Glue the coverslip (intended to be at the bottom of the chamber) carefully to a sample holder (available from Leica Microsystems, Mannheim). Try to avoid any tilting.
5. Put a thin layer of mounting medium (15–25 μl) on top of the coverslip. The choice of mounting medium depends on the objectives used in the 4Pi experiment (see below).
6. Mount the second coverslip with the specimen upside down in the sample holder.
7. Finally seal the samples with a special two-component kneading silicone, and check the thickness of the complete sample holder. The thickness of the layer between the two coverslips should not exceed 30 μm.

For oil immersion lenses in combination with 97 %, TDE as embedding medium (*see* **Note 5**), the best results have been reported by a stepwise increase of TDE concentration during several washing steps of the fixed specimen [26].

With glycerol immersion lenses, all components between the two opposing objective lenses have to be adjusted to a refractive index close to 1.46. This can be achieved by using quartz coverslips and immersing cells in 87 % PBS-buffered glycerol (*see* **Note 6**). Of course, quartz coverslips are much more costly than standard BK7 glass coverslips.

With water immersion lenses, samples can be mounted in aqueous buffer ($n = 1.33–1.34$), but special care has to be taken to avoid even the slight tilting of the coverslips.

3.1.2 Deconvolution of Raw Data

To obtain full image resolution, 4Pi data have to be post-processed to remove ghost images. Various methods have been described for this purpose ranging from three- or five-point linear filters [32] to nonlinear mathematical image restoration algorithms [8]. Like in any imaging system, the image can be described by a convolution of the unknown object function with the PSF of the microscope. In a first approximation, the 4Pi PSF can be separated into independent radial and axial contributions allowing for fast deconvolution algorithms. Here, the axial profile is approximated by a convolution of a peak intensity function describing a single maximum and a lobe function representing relative position and height of the three maxima. Side lobes can be then removed by convolution of the image function with the inverse of the lobe function. This so-called three- or five-point linear deconvolution is fast and robust and does not require highly accurate PSF measurements. But two requirements have to be fulfilled to make this approach feasible. First, the relative height of the side lobes must be constant with respect to a lateral offset from the optical axis. Second, the PSF has to be spatially invariant in the image. When these requirements are met, linear point deconvolution enables easy side lobe removal without highly accurate PSF measurements, but at the expense of a decreased effective signal-to-noise ratio and no further enhancement of resolution.

In contrast, resolution can be further enhanced by direct linear deconvolution, i.e., inverse filtering of the complete image with the 4Pi PSF. This works well for noise-free images and a spatially invariant and perfectly known PSF. In reality, however, an additional filter (like, e.g., Wiener filter) has to be implemented to account for noise. Though an additional resolution enhancement up to 50 % can be achieved using linear deconvolution, a limited signal-to-noise ratio and improper description of the 4Pi PSF make this approach unfeasible in many cases.

Nonlinear image restoration methods, e.g., based on Richardson-Lucy deconvolution, use a maximum-likelihood algorithm to iteratively minimize the deviation between the measured image and estimated object. These algorithms offer the advantage of noise reduction and resolution enhancement but are slow and susceptible to poor PSF measurements.

One prerequisite for all deconvolution methods described here is a spatial invariant PSF in the image. In practice, this is not always the case, i.e., the PSF depends on the position in the sample most often manifested in a phase shift of the interference pattern along the optical axis. Methods for deconvolution with a variable PSF have been described to account for this problem [33].

3.1.3 Localization of Single Epitopes

The position of single point-like objects, although imaged as diffraction limited spots, can be determined with a precision that is one order of magnitude higher than the optical resolution by fitting the measured photon distribution to an ideal Gaussian [34]. In 4Pi microscopy, the main peak of the PSF has an FWHM of 100 nm in the direction of the optical axis at optimal conditions and thus is 6–7-fold smaller than that of a confocal PSF. The localization precision of diffraction-limited signals scales with ~FWHM/$\sqrt{n}$, with n being the number of photons detected, meaning that improved optical resolution, at least in principle, provides higher accuracy. Additionally, two opposing lenses are capable of detecting more photons than a single lens which leads to a further increase of localization accuracy. As the 4Pi PSF is intrinsically elliptical, a true 2D fitting routine is essential for proper centroid localization (*see* **Note** 7). Taking these parameters into account, a localization accuracy of only a few nm has been demonstrated for 4Pi microscopy [35, 36].

3.2 4Pi Microscopy of the Nuclear Pore Complex

3.2.1 Imaging of Single Nuclear Pores in Fixed Specimens

Labeling of mammalian cell nuclei with fluorescent NPC-specific antibodies typically results in a punctate staining of the nuclear periphery. The dots of the punctate pattern usually have a density of ~5/μm^2 and a corresponding nearest neighbor distance of ≤0.4 μm. By confocal scanning microscopy it has been shown that the dots predominantly represent single NPCs, while NPCs which occur as part of a cluster cannot be resolved [37, 38]. The central axis of the NPC is perpendicular to the plane of the nuclear envelope, and therefore the central axis of NPCs in the upper and lower nuclear membrane co-aligns with the optical axis of the microscope. All these parameters—size, density, and orientation—make the NPC an ideal object for 4Pi studies. We started 4Pi analysis of the NPC by using a primary antibody against Nup358, the major component of the cytoplasmic filaments of the NPC.

1. Grow HeLa cells on quartz coverslips (220 μm thickness) to 70 % confluency.
2. Fix cells in 4 % paraformaldehyde for 20 min at room temperature, wash three times with phosphate-buffered saline (PBS, 138 mM NaCl, 2.7 mM KCl, 10 mM Na_2HPO_4, 2 mM KH_2PO_4, pH 7.4), and permeabilize in 0.25 % Triton X-100.
3. Wash three times with PBS, block unspecific binding with 0.5 % fish skin gelatin for 30 min at room temperature, and incubate with a primary antibody directed against Nup358 (1:2,000, kind gift from Dr. E. Coutavas) for 1 h at room temperature. Wash for 20 min in PBS, and incubate with secondary antibody (goat-α-rabbit, Alexa488 conjugated, 1:1,000, Invitrogen) for 1 h at room temperature. Wash cells for 20 min in PBS.
4. Prepare the coverslip intended to be at the bottom of the sample, and glue it in a sample holder as described above. Apply 15 μl of PBS-buffered glycerol (87 % w/w) onto the coverslip.
5. Mount the second coverslip with attached cells upside down. Seal the sample with two-component silicone.

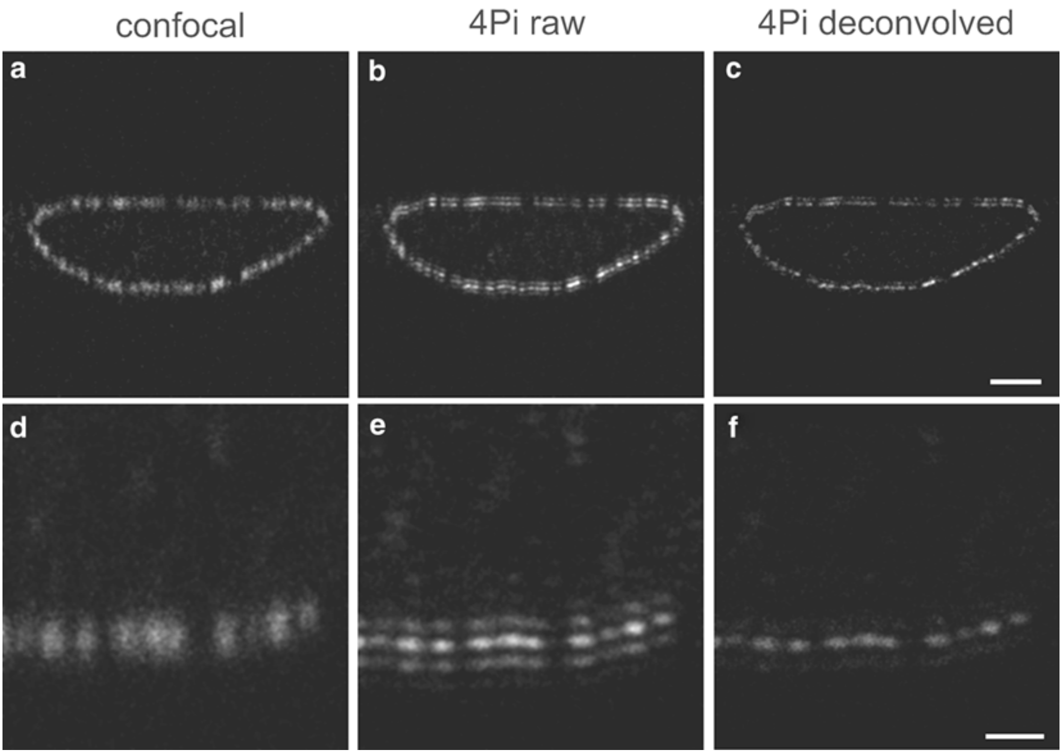

Fig. 2 Imaging of single NPCs by 4Pi microscopy. HeLa cells were labeled by secondary immune fluorescence techniques using a primary antibody against the NPC protein Nup358 and an Alexa488-labeled secondary antibody. Images show an axial section of a HeLa cell nucleus imaged in confocal (**a**) and 4Pi mode, the latter as raw data in (**b**) and after removal of side lobes by deconvolution in (**c**). A detailed view from the same nucleus acquired at a higher zoom factor is shown for the confocal mode in (**d**), corresponding 4Pi raw and deconvolved images are shown in (**e**) and (**f**). Scale bars: 2 μm and 0.5 μm, respectively (adapted by permission from Elsevier Ltd: Biophysical Journal, copyright 2008 [35])

6. Transfer the sample to the 4Pi microscope equipped with glycerol immersion lenses using glycerol (87 % w/w) as immersion medium. Set the excitation wavelength of the Ti:sapphire laser to 820 nm, the beam expander to 6, and the confocal pinhole size to 0.8 Airy units to further reduce relative side lobe height [35].
7. Align focus and phase of the counter-propagating beams using immobilized beads as a reference. When focus and phase are properly adjusted, the FWHM of the main peak of the PSF should be 110–115 nm with relative side lobe height of 30 %.
8. Switch the focal plane to the upper coverslip with attached cells and record xz scans of cell nuclei.

A comparison of confocal and 4Pi axial sections is shown in Fig. 2. In confocal images NPCs appear as diffraction limited spots which are blurred in *xz*-direction (Fig. 2a, d). In contrast, 4Pi images of NPCs consist of a narrow main maximum (FWHM ~ 110 nm) accompanied by two ghost images of ~30 % relative intensity (Fig. 2c, e). These ghost images could be removed by using simple 3-point linear deconvolution (*see* **Note 8**) resulting in a true resolution of 110 nm along the optical axis (Fig. 2f). Since the density of NPCs is relatively large in HeLa cells, the increase in resolution simplifies discrimination of single NPCs in 4Pi images. However, a close inspection of the representative optical section through a complete HeLa cell nucleus reveals that even using an almost isotropic refractive index throughout the optical path, the 4Pi PSF still depends on optical path length in the specimen (Fig. 2e). While in the lower nuclear membrane, the 4Pi raw images of the NPC consist of strong main peaks and weak side lobes, one of the side lobes is almost as strong as the main peak at the upper nuclear membrane, making the PSF asymmetric. Therefore, the applied deconvolution scheme is quite successful on the lower, but not on the upper nuclear envelope. An improvement in such cases could be achieved by active external phase compensation or more sophisticated deconvolution algorithms.

3.2.2 Distance Determination Between Two Epitopes Using a Two-Color Localization Method

In the past, structural properties of the NPC have been mainly studied by electron microscopy of fixed or frozen specimen and by X-ray diffraction of isolated crystallized proteins. However, protein complexes are highly dynamic entities, and to account for this dynamics, functional and structural properties have to be studied at physiological conditions and eventually even in living cells. Therefore we asked if it is possible to resolve topographic features of single NPCs by 4Pi microscopy. As a first step towards live cell imaging, we used fixed specimens and aimed to determine the distance along the central axis between different epitopes in single NPCs using a two-color localization method [35].

Two different epitopes in the NPC of HeLa cells were labeled by means of immune fluorescence. We chose the NPC proteins Nup358 and Tpr, which are both present in eight copies per single NPC, but should be arranged around the central axis of the NPC in a relatively fixed distance to the midplane of the NPC. While Nup358 is the major component of the cytoplasmic filaments, Tpr is a major component of the nuclear basket. The anti-Tpr antibody was directed against an epitope in the C-terminus of Tpr, which according to immuno-electron microscopic studies is localized at the distal part of the nuclear filaments. The secondary antibodies against Nup358 and Tpr were labeled with Alexa488 (green fluorescence) or Alexa594 (red fluorescence). These fluorophores can be spectrally separated by means of their different emission spectra. They can be excited, however, at the same wavelength (800 nm) using two-photon excitation thus avoiding chromatic aberrations due to different excitation volumes. A small axial offset, introduced by the pinhole, remains when two different detection colors are used. But this effect was estimated to be <3 nm. After immuno-labeling cells were embedded in 87 % glycerol and imaged by two-photon 4Pi microscopy with glycerol immersion lenses. A representative example is shown in Fig. 3a. In confocal sections, the green (Nup358) and red (Tpr) fluorescent epitopes overlap to a large extent, while in 4Pi sections

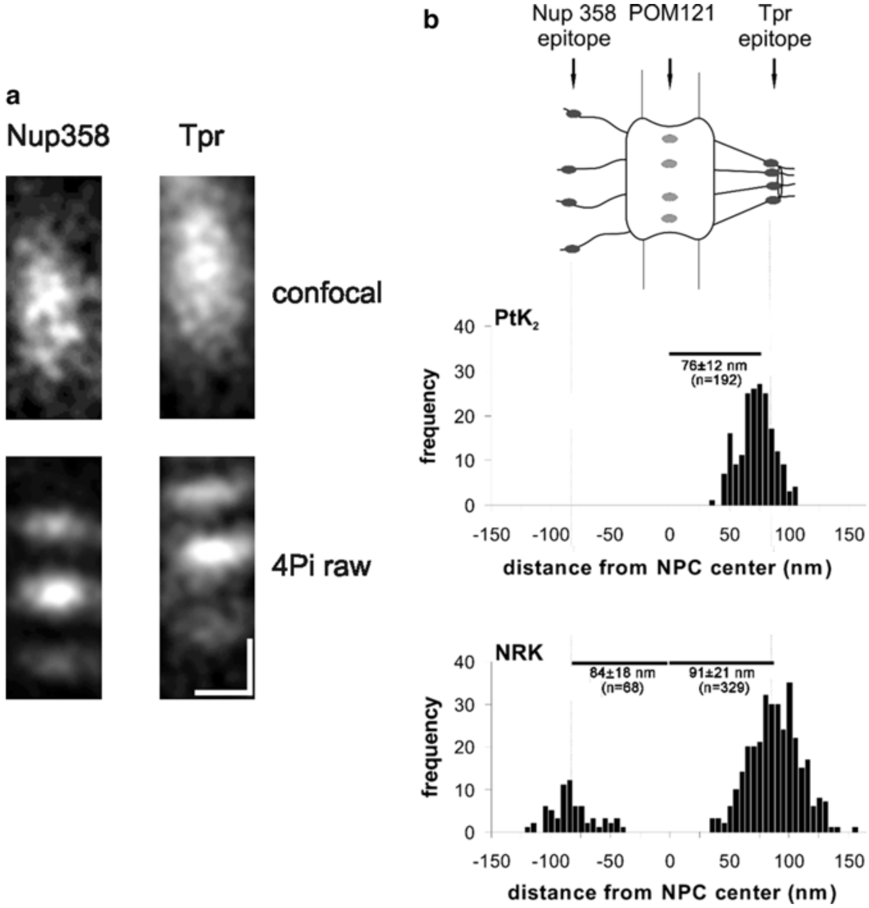

Fig. 3 Distance determination of epitopes in single NPCs. (**a**) In HeLa cells, epitopes of the NPC proteins Nup358 and Tpr were labeled by secondary immune fluorescence methods and imaged by confocal and two-color two-photon 4Pi microscopy. Representative images of a single NPC, derived from the green Nup358-associated fluorescence and the red Tpr-associated fluorescence comparing confocal with 4Pi images, are shown. In the confocal mode, epitopes overlap largely in both detection channels. However, epitopes can be clearly separated in 4Pi images. Scale bar: 0.2 μm. (**b**) Distance between molecular sites in single NPCs as determined by two-color localization 4Pi microscopy. A sketch of the NPC indicates the positions of the sites that were fluorescently labeled, negative values indicate the cytoplasmic face of the NPC, and positive values indicate nuclear contents. Distances were analyzed in single NPCs of PtK$_2$ cells between the Tpr epitope and POM121-eGFP$_3$, and in NRK cells between the Tpr epitope and POM121-eGFP$_3$, as well as between POM121-eGFP$_3$ and the Nup358 epitope. Obtained distances are represented as the mean ± SD of *n* measurements (adapted by permission from Elsevier Ltd: Biophysical Journal, copyright 2008 [35])

the epitopes are clearly separated. These results demonstrate unequivocally that it is possible to resolve the nanoscopic substructure of single protein complexes by light microscopy. However, it should be recalled that eight copies of Nup358 and Tpr, respectively, are arranged around on a radius of 80–120 nm the central axis of the NPC. This octagonal arrangement around the central axis could not be resolved so far.

For quantitative distance analysis, only those NPCs were considered, which were axially co-aligned with the optical axis of the microscope, i.e., the direction of the highest resolution. The epitopes were individually localized using a routine that provides a true two-dimensional elliptical Gaussian fit, and their distance along the central axis of the NPC was determined. These distance measurements were based on raw, i.e., non-deconvolved images. The displacement between main image and ghost images is large when using two-photon excitation, and the localization of the main maximum can be performed even more accurately when deconvolution is omitted. Measurements for a total of $n=218$ NPCs yielded a distribution with a mean value of 152 ± 30 nm, a value in good accordance with predictions based on electron microscopy data.

In a further series of experiments dual-color measurements were extended to cells constitutively expressing a fluorescent Nup. We used HeLa and Ptk_2 cells, in which the Nup POM121 was fused to three molecules of enhanced GFP (eGFP). POM121 anchors the NPC in the nuclear envelope and is localized in or very close to the center plane of the NPC. Cells expressing Pom121-$eGFP_3$ were fixed and labeled with the anti-Tpr or Nup358 antibody. After reaction with an Alexa594-labeled secondary antibody, NPCs were imaged by 4Pi microscopy, and topographic analysis was performed. The results are summarized in Fig. 3b. All values obtained were in good agreement with recent electron microscopy estimates.

3.2.3 Determination of Binding Site Distributions Under Physiological Conditions at Single NPCs

The mechanism of cargo translocation through the NPC is still debated. Crucial but yet incompletely understood parameters are the molecular arrangement of FG domains and the distribution of NTR binding sites within the central channel of the NPC. While the topographic analysis described above was performed on fixed specimens using glycerol immersion lenses, in the following we applied water immersion lenses, permitting to image functional NPCs of permeabilized cells at physiological concentrations of transport factors. We started our analysis focusing on Ran, a GTP-binding protein mediating directionality of nucleocytoplasmic transport. Ran does not directly interact with FG repeats. However, the NPC contains a number of Ran-binding sites located in non-FG sites of certain Nups. In addition, shuttling of Ran through the NPC is facilitated by a special transport factor, NTF2, which binds both Ran and FG repeats:

1. Grow NRK cells, stably expressing a Pom121-GFP$_3$ fusion protein, on BK7 coverslips to 70 % confluency.
2. Permeabilize the plasma membrane with 50 µg/ml digitonin in transport buffer (50 mM Hepes/KOH, pH 7.3, 110 mM potassium acetate, 5 mM sodium acetate, 2 mM magnesium acetate, 1 mM EGTA, and 2 mM DTT) for 3 min on ice (*see* **Note 9**).
3. Wash cells with transport buffer and incubate with 5 µM Ran-Alexa633 in transport buffer in the absence or presence of 10 µM NTF2.
4. Prepare the coverslip intended to be at the bottom of the sample and glue it in a sample holder as described above.
5. Add 15 µl of transport buffer containing 5 µM Ran-Alexa633 (±NTF2) onto the prepared coverslip with immobilized beads, and mount the second coverslip with attached cells upside down.
6. Choose the excitation wavelength of the Ti:sapphire laser such that eGFP and Alexa633 fluorescence show approximately equal brightness in their respective detection channel (870–890 nm). Set the beam expander to 3 and the pinhole to 1 Airy unit.
7. Mount the sample onto the 4Pi microscope equipped with water immersion lenses and ddH$_2$O as immersion medium. Align focus and phase of the counter-propagating beams using immobilized beads as a reference. When focus and phase are properly adjusted, the FWHM of the main peak of the PSF should be 150–160 nm with relative side lobe height of <50 %.
8. Image single NPCs, which happened to be oriented with their main axis in direction of the *z*-axis of the optical system and record xz stacks with a pixel size of 14.5 × 14.5 nm in xz-direction and a step size of 480 nm in *y*-direction to avoid prebleaching of fluorescence in the following image section.
9. Fit the intensity profiles of the two PSFs main maxima independently to an elliptical 2D Gaussian, and calculate the distance between the two centers (*see* **Note** 7).
10. Correct distance values for offset introduced by the two detection colors (*see* **Note 10**).

Examples for the imaging of single NPCs by water immersion two-photon 4Pi microscopy are shown in Fig. 4a. The recorded signals showed the typical 4Pi intensity distribution, even though the background in the nucleus was high because of imported Ran molecules. The use of water immersion objectives broadens the point spread function and reduces the axial resolution to 150–170 nm as compared with 110–130 nm with glycerol immersion. However, the localization accuracy, which directly scales with resolution but

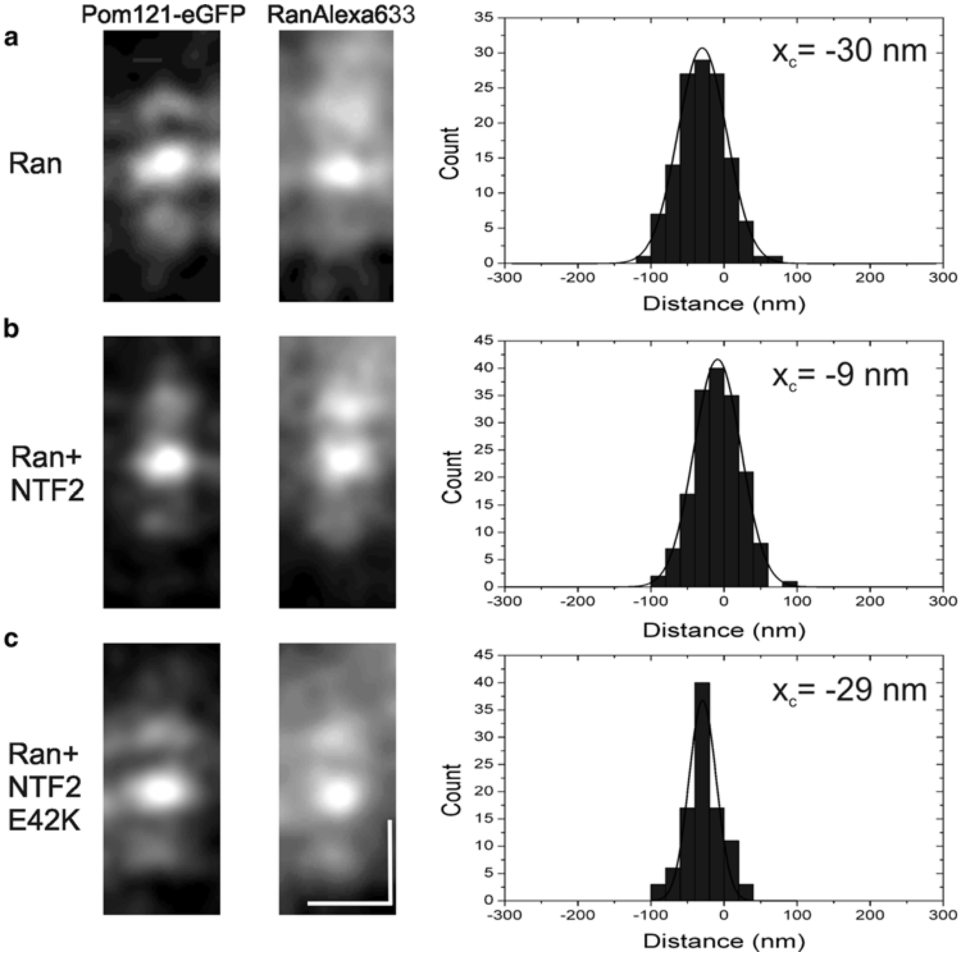

Fig. 4 Binding of Ran-Alexa633 to single NPCs analyzed by 4Pi microscopy. 4Pi images using water immersion lenses of single NPCs in permeabilized NRKPom121-eGFP$_3$ cells are shown in (**a**–**c**). *Left*: eGFP fluorescence detected in the green emission channel. *Middle*: Alexa633 fluorescence detected in the red emission channel. Analysis was performed for 5 μM Ran-Alexa633 (**a**), 5 μM Ran Alexa633 with an excess of 10 μM NTF2 (**b**), and 5 μM Ran-Alexa633 with an excess of 10 μM NTF2 E42K (**c**), a mutant Scale bar in both dimensions: 0.6 μm. The corresponding distance distributions of Ran-Alexa633 relative to Pom121-eGFP$_3$ are shown at the right, directed from the cytoplasm (negative values) through the NE center (origin) into the nuclear contents (positive values) (adapted by permission from John Wiley and Sons: Traffic, copyright 2009 [31])

also depends on the signal-to-noise ratio, was virtually not affected, and the distance between single epitopes within the NPC could be determined with a precision similar to the one obtained with glycerol immersion lenses. Again, removal of the side lobes by deconvolution was dispensable in our analysis, and therefore the confocal pinhole could even be set to >1 Airy unit to increase the number of detected photons. The distribution of the obtained distance values is shown in Fig. 4b. In the absence of NTF2, the distribution could be well fitted by a Gaussian with a maximum at $x_c = -30$ nm and an FWHM of 78 nm. In the presence of NTF2, the distribution of Ran was also almost symmetric and had a maximum at $x_c = -9$ nm and an FWHM of 76 nm. We defined the localization such that negative distance values report binding sites shifted in the direction of cytoplasm relative to Pom121. The difference between the distributions is highly significant (significance level $<10^{-6}$ in a one-way ANOVA). Thus, the NTF2-induced redistribution of RanGDP in the NPC was clearly resolved by 4Pi microscopy. As a control, we repeated the analysis in presence of the NTF2 mutant E42K. This mutant binds to FG repeats with normal affinity but has lost the ability to interact with Ran. 4Pi analysis of the Ran distribution in the presence of 10 μM NTF2 (E42K) showed a localization maximum at $x_c = -29$ nm, not significantly different from the value obtained in the absence of NTF2.

In the same manner we analyzed the distribution of the NTR Kapβ1- and a Kapβ1-based transport complex and found them to have also binding maxima at approximately −10 nm. These observations support transport models in which NTR binding sites are distributed all along the transport channel and argue against models in which the cytoplasmic entrance of the channel is surrounded by a cloud of binding sites.

In essence, this chapter shows that structural aspects of single cellular protein complexes and the distribution of binding sites on single complexes can be studied by super-resolution fluorescence microscopy. Of course, the studies presented are just a humble starting point. The resolution obtained currently by 4Pi microscopy is still insufficient for drawing conclusions on the detailed arrangement of FG repeats and NTR binding site within the central channel of the NPC. However, fluorescence techniques such as STED or STORM have emerged recently further enhancing resolution. Thus, live cell studies at nanometer resolution eventually are becoming more than just a dream.

4 Notes

1. In an attempt to increase the speed of data acquisition, lens arrays have been employed. By these means up to 64 4Pi foci could be produced and simultaneously scanned across the specimen, reducing acquisition times by one order of magnitude [39].
2. The glycerol immersion lenses (HCX PL APO 100/1.35 GLYC CORR) require quartz coverslips of 220 μm thickness, while the water immersion lenses (HCX PL APO 63/1.2W CORR) are designed for BK7 glass of 170 μm thickness.

Custom-made coverslips of well-defined thickness (e.g., 170 ± 2 μm) have to be used, and new batches should be tested with a sliding caliper.

3. To optimize the adjustment of the correction collars, coverslips with a reflective coating at the periphery might be useful. Maximizing the detected signal in reflection mode can help to find the best position of the correction collars for an individual sample.

4. It is essential to have a sufficiently bright and stable reference probe of sub-diffraction size for the alignment of the 4Pi PSF. We recommend a 1:2,500 dilution of TransFluoSpheres NeutroAvidin, 0.1 μm microspheres in ddH_2O (Invitrogen, NY, USA). Due to the large Stokes shift (λ_{Ex}: 488 nm, λ_{Em}: 605 nm), they show good performance in two-photon microscopy with a broad excitation spectrum ranging from 760 to 960 nm.

5. It has to be mentioned that some fluorophores such as eGFP are quenched at high TDE concentrations [26].

6. The refractive indices of glycerol-based immersion and embedding media should be checked using a refractometer.

7. To determine the position of single epitopes, we used a routine that provides for a true two-dimensional (2D) fit (IL-Tracker, Ingo Lepper Software/Consulting, Münster, Germany). Some fitting algorithms separate the measured intensity distribution into orthogonal intensity profiles which are independently fitted to a 1D Gaussian. Although this procedure is sometimes referred to as a 2D fit, it is basically a 1D fit, and difficulties arise when combining the two 1D Gaussians. Thus, this method usually leads to less accurate results than fitting a proper 2D Gaussian function to the whole 2D intensity profile. IL-Tracker is a commercial plug-in for ImageJ, and 2D Gaussian fitting is based on nonlinear least-squares routine according to the Levenberg-Marquardt method [35].

8. For simple 3- or 5-point linear deconvolution, we used a routine provided by the Leica software. For more sophisticated linear as well as nonlinear deconvolution, we recommend Imspector Image Analysis and Acquisition Software (http://www.imspector.de).

9. Treatment of mammalian cells with a defined concentration of digitonin results in selective perforation of the plasma membrane, leaving the nuclear envelope intact [40]. Integrity of the nuclear envelope can be checked by adding a fluorescently labeled substrate >40 kDa (e.g., BSA-Alexa488) which should be still excluded from the nucleus after treatment.

10. In contrast to glycerol immersion lenses, where an offset introduced by the two detection colors was negligible, we found a substantial chromatic error when using water immersion lenses. We quantified this error by imaging a thin layer of Atto532, which showed similar brightness in both detection channels. The position of the main maxima of the 4Pi profiles in the two detection channels was determined by independently fitting the intensity profiles in *z*-direction row by row to a 1D Gaussian. From the resulting histograms of maxima positions, the chromatic error was determined to be ~14 nm in *z*-direction.

Acknowledgments

We thank Dr. R. Wesselmann and P. Lehrich for their experimental contributions and Dr. E. Coutavas for providing anti-Nup358 and anti-Tpr antibodies. This work was supported by the National Institutes of Health, Bethesda, MD, grant No. 1 R01 GM071329-01, and the Deutsche Forschungsgemeinschaft, grant PE-138/19-1.

References

1. Peters R (2006) Checking and fixing the cellular nanomachinery: towards medical nanoscopy. Trends Mol Med 12:83–89
2. Betzig E, Patterson GH, Sougrat R et al (2006) Imaging intracellular fluorescent proteins at nanometer resolution. Science 313:1642–1645
3. Hess ST, Girirajan TP, Mason MD (2006) Ultra-high resolution imaging by fluorescence photoactivation localization microscopy. Biophys J 91:4258–4272
4. Rust MJ, Bates M, Zhuang X (2006) Sub-diffraction-limit imaging by stochastic optical reconstruction microscopy (STORM). Nat Methods 3:793–795
5. Hell SW, Wichmann J (1994) Breaking the diffraction resolution limit by stimulated emission: stimulated-emission-depletion fluorescence microscopy. Opt Lett 19:780–782
6. Hell SW, Stelzer EH (1992) Properties of a 4Pi confocal fluorescence microscope. J Opt Soc Am A 9:2159–2166
7. Hell SW, Stelzer EH (1992) Fundamental improvement of resolution with a 4Pi-confocal fluorescence microscope using two-photon excitation. Opt Commun 93:277–288
8. Schrader MS, Hell SW, van der Voort HTM (1998) Three-dimensional super-resolution with a 4Pi-confocal microscope using image restoration. J Appl Phys 84:4033–4042
9. Lang MC, Engelhardt J, Hell SW (2007) 4Pi microscopy with linear fluorescence excitation. Opt Lett 32:259–261
10. Hell SW, Stelzer EH, Lindek S et al (1994) Confocal microscopy with an increased detection aperture: type-B 4Pi confocal microscopy. Opt Lett 19:222
11. Peters R (2006) Introduction to nucleocytoplasmic transport: molecules and mechanisms. Methods Mol Biol 322:235–258
12. Wente SR, Rout MP (2010) The nuclear pore complex and nuclear transport. Cold Spring Harb Perspect Biol 2:a000562
13. Strambio-De-Castillia C, Niepel M, Rout MP (2010) The nuclear pore complex: bridging nuclear transport and gene regulation. Nat Rev Mol Cell Biol 11:490–501
14. Wozniak R, Burke B, Doye V (2010) Nuclear transport and the mitotic apparatus: an evolving relationship. Cell Mol Life Sci 67: 2215–2230
15. Beck M, Forster F, Ecke M et al (2004) Nuclear pore complex structure and dynamics revealed by cryoelectron tomography. Science 306:1387–1390

16. Beck M, Lucic V, Forster F et al (2007) Snapshots of nuclear pore complexes in action captured by cryo-electron tomography. Nature 449:611–615
17. Stoffler D, Fahrenkrog B, Aebi U (1999) The nuclear pore complex: from molecular architecture to functional dynamics. Curr Opin Cell Biol 11:391–401
18. Cronshaw JM, Krutchinsky AN, Zhang W et al (2002) Proteomic analysis of the mammalian nuclear pore complex. J Cell Biol 158:915–927
19. Rout MP, Aitchison JD, Suprapto A et al (2000) The yeast nuclear pore complex: composition, architecture, and transport mechanism. J Cell Biol 148:635–651
20. Alber F, Dokudovskaya S, Veenhoff LM et al (2007) The molecular architecture of the nuclear pore complex. Nature 450:695–701
21. Devos D, Dokudovskaya S, Williams R et al (2006) Simple fold composition and modular architecture of the nuclear pore complex. Proc Natl Acad Sci U S A 103:2172–2177
22. Kahms M, Hüve J, Wesselmann R et al (2011) Lighting up the nuclear pore complex. Eur J Cell Biol 90:751–758
23. Peters R (2009) Translocation through the nuclear pore: Kaps pave the way. Bioessays 31:466–477
24. Solmaz SR, Chauhan R, Blobel G et al (2011) Molecular architecture of the transport channel of the nuclear pore complex. Cell 147:590–602
25. Nagorni M, Hell SW (2001) Coherent use of opposing lenses for axial resolution increase in fluorescence microscopy. I. Comparative study of concepts. Vis J Opt Soc Am A Opt Image Sci 18:36–48
26. Staudt T, Lang MC, Medda R et al (2007) 2,2′-Thiodiethanol: a new water soluble mounting medium for high resolution optical microscopy. Microsc Res Tech 70:1–9
27. Lang MC, Staudt T, Engelhardt J et al (2008) 4Pi microscopy with negligible sidelobes. New J Phys 10:1–13
28. Lang M, Muller T, Engelhardt J et al (2007) 4Pi microscopy of type A with 1-photon excitation in biological fluorescence imaging. Opt Express 15:2459–2467
29. Martini N, Bewersdorf J, Hell SW (2002) A new high-aperture glycerol immersion objective lens and its application to 3D-fluorescence microscopy. J Microsc 206:146–151
30. Bahlmann K, Jakobs S, Hell SW (2001) 4Pi-confocal microscopy of live cells. Ultramicroscopy 87:155–164
31. Kahms M, Lehrich P, Hüve J et al (2009) Binding site distribution of nuclear transport receptors and transport complexes in single nuclear pore complexes. Traffic 10: 1228–1242
32. Hänninen PE, Hell SW, Salo J et al (1995) Two-photon excitation 4Pi confocal microscope: enhanced axial resolution microscope for biological research. Appl Phys Lett 66:1698–1700
33. Baddeley D, Carl C, Cremer C (2006) 4Pi microscopy deconvolution with a variable point-spread function. Appl Opt 45: 7056–7064
34. Thompson RE, Larson DR, Webb WW (2002) Precise nanometer localization analysis for individual fluorescent probes. Biophys J 82:2775–2783
35. Hüve J, Wesselmann R, Kahms M et al (2008) 4Pi microscopy of the nuclear pore complex. Biophys J 95:877–885
36. Schmidt M, Nagorni M, Hell SW (2000) Subresolution axial distance measurements in far-field fluorescence microscopy with precision of 1 nm. Rev Sci Instrum 71:2742–2745
37. Kubitscheck U, Wedekind P, Zeidler O et al (1996) Single nuclear pores visualized by confocal microscopy and image processing. Biophys J 70:2067–2077
38. Kubitscheck U, Grunwald D, Hoekstra A et al (2005) Nuclear transport of single molecules: dwell times at the nuclear pore complex. J Cell Biol 168:233–243
39. Egner A, Verrier S, Goroshkov A et al (2004) 4Pi-microscopy of the Golgi apparatus in live mammalian cells. J Struct Biol 147:70–76
40. Adam SA, Marr RS, Gerace L (1990) Nuclear protein import in permeabilized mammalian cells requires soluble cytoplasmic factors. J Cell Biol 111:807–816

Chapter 12

Application of STED Microscopy to Cell Biology Questions

Natalia H. Revelo and Silvio O. Rizzoli

Abstract

The increasing interest in “seeing” the molecular environment in biological systems has led to the recent quest for breaking the diffraction barrier in far-field fluorescence microscopy. The first nanoscopy method successfully applied to conventional biological probes was stimulated emission depletion microscopy (STED). It is based on a physical principle that instantly delivers diffraction-unlimited images, with no need for further computational processing: the excitation laser beam is overlaid with a doughnut-shaped depleting beam that switches off previously excited fluorophores, thereby resulting in what is effectively a smaller imaging volume. In this chapter we give an overview of several applications of STED microscopy to biological questions. We explain technical aspects of sample preparation and image acquisition that will help in obtaining good diffraction-unlimited pictures. We also present embedding techniques adapted for ultrathin sectioning, which allow optimal 3D resolutions in virtually all biological preparations.

Key words Super-resolution microscopy, STED, Diffraction barrier, Cell imaging, Live imaging

1 Introduction

In recent decades far-field fluorescence microscopy has become an important tool in the investigation of cellular components, both in functional and structural terms. The easy sample preparation (compared with other techniques such as electron microscopy) and the possibility of imaging live specimens account for its popularity. Nevertheless, the acuity of lens-based instruments is limited by the diffraction of the light passing through the optical components of the microscope. In 1873 Ernst Abbe postulated that a point source emitting light of a wavelength λ, which travels through a medium with refractive index n and converges to a lens with an angle θ, will produce a spot with radius $d = \lambda/2(nSin\theta)$, where $nSin\theta$ is equivalent to what came to be known as the numerical aperture (NA) of the objective [1]. In practical terms, this means that conventional fluorescence microscopes using light sources in the range of the visual spectrum and objectives with NA close to 1 cannot resolve two structures that are closer than approximately 200–300 nm. This is an obvious diffi-

Peter J. Verveer (ed.), *Advanced Fluorescence Microscopy: Methods and Protocols*, Methods in Molecular Biology, vol. 1251, DOI 10.1007/978-1-4939-2080-8_12, © Springer Science+Business Media New York 2015

culty when dealing with protein complexes or small organelles (typically one order of magnitude smaller than the diffraction of light).

The first technique that overcame the Abbe's diffraction barrier was stimulated emission depletion (STED) microscopy. Here, the sample is scanned with an excitation beam spatially overlapped with a red-shifted depletion beam (*see* Fig. 1a). The wavelength of the depletion beam is carefully selected to fall in the red side tail of the fluorophore emission spectrum. The depletion beam is physically modified to produce a central area of zero intensity surrounded by an outer ring or "doughnut" of non-zero intensity. In the doughnut center, where only the excitation beam is present,

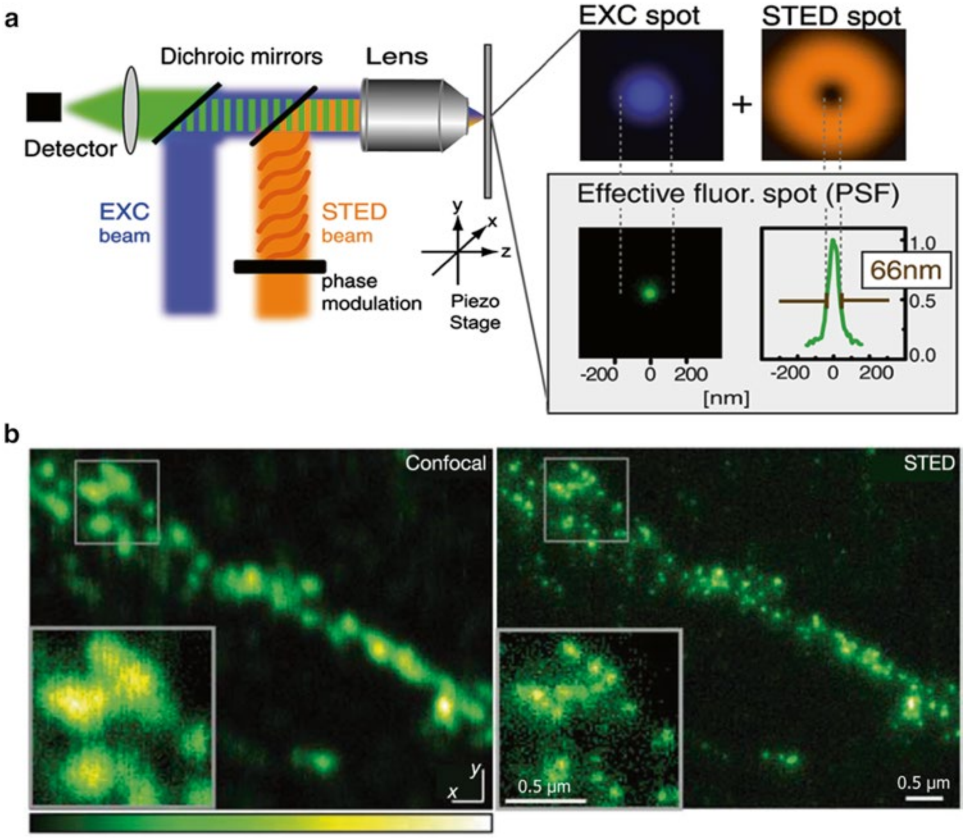

Fig. 1 STED microscopy breaks Abbe's diffraction barrier. (**a**) Working principle of a STED microscope. The sample is illuminated with an excitation beam (*blue*) and a doughnut-shaped depletion beam (*orange*) that are spatially aligned. In the center of the depletion beam, spontaneous fluorescence is allowed to occur, whereas fluorophores in the bright surrounding area are depleted. The result is a lateral reduction of the effective excitation volume with concomitant improvement of resolution. (**b**) STED microscopy applied on biological samples. Neuronal synaptic terminals revealed by immunostaining of the synaptic vesicle protein synaptotagmin were imaged with confocal and STED microscopy for comparison. Individual terminals can be differentiated only under the increased resolution of STED microscopy, due to their subdiffraction size. Reproduced with permission from Ref. [7]

fluorescence excitation and emission will occur just as in conventional fluorescence imaging techniques. In the outer area, however, where both excitation and depletion light coincide, the depletion beam will stimulate the excited fluorophores to emit photons at a longer wavelength than usual, far from the fluorescence detection window [2, 3]. As a result, fluorescence photons are only collected from a narrower central excitation volume that is smaller than the diffraction limit, its size Δr given by $\Delta r \approx \lambda / \left(2NA\sqrt{1 + I / I_S}\right)$. Here, I is the maximum intensity of the depletion beam, and the saturation intensity I_S is the intensity required to reduce the fluorescence probability by half [4]. Thus, larger depletion laser intensities will not only increase the likelihood of stimulated emission to occur but will also increase the resolution of the microscope by broadening the effective area of the depletion doughnut. Thus, STED microscopy allows the immediate acquisition of diffraction-unlimited images without requiring further computational post processing, as it is the case for other fluorescence nano-resolution techniques.

The principle of STED microscopy was first published by Stefan Hell and Jan Wichmann in 1994 [5]. In 2000 the technique was applied to living *Saccharomyces cerevisiae* and *Escherichia coli* cells labeled with organic dyes [3]. Since then, STED has been applied to diverse biological preparations, especially in the neuroscience field (*see* Fig. 1b). Once STED had successfully been applied on immunostained microtubules [6], later studies using immunofluorescence became relatively trivial. For example, the vesicle membrane protein synaptotagmin I was shown to remain clustered in the plasma membrane after vesicle fusion in cultured mammalian neurons [7]. Also, the doughnut-shaped structure of Bruchpilot, a protein important for accurate synapse assembly in the neuromuscular junction of *Drosophila*, was described with STED by using immunostaining [8]. Live imaging of antibody-labeled synaptic vesicles (using synaptotagmin I antibodies) was possible in 2008, featuring imaging speeds of ~28 frames per second [9]. The adaptation of STED microscopy for use with the green fluorescent protein (GFP) [10] opened further pathways for studying living preparations. Thus, STED imaging of fluorescent proteins has been used to reveal the axon arbors of serotonergic neurons in intact living organisms like *Caenorhabditis elegans* [11] and to study movements of dendritic spines in both brain slices [4, 12, 13] and, finally, the living mouse brain [14].

This general summary evidences how STED microscopy has been improved to fulfill the requirements of nowadays cell biology research. However, it is important to highlight that subdiffraction resolution will not only depend on the microscope setup or the strength of the depletion laser but also on the thickness of the sample, the fluorophore selection, and the sample preparation. In this chapter we will focus on the technical aspects needed for obtaining high-quality images and points relevant to the data interpretation.

2 Materials

2.1 STED Setups

In the last decade STED has undergone major technical improvements and enhancements. The achievable resolution in the lateral and axial dimensions can be changed by using different phase masks, which are used to modify the wavefront of the depletion beam to generate the necessary depletion patterns. The most commonly used is the vortex phase plate, which creates the well-known doughnut pattern for increasing the lateral resolution [15, 16]. Two-color STED has been performed by combining two pairs of excitation and depletion beams (one pair for each fluorophore) [17–19] or by selecting the fluorophores thus that the same depletion beam could be used for both fluorophores [20]. Three-color STED imaging was achieved (using only two different laser pairs) by separating the used dyes both spectrally and by their excited state lifetimes. This way, two spectrally similar dyes (KK114 and Atto 647 N) could be distinguished, even though they were excited and depleted with the same pair of lasers [21]. Such multicolor STED imaging enables nanoscale colocalization studies of macromolecules in biological systems. Moreover, an isotropic spatial resolution of ~30 nm has been demonstrated by applying STED through two opposing high numerical aperture objectives thereby generating an almost spherical focal spot. This technique was coined isoSTED [20, 22].

STED has been used in conjunction with other microscopy techniques, thus proving to be a tool with versatile implementations in the biological field. Two-photon excitation has been combined with STED microscopy [23], becoming useful in the study of neuronal architecture in deep planes of brain slices [24]. STED and electron microscopy were used in a correlative microscopy study, where fluorescently tagged proteins first localized by STED microscopy were spatially overlaid with subcellular structures later revealed by electron microscopy, all in the same samples [25]. Furthermore, STED microscopy and fluorescence correlation spectroscopy (FCS) were combined to characterize the diffusion dynamics of single protein and lipid molecules on the plasma membrane of living cells [26].

STED microscopy has remained technically challenging, because most of the improvements and fine-tuning to the particular fluorophores and sample requirements required the construction of customized STED setups. In the meantime, however, Leica Microsystems (Wetzlar, Germany. www.leica-microsystems.com/products/super-resolution/) has been constantly developing and refining commercial STED microscopes, which are also offered as upgrade to their confocal counterparts.

2.1.1 STED with Pulsed Lasers

The first setup developed for STED microscopy uses synchronized trains of light pulses for excitation and depletion [3]. The optimal durations of such excitation and depletion pulses range in the order of tens to hundreds of picoseconds; see, for example, [27].

Typically, an excitation pulse is immediately followed by a depletion pulse in order to prevent early spontaneous fluorescence coming from fluorophores located outside of the doughnut center. Keeping the duration of the excitation-depletion cycle shorter than the excited state lifetime of the fluorophore reduces the probability of detecting those early spontaneous events, which is important for setups where photons are continuously gathered throughout the experiment. However, in cases where this situation cannot be prevented, photons can be selectively gathered right after the depletion pulse by using a time-gated detection system [28].

The temporal separation of excitation and depletion in a pulsed STED configuration implies that relatively low average power is required for depletion. As only a given pool of fluorophores is excited at very specific time points (by the pulsed excitation laser), the depletion beam is only needed at specific points in time, at a moderately high intensity. Although the STED beam intensity required for pulsed systems is two orders of magnitude larger than the one for single-photon excitation (i.e., conventional laser scanning confocal imaging), this is still three orders of magnitude lower than the one for multiphoton excitation [29], thus representing a moderate damage to biological probes. Another benefit of pulsed STED is that excited fluorophores can relax from triplet states between pulses before being re-excited. This diminishes fluorophore photobleaching (by reducing further excitation and damaging of dyes found in the triplet state) and thus allows repeated imaging rounds, important for time-lapse experiments.

Pulsed STED setups are fairly expensive due to the high cost of most pulsed laser sources. As a further drawback, many pulsed depletion lasers are typically tunable in the far-red spectral range (~700–1000 nm), limiting the readily usable fluorescent dyes to the red and infrared spectral range. Imaging more commonly used dyes in the bluer spectral range (e.g., GFP and yellow fluorescent protein YFP) requires additional efforts, such as using an optic parametric oscillator (OPO, for nonlinear frequency conversion) to attain shorter wavelength light (by doubling the frequency of the wavelength to make it match with the red-sided tail of emission of the fluorophore) [7, 10]. Alternative light sources that are easily tunable include stimulated Raman scattering fiber sources [30] or supercontinuum lasers [28, 31].

In most figures presented below, we used a Leica pulsed STED microscopy setup (Leica Microsystems GmbH, Mannheim, Germany), based on a TCS SP5 confocal microscope equipped with a 100× 1.4 NA HCX PL APO oil objective. This microscope uses a pulsed diode laser (18 mW, 80 MHz, 640 nm emission, PicoQuant, Germany) for excitation and a pulsed infrared titanium/sapphire (Ti:Sa) tunable laser (1 W, 80 MHz, 720–1000 nm) for depletion (Mai Tai Broadband, Spectra-Physics, Santa Clara, CA, USA). Detection devices include two ultrasensitive avalanche photodiodes and high-sensitivity, low-noise PMTs (*see* Subheading 2.2).

2.1.2 STED with Continuous Wave (CW) Lasers

With the aim of making STED more easily applicable, the technique has also been implemented with continuous wave lasers [32]. In this configuration, the spatially overlapped excitation and depletion beams are continuously illuminating the sample during image acquisition, making the setup much simpler to implement as no synchronization or modification of laser pulses is necessary. CW STED is more affordable and flexible, since continuous wave lasers are less expensive and are commonly available throughout the visual spectral range, broadening the palette of usable dyes.

The main disadvantage of CW STED is that since the excitation beam functions continuously, the population of excited fluorophores is continuously renewed and thus needs to be constantly "surrounded" by sufficient depletion photons—resulting in a depletion beam power 3–5 times larger than the time-averaged power of the pulsed STED laser [32]. This difficulty in depleting all excited fluorophores leads to a less-defined fluorescence contrast at the doughnut inner border, resulting in less sharp images [27, 33]. CW STED was first introduced using for depletion a Ti:sapphire laser operating in the CW mode at 750 nm [32], but later visible fiber lasers emitting at 592 nm were used instead [34]. Another difficulty of CW STED is that the constant illumination of the sample promotes bleaching of the dyes through dark state excitation, requiring dyes less prone to reach triplet dark states.

2.2 Detectors

Sensitive detectors are necessary for STED microscopy, as a smaller focal volume results in a smaller amount of photons emitted from the sampled spot. To compensate for the reduced signal, pixel dwell times can be increased and more sensitive detectors can be implemented, so as to record more photons from the same spot.

Most commonly, avalanche photodiodes (APDs) are used as detection devices in STED setups. However, hybrid detectors (e.g., GaAsP-based detectors) have been used more recently, since they combine the wide dynamic range of photomultipliers (PMTs) and the high sensitivity of APDs, producing more contrasted images [35].

Particularly bright samples can be imaged with PMTs, although resolution might be suboptimal due to lower signal to noise ratio. As mentioned above, gating systems can be included in the detection process, to avoid collection of early produced photons that could contaminate the image [33].

2.3 Fluorophores and Sample Labeling

As mentioned in the Introduction, STED microscopy could produce in theory an infinitely small excitation volume from which fluorophores could be detected, by arbitrarily increasing the depletion laser intensity. Nevertheless, the main limitation for the application of STED microscopy to biological preparations is the availability of dyes that are stable enough under increasing powers of the depletion laser. Moreover, suitable dyes should have a high quantum yield for good detection and should have appropriate fluorescence lifetimes, in case of pulsed STED. At the beginning of STED microscopy, an additional limitation was the matching of emission spectrum of the fluorophores with the available pulsing STED lasers. Dyes in the red side of the spectrum like RH-414 and Pyridine 4 were used for labeling the vacuolar membrane of yeast cells and *E. coli* membranes, respectively [3].

Atto dyes have been successfully used in the commercial Leica pulsed STED setup, with Atto 647 N and Atto 655 being the most widely used. In our hands, Atto 647 N has worked well in combination with Chromeo 494 for two-color Leica pulsed STED. Technical improvements to double the wavelength frequency of a Ti:Sa pulsing laser allowed depletion of Alexa Fluor 594 [24]. With the advent of STED with CW lasers, blue-shifted fluorophores like Alexa Fluor 488 could be also used [34]. Dyes recommended for the Leica CW setup include BD Horizon V500, Oregon Green 488, Chromeo 488, Chromeo 505, and Atto 488, among others (*see* **Note 1**).

Most of the aforementioned dyes have been used conjugated to antibodies for immunofluorescence assays of fixed or live samples, easing the study of intermolecular interactions and structural details at the subcellular level. A big step in the study of live cells not only in culture but also in tissues was the application of STED on fluorescent proteins. The first report used a GFP-tagged protein imaged in rotavirus-like particles and GFP fused to an ER-targeting sequence in mammalian cells [10]. Morphological plasticity of neuronal dendrites was assessed in YFP-transgenic mice [4, 13]. A more stable and brighter version of YFP, citrine, was also targeted to the ER and imaged in living cells to detect morphological changes of this organelle in time [36]. A new monomeric far-red fluorescent protein, TagRFP657, was engineered by site-specific and random mutagenesis to fit into the excitation and depletion wavelengths of the commercial pulsing STED microscope [37]. The reversible switchable fluorescent proteins (RSFPs), also called photochromic fluorescent proteins, Dronpa and Padron were combined for double-label STED microscopy. Since both proteins are spectrally similar, only one excitation (488 nm) and one depletion beam (595 nm) were needed in combination with a beam at 405 nm that switches Padron off and Dronpa on [38].

Other mechanisms for protein labeling include genetically encoded tags. The SNAP-tag technology is based on the reaction of the protein O6-alkylguanine-DNA alkyltransferase for DNA repairing. The reaction can be used to transfer fluorophores from benzylguanines (BG) to the SNAP-tag, which can be fused with a protein of interest. Vimentin, MAP2, caveolin, and connexin-43 were SNAP-tagged and labeled with tetramethylrhodamine for STED imaging [39]. Another type of tag is the fluorogen-activating proteins (FAPs), which render nonfluorescent organic dyes fluorescent upon specific binding. Thus, actin molecules fused with FAPs were evidenced by activation of malachite green added to the media of living HeLa cells [40].

3 Methods

3.1 Samples

Different types of biological samples, fixed or living, can be studied under the STED microscope (*see* Subheading 1). Thin samples prepared on glass coverslips, including cell monolayer cultures, organelles, or membrane sheets, are very easy to image. The close proximity of the objects to the glass excludes major aberrations due to changes in the refractive index along the sample.

For live cell imaging the sensitivity of the detection device and the speed of movement can be limiting. Despite this, time-lapse recordings have been performed to follow morphological changes of the endoplasmic reticulum in living cells [36] or to track single vesicle fast movements in synaptic boutons and axons at video-rate imaging [9].

In thick preparations (e.g., tissue sections or in vivo imaging) the differences in refractive index between the oil-immersion medium and the biological specimen reduce the STED effect when focusing at deeper planes. Glycerol-immersion objectives with a correction collar have been successfully used to overcome this type of aberration, allowing subdiffraction resolution as deep as 120 μm into living brain slices [12] or up to 15 μm in the living mouse brain [14]. Nonetheless, these studies required abundant cytosolic expression of EYFP in neurons to get a sufficiently bright signal that could be imaged at such depths.

Immunostaining of thick fixed samples can be performed as for confocal microscopy, but special attention should be paid to the selection of the embedding medium (*see* below).

3.2 Embedding Procedures

Thin fixed samples (e.g., cell cultures, membrane sheets, isolated organelles) can be easily embedded in Mowiol, a polyvinyl alcohol-based, water-soluble polymer. For thicker samples the fluorescence intensity and STED resolution will drop at deeper planes due to spherical aberrations caused by a mismatch between the refractive index (n) of the embedding medium and the ones of the glass coverslip ($n = 1.515$) and the immersion oil ($n = 1.518$). Commonly used embedding media like Mowiol ($n = 1.49$) and glycerol ($n = 1.45$) are therefore not suitable [41]. 2,2′-Thiodiethanol (TDE) has been characterized as the best embedding medium to solve this problem, since its n can be easily adjusted by dilution with water ($n = 1.515$ for a 97 % TDE solution). TDE also compensates for changes of n generated by large cellular components and preserves the quantum yield of many fluorophores [41]. Drawbacks of TDE embedding are short life of samples (1–2

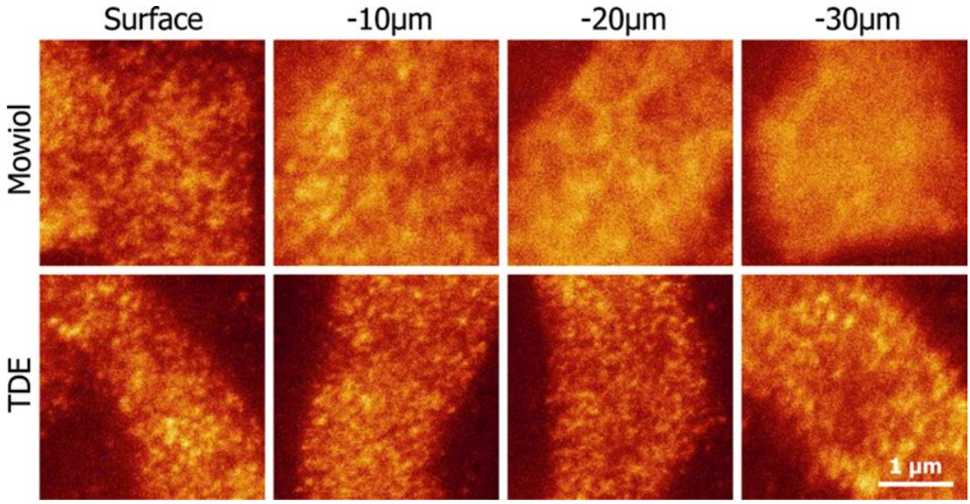

Fig. 2 TDE embedding preserves STED resolution along the axial plane in thick samples. The cranial muscle *levator auris longus*, responsible for ear movement, was dissected from a mouse. After immunostaining against the protein complexin (involved in the regulation of synaptic vesicle fusion), sections of the muscle were embedded in Mowiol (*see* Subheading 3.2.1) or TDE (*see* Subheading 3.2.2) for comparison. Complexin was imaged at the neuromuscular junctions (NMJs) by STED microscopy at four different planes: at the surface of the muscle and around 10, 20, and 30 μm of depth into the tissue. Note that STED resolution decreases at deeper planes of the Mowiol-embedded sample, due to spherical aberrations produced when the light beam reaches a medium of a refractive index different to those of the oil and the glass coverslip. In contrast, the perfect match in refractive index offered by TDE allows imaging at deep planes with preserved STED resolution

weeks) and higher mobility compared to Mowiol embedding (*see* **Note 2**). Figure 2 shows differences in STED resolution at different depths between a sample embedded in Mowiol and one embedded in TDE.

For even bigger fixed samples like whole brain preparations or small organisms, tissues can be embedded in a more stable matrix to allow subsequent slicing in ultrathin sections. This is an extremely important procedure, as (1) such samples are rarely easy to image in high-resolution microscopy, and correct embedding and sectioning procedures remove this difficulty; (2) ultrathin sectioning can be performed down to at least ~40 nm, thus offering a trivial (and cheap) method of obtaining super-resolution in the *Z*-axis.

Several plastic resins are available in the market with different polymerization temperatures, hardness, and pH values. Preliminary tests with different resins are advisable according to the type of sample and fluorophores used. For example, glycol methacrylate (GMA) was selected for imaging fluorescent proteins expressed in *C. elegans*, due to its good penetration and polymerization at pH 8, important for stability of the fluorophore [25]. In our laboratory we have successfully used melamine, a highly water-compatible resin that does not require previous dehydration of the tissue,

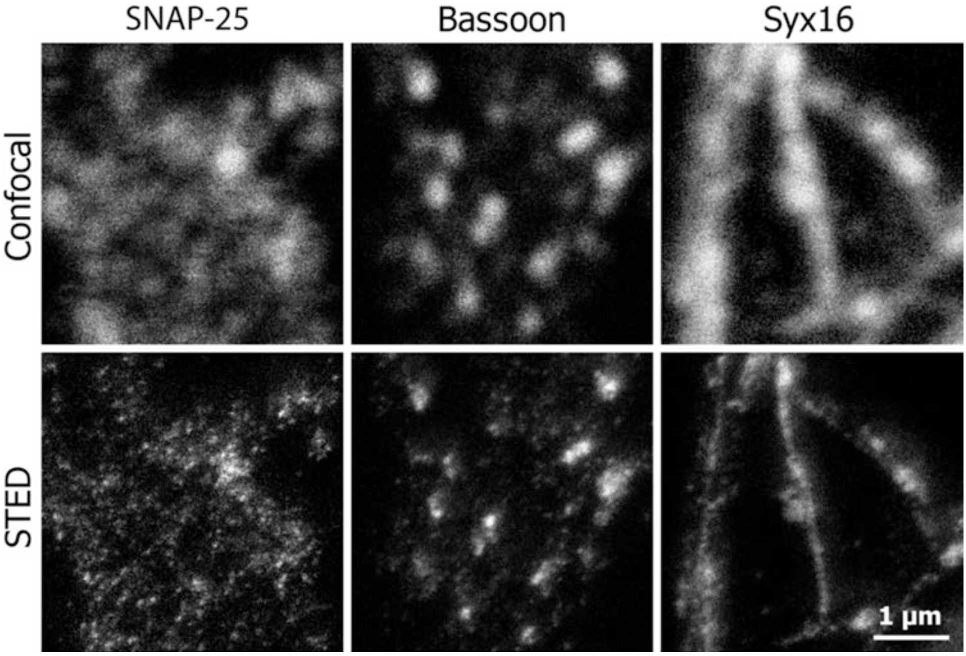

Fig. 3 Improving resolution in the *Z*-axis. Imaging large specimens (several millimeters thick) or generating high-resolution 3D reconstructions of cultured cells is possible using melamine embedding followed by ultrathin sectioning. This is an easy method to obtain subdiffraction axial resolution that complements the improved lateral resolution achieved with STED. As example, hippocampal neurons immunostained for the proteins synaptosomal-associated protein 25 (SNAP-25), bassoon, or syntaxin 16 (Syx16), embedded in melamine (*see* Subheading 3.2.3.) and sliced to 100–150 μm thick sections, were imaged in confocal and STED microscopy. The result in the STED image is clearly defined organelles, well differentiated from their surrounding environment, which is hardly achieved in the confocal image

ensuring its better preservation. Melamine embedding followed by thin sectioning has also been used with cell cultures in order to improve axial resolution for 3D reconstruction [42]. Figure 3 shows STED imaging of melamine sections from immunostained neurons. We have also used the acrylic resin LR White for samples labeled with chemical dyes, although dehydration steps are required, preserving membranes more poorly.

3.2.1 Mowiol Embedding

1. Bring 24 g glycerol, 9.6 g Mowiol 4-88 reagent (Merck Millipore, Merck KGaA, Darmstadt, Germany), 62.4 mL distilled water, and 9.6 mL 1 M Tris buffer into a conical cylinder. Mix with a magnetic stirrer for 5–7 days. Heat the mixture at 40–50 °C to help Mowiol dissolving. Let the mixture settle and aliquot only the supernatant in 1.5 mL tubes. Freeze the aliquots by dipping them into liquid nitrogen. Store at −20 °C.
2. Sample embedding: thaw an aliquot of the Mowiol solution. Place a 10–12 μL drop on a glass microscope slide (for 18 mm

diameter coverslips). With the help of curved forceps, hold the coverslip containing the cell culture vertically and dry it with a soft tissue from the lower border. Place the coverslip on top of the Mowiol drop. Mowiol hardens overnight at room temperature or in 20 min at 37 °C (*see* **Notes 3** and **4**).

3.2.2 TDE Embedding

1. Prepare solutions of 30, 50, 70, and 90 % TDE (Sigma Chemical Company, St. Louis, MO, USA) in distilled and filtered water.
2. After the last wash step of the labeling or immunostaining procedure, incubate the sample in 30 % TDE solution for 10 min. Repeat this step with 50, 70, and 90 % TDE solution sequentially. Incubate in 100 % TDE three times more for 10 min.
3. Sample embedding: place the sample on the center of a glass coverslip of 30 mm diameter. Add a drop of 100 % TDE on top of the sample and place a coverslip of 18 mm diameter on top. Apply nail polish on the rim of the 18 mm coverslip and let the sample dry for 1 h before imaging. This combination of coverslips allows imaging on either side of the sample—important for thick samples (the only ones for which TDE embedding is superior to Mowiol, as indicated above). Store the samples at 4 °C and image within 5 days after sample preparation, since the morphology of the samples is not well preserved beyond a few days.

3.2.3 Melamine Embedding

1. Weight 48 mg p-Toluenesulfonic acid monohydrate (Cat. No. 402885, Sigma-Aldrich Inc., St. Louis, MO, USA) and bring it to a 15 mL conical tube. Add 0.576 mL distilled water. Vortex until complete homogenization of the solution. Add 1.344 g 2,4,6-Tris[bis(methoxymethyl)amino]-1,3,5-triazine (melamine, Cat. No. T2059, TCI Europe, Zwijndrecht, Belgium) and vortex for several minutes. Flip the tube several times until all the melamine is in contact with the solution. Fix the tube with adhesive tape on a horizontal shaker and agitate it at 250 rpm for 2 h or until the melamine is completely dissolved. Vortex shortly every 30 min to speed up this process.
2. Label the sample fluorescently as for any other imaging procedure (e.g., by immunostaining).
3. Sample embedding: place the labeled sample on an 18 mm coverslip. Take into account the orientation of the tissue for later processing. With the help of a micropipette, remove as much buffer as possible surrounding the sample. Cut small pieces of Whatman filter paper and with their tips dry remaining buffer around the sample. Cut the bottom and the lid of a BEEM capsule (Beem Inc., West Chester, PA, USA) and place the capsule with the upper rim down surrounding the sample. Carefully add 200 μL of freshly prepared melamine solution (from **step 1**) drop by drop into the BEEM capsule while covering the sample.

Put the coverslip into the lid of a small plastic dish and this one into a box containing silica gel for desiccation (Sigma Chemical Company, St. Louis, MO, USA). Store in a dry and dark place 24 h at room temperature to ensure penetration of the embedding medium into the specimen.

4. With the sample still on the silica gel, incubate for 24 h at 40 °C.
5. Prepare Epon resin (Epofix kit, Cat. No. 40200029, Struers, Ballerup, Denmark) and pour over the melamine layer, filling the BEEM capsule to the top. Incubate for 72 h at 60 °C or until it is completely hardened (*see* **Note 6**).
6. The coverslip can be detached from the block by pressing it between the thumb and the index finger. Samples can be also dipped into liquid nitrogen. Check if the melamine is completely hard. If not incubate on silica gel for 24 h more at 60 °C.
7. Cut the BEEM capsule to obtain the polymerized block.
8. Trim around the sample where necessary. Use a microtome to cut sections of 50–200 nm (this procedure is identical to those performed in electron microscopy ultrathin processing). These sections can be dried on a glass coverslip and mounted with Mowiol on a slide for STED imaging (*see* **Notes 5** and **6**).

3.2.4 LR White Embedding for Large Specimens

For this embedding procedure one should use LR White medium grade resin and LR White accelerator (London Resin Company Ltd., Reading, Berkshire, England).

1. Prepare solutions of 30, 50, 70, 90, and 95 % EM grade ethanol in distilled and filtered water.
2. After the last wash step of the labeling or immunostaining procedure, a dehydration process with increasing concentrations of ethanol is required. Incubate the sample in a 30 % ethanol solution for 10 min. Repeat this step with 50, 70, 90, 95, and 100 % ethanol solutions, each 10 min. Incubate once more in 100 % ethanol for 10 min.
3. Sample embedding: place the sample on an 18 mm coverslip. Take into account the orientation of the tissue for later processing. With the help of a micropipette, remove as much ethanol as possible. Cut small pieces of Whatman filter paper and with their tips dry remaining ethanol around the sample. Cut the bottom and the lid of a BEEM capsule (Beem Inc., West Chester, PA, USA) and place the capsule with the upper rim down surrounding the sample. Carefully add a small volume of the LR White resin, enough to cover the sample. Incubate overnight at room temperature to allow penetration of the embedding medium into the specimen.
4. Prepare a mixture of 10 mL LR White resin and 1 drop of LR White accelerator. Fill the BEEM capsule with the mixture.

The resin will harden within 10–20 min. Cooling the preparation to 4 °C, or even lower, should be used at this step if better morphology preservation is required.

5. The coverslip can be detached from the block by pressing it between the thumb and the index finger. Remaining glass pieces can be removed under a microscope by manipulating them with a forceps or with razor blades.
6. Cut the BEEM capsule to obtain the polymerized block.
7. Trim the sample where necessary. Use a microtome to cut sections of about 50–200 nm and mount and embed them as above.

3.2.5 LR White Embedding for Cell Cultures

We have successfully used LR White embedding in cell cultures for cases when not only lateral, but also high axial resolution is required. One difficulty is that some cell types (e.g., COS7 cells) do not easily detach from the coating of the glass coverslip, making difficult the transfer into the embedding medium. The following protocol is a modification to the protocol from Subheading 3.2.4, introduced to overcome this difficulty.

1. After the last wash step of the labeling or immunostaining procedure, incubate the cultured coverslip in a solution of 30 % EM grade ethanol, three times each 5 min.
2. Incubate the coverslip in a 1:1 mixture of LR White resin and 30 % ethanol, for 30 min.
3. Incubate in 100 % LR White resin for 60 min.
4. Prepare a mixture of 10 mL LR White resin and one drop of LR White accelerator and vortex.
5. Dry out the excess of LR White from the coverslip by cleaning the border with a soft tissue. Place the coverslip with the cells facing up on a metal block covered with parafilm and previously cooled at 4 °C. Cut the bottom and the lid of a BEEM capsule (Beem Inc., West Chester, PA, USA) and place the capsule with the upper rim facing the cell culture.
6. Add the mixture of resin: accelerator (from **step 4**) into the BEEM capsule up to the upper border. Let it harden for 10–20 min.
7. Continue in **step 5** from the previous protocol (Subheading 3.2.4).
8. *See also* **Note 7**.

3.3 Data Interpretation

Special care must be taken when analyzing STED images from immunostained samples. The use of primary antibodies followed by fluorescently labeled secondary antibodies increases the distance between the recognized epitope and the fluorophore, affecting interpretation of the spatial distribution of the target protein. Moreover, the volume of an antibody recogniz-

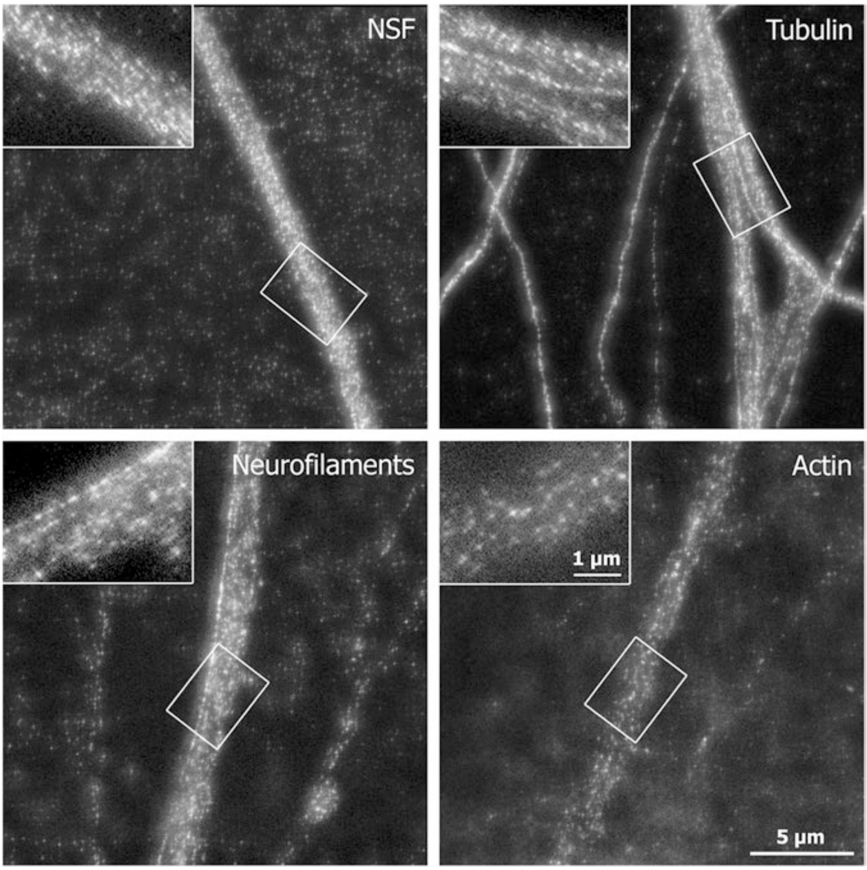

Fig. 4 Deficient immunostaining protocols show artifactual protein distributions. The large size of primary and secondary antibodies used in immunostaining methods imposes two difficulties: poor recognition of epitopes adjacent to an already recognized epitope and location of fluorophores decorating the secondary antibody far from the actual epitope position. To demonstrate this drawback, hippocampal neurons were incubated with primary antibodies against one cytoskeletal protein (actin, neurofilaments, or tubulin) or the cytoplasmic protein *N*-ethylmaleimide-sensitive fusion protein (NSF). Atto 647-labeled secondary antibodies were later used. Low-zoom images of neuronal processes show apparent filaments for actin, neurofilaments, and tubulin, while NSF is distributed more homogeneously. A larger zoom (*insets*) reveals that the filaments are not continuous and are actually featured by fairly separated spots, now difficult to differentiate from the enlarged NFS picture. Correlation and distribution analyses can be negatively affected by misleading information about the true location of the protein of interest

ing one epitope may hinder the recognition of adjacent epitopes, reducing in this way the accuracy and density [43] of the staining and offering and incomplete picture in a diffraction-unlimited image (*see* Fig. 4). In many cases the zoom in a STED picture will show a collection of spots that would not reflect the real molecular structure of the target. Although fluorescently labeled primary antibodies can be used, signal intensity might be reduced. It is important to optimize the immunostaining protocols according to the antibodies used and the protein of

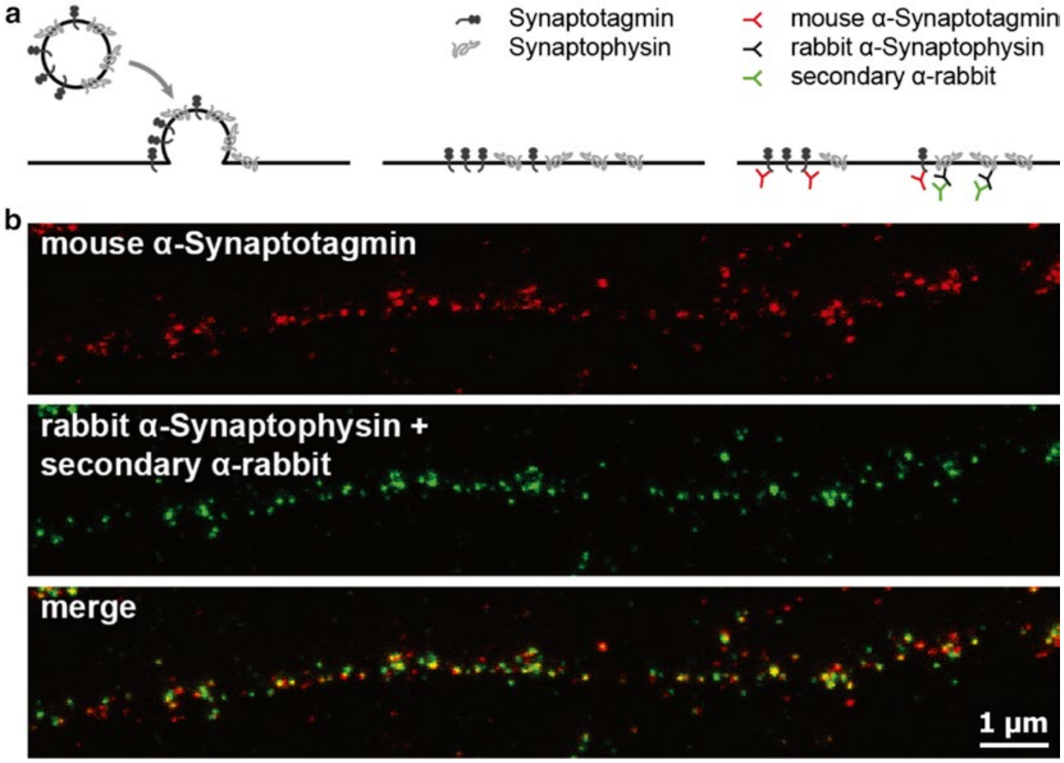

Fig. 5 Good immunostaining procedures allow reliable protein colocalization analyses. As an example, the synaptic vesicle proteins synaptophysin and synaptotagmin were shown to remain clustered on the plasma membrane after synaptic vesicle fusion. (**a**) Experimental paradigm: following stimulated exocytosis the luminal domain of synaptotagmin is labeled by Atto 647-coupled mouse anti-synaptotagmin antibodies (*red*), and synaptophysin is bound by rabbit primary anti-synaptophysin antibodies (*black*). After fixation, Atto 590-coupled anti-rabbit secondary antibodies (*green*) are added. (**b**) STED images of synaptotagmin (*upper panel*) and synaptophysin (*middle panel*) show perfect colocalization at several vesicle release sites in a neuronal process (*lower panel*). Reproduced with permission from Ref. [46]

interest. Different concentrations of fixatives, blocking solutions, and antibodies should be tested. With appropriate epitope access good quality images can be acquired, even suitable for correlation analyses (Fig. 5).

In a recent study, conventional antibodies (~150 KDa, ~10 nm in size) were replaced by smaller anti-GFP nanobodies (~13 KDa, 1.5 × 2.5 nm) coupled to Alexa Fluor 647, to label GFP-fused proteins in yeasts. High-resolution images showed increased label density and reduction of the full width at half maximum (FWHM) values almost by half, when compared to a conventional immunostaining protocol with primary and secondary antibodies [44]. In our laboratory we have also performed, for the first time, high-resolution STED microscopy of nucleotide-based aptamers. These are single-stranded oligonucleotides, RNA or DNA, that can specifically bind to other molecules and therefore can be used in a similar fashion to antibodies. Aptamers present several advantages over antibodies. They are synthetically generated, can be directly coupled to fluorophores, are small (up to a few tens of kDa), and can be easily engineered according to the experimenter needs [45].

3.3.1 Data Analysis

Images acquired with STED microscopy will need the standard noise reduction by filtering (using, e.g., median filtering). When imaging two molecular species by two-color STED, simple signal overlap will not be sufficient to estimate colocalization. Spatial analysis methods like measurement of distance between the spots can be a good option [46]. The Pearson's correlation analysis has also been applied in this kind of experiments [47]. For accurate results, it is important to verify that satisfactory resolution values were attained in both channels.

4 Notes

1. For a more detailed list of dyes used in STED microscopy, *see* [35] or visit nanobiophotonics.mpibpc.mpg.de/old/dyes.
2. We recommend to image TDE embedded samples within 5 days after preparation.
3. Application of nail polish on the rim of the coverslip adds to sample preservation and stability.
4. Samples embedded in Mowiol can be stored at 4 °C for several months depending on the quality of the fluorescent labeling.
5. Although the Z-resolution is obviously higher in thinner samples, they will be substantially dimmer than the thicker ones.
6. Melamine embedding can be also applied to cells cultured on coverslips (Fig. 3). When embedding cells, we recommend to trim the melamine only after it is completely hardened, to avoid modifying the flat surface of the cell layer, through the pressure applied during trimming. In contrast, when embedding large tissue preparations, we recommend to trim the samples when the melamine is still soft (~48 h after incubation at 60 °C, **step 5**) to prevent fracture of the sample. Different batches of reagents can have different hardening speeds, and therefore it is necessary to identify the appropriate length of the hardening period at 60 °C.
7. LR White embedding is preferred over melamine embedding when the samples need to be also analyzed by electron microscopy.

Acknowledgments

We thank Nicolai T. Urban for advice and for reading the manuscript, Felipe Opazo for providing images used in Fig. 4, and Christina Schäfer and Katharina Kröhnert for technical assistance. S.O.R. acknowledges the support of a Starting Grant from the European Research Council, Program FP7 (NANOMAP). N.H.R. acknowledges the support of the Deutsche Forschungsgemeinschaft (SFB 889).

References

1. Abbe E (1873) Beiträge zur theorie des mikroskops und der mikroskopischen wahrnehmung. Arch für Mikroskopische Anat 9:413–418
2. Hell SW, Dyba M, Jakobs S (2004) Concepts for nanoscale resolution in fluorescence microscopy. Curr Opin Neurobiol 14:599–609
3. Klar TA, Jakobs S, Dyba M et al (2000) Fluorescence microscopy with diffraction resolution barrier broken by stimulated emission. Proc Natl Acad Sci U S A 97:8206–8210
4. Nägerl UV, Willig KI, Hein B et al (2008) Live-cell imaging of dendritic spines by STED microscopy. Proc Natl Acad Sci U S A 105:18982–18987
5. Hell SW, Wichmann J (1994) Breaking the diffraction resolution limit by stimulated emission: stimulated-emission-depletion fluorescence microscopy. Opt Lett 19:780–782
6. Dyba M, Jakobs S, Hell SW (2003) Immunofluorescence stimulated emission depletion microscopy. Nat Biotechnol 21:1303–1304
7. Willig KI, Rizzoli SO, Westphal V et al (2006) STED microscopy reveals that synaptotagmin remains clustered after synaptic vesicle exocytosis. Nature 440:935–939
8. Kittel RJ, Wichmann C, Rasse TM et al (2006) Bruchpilot promotes active zone assembly, Ca2+ channel clustering, and vesicle release. Science 312:1051–1054
9. Westphal V, Rizzoli SO, Lauterbach MA et al (2008) Video-rate far-field optical nanoscopy dissects synaptic vesicle movement. Science 320:246–249
10. Willig KI, Kellner RR, Medda R et al (2006) Nanoscale resolution in GFP-based microscopy. Nat Methods 3:721–723
11. Rankin BR, Moneron G, Wurm CA et al (2011) Nanoscopy in a living multicellular organism expressing GFP. Biophys J 100:L63–L65
12. Urban NT, Willig KI, Hell SW et al (2011) STED nanoscopy of actin dynamics in synapses deep inside living brain slices. Biophys J 101:1277–1284
13. Tønnesen J, Nadrigny F, Willig KI et al (2011) Two-color STED microscopy of living synapses using a single laser-beam pair. Biophys J 101:2545–2552
14. Berning S, Willig KI, Steffens H et al (2012) Nanoscopy in a living mouse brain. Science 335:551
15. Keller J, Schönle A, Hell SW (2007) Efficient fluorescence inhibition patterns for RESOLFT microscopy. Opt Express 15:3361–3371
16. Wildanger D, Medda R, Kastrup L et al (2009) A compact STED microscope providing 3D nanoscale resolution. J Microsc 236:35–43
17. Donnert G, Keller J, Wurm CA et al (2007) Two-color far-field fluorescence nanoscopy. Biophys J 92:L67–L69
18. Blom H, Rönnlund D, Scott L et al (2012) Nearest neighbor analysis of dopamine D1 receptors and Na(+)-K(+)-ATPases in dendritic spines dissected by STED microscopy. Microsc Res Tech 75:220–228
19. Meyer L, Wildanger D, Medda R et al (2008) Dual-color STED microscopy at 30-nm focal-plane resolution. Small 4:1095–1100
20. Schmidt R, Wurm CA, Jakobs S et al (2008) Spherical nanosized focal spot unravels the interior of cells. Nat Methods 5:539–544
21. Bückers J, Wildanger D, Vicidomini G et al (2011) Simultaneous multi-lifetime multi-color STED imaging for colocalization analyses. Opt Express 19:3130–3143

22. Schmidt R, Wurm CA, Punge A et al (2009) Mitochondrial cristae revealed with focused light. Nano Lett 9:2508–2510
23. Moneron G, Hell SW (2009) Two-photon excitation STED microscopy. Opt Express 17:14567–14573
24. Ding JB, Takasaki KT, Sabatini BL (2009) Supraresolution imaging in brain slices using stimulated-emission depletion two-photon laser scanning microscopy. Neuron 63:429–437
25. Watanabe S, Punge A, Hollopeter G et al (2011) Protein localization in electron micrographs using fluorescence nanoscopy. Nat Methods 8:80–84
26. Eggeling C, Ringemann C, Medda R et al (2009) Direct observation of the nanoscale dynamics of membrane lipids in a living cell. Nature 457:1159–1162
27. Leutenegger M, Eggeling C, Hell SW (2010) Analytical description of STED microscopy performance. Opt Express 18:26417–26429
28. Galiani S, Harke B, Vicidomini G et al (2012) Strategies to maximize the performance of a STED microscope. Opt Express 20:7362–7374
29. Donnert G, Keller J, Medda R et al (2006) Macromolecular-scale resolution in biological fluorescence microscopy. Proc Natl Acad Sci U S A 103:11440–11445
30. Rankin BR, Hell SW (2009) STED microscopy with a MHz pulsed stimulated-Raman-scattering source. Opt Express 17:15679–15684
31. Wildanger D, Rittweger E, Kastrup L et al (2008) STED microscopy with a supercontinuum laser source. Opt Express 16:9614–9621
32. Willig KI, Harke B, Medda R et al (2007) STED microscopy with continuous wave beams. Nat Methods 4:915–918
33. Vicidomini G, Moneron G, Han KY et al (2011) Sharper low-power STED nanoscopy by time gating. Nat Methods 8:571–573
34. Moneron G, Medda R, Hein B et al (2010) Fast STED microscopy with continuous wave fiber lasers. Opt Express 18:1302–1309
35. Müller T, Schumann C, Kraegeloh A (2012) STED microscopy and its applications: new insights into cellular processes on the nanoscale. Chemphyschem 13(8):1986–2000. doi:10.1002/cphc.201100986
36. Hein B, Willig KI, Hell SW (2008) Stimulated emission depletion (STED) nanoscopy of a fluorescent protein-labeled organelle inside a living cell. Proc Natl Acad Sci U S A 105:14271–14276
37. Morozova KS, Piatkevich KD, Gould TJ et al (2010) Far-red fluorescent protein excitable with red lasers for flow cytometry and super-resolution STED nanoscopy. Biophys J 99:L13–L15
38. Willig KI, Stiel AC, Brakemann T et al (2011) Dual-label STED nanoscopy of living cells using photochromism. Nano Lett 11:3970–3973
39. Hein B, Willig KI, Wurm CA et al (2010) Stimulated emission depletion nanoscopy of living cells using SNAP-tag fusion proteins. Biophys J 98:158–163
40. Fitzpatrick JA, Yan Q, Sieber JJ et al (2009) STED nanoscopy in living cells using Fluorogen Activating Proteins. Bioconjug Chem 20:1843–1847
41. Staudt T, Lang MC, Medda R et al (2007) 2,2′-thiodiethanol: a new water soluble mounting medium for high resolution optical microscopy. Microsc Res Tech 70:1–9
42. Punge A, Rizzoli SO, Jahn R et al (2008) 3D reconstruction of high-resolution STED microscope images. Microsc Res Tech 71:644–650
43. McKinney SA, Murphy CS, Hazelwood KL et al (2009) A bright and photostable photoconvertible fluorescent protein. Nat Methods 6:131–133
44. Ries J, Kaplan C, Platonova E et al (2012) A simple, versatile method for GFP-based super-resolution microscopy via nanobodies. Nat Methods 9(6):582–584
45. Opazo F, Levy M, Byrom M et al (2012) Aptamers as potential tools for super-resolution microscopy. Nat Methods 9:938–939
46. Hoopmann P, Punge A, Barysch SV et al (2010) Endosomal sorting of readily releasable synaptic vesicles. Proc Natl Acad Sci U S A 107:19055–19060
47. Neumann D, Bückers J, Kastrup L et al (2010) Two-color STED microscopy reveals different degrees of colocalization between hexokinase-I and the three human VDAC isoforms. PMC Biophys 3:4

Chapter 13

Three-Dimensional Photoactivated Localization Microscopy with Genetically Expressed Probes

Kelsey Temprine, Andrew G. York, and Hari Shroff

Abstract

Photoactivated localization microscopy (PALM) and related single-molecule imaging techniques enable biological image acquisition at ~20 nm lateral and ~50–100 nm axial resolution. Although such techniques were originally demonstrated on single imaging planes close to the coverslip surface, recent technical developments now enable the 3D imaging of whole fixed cells. We describe methods for converting a 2D PALM into a system capable of acquiring such 3D images, with a particular emphasis on instrumentation that is compatible with choosing relatively dim, genetically expressed photoactivatable fluorescent proteins (PA-FPs) as PALM probes. After reviewing the basics of 2D PALM, we detail astigmatic and multiphoton imaging approaches well suited to working with PA-FPs. We also discuss the use of open-source localization software appropriate for 3D PALM.

Key words Super resolution, Single-molecule imaging, 3D microscopy, Cell biology

1 Introduction

Modern fluorescence microscopy is an invaluable tool for the biologist, combining contrast, molecular specificity, and biocompatibility to enable the visualization of cellular constituents. Unfortunately, diffraction limits the spatial resolution of a wide-field fluorescence microscope to ~250 nm laterally and 500–750 nm axially, and achieving even this "diffraction-limited" performance is difficult in practice. Methods for imaging beyond the diffraction limit are thus of great practical interest in cell biology, and the last decade has seen the emergence of such "super-resolution" optical imaging techniques [1].

In this chapter, we focus on photoactivated localization microscopy (PALM) [2] and related single-molecule imaging techniques (e.g., STORM [3], fPALM [4]). In these techniques, the specimen is labeled with a photoswitchable fluorescent probe. During data acquisition, the fluorescence emitted from a sparse subset ("sparse" means that the image of each molecule is resolvable) of probe

Peter J. Verveer (ed.), *Advanced Fluorescence Microscopy: Methods and Protocols*, Methods in Molecular Biology, vol. 1251, DOI 10.1007/978-1-4939-2080-8_13,

molecules is isolated by switching on only a few molecules at a time. The fluorescence is recorded using a camera, the probe molecules are switched off, and the process repeated until most or all molecules have been photoswitched. The raw data thus collected consist of thousands of individual frames, each containing diffraction-limited fluorescence images of single photoswitchable molecules. The image of each molecule (point-spread function or PSF) is analyzed to localize its center with high precision, and the resulting localizations are combined to generate a super-resolution (in optimal conditions, resolutions of ~20 nm or better can be achieved) image of the positions of the molecules (Fig. 1). Resolution is ultimately dependent on (a) localization precision (how precisely each probe molecule may be localized) and (b) density of localizations assembled in the final image (*see* **Note 1**). Localization precision and density are in turn dependent critically on the choice of switchable molecule, and it is this choice that largely determines the success or failure of a single-molecule super-resolution imaging experiment.

Broadly speaking, photoswitchable probes may be divided into two broad categories: those that may be genetically expressed (e.g., photoactivatable fluorescent proteins, PA-FPs [5]) and those synthetic dyes that may be exogenously introduced via antibodies or small-molecule labeling strategies [6]. Each class has its

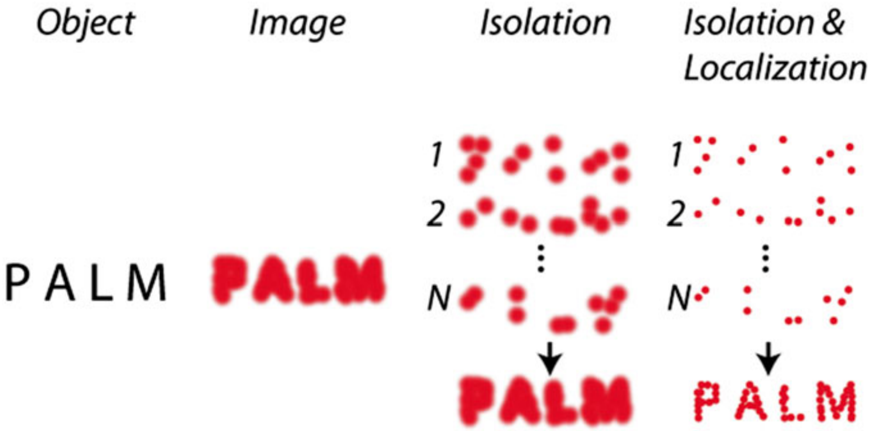

Fig. 1 Concept behind PALM. When labeled with a fluorescent probe and viewed through a conventional microscope, high spatial frequency detail in an object (*leftmost column*) is obscured, producing a diffraction-limited image (*middle left column*). PALM may be used to obtain a much higher-resolution image, if two criteria are met. First, the sample must be labeled with a photoswitchable probe and only a sparse subset of probes induced to activate and fluoresce in any given frame (*middle right column*). This "isolation" procedure alone is insufficient, as combining the recorded fluorescence from all *N* frames recovers the diffraction-limited image. However, if the optically resolved images of the individual molecules are also localized (*rightmost column*) with high precision, the aggregate image resulting from all such localizations may be combined to obtain a super-resolution image

own strengths and weaknesses: PA-FPs are small (a few nm in size), may be targeted with molecular precision and are thus highly specific, and may possess a high (>1,000) contrast ratio between bright and dark states, helpful in isolating a single fluorescent molecule from its neighbors and acquiring high-density (and thus high resolution) images. Unfortunately, PA-FPs are in general dimmer than most synthetic dyes, limiting localization precision and challenging the detection of activated single-molecule signal above cellular autofluorescence and residual faint background emission from the potentially large number of inactive molecules. They are also available only in limited colors, and the brightness and contrast ratio of the green-emitting PA-FPs is generally lower than the red-emitting PA-FPs (although the palette of PA-FPs continues to expand [7] and the performance of green PA-FPs continues to improve [8]). Switchable synthetic dyes can be very bright and are available in many colors [9], significant advantages over PA-FPs. However, the coupling method (e.g., to antibodies) can introduce significant uncertainty in their position, thus defeating the brightness advantage and effectively limiting resolution. Exogenously introduced dyes often label their target less specifically than PA-FPs, leading to an increased level of background in the reconstructed super-resolution image and sometimes introducing uncertainty as to whether localizations are real or spurious. Finally, many exogenous dyes require an additional chemical cocktail (typically reducing agents or oxygen scavengers) and/or high excitation intensities, limiting application in live cells. In this chapter, we focus on instrumentation particularly suited to the somewhat dimmer PA-FPs.

Initial PALM experiments were conducted in 2D [2, 10] near the coverslip surface, where optical aberrations and scattering are minimized, and the full numerical aperture (NA) of oil objectives may be used to maximize signal collection and aid in the localization precision of dim PA-FPs. An additional advantage of 2D imaging near the coverslip is that total internal reflection (TIR [11]) may be used to limit excitation to the focal plane and further aid in single-molecule detection. As it forms the basis for 3D experiments, we cover 2D PALM instrumentation in Subheading 3.1.

While suited to membrane [12] and focal adhesion [13] studies in live cells, the obvious drawback of TIRF is that the vast majority of the cell is inaccessible. The simplest way around this problem is to move the excitation out of TIRF, thus employing epi- or wide-field imaging to illuminate the entire cell. This imaging modality also creates several problems for 3D super-resolution imaging: (a) in addition to x and y, a molecule's z coordinate must be localized with subdiffractive precision, and the resulting information used in assembling a 3D PALM dataset; (b) axial drift must be measured and/or controlled; and (c) background photoactivation and subsequent fluorescence of probe molecules at axial locations other than the focal (imaging) plane must be minimized, lest their localizations be wasted and the extraneous background signal so created impede localization in the focal plane. We discuss technical solutions to (a–b) in Subheading 3.2 and (c) in Subheading 3.3. We also refer to the reader to [14, 15], as this chapter draws heavily from these sources.

2 Materials

2.1 2D PALM Instrumentation

1. IX-81 microscope frame equipped with TIRF illuminator, left-side port, DIC optics, filter cube turret, and 1.6× internal beam expander (Olympus America, IX2-RFACB2-R).
2. Automated XY stage (Applied Scientific Instrumentation, MS-2000).
3. High numerical aperture (1.49 NA) 60× objective lens, suitable for TIRF (Olympus America, APON 60XOTIRF).
4. Filters in microscope frame, used for PA-FP imaging:
   (a) mEos2/pa-mCherry1 dichroic mirror (Semrock, FF562-Di02-25x36); bandpass.
   (b) mEos2/pa-mCherry1 emission filter (Semrock, FF01-617/73-25).
   (c) Dronpa/PS-CFP2 dichroic mirror (Chroma, T495lp).
   (d) Dronpa/PS-CFP2 bandpass emission filter (Chroma, ET525/50).
5. Optical table (Technical Manufacturing Corporation).
6. Overhead shelf system (Newport, ATS-10).
7. Sticky pads to remove dust (Cole Static Control).
8. Temperature/humidity USB monitor (Practical Design Group LLC, THUM).
9. Excitation optics sled, optomechanics, and spacers for raising sled to TIRF port height (Thorlabs, PBH11106, BLP01, PF175, PS1, PS2, PS3, PS4).
10. Lasers for common PA-FPS:
    (a) Excitation for mEos2, pa-mCherry1, 200 mW, 561 nm (Crystalaser, CL561-200).
    (b) Excitation for Dronpa/PS-CFP2, 150 mW, 488 nm (Newport, Cyan scientific laser).
    (c) Photoactivation of PA-FPs, 100 mW, 405 nm (Coherent, 405-100 CIRCULAR).
11. Sled optics:
    (a) 561 nm beam expansion, 2.7×, Thorlabs $f = 15$ mm LA1540-A and $f = 40$ mm LA1304-A.
    (b) 488 nm beam expansion, 4×, Thorlabs $f = 25$ mm AC127-025-A-ML and $f = 100$ mm AC254-100-A-ML.

   - (c) 405 nm beam expansion, 2×, Thorlabs $f = 15$ mm LA1540-A and $f = 30$ mm LA1289-A.
   - (d) Neutral density filters (Edmund Scientific, NT54-460).
   - (e) Cage optomechanics for mounting beam expanders and neutral density filters (Thorlabs, CP02T, ER4, ER6).
   - (f) Shutter, controller, and power supply (Thorlabs, SH05, TSC001, TCH002).
   - (g) Visible mirrors and holders (Thorlabs, BB1-E02 and KS1).
   - (h) External dichroic mirror for integrating 488 nm laser (Semrock, FF506-Di02-25x36).
   - (i) External dichroic mirror for integrating 405 nm laser (Semrock, FF458-Di02-25x36).
   - (j) Dichroic mirror holders (Thorlabs, KM100C).
   - (k) Beam steering assembly (Thorlabs, GN05 and CVI/Melles Griot 12.5 mm diameter/5 mm thick fused silica windows).
   - (l) Focusing lens (Edmund Optics, $f = 50$ mm achromatic lens, NT49-356-INK) and holder (Thorlabs, ST1XY-S and SM1ZM).
   - (m) Collimating lens (Edmund Optics, $f = 100$ mm achromatic lens, NT49-360-INK) and holder (Thorlabs, ST1XY-S and SM1ZM).
   - (n) Translation stage for imaging focused beam at back focal plane of microscope (Newport, 461-X-M and SM-06).

12. Sample holder and stage insert (Applied Scientific Instrumentation, I-3033 and I-3033-25D).
13. 25 mm, #1.5 coverslips (Warner Instruments, CS-25R15).
14. Back-thinned, electron-multiplying CCD (Andor Technology, DU-888E-C00-#BV).
15. 1.2× emission-side beam expander (Diagnostic Instruments, DD12BXC).
16. Acquisition Computer (Advantech, SYS-4U-BTO with 2 TB hard drive, 2.5 GB RAM, Dual 2.13 GHz processors).

2.2 Additional Components for 3D PALM

1. Automated XY translation stage with z piezo (Applied Scientific Instrumentation, PZ-2000).
2. High numerical aperture (1.2 NA) 60× water-immersion objective lens (Olympus America, UPLSAPO60XW).
3. Focus-lock system to minimize z drift (Mad City Labs, C-Focus).
4. Gold fiducial particles, 100 nm (Microspheres-Nanospheres, 790122-010).

5. Data analysis computer (Xi Computer Corp, 2P64 workstation with 500 GB hard drive, 8 GB RAM, 2× AMD Opteron processors 2 GHz, 8 cores).
6. Network-attached storage device (Amazon.com, Netgear ReadyNAS + 2 TB internal hard drives).
7. Cylindrical lenses for astigmatic localization (Thorlabs, $f = 100$ mm, LJ1567RM-A; $f = 150$ mm, LJ1629RM-A; $f = 300$ mm, LJ1558RM-A).
8. Optomechanics for inserting cylindrical lenses between EM-CCD and microscope left-side port:
    (a) Filter wheel (Thorlabs, CFW6).
    (b) Adapter with external SM1 threads and internal C-mount threads (Thorlabs, SM1A10).
    (c) Adapters with (a) external C-mount threads and internal SM1 threads and (b) external SM1 threads (Thorlabs, SM1A9 and SM1T2).
    (d) 1″ travel translation stage (Thorlabs, DT25).
    (e) Support for 1.2× expander (Thorlabs, RS2P, extra spacers as needed).

2.3 Components for Two-Photon Activation of PA-FPs

1. Laser for two-photon activation (2PA), capable of producing pulses of 140 fs duration and tuned to 800 nm (Coherent, Chameleon Ultra II).
2. Power control:
    (a) Glan-Laser calcite polarizer (Newport, 10GL08AR.16).
    (b) Half-wave plate for infrared wavelengths (Newport, 10RP52-2).
    (c) Motorized rotation mount (Thorlabs, PRM1Z8E).
    (d) Beam dump (Newport, PL15).
3. Temporal focusing optics:
    (a) Periscope system for directing beam onto scanning mirror from above (Thorlabs, KCB1, CP02T, ER4, ER6, PH3, TR2).
    (b) Galvonometric scanner (Cambridge Technology, 6215HB).
    (c) Function generator for driving galvo (Stanford Research Instruments, DS340).
    (d) Focusing cylindrical lens (Thorlabs, LJ1653L2-B).
    (e) Cylindrical beam expander (Thorlabs, $f = 30$ mm, LJ1212L2-B, and $f = 200$ mm, LJ1653L1-B).
    (f) Low-dispersion silver mirrors, 1″ and 2″ diameter (Femtolasers, OA022 and OA248).

   (g) 830-groove-per-millimeter gold-coated reflective diffraction grating with 21.4° blaze angle (Newport, 53107BK02-035R).
   (h) Magnetic mount for diffraction grating (Thorlabs, KB3X3).
   (i) Lens pairs for demagnifying grating onto sample (Thorlabs, f = 300 mm AC508-300-B-ML and f = 100 mm AC254-100-B-ML) and (Thorlabs, f = 500 mm AC508-500-B-ML and Olympus, UPLSAPO60XW f = 3 mm objective).

4. Coupling optics for combining 800 nm light with visible wavelengths used in single-photon excitation:
   (a) Removable mirror mounted on a magnetic base (Thorlabs, BB1-E02 and KB1X1).
   (b) Visible achromatic lens, f = 400 mm (Edmund Optics, NT49-369-INK).
   (c) External dichroic mirror for combining visible and 800 nm illumination prior to microscope body (Semrock, Di01-R561-25x36).
   (d) Periscope unit for raising 800 nm illumination and directing it into the microscope frame (Thorlabs, KS2, RS4P, RS6, RS1, RM1C).
   (e) Right-side port attachment on microscope frame for illumination (Olympus, IX2-RFACB2-R).
   (f) Filter cube suitable for right-side port illumination (Olympus, IX2-MFB-SP-R).
   (g) Custom dichroic mirror to be placed inside filter cube (Chroma, ZT405/488/561/IR-RPC, reflects 405 nm, 488 nm, 561 nm, 700–1,100 nm).
   (h) Shortpass emission filter, for blocking 800 nm pump light, to be placed inside filter cube (Semrock, FF01-680/SP-25).

5. Diagnostics for measuring quality of temporal focus:
   (a) Quantum dot solution (Q dots; Ocean NanoTech, QSO-520-0010).
   (b) Ethylene vinyl acetate copolymer resin (DuPont, Elvax 410).
   (c) Toluene (Sigma, 244511).
   (d) Glass vial (Fisher Scientific, 03-339-22C).
   (e) Hot plate (Corning, PC-220).
   (f) Spin coater (Laurell Technologies Corporation, WS-650S-8NPP-LITE).

3 Methods

3.1 2D PALM Instrumentation

As instrumentation for 2D PALM has been covered extensively elsewhere [15], here we review major concepts only. Much of the following description also applies to 3D PALM; exceptions for TIRF are noted when appropriate. Data acquisition and processing are covered in Subheading 3.2.

3.1.1 Basic Considerations

PALM instrumentation should be housed in a clean, dust-free environment to reduce sample contamination and avoid the stray light and scattering caused by dust in the optical path. We place sticky pads outside the room housing the PALM to help reduce dirt brought in by users. While the undesirable effects of thermal drift may be compensated for by post-processing (Subheading 3.2.4), it is advantageous to control the temperature as much as possible to mitigate this problem. We periodically monitor the temperature using a USB device in order to ensure temperature is within specification. To reduce mechanical vibrations, we bolt all optics on a vibrationally isolated air table (*see* **Note 2**).

3.1.2 System Overview

Although it is possible to build a PALM system entirely from “the ground up” [2], we find it helpful to use a commercial microscope frame (Olympus, IX-81) as the base because the eyepieces, brightfield optics, objective holder, and filter cube turret make it easy to both screen samples and examine them with additional, non-PALM imaging modes (e.g., differential interference contrast (DIC)). Another advantage of buying a commercial frame is that the TIRF illuminator add-on facilitates TIRF by enabling the user to free-space couple high-intensity lasers of the appropriate wavelength into the system, thus minimizing PALM acquisition time. Also, the microscope manufacturer can provide an automated XY stage (e.g., ASI, MS-2000), helpful in scouting for appropriate samples and in marking their positions. With the frame bolted to the optical table, the main additional components are the excitation and activation optics, the optics housed within the microscope frame itself, and the detection optics (Fig. 2a).

3.1.3 Excitation and Photoactivation

As almost all PA-FPs are photoactivated with near-ultraviolet light, we use the commonly available 405 nm laser for PALM (Coherent, 405-100 CIRCULAR). Red PA-FPs (pa-mCherry1 or mEos2) are efficiently excited with a 561 nm laser (Crystalaser, CL561-200); for green PA-FPs (Dronpa or PS-CFP2), we use a 488 nm laser (Newport, Cyan scientific laser). We bolt all lasers to a small optical sled (Thorlabs, PBH11106), beam expand each to a common diameter, and combine their output with dichroic mirrors (Fig. 2b). We introduce beam-steering assemblies in front of each laser to correct for small differences in laser height or lateral position. Cage-mount optomechanics (Thorlabs, CP02T, ER4, ER6) are

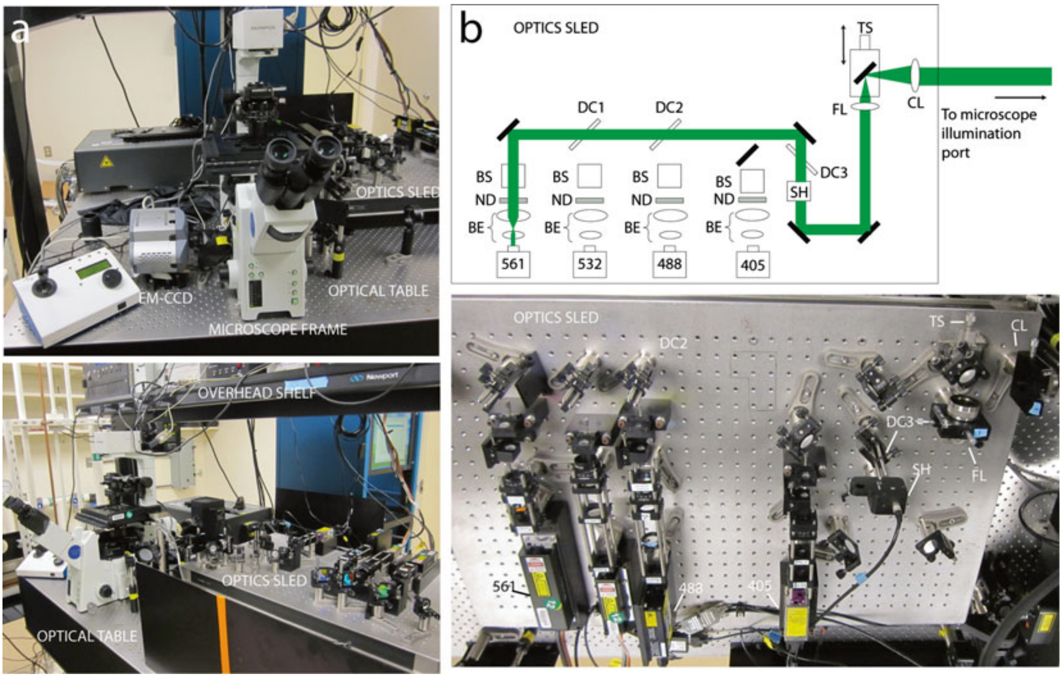

Fig. 2 Basic (2D) PALM system. (**a**) Front (*top*) and side (*bottom*) views, showing major items referred to in text including microscope frame, vibration isolation table, overhead shelf, and excitation sled. (**b**) Expanded schematic (*top*) and photograph (*bottom*) of excitation/activation lasers, associated optics, and optomechanics. Symbol key: *DC* dichroic mirror, *BS* beam-steering assembly, *ND* neutral density filter, *BE* beam expander, *SH* shutter, *TS* translation stage, *FL* focusing lens, *CL* collimating lens. Lasers are labeled according to wavelength, as referred to in the text. Lenses are drawn as *ellipses* in the schematic, reflective mirrors as *filled-in rectangles*. Note that DC1 and the 532 nm laser are not used for exciting PA-FPs and are thus not referenced in the text. Panel (**b**) is modified from York 2011, supplementary Fig. 1 with permission from Nature Methods

particularly useful in mounting beam expanders or neutral density filters and assure colinearity of optics along the beam path. Finally, we place a computer-controlled, mechanical shutter (Thorlabs, SH05, TSC001, and TCH002) after the coaligned beams, allowing the user to easily turn off the illumination to the sample.

3.1.4 Achieving TIRF

As discussed elsewhere [15], TIRF is achieved by focusing the coaligned beams at the edge of the back focal plane (BFP) of the objective lens. We focus the laser illumination on a sled with lens FL and recollimate the beam with lens CL. By positioning the entire laser system such that the back focal plane of lens CL is coincident with the front focal plane of the 200 mm relay lens internal to the TIRF illuminator (*see* **Note 3**), the focus created by FL is imaged at the BFP. In this geometry, the image of the focus can be moved at the BFP by translating a mirror placed on translation stage TS. The “U-DP” attachment on the TIRF illuminator is useful for switching between arc lamp and TIRF illumination, but only the 200 mm relay lens within the illuminator is necessary; the entire fiber-coupling assembly can be removed.

3.1.5 Microscope Body and Sample Holder

Dichroics and emission filters suitable for green or red PA-FPs can be placed directly into commercially available filter cubes and placed into the filter turret assembly (*see* **Note 4**). Most PALM samples are cells that may be cultured directly on glass coverslips. We use 25 mm round coverslips (Warner Scientific) and place them in a round coverslip holder (ASI, I-3033-25D). The holder and coverslip may be placed inside an insert (ASI, I-3033) that can be secured on the automated stage.

3.1.6 Detection Optics and Camera

For optimal single-molecule localization, the pixel size of the detector must properly sample the point-spread function [16]. Given the pixel sizes of most cameras, this usually implies additional magnification besides the magnification provided by the objective lens. With a 60× objective, we use the 1.6× internal magnifier housed within the microscope frame and a 1.2× external lens, thus providing a total magnification of 115.2 between sample and camera.

We currently employ a back-thinned EM-CCD (Andor, DU-888E-C00-#BV, *see* **Note 5**) with 13 μm pixels, for a final imaging pixel size of 113 nm.

3.2 3D PALM

With relatively few additional components, the microscope described above can be converted to a 3D PALM system capable of sub-100 nm resolution in all three dimensions. Major additional requirements include a water-immersion objective better suited for 3D samples, minimization and compensation of drift during the acquisition period, cylindrical optics for converting a molecule's axial position into a PSF shape change, and data processing software capable of processing the raw data into a list of 3D coordinates and rendering the coordinates into a PALM image.

3.2.1 Water-Immersion Objective

For 3D samples that are immersed in aqueous buffer and that are more than a few 100 nm thick, water-immersion objectives are better suited for PALM than the oil objectives used in TIRF. This is for several reasons: (a) the refractive index of most cellular samples is between 1.33 and 1.38; thus, an objective with greater NA does not realize its full resolution potential or collection efficiency. (b) Spherical aberration (due to refractive index mismatch between the oil immersion media and the aqueous sample) causes an oil objective's performance to degrade at increasing depths from the coverslip. The resulting broadening of the PSF (especially axially) spreads the available signal out, decreasing the signal-to-noise ratio (SNR) per pixel in the raw images. This is especially problematic when localizing dim PA-FPs, where signal is precious and a significant decrease lowers the localization precision or renders the molecule undetectable. At the macroscopic level, the "focal shift" introduced by the refractive index mismatch introduces undesirable axial image distortion. Such deleterious effects may be partially compensated for by adding index-matching reagents to the sample (e.g., glycerol) or by scaling the axial localizations by the ratio of refractive indices [17]. We find it simpler to use a water-immersion objective (Olympus America, UPLSAPO60XW), matching the refractive index of our fixed cellular samples (*see* **Note 6**) and avoiding these effects while simultaneously maintaining a relatively high NA (1.2) (*see* **Note 7**). This objective also has good infrared transmission, important for activating PA-FPs with 800 nm light (Subheading 3.3).

3.2.2 Piezoelectric z Stage and Axial Drift Reduction

To assemble a "z stack" or collection of imaging planes that span a 3D sample, it is necessary to move the sample relative to the imaging plane. We use an automated XY stage with an additional z piezo upgrade that permits 100 μm axial displacement of the sample (Applied Scientific Instrumentation, PZ-2000). This replaces the 2D stage in Subheading 3.1.

Drift during single-molecule imaging is a serious problem and must be reduced and/or removed before the final images are rendered. Although it is possible to track fiducial markers (Subheading 3.2.6) to remove the drift after acquisition, the drift during the experiment (especially in z) is sometimes so bad that real-time drift cancellation is needed. "Focus-lock" systems [17] that use a reflection (e.g., from an infrared laser beam) from the coverslip/buffer interface to feedback directly to the piezoelectric stage or objective are likely the best approach, as drift is measured at or near the sample plane. Most major microscope manufacturers and several smaller companies provide these drift-canceling systems as "add-ons" to commercially available microscope frames. Unfortunately, the magnitude of the reflection feedback signal diminishes greatly when refractive index mismatches are minimized (as happens when using a water-immersion objective), so we opt instead for a system that corrects objective drift only (Mad City Labs, C-Focus). This feedback system consists of a piezoelectric collar that houses the objective and contains a glass scale grating and a sensing arm containing a laser and detector. If the reading from the grating changes in response to axial drift, the piezoelectric collar shifts the objective to compensate.

One drawback of the C-Focus is that it requires both the objective and the sample stage to be raised to accommodate the piezoelectric collar. Although the manufacturer includes spacers for this purpose, we find that the additional circumference of the piezoelectric collar precludes easy use of other objectives in the Olympus filter turret. Rotating the focus-lock housing away from the imaging position in the turret causes it to smash into the turret base. Other objectives may be screwed into the piezoelectric collar to inspect the sample at other magnifications, but this process is somewhat tedious. Nevertheless, we find that we can reduce axial drift to <200 nm over a 15-min period (Fig. 3) using this system, long enough for PALM imaging a single plane in a z stack.

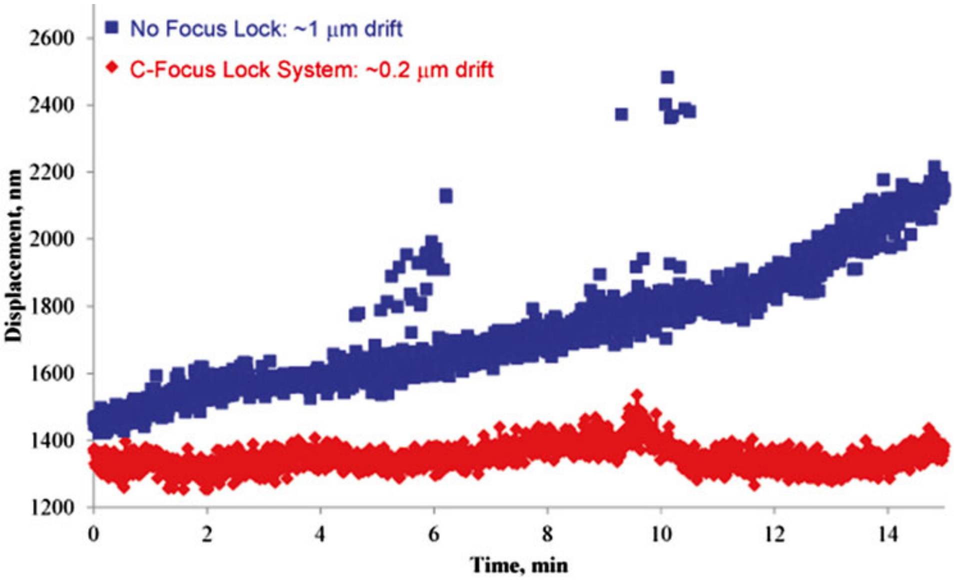

Fig. 3 Performance of commercial focus-lock system in reducing axial drift. A 100 nm gold fiducial marker stuck on a glass coverslip was localized repeatedly over a 15-min period. *Blue curve* indicates native axial drift; *red curve* demonstrates significant reduction in axial drift when the Mad City Labs C-Focus module is used

3.2.3 Astigmatic Imaging for 3D Subdiffractive Localization

A variety of methods can be used to reshape the PSF of a subdiffractive particle in order to estimate both axial and lateral position. Such techniques include biplane imaging (introducing defocus into the emission path and collecting two images located at offset *z* planes, thus providing extra shape information that aids in axial localization) [18], generation of a helical PSF (converting axial position into angular position of a "dumbbell" PSF, usually by placing a spatial light modulator or phase mask in the emission path) [19], and astigmatic imaging (using a cylindrical lens to force rays in vertical and horizontal directions to focus at different axial planes, thus generating a PSF whose ellipticity varies with axial position) [20].

Regardless of the specific implementation, a feature common to all of these methods is that the detected signal in each PSF image is spread out over more camera pixels than in the ideal 2D Airy function. This fact has two consequences: (a) the signal-to-noise per pixel is reduced, reducing localization precision relative to 2D PALM, particularly for dim PA-FPs; and (b) extra care must be taken with the photoactivation laser, to ensure that too many single molecules are not simultaneously activated as their images are larger and thus more likely to overlap.

For dim PA-FPs, the first consequence suggests that maximizing detection efficiency is critical in achieving acceptable SNR and 3D localization precision for PA-FPs. As cylindrical or astigmatic imaging introduces only one additional optical element, minimizing light loss in the emission path, and because it is easy to implement, we chose to adopt this method for 3D localization.

When deciding on the placement of the cylindrical lens in the emission path, we considered first placing it beneath the filter cube, in the accessible space where the DIC analyzer usually sits. Unfortunately, we found cylindrical lenses with focal length <1 m (conveniently available from Thorlabs) placed in this location introduced far too much astigmatism in the PSF, thus spreading out the available signal too much and rendering such PSFs unusable for single-molecule localization (*see* **Note 8**). Instead, we place the cylindrical lens directly after the 1.2× expander external to the microscope and immediately before the EM-CCD (Fig. 4). We find it useful to install the cylindrical lens in a filter holder, permitting us to switch between cylindrical lenses of varying focal length and allowing us the option of operating the microscope with minimal or no astigmatic distortion (to maintain 2D PALM/TIRF operation). Smaller focal length cylindrical lenses introduce greater axial variation of the PSF, but more image distortion (Fig. 5). The correct pixel sizes to restore the image to the correct aspect ratio can be calculated by measuring the apparent shift of gold fiducial markers (*see* **Note 9**).

In order to maintain the proper distance between sample and camera, given the extra path introduced by the filter wheel and the adapters, we found it necessary to shave the filter wheel down to the proper thickness. This thickness is best determined empirically, by adjusting the camera position until the image of a thin fluorescent layer is in focus (*see* **Note 10**). In our system, the total distance between the external surface of the camera and the left edge of the expander is 32 mm, but this distance may vary depending on the exact optics used. Fine adjustments of the axial distance between the filter wheel assembly and left microscope side port may be made by mounting the entire assembly on a translation stage (Fig. 4). In this case, we place a mechanical post beneath the final resting position of the 1.2× expander unit, for mechanical stability (*see* **Note 11**).

3.2.4 Cross-Correlation Code for 3D Subdiffractive Localization

When using the water-immersion objective, we found it very sensitive to tilt of the coverslip (Fig. 6). This feature has been previously documented [21] and usually introduces aberrations into the PSF that make it hard to model theoretically. Naively fitting a 2D elliptical Gaussian function to the molecular images in Fig. 6 can result in a localization error of hundreds of nanometers. We find it difficult to completely remove this aberration by adjusting the tilt of our coverslip holder, and every time we perform an experiment with a different coverslip, the observed PSFs differ slightly (presumably in response to different degrees of sample tilt). Furthermore, most localization code that relies on experimentally fitting a model function to a PSF also attempts to account for background levels and noise. Experimental noise is difficult to model accurately and background subtraction is complicated in

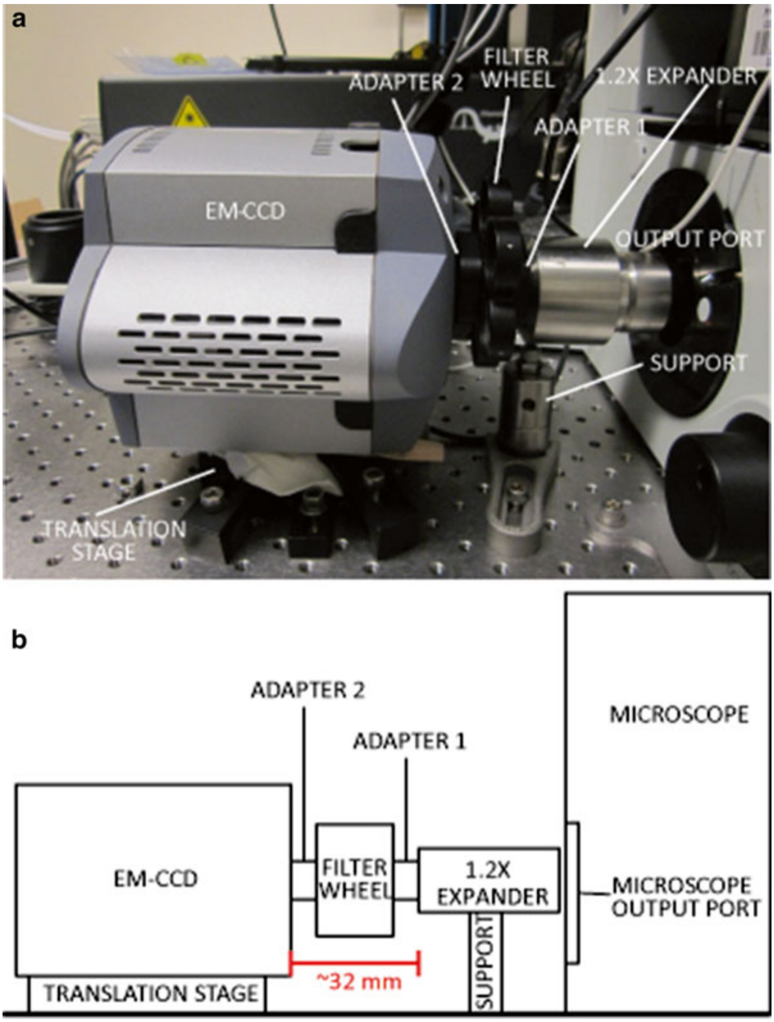

Fig. 4 Optomechanics for coupling cylindrical lenses to emission path of microscope. (**a**) Photograph and (**b**) accompanying schematic. Adapter 1 has external SM1 threads and internal C-mount threads and connects the 1.2× expander to the filter wheel that holds the cylindrical lenses. Adapter 2 is made up of two parts that mate together, one that has external C-mount threads and internal SM1 threads (for connecting the camera) and a second with external SM1 threads (for connecting the filter wheel). We find it useful to position a small support beneath the 1.2× expander to provide mechanical stability. A translation stage is used to position the imaging plane in an optimal position with respect to the excitation (see discussion in Subheadings 3.2.3 and 3.3.5)

thick, 3D samples where out-of-focus fluorescence varies spatially and temporally during acquisition.

For these reasons, rather than using a model PSF that imperfectly reflects reality, we prefer to directly measure the PSF with a 100 nm gold fiducial and perform a cross-correlation between the

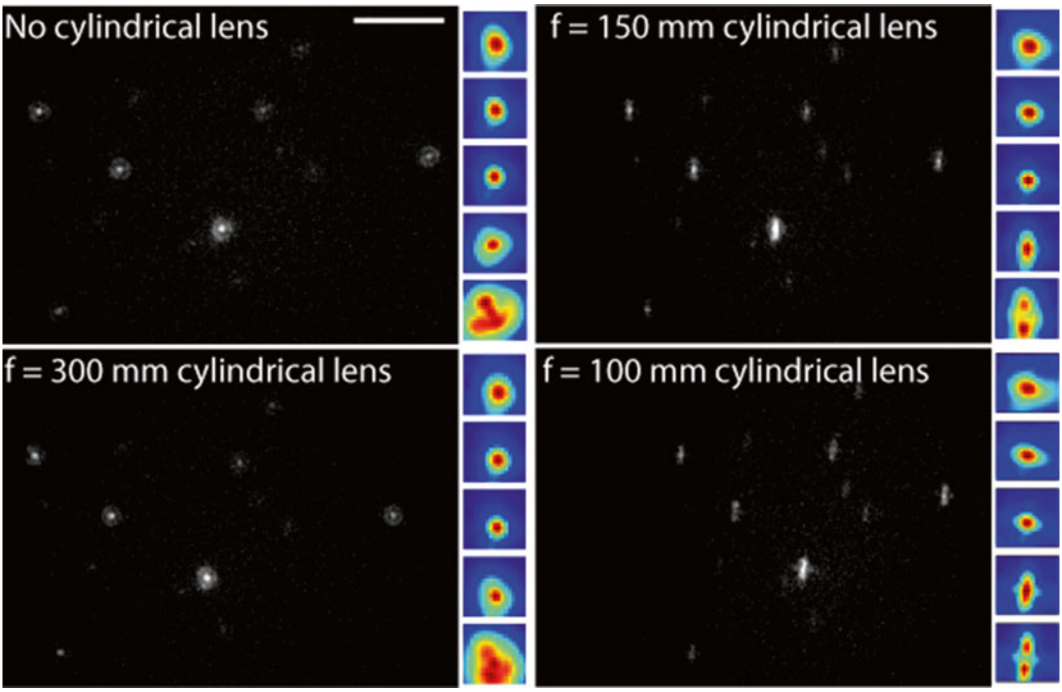

Fig. 5 Effect of cylindrical lenses with different focal length on imaging field and PSF. The same field ($z = 1$ μm above the coverslip surface) was imaged conventionally and with 300, 150, and 100 mm focal length cylindrical lenses. Selected slices (−2, −1, 0, 1, and 2 μm from the coverslip surface) from PSFs measured on the same gold bead are also displayed next to each imaging condition. Shorter focal lengths introduce greater distortion of the imaging field (particularly in horizontal direction) but introduce more astigmatic character in the PSF. Scale bar in *top left image*: 5 μm

experimentally measured PSF and the raw single-molecule images to localize each molecule's *xyz* position. This functionality is accomplished using our open-source software program, "palm3d.py," which: (a) crops and smoothes the raw measured PSF data into a calibration stack, (b) identifies candidate molecules from the raw PALM data, (c) localizes the candidates via cross-correlation with the calibration stack, (d) links localizations into molecules and then re-localizes linked localizations (this step is optional), and (e) bins localizations into a 3D histogram. More information about "palm3d.py" and a step-by-step user tutorial can be found at: http://code.google.com/p/palm3d/. Other useful programs referenced in the text and notes may be obtained at http://code.google.com/p/palm3d/source/browse/#hg%2Ftest.

3.2.5 Control of Data Acquisition

The majority of our hardware is controlled manually during data acquisition. However, our drift correction method requires frequent adjustment of the piezoelectric z stage, so we automate this step. We initially used MicroManager to simultaneously control our camera and sample positioning stage but found that MicroManager

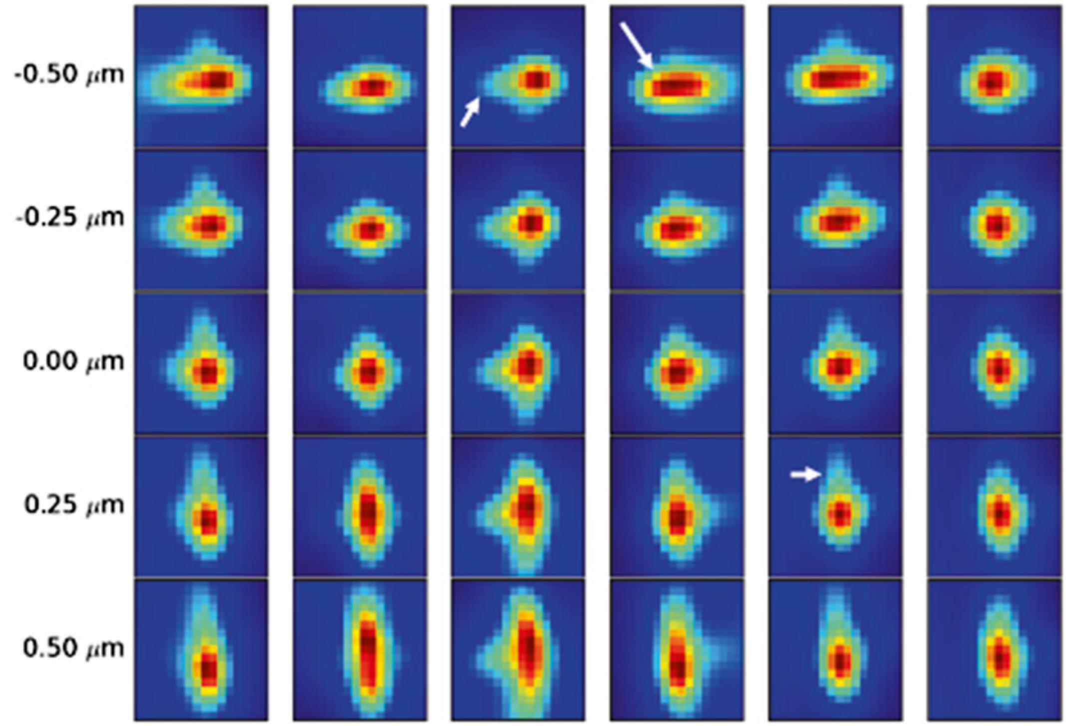

Fig. 6 Images of 100 nm gold fiducial markers at indicated *z* position, taken on different coverslips with different tilt and thickness. *Arrows* indicate features that cannot be easily accounted for with a theoretical PSF, such as "wings" in horizontal or vertical directions or an asymmetric intensity distribution in the center of the PSF. Reproduced from York 2011, supplementary material with permission from Nature Methods

could not operate the Andor EM-CCD at top speed without crashing occasionally. Since whole-cell PALM can take hours, crashes are unacceptable, and we now use the Andor software (Andor SOLIS for Imaging) that comes with the EM-CCD. Andor's software does not crash during acquisition but presents several serious annoyances. First, the Andor software is "deaf" and cannot be controlled by an external program. Next, it saves in a proprietary, undocumented ".sif" format, which inefficiently uses 32-bit floating-point numbers, even though the camera outputs unsigned 16-bit data. Andor's software can convert the ".sif" format to other formats for processing and viewing, but the batch conversion is buggy and frequently crashes. The Andor software has extremely limited scripting capability and cannot write to a USB serial port, so it cannot directly control our axial positioner. However, the Andor scripting language can issue DOS commands, which is its saving grace. We use this functionality to launch scripts written in Python, which lets us overcome the Andor software's annoyances. During acquisition, one such Python script writes data to the USB serial port to move our piezoelectric z stage ("piezo.py"). After each acquisition, Andor's software launches another Python script to convert Andor's ".sif" files to raw binary (*see* **Note 12**, "process_palm.py"). Finally, after acquiring calibration images, the Andor software launches a Python program to process the calibration images into a smoothed, cropped estimate of the microscope's point-spread function. We save image data directly to our network-attached storage device (Amazon.com, Netgear ReadyNAS), so the operator can process each dataset as soon as it is acquired without interrupting data acquisition.

3.2.6 Sample Data Acquisition Procedure

1. *Alignment*: It is a good idea to check the alignment of activation and excitation lasers before data acquisition, especially if the temperature fluctuates. We use a quantum dot sample (*see* **Note 10**) for alignment, as it fluoresces over a broad excitation wavelength range. After alignment, we set a region of interest (ROI) using camera software. We take care to cover only the illuminated area covered by coaligned activation and excitation beams (we typically use a ~40 μm × 40 μm area, 350 by 350 pixels).
2. *Fiducials*: We minimize axial drift during our potentially long acquisition periods by using a commercial focus-lock system (Subheading 3.2.2, Mad City Labs, C-Focus). To correct for residual drift, we add 100 nm gold particles (Microspheres-Nanospheres, 790122-010) as fiducials (bright particles that do not bleach) to the sample and track their *xyz* displacement over data acquisition.

   We typically add ~0.2–1 mL of 1× fiducials to our samples and then wait 15–20 min for them to settle. This process should be monitored on the microscope as we have found variability in the "stickiness" of different batches of fiducials and in the same batch over time, which could affect the necessary time or volume to be added. Once a typical field of view has about 1–3 fiducials, the sample is washed with 1× PBS to remove fiducials that have not settled.
3. *Calibration*: Calibration is the final step that must be performed before data acquisition commences. During calibration, a z stack (PSF) is taken of a single fiducial, which is later used during data processing to localize each PA-FP. Calibration should be performed for each sample, as the PSF changes slightly each time a new sample is loaded onto the microscope. We take the z stack from −2 μm to 2 μm (0 μm is the "best focus" position) in 50 nm steps with ten images taken at each z position (later averaging these frames to increase SNR), and repeat this process once to check if thermal drift occurred (a sample calibration program, "calibration.pgm," is available online).

   After the z stack is taken, the user selects and crops the fiducial out from the entire field of view. This is a crucial step, and the cropped area should be big enough to include the entire fiducial with the fiducial centered in the cropped area. We find it useful to compute the axial cross-correlation function of the fiducial and display it for the user ("process_palm.py"). Large positive areas in the cross-correlation plot indicate the shape change of the fiducial does not depend strongly on z. This is a problem because the calibration data is used during data processing to determine the *z* coordinate of each molecule, and if many different *z* positions look similar, it is difficult to perform a precise *z* localization (Fig. 7).

4. *Data acquisition*: Once an acceptable calibration has been taken, the user may start acquiring data. An ideal imaging field includes (a) 1–3 fiducials (*see* **Note 13**), (b) photoactivatable molecules (this can be quickly checked by turning the activation laser on and off and observing the effect on the level of blinking molecules), and (c) low background (i.e., there should only be blinking where your sample is and not on the coverslip itself). After finding a good field of view, the user should focus on the fiducial (if there are multiple fiducials in the field of view, select the best one as the primary fiducial and focus on it each time) and turn on the focus-lock system. The "track_fid.pgm" program (available online) can then be used for data acquisition.

   With thick samples, often the fiducial and the imaging plane are at different *z* positions, resulting in a dim and out-of-focus fiducial at the desired *z* position. The "track_fid.pgm" program addresses this potential issue via jumping between the imaging plane and plane of best fiducial focus. Two hundred images are taken at the desired plane (slice images), then 20 images are taken at the *z* position of the fiducial (tracking images), and this process is repeated a total of 50 times. The program treats the fiducial's *z* position as "$z = 0$" and allows the user to determine the *z* position to image at by modifying the "slicePosition = 0 // ×100 nm" line in the code. During each acquisition round, a total of 11,000 frames are taken, divided amongst slice and tracking images. After completing one acquisition round, the entire process can be repeated at either the same plane or a different plane until all the photoactivable molecules have been bleached. Imaging the same plane multiple times can help add additional detail to that plane, while imaging many different planes (especially when using the cylindrical lens) is advantageous for 3D imaging.

3.3 Two-Photon Photoactivation of PA-FPs for 3D PALM

Close to the coverslip surface (within a few μm), the methods in Subheading 3.2 enable 3D super-resolution imaging with <50 nm lateral and <100 nm axial resolution, if bright and high-contrast photoactivable proteins are used and a sufficiently high density of localizations are extracted during PALM. Further from the coverslip and for thicker samples, astigmatic imaging becomes increasingly

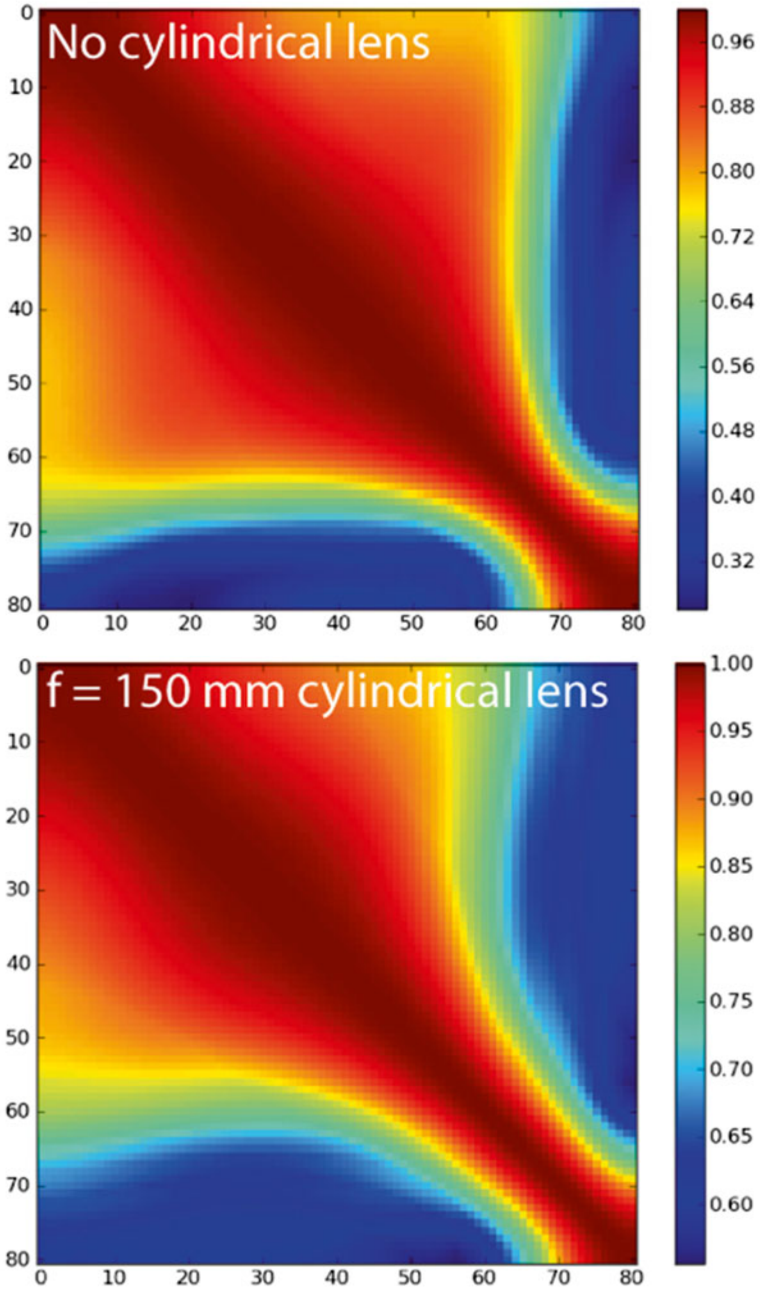

Fig. 7 Example cross-correlation plots. Comparing the maximum cross-correlation between each slice of the calibration stack (Subheading 3.2.6) is useful in judging the suitability of the imaging conditions for 3D PALM. With no cylindrical lens (*top*), most axial slices of the fiducial marker resemble each other, resulting in large areas of high cross-correlation. This results in a PSF that will confuse the cross-correlation localization algorithm and cause poor axial localization. With an *f* = 150 mm cylindrical lens (*bottom*), the usable axial localization range is extended as there are fewer regions of high cross-correlation

difficult for PA-FPs. The main reason for this is that the wide-field illumination employed in Subheading 3.2 activates and excites out-of-focus molecules, increasing background and overwhelming the fluorescence from dim PA-FPs. If an out-of-focus molecule is not detected and localized, it is wasted, decreasing the effective label density and reducing image resolution.

Methods that confine photoactivation to the focal plane, such as two-photon microscopy [22], alleviate such out-of-focus background. As PALM images the entire field at once, the ideal implementation of two-photon activation (2PA) would create a plane of activation at the focal plane. Temporal focusing microscopy [23] achieves such a planar illumination geometry by scanning an intense line focus across the sample on a picosecond timescale. We originally implemented 2PA with temporal focusing in conjunction with the green PA-FP Dronpa, confining activation to ~±1 μm of focus and enabling PALM imaging with lateral localization precisions of ~50 nm in single planes throughout whole cells. More recently, we implemented an improved, line-scanning version of temporal focusing [24] that further confines activation to ~±0.5 μm of focus [14]. When combined with the better PA-FP pa-mCherry1, this implementation enables 3D imaging of whole fixed cells at depths up to 8 μm (Fig. 8 and [14]). We describe how to add such functionality to the microscope described in Subheading 3.2 here.

3.3.1 Femtosecond Laser Choice

A multiphoton laser system suitable for line-scanning temporal focus, 2PA of PA-FPs, must satisfy the following requirements: (a) sufficient average power to drive photoactivation, ideally several watts at 800 nm for maximal photoactivation of pa-mCherry1; and (b) ability to generate pulses of 100–200 fs duration, providing enough dispersion for temporal focusing but not so much dispersion that the pulse broadens unacceptably before reaching the sample. We use the Chameleon Ultra II (Coherent) laser as it satisfies both criteria and is additionally a turnkey system that is easy to use. We note that this laser system is quite expensive (~$150,000). Cheaper alternatives are available that provide similar pulses and repetition rates but are not tunable. Tunability is not essential, as our experience with Dronpa and pa-mCherry1 suggests that wavelengths near 800 nm are suitable for 2PA of these PA-FPs. The optical setup (Fig. 9a) covered in the following description is optimized for the Ultra II; general considerations that may help in the selection of other laser sources are covered in [14] Supplementary Note 1.

3.3.2 Power Control

As the average power delivered by the laser system may be as high as 4 W, we use polarization optics to control power instead of neutral density filters. As the light from the laser is polarized, we place a half-wave plate (Newport, 10RP52-2) in a motorized rotation mount (Thorlabs, PRM1Z8E) and follow it with a polarizer

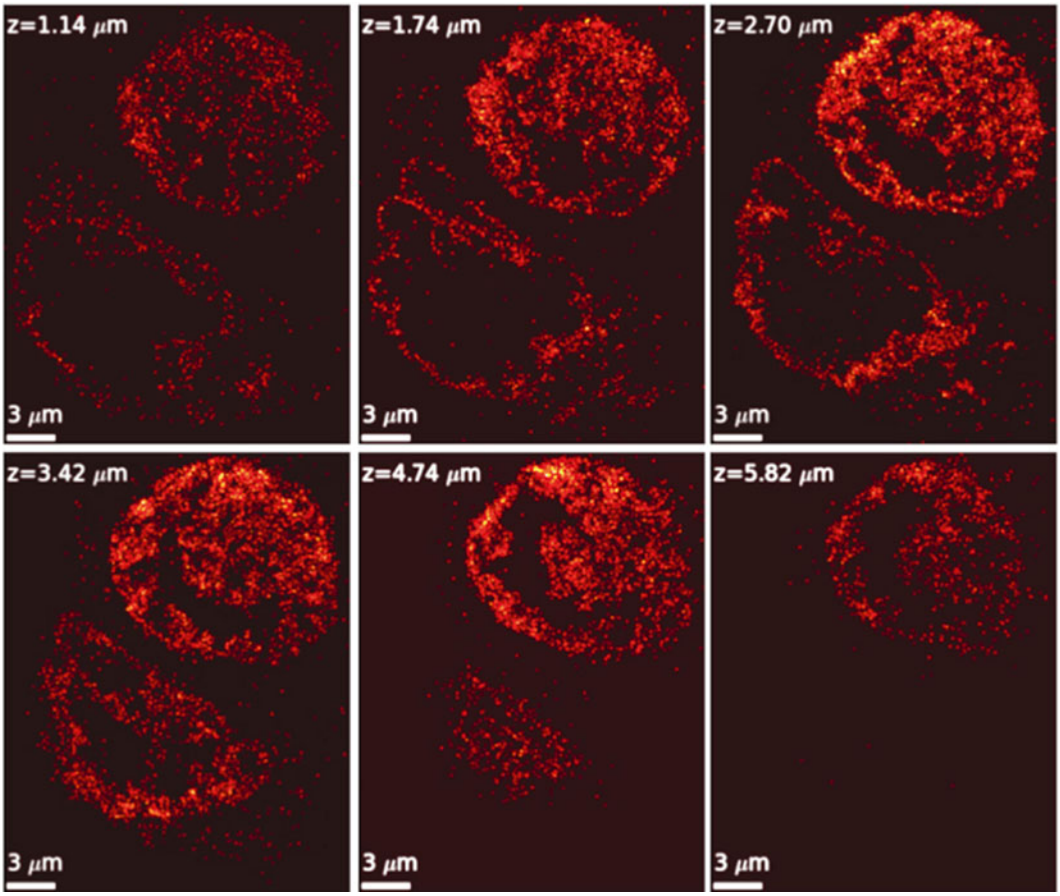

Fig. 8 Example of 3D PALM. Selected slices from a volumetric 3D PALM dataset of pa-mCherry1 lamin fusion proteins at indicated position above the coverslip surface highlighting two nuclei in fixed Cos7 cells. The sample was photoactivated with 2P line-scanning temporal focus as described in Subheading 3.3, resulting in a high volumetric localization density. *XYZ* pixel sizes are 60 × 60 × 60 nm; Gaussian smoothing of 1 pixel was applied to the data. Sections of the nuclear membrane are resolved to better than 100 nm

(Newport, 10GL08AR.16) and beam dump (PL15) (Fig. 9b). During the experiment, we control the degree of photoactivation by controlling the rotation of the half-wave plate from our acquisition computer.

3.3.3 Optical System for Achieving Line-Scanning Temporal Focus

Line-scanning temporal focusing offers the sectioning quality of point-scanning two-photon microscopy but the increased scan speed of line-scanning two-photon microscopy by combining spatial focusing and temporal focusing in orthogonal directions. The temporal focus scans an intense point from left to right on a picosecond timescale (by illuminating the diffraction grating with a line focus), and a galvanometric mirror scans this illuminated line up-down on a millisecond timescale to cover the full imaging field. The task for the user thus involves focusing the 2P excitation into

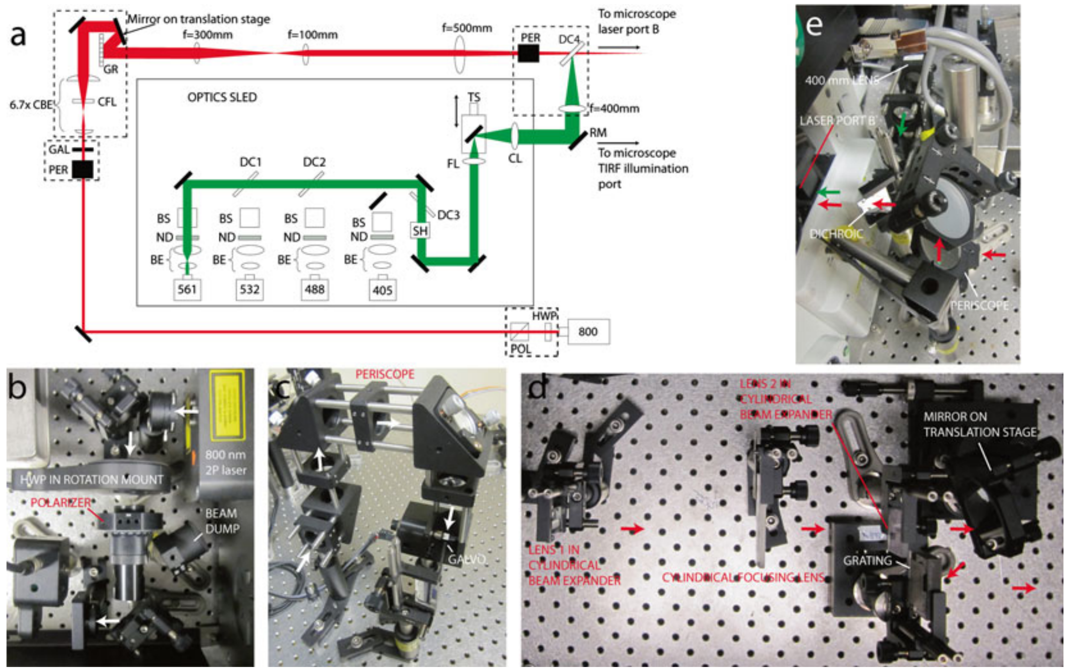

Fig. 9 Optical setup for 2PA of PA-FPs. (**a**) Optical schematic, including 1P optical sled (Fig. 1b), 2P optics, and coupling optics. Symbol key is as in Fig. 1b, with the following additions: *HWP* half-wave plate, *POL* polarizer, *PER* periscope assembly, *GAL* galvanometric scan mirror, *CFL* cylindrical focusing lens, *CBE* cylindrical beam expander, *GR* grating, *RM* removable mirror. *Dashed boxes* indicate setup components further detailed in photographs (**b**)–(**e**). (**b**) 2P power control. (**c**) Periscope assembly that directs beam onto scanning mirror. (**d**) Cylindrical optics and diffraction grating. (**e**) Periscope and coupling optics that direct 2P and 1P illumination into laser port B. In (**b**)–(**e**), *arrows* indicate direction of illumination through the setup. Panel (**a**) is modified from York 2011, supplementary Fig. 1 with permission from Nature Methods

a line focus onto the grating, and imaging the surface of the grating onto the sample plane. After directing the beam onto a galvanometric scanner (Cambridge Technology, 6215HB), we place a 200 mm focal length cylindrical lens (Thorlabs, LJ1653L2-B) 200 mm from the galvo and focus the excitation into a line shape on a diffraction grating (Newport, 53107BK02-035R) placed 200 mm from the cylindrical lens. The galvo is oriented so that the scan direction is parallel to the grooves on the grating; this necessitates a mounting scheme that directs the beam onto the galvo from above. We achieve this by periscoping the beam up and directing it downwards onto the galvo (Fig. 9c). We direct the beam onto the grating face at 41.6° incidence angle (Fig. 9d), chosen so that the first diffracted order at 800 nm emerges normal to the grating face. In the intermediate space between galvo, cylindrical lens, and grating, we place a cylindrical lens beam expander, thus expanding the beam 6.7× in the direction perpendicular to the grating grooves (this cylindrical lens expander is thus oriented so that it expands the beam in a direction perpendicular to the focusing cylindrical lens).

To achieve near-diffraction-limited sectioning, it is important to demagnify the image of the grating enough so that the back focal plane is overfilled [14]. We achieve this condition by using a demagnification of 500× between grating and sample. Given the 3 mm focal length of our objective lens, a single $f = 1{,}500$ mm lens after the grating would accomplish this job but would require a total of $\sim 2 \times (1{,}500 + 3) \approx 3$ m path length on our optical table. A more space-efficient solution is to break up the demagnification with two telescopes: a 3:1 demagnification followed by a 167× demagnification (Fig. 9a).

3.3.4 Injection of 2P Illumination into Microscope and Combination with Visible Illumination

We find it easiest to couple 2P illumination into the optical system by using the Olympus laser port B addition to the filter cube turret. Using this accessory requires: (a) periscoping the 2P illumination beam to the height of laser port B, (b) combination with 1P excitation light from the excitation sled (Fig. 9e), and (c) appropriate optics housed within the microscope body.

We periscope the scanned temporal focus activation beam with the aid of 2″ mirrors (Femtolasers, OA022 and OA248) attached to a pillar post (Thorlabs, RS4P, RS6, RS1) with appropriate optomechanics (Thorlabs, KS2, RM1C). To couple the visible laser output from the excitation sled into laser port B, while maintaining the possibility of TIRF excitation, we place a removable mirror in front of the TIRF port. With the removable mirror in place, visible light is reflected into laser port B with a dichroic mirror (Semrock, Di01-R561-25x36) designed to reflect wavelengths <561 nm but transmit the 800 nm illumination emerging from the periscope. We place a 400 mm lens (Edmund Optics, NT49-369-INK) in the visible path before the dichroic, thus focusing the visible light to the objective back focal plane and enabling wide-field excitation. Finally, we place a custom dichroic mirror (Chroma, ZT405/488/561/IR-RPC) that reflects 405, 488, 561, and 700–1,100 nm illumination while transmitting the intermediate wavelengths into a side-mounted filter cube (Olympus, IX2-MFB-SP-R) placed in the filter turret. We also place a shortpass emission filter (Semrock, FF01-680/SP-25) into this cube, thus blocking transmitted infrared light from reaching the camera. As this filter does not leave room for the emission filter typically used for PA-mCherry1 (Semrock, FF01-617/73-25), we instead place it in an empty DIC filter holder and place it beneath the filter turret.

3.3.5 Alignment of 2P Excitation Optics and Matching Plane of Temporal Focus to the Imaging Plane

If the temporal focus optics are correctly aligned, it should be possible to obtain near-diffraction-limited two-photon illumination, or a thin sheet of illumination ~1 μm in thickness. We measure the performance of the temporal focusing by scanning a thin quantum dot layer (*see* **Note 10**) axially through the fixed illumination path. An example of optimal performance is shown in Fig. 10. An apparent thickness >1.5 μm (using the 60×, 1.2 NA water-immersion

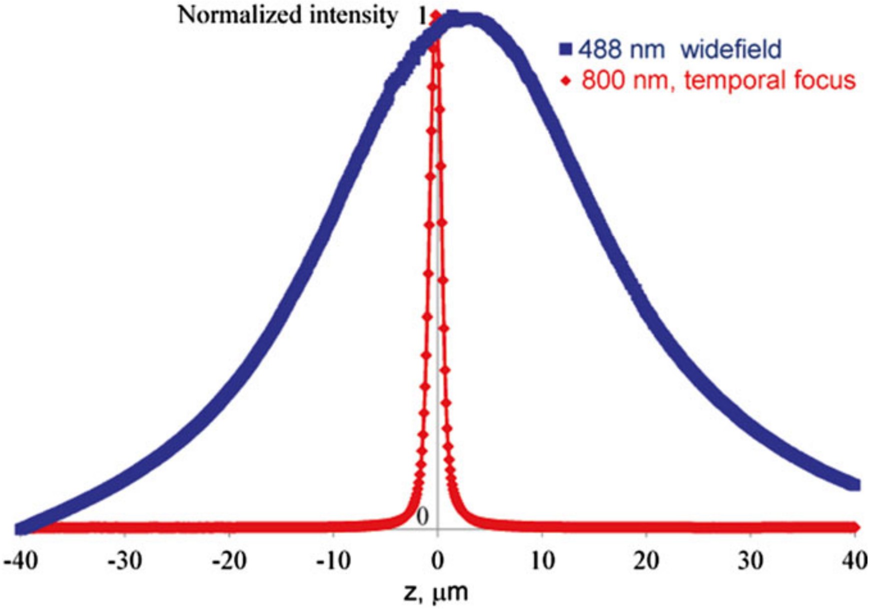

Fig. 10 Temporal focus optical sectioning. An 800 nm thick quantum dot layer was scanned in 100 nm axial steps through a line-scanning temporal focus illumination and the fluorescence recorded at each step. The normalized, integrated fluorescence at each frame is shown. Note the greatly reduced axial FWHM of 2P, line-scanning temporal focus illumination (~1.3 µm) relative to wide-field, 488 nm illumination

objective) indicates either a problem with optical alignment or a thicker than ideal test sample.

Achieving optimal temporal focus sectioning is contingent on proper alignment, yet how to achieve optimal alignment is not obvious. We find it useful to work backwards from the microscope, by following these steps:

1. Starting with the objective and dichroic in the Olympus microscope, we set a reference beam. This beam must be well collimated, since it will be used to set the axial position of several lenses in the system. We collimate our beam by adjusting a beam expansion telescope and measure its collimation by deflecting it off the optical table with a mirror. If the beam is made to travel several meters before hitting a wall, we can tell accurately if it's expanding or contracting. The beam diameter should be reasonably large (at least a centimeter), ideally with an adjustable iris to allow easy changing of the beam diameter. The back reflection of the reference beam from the objective should be very well aligned with the reference beam, indicating normal incidence on the back focal plane of the objective. Note that any back reflection which makes its way back into the femtosecond laser source will cause instability and prevent mode-locking, so we align just poorly enough to prevent this.

With the objective removed, the reference beam should propagate in the same direction the objective points. We find it helpful to use a plumb line to mark a spot on the ceiling directly above the objective (assuming the objective is mounted vertically) and ensure that the center of the beam falls on this spot with/without the objective lens.

2. With a reference beam set, the next lens (working backwards from the objective, this is the $f = 500$ mm lens in Fig. 9a) can now be aligned. The axial position of the lens is correct when the combination of the lens and the objective produces a nearly collimated beam, i.e., the diameter of the beam on the ceiling mark is minimized (position the objective's z position near its operating position while making this alignment). The transverse position of the lens is correct when it does not deflect the reference beam; the reference beam should hit the same spot on the ceiling that it does with this lens and the objective removed. The tilt of this lens is correct when the back reflection from this lens points back along the reference beam. The curved surface of the lens is normally placed towards a collimated beam. Note that with temporally focused beams, it can be confusing whether or not a beam is "collimated" or converging/diverging. In this case, note that the beam in the sample is "temporally focused," which at any given instant is equivalent to a point focus. Therefore, we can regard the beam between the $f = 500$ mm lens and the objective as collimated and place the curved side of the $f = 500$ mm lens facing this direction. With this lens in place, we can remove the objective and check if the reference beam still hits the reference mark on the ceiling. If it doesn't, this means the beam was not well centered on the objective. Reset the reference beam, and repeat the alignment of this first lens.
3. Two more lenses ($f = 100$ mm and $f = 300$ mm in Fig. 9a) are now added by the same procedure: back reflection, non-deflection, and preserving collimation (*see* **Note 14**).
4. Next we align our diffraction grating. Since some alignment processes are easier without the grating, we use a magnetic mount (Thorlabs, KB3X3) that allows us to switch the grating for a flat mirror. Since different wavelengths of light diffract off the grating at different angles, we deliver light to the grating with a mirror on a linear translation stage (Fig. 9a, d) very close to the grating to allow adjustment when we tune our femtosecond laser to different wavelengths. In practice, however, we almost always use this laser at 800 nm. To position the grating axially, we find it is sufficient to measure the distance from the grating to the next lens ($f = 300$ mm in Fig. 9a) with a ruler, placing it one focal length away. To position the grating transversely, we center it on the reference beam before

redirecting the reference beam to the mirror on the linear translation stage. We then set a new reference beam, roughly parallel to the old one but displaced to the side, bouncing off the mirror on the linear translation stage towards the grating. We tune the input angle of the grating by moving the linear translation stage and rotating the mirror mounted on it. We choose the input angle so that the first-order diffraction of the grating hits the next lens ($f = 300$ mm in Fig. 9a) directly on center. We choose the tilt angle of the grating such that the output beam is normal to the grating face (*see* **Note 15**).

5. With the grating positioned, we next place a cylindrical lens one focal length away from the grating, centered on the reference beam (CFL in Fig. 9a). This lens produces a horizontal line focus on the grating. Since the beam does not impact the grating at normal incidence, the line is only truly in focus at one point on the grating. However, the axial demagnification of the lens system between the grating and the sample is quite large (250,000×), so the effects of this defocus are negligible in the sample. As with previous lens alignment, the vertical position can be set by non-deflection, and the tilt can be set by back reflection. The horizontal position of this lens is unimportant, as long as it doesn't clip the beam.
6. Next we place a cylindrical beam expander in the reference beam (6.7× CBE in Fig. 9a). The axial position of this expander is not critical, but the relative axial positions of the two cylindrical lenses in the expander are quite important. As before, non-deflection, back reflection, and collimation tests are used to insert these lenses in the reference beam. We make sure to position this expander close enough to the diffraction grating that enough room is left for the galvanometric mirror.
7. Positioning the galvanometric mirror may be the most difficult step in the process. We measure one focal length from the cylindrical focusing lens (in the direction away from the microscope, towards the reference beam) and place a reference object at this point, centered on the reference beam. We typically use a small-diameter Allen key attached to the end of an optical post. The location of this reference object is used to determine where the galvanometric mirror should be positioned. Once the reference object is set, we place the galvanometric mirror with its periscope assembly in its final position and send a new reference beam through the optical system. Even with a good reference object, finely aligning the galvanometric mirror is challenging, since the entire assembly must be moved to rotate the galvanometric mirror about a vertical axis, but this motion disrupts the reference beam passing through the galvo. We iterate, adjusting the rotation and resetting the reference beam several times.

8. With two-photon illumination optics aligned, we check the depth at which the two-photon beam reaches maximum intensity. We use a thin layer of quantum dots for this measurement (*see* **Note 10**) and illuminate the quantum dot sample with 800 nm light while viewing its fluorescence on the EM-CCD. The layer has bumps and features that inform us when the camera emission path is focused on the quantum dots, and the fluorescent brightness of this informs us when the illumination path is focused on the quantum dots. Hopefully, these two depths match closely. If not, we move the camera axially using the attached linear translation stage (Thorlabs, DT25) to align the camera's focus with the illumination's focus.

For 3D PALM, the best localization precision is often obtained for molecules which are moderately out of focus. To bias activation towards slightly out-of-focus molecules, we translate the camera axially a small degree. The optimal level of defocus can be estimated by imaging a sample of gold fiducials, with a cylindrical lens in the imaging path. We start with the camera initially axially coaligned with the illumination then switch to a gold fiducial sample. We focus on the gold fiducials such that they appear maximally round and then axially translate the camera until they appear slightly elliptical.

3.3.6 Data Acquisition

Taking data follows the same scheme as Subheading 3.2.6, but with a few differences. During acquisition, we photoactivate the sample using 2PA illumination by scanning the galvanometric mirror at 500 Hz. As this speed is much higher than our acquisition rate (usually 10–13 Hz), we drive the galvo with the aid of a function generator (Stanford Research Instruments, DS340), finding it unnecessary to synchronize scanning with camera exposure. During acquisition we modify the 2P illumination power by rotating the half-wave plate placed in the automated rotation mount, as appropriate for the desired degree of photoactivation.

4 Notes

1. Localization precision (how well the center of each PSF can be determined) and the density of available photoswitchable molecules are two factors that determine the resolution of PALM. In the case of negligible background, the error in the PSF center determination is inversely proportional to the square root of the number of collected photons [16]. Thus, a photoactivatable tag that emits 100-fold more photons than another would give a 10-fold increase in localization precision. Although a high number of collected photons are desirable

from a localization standpoint, in practice other factors (errors in the localization estimate, drift correction, background due other fluorescent tags present at high density, or autofluorescence of the sample) limit the localization precision to ~10 nm for the majority of photoactivatable molecules.

The other key determinant of resolution is the density of molecules. According to the Nyquist-Shannon sampling theorem, the sampling interval (mean distance between neighboring localized molecules) must be at least twice as fine as the desired resolution; otherwise, the feature of interest will be undersampled and unresolved. As an example, to achieve 10 nm resolution in two dimensions, molecules must be spaced 5 nm apart in each dimension, for a minimum density of 4×10^4 molecules/μm^2 or ~2,000 molecules in a diffraction-limited region 250 nm in diameter. Achieving a high density of localizations in practice is dependent not only on the labeling strategy (PA-FPs vs. exogenous photoswitchable dyes) but also on the contrast ratio (ratio in fluorescence intensity between the inactive and active state of the photoswitchable molecule). If the contrast ratio is less than the density of the probe in a given diffraction-limited region, the weak intensity from the inactive molecules will overwhelm the intensity from a single activated molecule, confounding both localization and the interrogation of densely labeled samples.

2. We find an overhead shelf system (e.g., Newport, ATS-10) useful for mounting laser (and other) power supplies in a space-efficient manner near the optical table.
3. The laser sled's axial position may be adjusted with appropriate "feet" and spacers from Thorlabs (BLP01, PF175, PS1, PS2, PS3, PS4).
4. We sometimes find it useful to place an additional bandpass filter (or laser-line blocking filter) into the emission path in order to provide more rejection of the excitation light. A particularly useful component for this is an extra analyzer holder (used in DIC) without the polarizer. This part is available from the manufacturer and provides a convenient space for additional 25 mm diameter optics.
5. An electron-multiplying charge-coupled device (EM-CCD) camera is still the detector of choice for most single-molecule imaging studies, due to its high quantum efficiency, moderate frame rate, and negligible read noise. We note that EM-CCDs may soon be surpassed by cheaper and faster scientific complementary-symmetry metal-oxide-semiconductor detectors, especially as their quantum efficiency improves.
6. We typically fix samples in a 2–4 % paraformaldehyde/1× PBS (or similar buffer) solution for 15 min, rinsing 3× in 1× PBS before imaging in 1× PBS. A complete protocol is available in ref. 15.

We note that fixing in this way and imaging with a water-immersion objective obviates the need for Mowiol or other oil-based mounting schemes and minimizes perturbations to the sample.

7. Silicone oil objectives may provide a higher NA (1.3) while still minimizing refractive index mismatch, but we have not tested their suitability for PALM.

8. We note that Rocky Mountain Instruments manufactures cylindrical lenses with up to 10 m focal length.

9. In order to construct a histogram of the processed PALM data, the user must know the nanometers per *x* and *y* pixel ("nm_per_x/y_pixel" in the palm3d processing code, code.google.com/p/palm3d). These values are determined by the magnification of the microscope, the camera's pixel size, and whether and what focal length cylindrical lens is used. An easy way to determine these quantities is by using the "xy_grid.pgm" and "xy_stage.py" programs (http://code.google.com/p/palm3d/source/browse/#hg%2Ftest). These programs record images of a single fiducial marker at its initial position and after defined stage movements in *x* and *y*. Creating a maximum projection of all the generated images in ImageJ results in a 5-by-5 grid with 3 μm spacing between the fiducial location at each node in the grid. The number of pixels between each location in each dimension can then be determined, and dividing the 3,000 nm step size by this value will give the "nm_per_x/y_pixel" to be used for that lens. Before using "xy_grid.pgm," we set the "kinetic series length" in our camera software to 1, so that only one image is taken at each xy position. Using a field of view with only one fiducial is best, since the presence of additional fiducials will result in a confusing maximum projection with multiple 5-by-5 grids overlapping each other.

10. A good alignment sample is essential for checking the overlap of excitation and activation lasers, as well as measuring the thickness of the 2P temporal focus activation plane. We find a particularly good choice is a thin (<1 μm) layer of quantum dot nanoparticles, spin coated on a glass coverslip. The quantum dots are bright and photostable, fluoresce over a broad spectral region, and last months if prepared properly.

    The quantum dots we start with are bare, i.e., do not have a polymer shell encapsulating them (Q dots; Ocean NanoTech, QSO-520-0010). For this reason, they are hydrophobic (shipped in toluene) and must be embedded in a polymer resin before attachment to a glass coverslip. We prepare a dilution of 4 % (weight by volume) solution of Elvax 410 ethylene-vinyl acetate copolymer resin (DuPont) in toluene by overnight heating on a hotplate. Care must be taken to ensure that the polymer does not bubble, by keeping the temperature stable at or below 40 °C.

We next dilute this solution to 1 % by diluting in a 1:1.5:1.5 4 % Elvax 410/quantum dots/toluene ratio. This solution is stable for ~1 month, if stored in a capped glass vial with a good seal (capping is necessary as the toluene is volatile; glass is important as it is inert and will not be dissolved by toluene). The 1 % Elvax/Q dot solution is spin coated onto a cleaned 25 mm diameter glass coverslip. We use model # WS-650S-8NPP-LITE (Laurell Technologies Corporation) and ramp the speed from 0 to 500 r.p.m. over 7 s then maintain 500 r.p.m. for 40 s. Other spin coaters work too, and the proper settings may require repeated trials to get a thin layer repeatedly. We find it useful to verify the thickness of the layer with atomic force microscopy, as <1 μm thickness is preferable for measurement of the thickness of the temporal focus layer. Once made, we store the samples in the dark at room temperature.

11. When taking data, we drape black fabric around the entire assembly, thus minimizing external light leakage into the camera.
12. The main functions of "process_palm.py" are: (a) Conversion of the ".sif" images generated by Andor into ".dat" images (a much easier to use format). Once we realized the ".sif" format appears to consist of a header, followed by numerical data stored as floating-point 32-bit numbers, reverse engineering consisted of learning how to read the header to determine where the numerical data would start and stop within the file. Different versions of the Andor software use slightly different headers, however, so use caution if attempting to reuse our conversion code. (b) Taking the user through cropping and then smoothing the calibration fiducial before generating the cross-correlation plot (*see* Subheading 3.2.6).
13. Sometimes trash on the coverslip can be mistaken as fiducials; it is useful to inspect the putative fiducial for a few minutes to verify it does not bleach before using it.
14. When there is an even number of lenses (including the objective), this process works very well. When there is an odd number of lenses, the output of the objective diverges rapidly and deflection is very hard to judge. In this case, unscrew the objective during alignment, and restore it when it's time to add the next lens.
15. Pay attention to the blaze of the grating; there are two orientations of the grating which will work, but one will be substantially more efficient at reflecting the first-order diffracted beam.

Acknowledgments

This research was supported by the Intramural Research Program of the NIH, including the National Institute of Biomedical Imaging and Bioengineering.

References

1. Hell SW (2007) Far-field optical nanoscopy. Science 316:1153–1158
2. Betzig E, Patterson GH, Sougrat R et al (2006) Imaging intracellular fluorescent proteins at nanometer resolution. Science 313:1642–1645
3. Rust MJ, Bates M, Zhuang X (2006) Sub-diffraction-limit imaging by stochastic optical reconstruction microscopy (STORM). Nat Methods 3:793–796
4. Hess ST, Girirajan TPK, Mason MD (2006) Ultra-high resolution imaging by fluorescence photoactivation localization microscopy. Biophys J 91:4258–4272
5. Lukyanov KA, Chudakov DM, Lukyanov S et al (2005) Photoactivatable fluorescent proteins. Nat Rev Mol Cell Biol 6:885–890
6. Chen I, Ting AY (2005) Site-specific labeling of proteins with small molecules in live cells. Curr Opin Biotechnol 16:35–40
7. Patterson GH (2011) Highlights of the optical highlighter fluorescent proteins. J Microsc 243:1–7
8. Chang H, Zhang M, Ji W et al (2012) A unique series of reversibly switchable fluorescent proteins with beneficial properties for various applications. Proc Natl Acad Sci U S A 109: 4455–4460
9. Dempsey GT, Vaughan JC, Chen KH et al (2011) Evaluation of fluorophores for optimal performance in localization-based super-resolution imaging. Nat Methods 8:1027–1036
10. Shroff H, Galbraith CG, Galbraith JA et al (2007) Dual-color superresolution imaging of genetically expressed probes within individual adhesion complexes. Proc Natl Acad Sci U S A 104:20308–20313
11. Axelrod D (2001) Total internal reflection fluorescence microscopy in cell biology. Traffic 2:764–774
12. Manley S, Gillette JM, Patterson GH et al (2008) High-density mapping of single-molecule trajectories with photoactivated localization microscopy. Nat Methods 5:155–157
13. Shroff H, Galbraith CG, Galbraith JA et al (2008) Live-cell photoactivated localization microscopy of nanoscale adhesion dynamics. Nat Methods 5:417–423
14. York AG, Ghitani A, Vaziri A et al (2011) Confined activation and subdiffractive localization enables whole-cell PALM with genetically expressed probes. Nat Methods 8:327–333
15. Shroff H., White H., Betzig E. (2008) Photoactivated localization microscopy (PALM) of adhesion complexes. Curr Protoc Cell Biol 41, 4.21.21–24.21.27
16. Thompson RE, Larson DR, Webb WW (2002) Precise nanometer localization analysis for individual fluorescent probes. Biophys J 82: 2775–2783
17. Huang B, Jones SA, Brandenburg B et al (2008) Whole-cell 3D STORM reveals interactions between cellular structures with nanometer-scale resolution. Nat Methods 5: 1047–1052
18. Juette MF, Gould TJ, Lessard MD et al (2008) Three-dimensional sub-100 nm resolution fluorescence microscopy of thick samples. Nat Methods 5:527–529
19. Pavani SRP, Thompson MA, Biteen JS et al (2009) Three-dimensional, single-molecule fluorescence imaging beyond the diffraction limit by using a double-helix point spread function. Proc Natl Acad Sci U S A 106:2995–2999
20. Huang B, Wang W, Bates M et al (2008) Three-dimensional super-resolution imaging by stochastic optical reconstruction microscopy. Science 319:810–813
21. Arimoto R, Murray JM (2004) A common aberration with water-immersion objective lenses. J Microsc 216:49–51
22. Denk W, Strickler JH, Webb WW (1990) Two-photon laser scanning fluorescence microscopy. Science 248:73–76
23. Oron D, Tal E, Silberberg Y (2005) Scanningless depth-resolved microscopy. Opt Express 13:1468–1476
24. Tal E, Oron D, Silberberg Y (2005) Improved depth resolution in video-rate line-scanning multiphoton microscopy using temporal focusing. Opt Lett 30:1686–1688

Chapter 14

Direct Stochastic Optical Reconstruction Microscopy (*d*STORM)

Ulrike Endesfelder and Mike Heilemann

Abstract

Single-molecule localization-based super-resolution microscopy can be performed with regular, bright, and photostable organic fluorophores. We review a concept termed *direct* stochastic optical reconstruction microscopy (*d*STORM), which operates conventional fluorophores as photoswitches and provides an optical resolution of ~20 nm. We introduce the principle of *d*STORM, illustrate experimental schemes, and discuss approaches for data analysis.

Key words Super-resolution fluorescence microscopy, *d*STORM, Single-molecule fluorescence imaging, Single-molecule localization, Photoswitching, Organic fluorophores, Cluster analysis

1 Introduction

Single-molecule based super-resolution techniques employ photoswitchable fluorophores, single-molecule localization, temporal separation, and image reconstruction and achieve an optical resolution of down to ~20 nm in the imaging plane [1–3]. Among the various techniques introduced, *direct* stochastic optical reconstruction microscopy (*d*STORM) [2, 4] operates conventional organic fluorophores as photoswitches by making use of their photophysical and photochemical transitions. *d*STORM imaging relies on three key points (Fig. 1): (1) the use of photoswitchable fluorophores, (2) stochastic activation and temporal separation of the fluorescence signal to separate single molecules in space and time, and (3) single-molecule localization with nanometer precision [2, 3]. *d*STORM imaging was demonstrated with multiple colors [5–7], in combination with photoactivatable fluorescent proteins [8] or chemical tags [9], for dynamics in vitro [10] as well as in live cells [11, 12], also extended to three-dimensional by optical [13] or physical [14] sectioning of thick tissue.

In a *d*STORM experiment, single fluorophores are stochastically activated and read out over time, and an image stack is recorded.

Peter J. Verveer (ed.), *Advanced Fluorescence Microscopy: Methods and Protocols*, Methods in Molecular Biology, vol. 1251, DOI 10.1007/978-1-4939-2080-8_14, © Springer Science+Business Media New York 2015

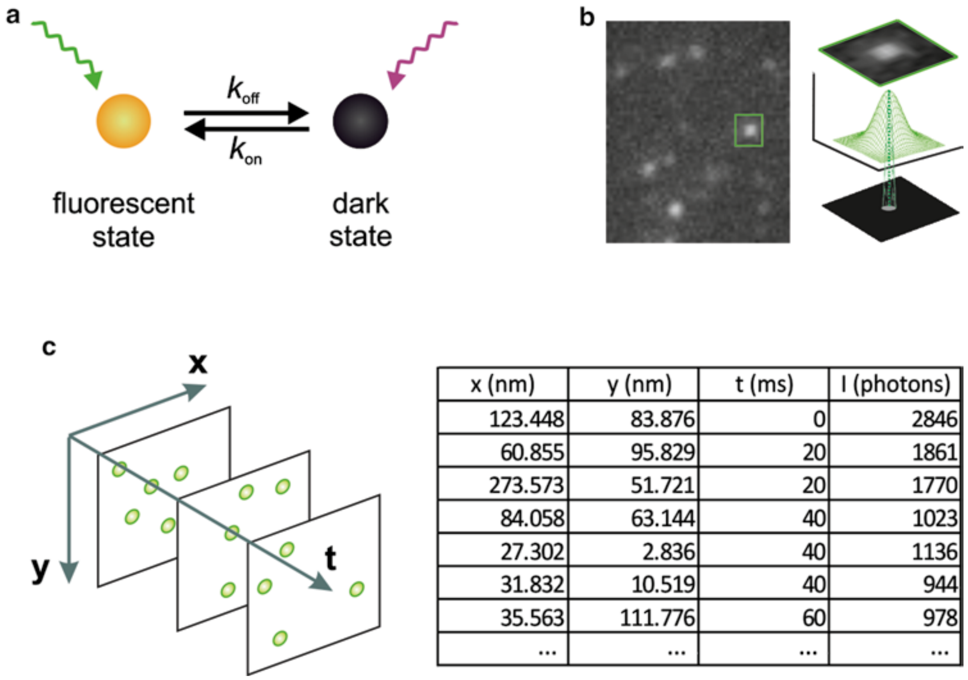

x (nm)	y (nm)	t (ms)	I (photons)
123.448	83.876	0	2846
60.855	95.829	20	1861
273.573	51.721	20	1770
84.058	63.144	40	1023
27.302	2.836	40	1136
31.832	10.519	40	944
35.563	111.776	60	978
...	...	...	...

Fig. 1 Principle of single-molecule super-resolution microscopy. (**a**) Photoswitchable fluorophores are transferred from a fluorescent bright state into a nonfluorescent dark state by the irradiation of light. (**b**) By activating only a sparse subset of fluorophores at a time, the position of single fluorophores can be determined by approximating their point-spread function. (**c**) A super-resolved image is reconstructed from single-molecule coordinates

In each single image of the stack, the fluorescence emission pattern (or point-spread function) of single molecules is approximated with a Gaussian function and provides information on the location of a fluorophore. From a large number of single-molecule coordinates, an artificial image can be reconstructed (exemplary *d*STORM images are shown in Fig. 2). As a result, *d*STORM and similar methods provide a list of single-molecule coordinates, which is in contrast to conventional microscopy techniques which provide intensity information directly. In addition to generating super-resolution images and resolving cellular structures, this technique allows developing analytical localization-based algorithms to extract single-molecule information.

2 Materials

*d*STORM utilizes conventional organic fluorophores for super-resolution fluorescence microscopy, which are "programmed" to become photoswitches in the presence of reducing agents. The main classes of common organic fluorophores that can be photoswitched are carbocyanines [2], rhodamines, and oxazines [15].

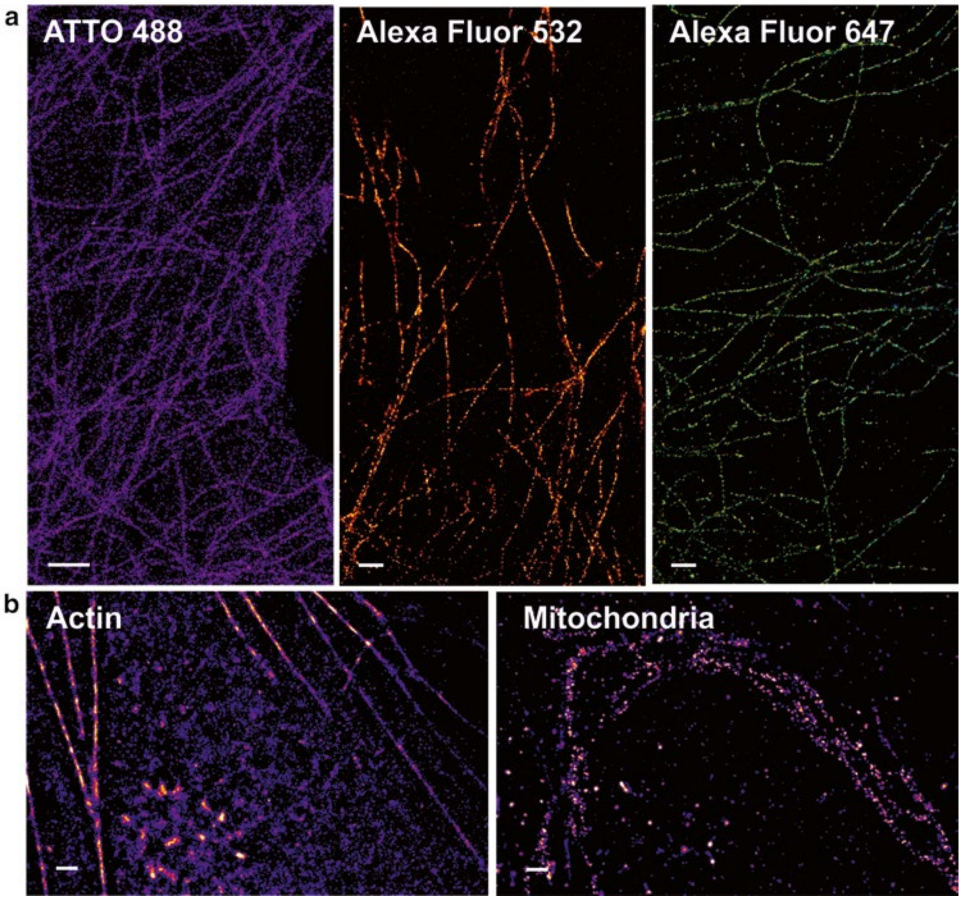

Fig. 2 *d*STORM images of cellular structures. (**a**) Exemplary *d*STORM images of microtubulin immunostained with different fluorophores. (**b**) Dual-color measurement of a cell stained for actin (EosFP) and mitochondria (Alexa Fluor 647). Scale bars represent 1 μm

3 Methods

Here we describe the basic approach for measuring dSTORM images in two dimensions in a static sample. It is possible to extend these methods for imaging dynamic samples, multiple colors, and three-dimensional structures (*see* **Notes 1–3**).

3.1 Labeling Strategy

Organic fluorophores are available as active esters and can be chemically conjugated to various functional groups found in biomolecules (e.g., $–NH_2$ or –SH). This strategy enables labeling of small receptor-binding peptides, antibodies and proteins, oligonucleotides (e.g., molecular beacons), or small specific drug molecules (e.g., the actin-binding peptide phalloidin) as well as other substrates.

The most common labeling strategies for cellular structures that are compatible with *d*STORM are:

1. Immunocytochemistry: two complementary antibodies are applied as sandwich system, with a primary antibody targeting a specific antigen and a secondary antibody (or $F(ab)_2$ fragment) carrying a fluorophore and targeting the first antibody.
2. Chemical tags: The introduction of a chemical tag like the TMP tag [16], the SNAP tag [17], the CLIP tag [18], and the Halo tag [19] represents a simple, live cell compatible method for target-specific labeling with organic fluorophores. The protein of interest is genetically fused to a marker protein, which then covalently or non-covalently binds to a fluorescent tag.
3. Click chemistry: The basic chemical reaction that underlies "click chemistry" is a Cu(I)-catalyzed cycloaddition of an azide and an alkyne to a triazole. This approach is very specific, as neither of the reactive groups is found in biological samples. Cells are treated with an azide or alkyne analogon (e.g., 5-ethynyl-2′-deoxyuridine (EdU) instead of thymidine for DNA labeling, or L-homopropargylglycine (HPG) or L-azidohomoalanine (AHA) for amino acid labeling), which is incorporated into biomolecules and subsequently labeled with a fluorophore carrying an alkyne or azide group [20, 21].

3.2 Photoswitching of Organic Fluorophores

Redox-induced photoswitching is best visualized and explained with a Jablonski diagram (Fig. 3). A fluorophore is first excited from the ground state (S_0) into a higher electronic state (S_1, S_2, …, S_N). After internal conversion and vibrational relaxation to the lowest excited state (S_1), spontaneous emission of a photon (fluorescence) brings the molecule back into the ground state S_0. Alternatively, a non-radiative transition into S_0 can occur, as well as intersystem crossing into the triplet state (T_1).

In the presence of reducing agents which match the redox potential of the fluorophores, an electron transfer can occur. In the presence of thiol group containing reducing agents, many fluorophores are reduced out of the triplet state and form stable radical anions [22]. This radical state represents the nonfluorescent OFF-state of the fluorophore, which was demonstrated to exhibit a thermal stability of many minutes to hours in aqueous solution [22]. Upon reaction with molecular oxygen or irradiation with UV light, the molecule returns to the ground state, and fluorescence is recovered. The radical anion of some fluorophores (e.g., ATTO 655) exhibits a high electron affinity and can be further reduced to the leuco-form of a fluorophore [23].

The rate for the transition from the fluorescent ON-state into the nonfluorescent OFF-state (k_{off}) is controlled by the concentration of the reducing thiol reagent and the irradiation intensity. The lifetime of the OFF-state and thus the rate of the transition into the

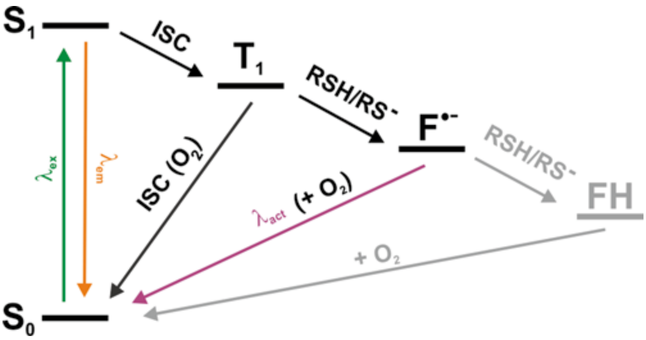

Fig. 3 Reversible photoswitching of organic fluorophores in the presence of reducing agents. Upon irradiation, the fluorophore is excited from its singlet ground state S_0 into higher electronic states. From the first excited state S_1, either fluorescence emission or intersystem crossing into the triplet state T_1 occurs. The long-lived triplet state can further react with molecular oxygen to recover the singlet ground state or react with reducing agents (such as thiols) to form a radical anion ($F^{\bullet-}$). The singlet ground state can be recovered by oxidization with oxygen or excitation of the radical with near-UV light. For some fluorophores (e.g., the oxazine fluorophore ATTO 655) were found to become fully reduced to the leuco-form (FH), which can also recover into ground state by reaction with oxygen

ON-state (k_{on}) depends on the thermal stability and the concentration of molecular oxygen. In addition, the OFF-state can be depopulated by irradiation with low-intensity near-UV light, which is in resonance with the absorption band of the radical anion of many fluorophores.

An important experimental parameter for high-quality *d*STORM super-resolution imaging is an appropriate ratio of the ON- and OFF-switching rates, $r = k_{\text{off}}/k_{\text{on}}$. The higher the fluorophore density, the higher must be the ratio r, to ensure that each fluorophore is recorded as a single molecule at a given time. This implies rates $k_{\text{off}} \gg k_{\text{on}}$ which guarantee sufficiently low spot densities per imaging frame as the active fraction of fluorophores is low compared to the total number [24].

3.3 Microscope Setup

Localization-based super-resolution microscopy is a technique operated on microscopy setups with wide-field illumination (Fig. 4).

1. Excitation pathway: a multiline laser (e.g., argon-krypton laser) or single laser sources (e.g., diodes or Ti:sapphire lasers) are filtered by an acousto-optic tunable filter to select for the appropriate excitation wavelength. The laser beam is then focused on the back focal aperture of the objective. A movable mirror enables to switch between wide-field illumination, total internal reflection (TIR) illumination, and highly inclined and laminated optical sheet (HILO) microscopy [25].

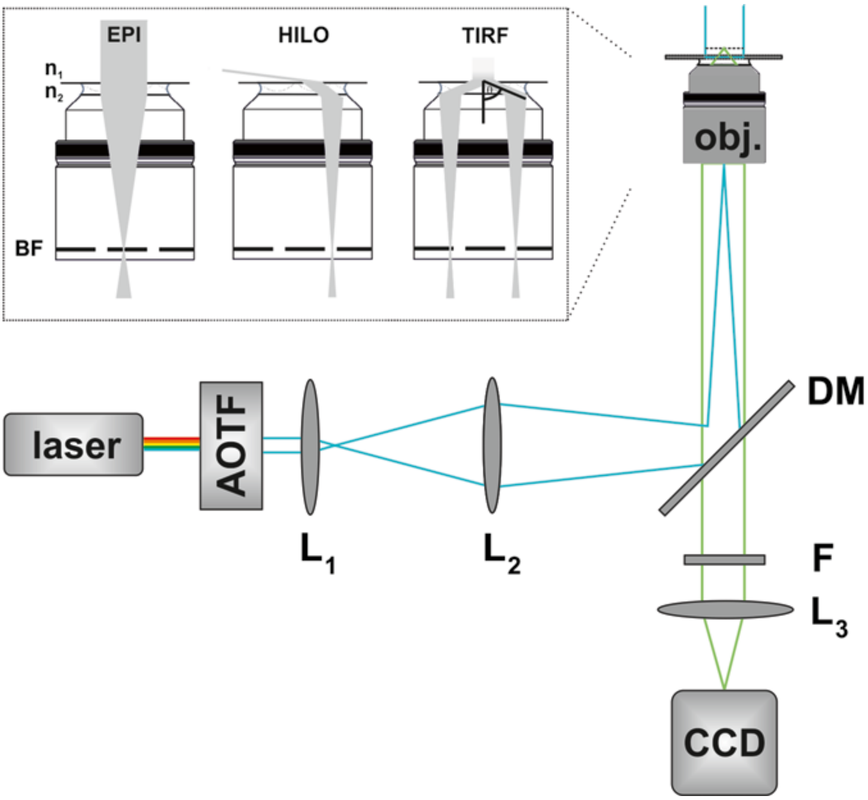

Fig. 4 Experimental setup for single-molecule super-resolution microscopy. An acousto-optical filter (AOTF) is used to select an excitation wavelength. The laser light is focused (e.g., by a telescope consisting of the lenses L1 and L2) onto the back focal (BF) plane of a high numerical aperture oil-immersion objective (OBJ). Excitation and emission light are separated by a dichroic mirror (DM). Fluorescence light is spectrally filtered by long-pass and/or bandpass filters (F) and projected (L3) on a camera. Additional lenses (not sketched) can be arranged in the detection path to adjust for a different pixel size

2. Microscope configuration: an inverted microscope is equipped with an oil-immersion objective suitable for total internal reflection fluorescence microscopy (TIRFM). Excitation and fluorescence light are separated using a dichroic mirror.
3. Detection pathway: the fluorescence light is directed onto a single-molecule sensitive electron-multiplying charge-coupled device (EMCCD) camera. Additional lenses may be introduced in the detection path to adjust for an optimal pixel size (70–160 nm) on the camera chip.

Examples for some commonly used fluorophores and appropriate filter sets are highlighted in Tables 1 and 2.

3.4 dSTORM Imaging

Typically, a stack of 4,000–20,000 images with a frame rate between 10 Hz and 2 kHz is recorded. The EMCCD camera should be operated in the most sensitive mode, applying sufficient cooling for

Table 1
Exemplary fluorophores suitable for *d*STORM

Fluorophore	Absorption/emission ($\lambda_{abs}/\lambda_{em}$)	Switching buffer
Alexa Fluor 488	491/517	100 mM MEA, pH 8
ATTO 488	501/523	100 mM MEA, pH 9
Alexa Fluor 532	532/552	100 mM MEA, pH 7.4–8
Alexa Fluor 568	572/600	100 mM MEA, pH 8–8.5
Alexa Fluor 647/Cy5	649/670	100 mM MEA, pH 7.4 (+oxygen scavenger system)
ATTO 655	663/684	10 mM MEA, pH 7.4–8

Table 2
Exemplary filter sets for single-color *d*STORM measurements

Dyes	Cleanup	Dichroic mirror	Detection filter set
ATTO 488 Alexa Fluor 488	Z488/10, Chroma	HC-Quad 410/504/582/669, Semrock	LP 488 RU RazorEdge, Semrock HC 550/88 Brightline, Semrock
ATTO 568 Alexa Fluor 568	Z568/10, Chroma	HC-Dual 560/659, Semrock	LP 568 RU RazorEdge, Semrock HQ 610/75, Chroma
Cy5 Alexa Fluor 647 ATTO 655	Z488/568/647 RPC, Chroma	HC-Dual 560/659, Semrock	LP 647 RU RazorEdge, Semrock ET 700/75, Chroma

reduced thermal background noise, the highest dynamical range settings, and the fastest readout option by, e.g., a frame transfer mode and optimal gain settings. To achieve an optimal signal-to-noise ratio, the frame rate should be adjusted with respect to the average time a fluorophore resides in the fluorescent ON-state, which is controlled by the applied irradiation intensity. The appropriate recording time is dependent on the target (e.g., abundance and dimensionality), the labeling density, and the switching properties of the dye. The spot density, controlled by the transition rates between fluorescent “ON”- and nonfluorescent “OFF”-states, has to be sufficiently low for robust single-molecule detection. Furthermore, all fluorophores should be detected at least once, in order to allow for a proper visualization of a structure.

3.4.1 Drift Control

Due to the separation of single fluorophores in time, it is necessary to acquire enough images in order to reconstruct a representative super-resolution image, such that a *d*STORM experiment typically lasts several minutes. As a consequence, localization-based super-resolution microscopy is very sensitive to drift occurring during the acquisition time. Small movements in the nanometer range can already introduce image artifacts and impact image quality and interpretation. Drift can be corrected for by adding photostable fluorescent beads as fiducial markers to the sample. Due to the stable and long-lasting fluorescence emission of the beads, the drift can be traced, and the individual frames of image stack can be realigned. Alternatively, image correlation can be used for drift correction, but requires a minimum of structural information.

3.5 Image Reconstruction

Single-molecule super-resolution methods such as *d*STORM provide coordinates of individual point-spread functions recorded from single fluorophores. For each frame, the subset of active fluorophores needs to be identified and fitted precisely and rapidly using the post-processing software.

Commonly, the point spread function (PSF) of a single fluorophore is approximated by a Gaussian function:

$$\mathrm{I}\left(x_c, y_c, A, B\right) = \frac{A}{2\pi\sigma_x\sigma_y}\exp\left(-\frac{\left(x-x_c\right)^2}{2\sigma_x{}^2}-\frac{\left(y-y_c\right)^2}{2\sigma_y{}^2}\right)+B$$

with σ_x and σ_y as standard deviations, (x_c, y_c) the coordinates of the center, and the amplitude A and the background signal B.

Single-molecule localization software, like the freely available rapidSTORM [24, 26] and QuickPALM [27]), are based on two consecutive main tasks performed for each frame of the imaging stack:

1. Spot identification: the PSF of single fluorophores is identified, e.g., by blurring and non-maximum suppression routines.
2. Spot fitting: for each identified single fluorophore, the optimal fit is computed and validated, e.g., by least-squares fitting. Subsequently, the parameters of the fit are evaluated, and those which are, e.g., below an intensity threshold or exhibit asymmetry are discarded.

3.5.1 Localization Accuracy

The accuracy of single-molecule localization primarily increases with the number of detected photons. It is also dependent on the pixel size, the shot noise of the camera, and the background signal originating from out-of-focus fluorescence and detector noise. Several formulas have been introduced to estimate the uncertainty of single-molecule localization [28–30]. For high signal-to-noise ratios, the contribution of background signal and pixilation is negligible, and the localization error ϵ can be estimated from

$$\varepsilon \sim \frac{\sigma_{\mathrm{PSF}}}{\sqrt{N}}$$

with σ_{PSF} being the standard deviation of the PSF and N the number of photons detected within the PSF. The localization accuracy can also be determined experimentally by measuring the standard deviation of multiple localizations of the same single fluorophore. Knowledge of the localization accuracy is necessary to understand the resolution that can be achieved (*see* **Notes 4** and **5**).

3.6 Image Representation

Different to other microscopic techniques, single-molecule localization-based super-resolution techniques provide no direct intensity information, but single-molecule coordinates. Various ways of reconstructing intensity-like images from single-molecule localization data have been introduced. The simplest approach is to map the single-molecule localizations in a scatter plot. This does not reflect intensities, and information is lost at higher localization densities. A more image-like representation is achieved by blurring each single-molecule localization with a Gaussian function with its width reflecting the localization accuracy. The blurred spots are summed up to an artificial image in which the intensity is proportional to the local density of single-molecule localizations. These images can be used for, e.g., image-based colocalization analysis. Another possibility is the binning of all single-molecule localizations into a 2D histogram. This generates a pixelated intensity image in which the intensity information per pixel reflects the number of events detected in this area. Furthermore, also more complex representation schemes were introduced [31].

3.7 Data Interpretation

In contrast to microscopy techniques which provide intensity images, single-molecule localization methods provide a list of single-molecule coordinates. On the basis of reconstructed images, all kinds of data analysis can be performed as if for conventional fluorescence microscopy. In addition, coordinate-based analysis for, e.g., clustering or colocalization, can be performed.

3.7.1 Cluster Analysis

The choice of an appropriate cluster algorithm depends on the individual data set and the specific question to be addressed. Different cluster algorithms are optimized for different tasks, such as the efficient identification of cluster numbers, shape, or separation. Single-molecule localization microscopy data provides single-molecule coordinates, such that cluster algorithms that operate with the Euclidean distance as basic parameter can be used. However, in single-molecule super-resolution imaging, a single fluorophore is often detected more than once, either in multiple adjacent imaging frames or with interruptions induced by blinking or reversible photoswitching. Single-molecule localizations at the same position in adjacent frames most likely do not correspond to two molecules, but to the same single fluorophore which was detected multiple times. These multiple localizations can be corrected for, which was demonstrated by either using correlation algorithms [32] or tracking algorithms [33, 34].

Cluster analysis can be performed by, e.g., calculating nearest neighbor distances of single-molecule localizations. As these distributions are measured by a single distance parameter, characteristic distances can be detected and compared to a random distribution of single-molecule localizations. Other algorithms consider all single-molecule positions, such as Ripley's K function [35].

3.7.2 Colocalization Analysis

The colocalization of two different fluorophores can be investigated using image-based spatial colocalization algorithms [36, 37]. In a similar way, these algorithms can be applied to reconstructed super-resolution images. However, the results depend on post-processing parameters chosen for the reconstruction of the artificial images, e.g., blurring or pixelation. On the other hand, colocalization analysis can be performed on the basis of single-molecule coordinates. This way, it is possible to provide a measure on how each localization of one species is surrounded by a second species, and heterogeneities and subpopulations can be revealed [38].

4 Notes

1. For following dynamic processes, the acquisition rate has to be sufficiently faster than the dynamics of the observed biological process (Fig. 5a). Dynamic processes can be visualized using a sliding window algorithm [10], or heterogeneous dynamics of small unresolved assemblies can be observed [11]. Most cells already contain glutathione (GSH), a tripeptide containing a thiol group, at millimolar concentrations, depending on the cellular environment [39]. This has been proven to be suited for *direct* photoswitching of some organic fluorophores like rhodamine or oxazine derivatives in living cells [11, 12].
2. Addressing biological questions often requires observing multiple targets at once, such that multicolor imaging is needed. In *d*STORM imaging, this translates to the need of (1) at least a dye pair with spectrally separated fluorescence emission, (2) similar switching properties, and (3) similar brightness. Various solutions for multicolor imaging were introduced [6–8]. Chromatic aberrations need to be corrected carefully, e.g., by using multicolor fiducial markers or by recording a reference sample (Fig. 5b). Live cell imaging is only practicable with simultaneous or alternating imaging schemes.

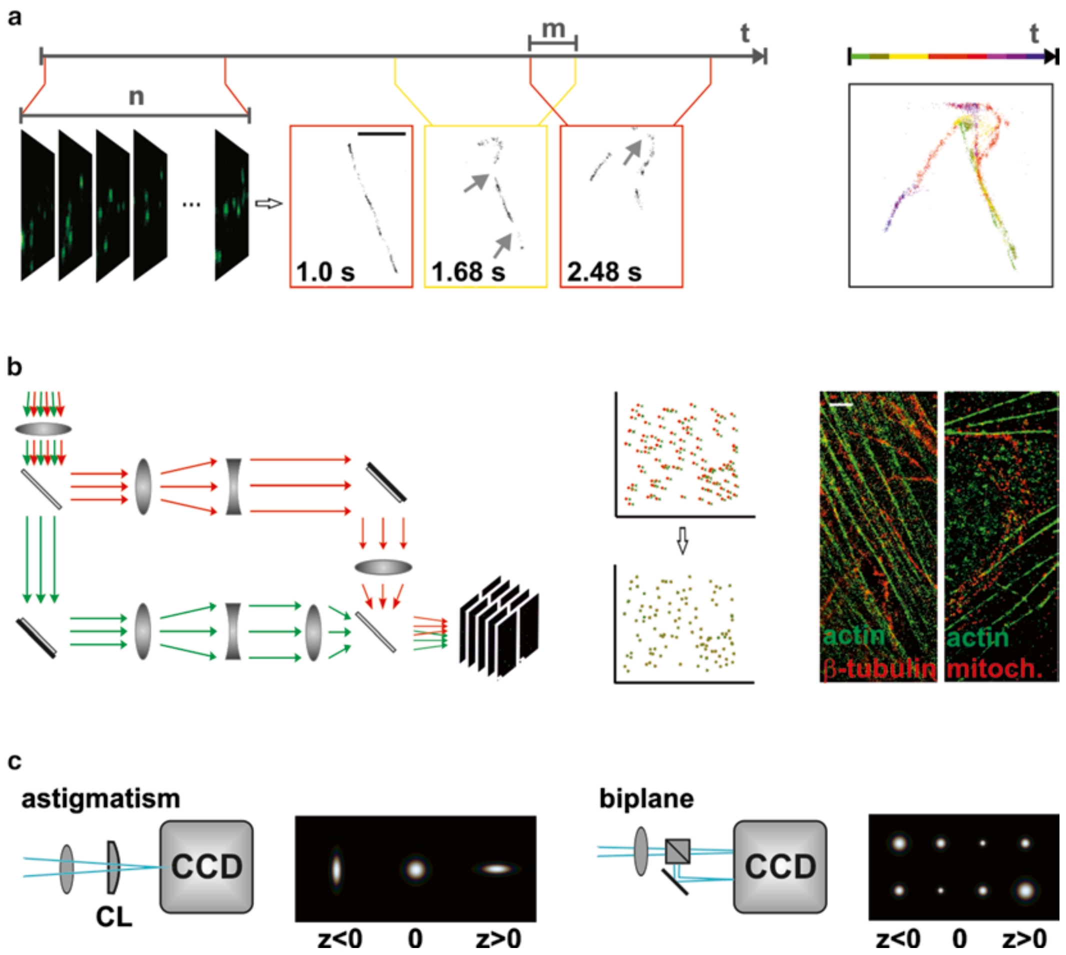

Fig. 5 Advanced imaging schemes. (**a**) Video-like *d*STORM data of dynamic samples can be obtained by applying a sliding window algorithm to an image stack. Here, the example of in vitro actin filaments gliding on a myosin surface is shown, each *d*STORM image reconstructed from 100 individual TIRF images (integration time 10 ms). A reconstructed image including all localizations color-coded for time projects the movement of the filaments (*right*). *Gray arrows* indicate the disruption of a filament, typically occurring for filaments subjected to strong curvature (scale bar 1 μm). (**b**) A possible detection pathway for two-color imaging with parallel data acquisition and one EMCCD camera. The two detection channels are separated using two identical dichroic mirrors. The two images are superimposed and corrected for aberration by a nonlinear local weighted mean matrix. Exemplary aligned dual-color images of cells stained for actin (*green*) and β-tubulin (*red*) or cytochrome c oxidase (*red*) were superimposed with an accuracy of below 10 nm (scale bar 2 μm). (**c**) Schematic view of two approaches for single-molecule localization in 3D by distortion of the single-molecule PSF. Astigmatic distortion by a cylindrical lens (CL) causes lengthening of the PSF in either the *x*- or *y*-plane (*left*). The biplane approach records images in two focal planes (*right*)

3. In its simplest experimental configuration, information on the axial position of a single fluorophore is not accessible, as a two-dimensional detector is used. However, the axial position can be determined by introducing a distortion into the PSF of single fluorophores (Fig. 5c), e.g., through astigmatism introduced by

a cylindrical lens [40], biplane imaging with two cameras at different focal planes [41], or the generation of a double-helical PSFs [42] using a spatial light modulator. Thick tissue samples can be imaged in 3D by applying physical or optical sectioning [14, 43].

4. The spatial resolution is the distance at which two objects can still be discerned as individual objects [44]. In single-molecule localization microscopy, the spatial resolution can be related to the localization accuracy and can be estimated by calculating the full width at half maximum $\left(\mathrm{FWHM} = 2\sqrt{2\ln 2}\times\varepsilon \approx 2.35\times\varepsilon\right)$ [45].
5. In fluorescence microscopy, the target is not directly observed itself, but the fluorescent label which is attached to a target. In order to resolve a structure, not only the spatial or optical resolution is important but also the labeling density which determines the structural resolution. This fact is addressed in the Shannon-Nyquist sampling theorem, which states that the sampling interval must be at least twice as small as the desired resolution [46]. Applied to single-molecule localization microscopy, a structural resolution of 20 nm thus requires that every 10 nm a fluorophore is localized.

Acknowledgments

The authors thank Marina Dietz, Franziska Fricke, and Bianca Nouvertné for providing super-resolution images. This work was supported by the Bundesministerium für Bildung und Forschung (FORSYS program, grant number 0315262).

References

1. Betzig E, Patterson GH, Sougrat R et al (2006) Imaging intracellular fluorescent proteins at nanometer resolution. Science 313:1642–1645
2. Heilemann M, van de Linde S, Schuttpelz M et al (2008) Subdiffraction-resolution fluorescence imaging with conventional fluorescent probes. Angew Chem Int Ed Engl 47:6172–6176
3. Rust MJ, Bates M, Zhuang X (2006) Sub-diffraction-limit imaging by stochastic optical reconstruction microscopy (STORM). Nat Methods 3:793–795
4. van de Linde S, Loschberger A, Klein T et al (2011) Direct stochastic optical reconstruction microscopy with standard fluorescent probes. Nat Protoc 6:991–1009
5. Bates M, Dempsey GT, Chen KH et al (2012) Multicolor super-resolution fluorescence imaging via multi-parameter fluorophore detection. ChemPhysChem 13:99–107
6. Lampe A, Haucke V, Sigrist SJ et al (2012) Multi-colour direct STORM with red emitting carbocyanines. Biol Cell 104:229–237
7. van de Linde S, Endesfelder U, Mukherjee A et al (2009) Multicolor photoswitching microscopy for subdiffraction-resolution fluorescence imaging. Photochem Photobiol Sci 8:465–469
8. Endesfelder U, Malkusch S, Flottmann B et al (2011) Chemically induced photoswitching of fluorescent probes – a general concept for super-resolution microscopy. Molecules 16: 3106–3118
9. Eckhardt M, Anders M, Muranyi W et al (2011) A SNAP-tagged derivative of HIV-1 – a versatile tool to study virus-cell interactions. PLoS One 6:e22007
10. Endesfelder U, van de Linde S, Wolter S et al (2010) Subdiffraction-resolution fluorescence microscopy of myosin-actin motility. ChemPhysChem 11:836–840

11. Wombacher R, Heidbreder M, van de Linde S et al (2010) Live-cell super-resolution imaging with trimethoprim conjugates. Nat Methods 7:717–719
12. van de Linde S, Heilemann M, Sauer M (2012) Live-cell super-resolution imaging with synthetic fluorophores. Annu Rev Phys Chem 63:519–540
13. Jones SA, Shim SH, He J et al (2011) Fast, three-dimensional super-resolution imaging of live cells. Nat Methods 8:499–508
14. Nanguneri S, Flottmann B, Horstmann H et al (2012) Three-dimensional, tomographic super-resolution fluorescence imaging of serially sectioned thick samples. PLoS One 7:e38098
15. Heilemann M, van de Linde S, Mukherjee A et al (2009) Super-resolution imaging with small organic fluorophores. Angew Chem Int Ed Engl 48:6903–6908
16. Miller LW, Cai Y, Sheetz MP et al (2005) *In vivo* protein labeling with trimethoprim conjugates: a flexible chemical tag. Nat Methods 2:255–257
17. Keppler A, Gendreizig S, Gronemeyer T et al (2003) A general method for the covalent labeling of fusion proteins with small molecules *in vivo*. Nat Biotechnol 21:86–89
18. Gautier A, Juillerat A, Heinis C et al (2008) An engineered protein tag for multiprotein labeling in living cells. Chem Biol 15:128–136
19. Los GV, Encell LP, McDougall MG et al (2008) HaloTag: a novel protein labeling technology for cell imaging and protein analysis. ACS Chem Biol 3:373–382
20. Salic A, Mitchison TJ (2008) A chemical method for fast and sensitive detection of DNA synthesis *in vivo*. Proc Natl Acad Sci U S A 105:2415–2420
21. Besanceney-Webler C, Jiang H, Zheng T et al (2011) Increasing the efficacy of bioorthogonal click reactions for bioconjugation: a comparative study. Angew Chem Int Ed Engl 50:8051–8056
22. van de Linde S, Krstic I, Prisner T et al (2011) Photoinduced formation of reversible dye radicals and their impact on super-resolution imaging. Photochem Photobiol Sci 10: 499–506
23. Kottke T, van de Linde S, Sauer M et al (2010) Identification of the product of photoswitching of an oxazine fluorophore using fourier transform infrared difference spectroscopy. J Phys Chem Lett 1:3156–3159
24. Wolter S, Endesfelder U, van de Linde S et al (2011) Measuring localization performance of super-resolution algorithms on very active samples. Opt Express 19:7020–7033
25. Tokunaga M, Imamoto N, Sakata-Sogawa K (2008) Highly inclined thin illumination enables clear single-molecule imaging in cells. Nat Methods 5:159–161
26. Wolter S, Sauer M (2012) Follow-up to paper by S. Wolter, M. Schuttpelz, M. Tscherepanow, S. van de Linde, M. Heilemann and M. Sauer, entitled Real-time computation of subdiffraction-resolution fluorescence images. J Microsc 245:109
27. Henriques R, Lelek M, Fornasiero EF et al (2010) QuickPALM: 3D real-time photoactivation nanoscopy image processing in ImageJ. Nat Methods 7:339–340
28. Thompson RE, Larson DR, Webb WW (2002) Precise nanometer localization analysis for individual fluorescent probes. Biophys J 82: 2775–2783
29. Mortensen KI, Churchman LS, Spudich JA et al (2010) Optimized localization analysis for single-molecule tracking and super-resolution microscopy. Nat Methods 7:377–381
30. Smith CS, Joseph N, Rieger B et al (2010) Fast, single-molecule localization that achieves theoretically minimum uncertainty. Nat Methods 7:373–375
31. Baddeley D, Cannell MB, Soeller C (2010) Visualization of localization microscopy data. Microsc Microanal 16:64–72
32. Veatch SL, Machta BB, Shelby SA et al (2012) Correlation functions quantify super-resolution images and estimate apparent clustering due to over-counting. PLoS One 7:e31457
33. Annibale P, Vanni S, Scarselli M et al (2011) Quantitative photo activated localization microscopy: unraveling the effects of photoblinking. PLoS One 6:e22678
34. Lando D, Endesfelder U, Berger H et al (2012) Quantitative single-molecule microscopy reveals that CENP-ACnp1 deposition occurs during G2 in fission yeast. Open Biol 2:120078
35. Ripley BD (1977) Modelling spatial patterns. J R Stat Soc B 39:172–212
36. Bolte S, Cordelieres FP (2006) A guided tour into subcellular colocalization analysis in light microscopy. J Microsc 224:213–232
37. Zinchuk V, Zinchuk O (2008) Quantitative colocalization analysis of confocal fluorescence microscopy images. Curr Protoc Cell Biol, Unit 4.19
38. Malkusch S, Endesfelder U, Mondry J et al (2012) Coordinate-based colocalization analysis of single-molecule localization microscopy data. Histochem Cell Biol 137:1–10
39. Jones DP (2010) Redox sensing: orthogonal control in cell cycle and apoptosis signalling. J Intern Med 268:432–448

40. Huang B, Jones SA, Brandenburg B et al (2008) Whole-cell 3D STORM reveals interactions between cellular structures with nanometer-scale resolution. Nat Methods 5:1047–1052
41. Juette MF, Gould TJ, Lessard MD et al (2008) Three-dimensional sub-100 nm resolution fluorescence microscopy of thick samples. Nat Methods 5:527–529
42. Pavani SR, Thompson MA, Biteen JS et al (2009) Three-dimensional, single-molecule fluorescence imaging beyond the diffraction limit by using a double-helix point spread function. Proc Natl Acad Sci U S A 106: 2995–2999
43. Cella ZF, Lavagnino Z, Perrone DM et al (2011) Live-cell 3D super-resolution imaging in thick biological samples. Nat Methods 8:1047–1049
44. Rayleigh L (1896) On the theory of optical images, with special reference to the microscope. Philos Mag 42:167–195
45. Huang B, Wang W, Bates M et al (2008) Three-dimensional super-resolution imaging by stochastic optical reconstruction microscopy. Science 319:810–813
46. Shannon CE (1949) Communication in the presence of noise. Proc Inst Radio Eng 37: 10–21

Chapter 15

Optogenetics: Optical Control of a Photoactivatable Rac in Living Cells

Taofei Yin and Yi I. Wu

Abstract

Recent developments in optogenetics have extended optical control of signaling to intracellular proteins, including Rac, a small G protein in the Rho family. A blue light-sensing LOV (light, oxygen, or voltage) domain derived from *Avena sativa* (oat) phototropin was fused to the N-terminus of a constitutively active mutant of Rac, via an α-helix (Jα) that is conserved among plant phototropins. The fused LOV domain occluded binding of downstream effectors to Rac in the dark. Exposure to blue light caused a conformational change of the LOV domain and unwinding of the Jα helix, relieving steric inhibition. The LOV domain incorporates a flavin as the photon-absorbing cofactor and can be activated by light in a reversible and repeatable fashion. In cultured cells, global illumination with blue light rapidly activated Rac and led to cell spreading and membrane ruffling. Localized and pulsed illumination generated a gradient of Rac activity and induced directional migration. In this chapter, we will describe the techniques in detail and present some examples of applications of using photoactivatable Rac (PA-Rac) in living cells.

Key words Optogenetics, Rho GTPases, Rac or Rac1, Photoactivatable, PA-Rac, LOV domain, Cell migration

1 Introduction

Signaling events inside a living cell are often subject to stringent spatial and temporal control. Such regulatory mechanisms are being increasingly appreciated because they are essential to achieve specificity in signaling transduction, preserve fidelity of cellular processes, and enable coordination between complex cellular behaviors. A thorough understanding of how cells accomplish this requires complementary methods both in measurement and perturbation. While increasing numbers of fluorescence imaging technologies are developed to resolve subcellular structures [1, 2] and to capture fast dynamics [3], the majority of methods of perturbation rely on global perfusion of pharmacological agents and slow genetic modifications such as RNAi and overexpression. A method of perturbation of signaling that achieves comparable spatiotemporal

Peter J. Verveer (ed.), *Advanced Fluorescence Microscopy: Methods and Protocols*, Methods in Molecular Biology, vol. 1251, DOI 10.1007/978-1-4939-2080-8_15, © Springer Science+Business Media New York 2015

resolution is needed. With the emergence of a research field called optogenetics [4], it became feasible to switch on or off specific signaling proteins with light at precise times and subcellular locations. For example, microbial channelrhodopsins are broadly applied in neuroscience to trace a transient firing of a single neuron to a map of functionally connected neuronal networks [5]. Similarly, engineering of light-induced gene expression [6–8] or protein-protein interactions [9] enables rewiring of signaling networks for synthetic biology applications. Despite these rapid developments, direct control of the activities of signaling proteins in optogenetics has been limited to homologous proteins such as ion channels [10] and GPCRs [11] due to the reliance on the existence of native photoreceptor homologues. The vast majority of intracellular signaling proteins remains out of reach.

The LOV (light, oxygen, or voltage) domain denotes a subgroup of the Per-ARNT-Sim (PAS) domains, named for homologous domains that occur within signaling proteins initially identified in *Drosophila* period circadian rhythm (Per), single-minded (Sim), and the vertebrate aryl hydrocarbon receptor nuclear transporter (ARNT) [12]. Photochemistry studies of the LOV domain revealed that excitation of the flavin molecule leads to the formation of a covalent linkage between the C4(a) atom in the flavin and a thiol from a conserved Cys residue in the LOV domain. This reaction is reversible and undergoes recovery in the dark over seconds [13]. C-terminal to the LOV domain in plant phototropin is an α-helix (named Jα) that is docked on the β-sheet of the LOV domain. Upon light illumination, the LOV domain undergoes conformational changes including dissociation and unwinding of a C-terminal helical extension (Jα) [14]. We tethered these sequences to the N-terminus of a constitutively active mutant of Rac, a member of the Rho family of small G proteins, so that the LOV domain sterically blocked its interactions with downstream effectors until illumination with blue light (*see* Fig. 1) This produced a genetically encoded photoactivatable analogue of Rac (PA-Rac) that enables precise modulation of Rac activity at regions that are submicrons in size and capable of controlling activation with microsecond precision in living cells and animals [15, 16]. Here we describe in detail how to apply the PA-Rac reagents in live cells and how conventional imaging systems can be customized to be compatible with such applications.

2 Materials

2.1 DNA Plasmids for PA-Rac and Its Controls

The majority of the DNA constructs used in the current protocol can be obtained from the addgene website (www.addgene.org, search for reagents from Dr. Klaus Hahn's laboratory) or from our

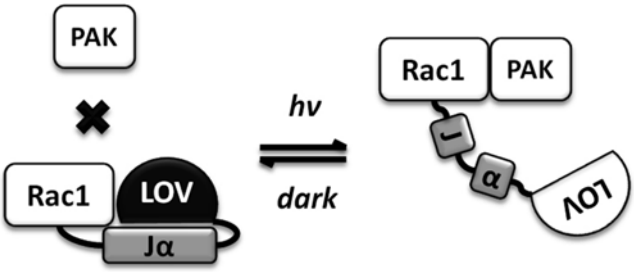

Fig. 1 Cartoon diagram of the photoactivatable Rac (PA-Rac). A LOV domain and its C-terminal Jα helix are fused to the N-terminus of a constitutively active mutant of Rac1 and block its interaction with downstream effectors (e.g., PAK) in the dark. Upon illumination, the Jα helix dissociates from the LOV domain and unwinds, restoring PAK binding and activation

Table 1
Available constructs of PA-Rac from addgene website or upon request

Vector:	pTriEx-4 (transient transfection) or pBabe-TetCMV-puro (stable cell line and inducible expression)
Fluorescent protein tags:	mCerulean, mVenus, or mCherry
Modifications of the LOV domain:	WT (photoactivatable), C450A and C450M (dark), or I539E (lit)
Modifications of Rac1:	Q61L/E91H/N92H (active) or T17N (dominant negative)

lab upon request (Table 1). PA-Rac contains the following protein sequences: LOV(404-546)-Rac(4-192, Q61L/E91H/N92H). Q61L is a constitutively active mutation in Rac that renders it GTP hydrolysis deficient. The mutations E91H and N92H were introduced empirically to disrupt Rac-GAP interactions. Overexpression of the LOV-Rac fusion that harbors only the Q61L mutation led to apparent membrane ruffles in cells in the dark, consistent with an elevated background of Rac activation. We speculated that this is due to a dominant-negative effect of this earlier construct on endogenous Rac because it may sequester GAP proteins. The GAP-binding mutations in PA-Rac resulted in improved binding of effector PAK in the light yet substantially reduced the background Rac activity in the dark.

We generated PA-Rac constructs with various fluorescent protein tags, including mCerulean, mVenus, and mCherry, to facilitate the identification of cells expressing PA-Rac in transient experiments. Based on the excitation wavelengths of these fluorescent proteins, mCherry (~590 nm) can be monitored without concern for excitation of the LOV domain. The standard commercial excitation filters for mVenus pass light below 500 nm which can activate the LOV domain. As a result, we recommend using different, somewhat suboptimal, excitation filters that blocks transmission below 510 nm, together with imaging routines that use attenuated excitation intensity and brief exposure time, to avoid unintended photoconversion of the LOV domain. Because the excitation wavelength of mCerulean (433 nm max) falls in the photoactivation spectrum, fluorescence imaging of mCerulean is best used for confirmation of expression at the end of experiments.

For transient transfections, plasmids in pTriEx-4 vector (Novagen) should be used. Alternatively plasmids in tetracycline-inducible expression (Tet-Off) retroviral vector pBabe-TetCMV-puro can be used to generate cell lines that have stable expression. With retroviral gene delivery, lower but more uniform expression of PA-Rac can be achieved, which is beneficial in obtaining consistent photoactivation responses among different cells. The inducible expression system is of favor because of the lack of expression of PA-Rac in cells in the presence of low concentration of doxycycline in the medium. The cells can be maintained and passaged in the light without worrying about unintended photoactivation. We recommend using the included fluorescent protein tag to gauge expression level, determining optimum expression for light-induced Rac activation with minimal background activity in the dark. The expression level, if needed, can be further controlled through titration with different concentrations of doxycycline. Alternatively, populations of stable cells with optimal expression level can be isolated using fluorescence activated cell sorting (FACS).

2.2 Cell Culture, Transfection, and Retroviral System

1. HeLa, mouse embryonic fibroblast (MEF), and LinXE cells are maintained in high-glucose DMEM supplemented with 10 % fetal bovine serum (FBS), GlutaMAX, and Pen/Strep (Invitrogen). For convenience, we use a prior established Tet-Off MEF cell line (Clontech) that stably expresses tetracycline transactivator (tTA). When the Tet-Off cell line is not available, coinfecting other murine cells with retroviral particles produced from the plasmid pRev-Tet-Off (Clontech) may be necessary. The Tet-Off MEFs are maintained in above culture medium with 100 μg/ml of G418 for drug-resistance selection of the tTA gene. LinXE is a HEK293-derived retroviral producer cell line. It stably expresses packaging and envelope proteins for the production of ecotropic, MoMuLV-based retroviruses that infect dividing murine (mouse and rat) cells. LinXE cells are maintained in above medium with 100 μg/ml of hygromycin.
2. X-tremeGENE (Roche) and Opti-MEM I reduced serum medium (Invitrogen) are needed for transient transfection.
3. Medium 199 without phenol red (Invitrogen) or F-12K nutrient mixture without phenol red (custom made from Invitrogen) is used in epifluorescence imaging.

4. 25 mm round coverslips that are cleaned with detergent and by sonication. After extensive rinsing, the coverslips can be stored in 70 % ethanol in a sealed jar.
5. A stock solution (10,000×) of doxycycline (Clontech) at 100 μg/ml is prepared for switching off protein expression in Tet-Off MEFs and a stock solution (1,000×) of puromycin (Gold Biotechnology) at 10 μg/μl for selection of stable cells after retroviral infection.
6. 2× HBS (HEPES-buffered saline): 50 mM HEPES, 280 mM NaCl, and 1.5 mM Na_2HPO_4, adjust pH exactly to 6.95 with HCl. Sterile filter the solution through 0.2 μm filter and store at 4 °C.
7. 2 M $CaCl_2$. Filter sterilize through 0.2 μm filter and store at 4 °C.
8. 0.45 μm PES filter and 5 ml syringes with luer lock.
9. Polybrene (Sigma) stock solution (1,000×) at 6 mg/ml.

Other common reagents for cell culture can be obtained from Invitrogen. Additional reagents for specific imaging applications will be described in Subheading 3.

2.3 Illumination Control and Microscope Customizations

Localized illumination with precise computer control can be accomplished using most laser scanning confocal microscopes, and applications using PA-Rac on these systems should be relatively straightforward (*see* **Note 1**). Alternatively, localized illumination can be achieved using most conventional wide-field microscopes that have a field stop/diaphragm in place or can be modified to incorporate a pinhole in a conjugate image plane. The broad-spectrum light source used for epifluorescence excitation can be used to illuminate a small region of the cell. Commercial vendors have devised a variety of add-on solutions for laser irradiation of small portions of the field of view, usually for FRAP studies. A laser beam can be coupled into the light path and focused on the focal plane to a diffraction-limited spot or dilated to bigger areas through z offset. These spots can also be mobilized to scan across different shapes either manually or using galvanometer-driven mirrors. Complex patterns can be achieved using digital micromirror-based devices such as the commercially available Mosaic active illumination system (Andor) or more advanced methods based on liquid-crystal spatial light modulators, realized in applications involving laser tweezers [17] and adaptive optics [18]. We opted for the Mosaic active illumination system because of its ability to simultaneously illuminate multiple regions of interest and fast switching time. One of the concerns with this method is insufficient intensity output. Because the LOV domain has a reasonable extinction coefficient ($\varepsilon_{449} = 12,\ 200\ \text{mol}^{-1}\ \text{cm}^{-1}$) but high quantum yield (0.44) [19], we found that even collimated consumer LED light source (<1 W output) can induce membrane protrusion in live cells upon brief (seconds), localized illumination. We found that recent versions (TE2000 and Ti) of Nikon inverted epifluorescence microscopes are convenient for such applications because they have a "stage-up" design (*see* **Note 2**), proven advantageous over systems from other microscope manufacturers. The stage-up design allows an ideal incorporation of the Mosaic system so that epifluorescence excitation and Mosaic active illumination can be incorporated independently in the infinity space between objective and camera. Two motorized turrets for filter blocks also permit rapid and independent control of filter settings for imaging and photoactivation (*see* Fig. 2). Additional components needed for the customization of such an imaging system are:

1. LED light source to be mounted on the Mosaic active illumination system: a high-power LED (Thorlabs) at 455 nm wavelength, with a power output rated at 900 mW, and with a beam collimator and an adapter to the Mosaic system.

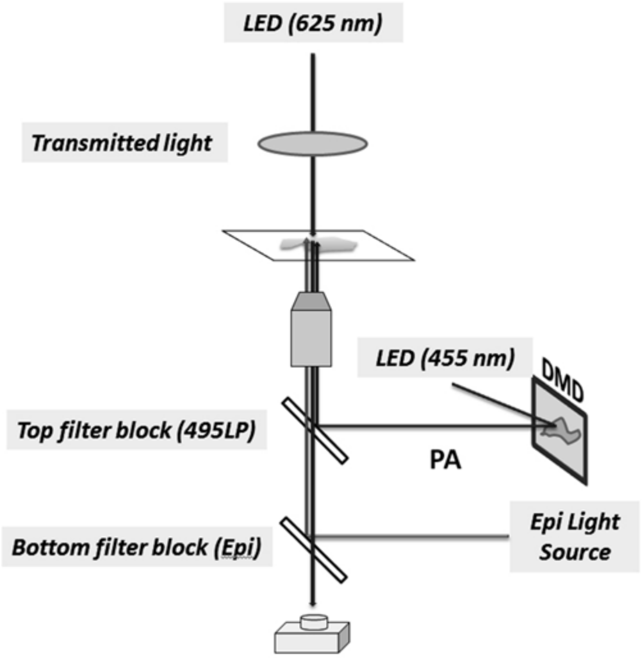

Fig. 2 Schematic diagram of customization of an epifluorescence microscope for application of PA-Rac. A digital micromirror device (DMD) is used to generate active spatial patterns of illumination. The DMD is coupled to the image conjugate plane of the microscope and reflects a collimated light beam from a high-power LED source (455 nm) which activates the LOV domain. An additional dichroic mirror (495LP) is inserted in the infinity space of the conventional epifluorescence imaging path to incorporate the activation light beam. The transmitted light source, typically halogen, is replaced with a red light-emitting (625 nm) high-power LED to avoid activation of the LOV domain during acquisition of DIC images

2. Modification of transmitted light: replace the halogen light source with a high-power LED (Thorlabs) at 625 nm wavelength, with a power output rated at 440 mW, and with a beam collimator and an adapter to the transmitted lamp house.
3. LED DC current drivers with TTL inputs (Thorlabs) and a DAQ board for shutter-free switching of LEDs using TTL outputs (NI, USB-6259).
4. A 495LP dichroic mirror is installed in the top filter block to reflect the photoactivation beam “shaped” by the Mosaic system to the samples while passing excitation and emission at longer wavelengths during image acquisition. Because the LEDs have well-confined spectrum range (~20 nm full width at half maximum (FWHM)), it was unnecessary to use cleanup filters in front of the LEDs in our hands.

We also installed a small CO_2 incubator near the microscope in the darkroom and yellow or red consumer LEDs (PAR38) for darkroom lightings for convenience in sample handling.

3 Methods

3.1 Transient Expression of PA-Rac in HeLa Cells

1. Day 1: trypsinize a well-maintained stock of HeLa cells, and seed the cells at 30–50 % confluency in a 35 mm culture dish in the morning. The cells should adhere and spread within a few hours and will be ready for transfection at the end of the day.
2. At the end of day 1, prepare transfection of PA-Rac constructs using X-tremeGENE DNA transfection reagent according to manufacturer’s instructions. Briefly, 0.25 μg of PA-Rac DNA plasmid and 3 μl of X-tremeGENE reagent are added sequentially to 100 μl of Opti-MEM in a 0.5 ml centrifuge tube. Gently mix the solution by tapping the tube and briefly centrifuge the tube at low speed, followed by incubation at room temperature for 30 min.
3. Add the DNA mix dropwise onto the cells covering different areas of the 35 mm culture dish, and gently rock the dish horizontally to help spread the DNA mix onto cells. Replace the culture dish back in the incubator until day 2.
4. Pick a 25 mm round coverslip that was previously cleaned. Rinse the coverslip with PBS for three times in a new 35 mm culture dish and flip the coverslip with a pair of forceps between washes to remove residue amount of ethanol trapped underneath the coverslip. Add 2 ml of 10 μg/ml fibronectin in PBS and move the culture dish on a rocker and incubate with gentle shaking at 4 °C overnight.
5. Day 2: first thing in the morning, check transfection efficiency and expression level of PA-Rac by monitoring the fluorescent

protein tag using a tissue culture microscope equipped with epifluorescence. Take out the culture dish containing the fibronectin-coated coverslip and rinse briefly with PBS at room temperature. Trypsinize the transfected cells and seed them at 10–20 % confluency on the coated coverslip. Move the culture dish to the incubator located in the dark room where the imaging system is located (*see* **Note 3**).

6. Warm up imaging medium and equilibrate it with CO_2 in the same incubator until imaging.

3.2 Viral Production and Infection, and Inducible Expression of PA-Rac

1. In the morning of day 1, passage well-maintained LinXE cells at 70–90 % confluency into a 60 mm culture dish with 4 ml medium.
2. At the end of day 1, set up calcium-phosphate transfection of viral constructs. Equilibrate plasmid, buffers, and sterile water to room temperature before mixing the solutions. Add 300 μl of 2× HBS in a polystyrene tube.
3. Prepare DNA mix (final volume 300 μl) in a 0.5 ml centrifuge tube as follows: 10 μg pBabe-TetCMV-puro plasmid, dilute DNA with sterile water to 262.5 μl, add 37.5 μl 2 M $CaCl_2$, and mix gently.
4. Add DNA mix dropwise to the polystyrene tube containing 2× HBS while vortexing the polystyrene tube at low speed. Incubate the mixture at room temperature for 30 min. The solution should become cloudy due to DNA-calcium phosphate complex formation.
5. Briefly vortex the DNA-calcium phosphate complex and add dropwise onto LinXE cells.
6. In the morning of day 2, the LinXE cells should become highly fluorescent. Replace the medium with 2 ml fresh culture medium. Note that the supernatant already contains infectious virus particles and safety procedures for retroviral production should be in place.
7. At the end of day 2, also seed MEF-Tet-Off cells at 50 % confluency in a 35 mm culture dish.
8. Day 3: collect the first round of viral supernatant and add 2 ml fresh medium to the cells for the second round collection. Centrifuge the supernatant at 1,500 ×*g* for 5 min to remove cell debris and pass the supernatant through a 0.45 μm PES filter using a 5 ml syringe.
9. Add polybrene to the viral supernatant at a final concentration of 6 μg/ml. After briefly mixing, replace the culture medium of MEF cells with the viral supernatant and incubate overnight.
10. Day 4: check whether the MEF cells start expressing fluorescent protein markers. Depending on viral titer, one round of

infection may be sufficient. The maximal expression level may be achieved between 24 and 48 h after infection. If necessary, a second or up to third round of infection can be performed by repeating **steps 8** and **9** with the transfected LinXE cells.

11. Replace with fresh medium and proceed with **steps 5** and **6** in Subheading 3.1 for imaging experiments. Alternatively, the expression can be switched off for long-term culture (*see* **Note 4**) by adding doxycycline at a final concentration of 10 ng/ml. Expression can be restored by passaging cells into doxycycline-free medium and incubate for 24–48 h.

3.3 Photo Manipulation of PA-Rac in Living Cells

3.3.1 Global Illumination to Induce or Inhibit Rac Activity

Global illumination of cells expressing PA-Rac or its variants can be conveniently achieved by exposing the culture dish to ambient light or designated light source with ample irradiance in the blue light range to induce (PA-Rac) or inhibit (T17N) Rac activity. The C450A or C450M mutants can be used in these experiments as light-insensitive controls. The cells can be lysed for biochemical analysis or can be fixed after a brief dose of irradiation, followed by standard immunocytochemistry protocols that stain F-actin (fluorescently labeled phalloidin) or detect translocation and phosphorylation of proteins downstream of Rac. Alternatively, live-cell imaging experiments can be performed with global illumination using a motorized epifluorescence microscope. We found that traditional mercury Arc lamp used in epifluorescence has sufficient irradiance in the blue light range. Photo cytotoxicity can be minimized by using a standard filter for cyan fluorescent protein (CFP) or green fluorescent protein (GFP) excitation and neutral density filters. Depending on the power of the light source, the expression level of PA-Rac, and how sensitive the cells used are to Rac activation, the illumination can be applied as milliseconds or seconds of pulses or constant during image acquisition. Because the LED transmitted light source has a well-defined emission range (625/17 nm FWHM) that is distant from the absorption spectrum of the LOV domain, we typically acquire DIC images at high frame rate (2–10 frames/s) to capture the dynamics of cell shape changes without interfering activation of the LOV domain. We found that 10–20 min post illumination is sufficient for capturing cellular response to Rac activation with an initial cellular response becoming apparent within 30 s, although we typically acquire equal duration/numbers of images prior to illumination to set the background cellular activity. The DIC images can be assembled to time-lapse movies for viewing or analyzed in kymograph for activities of membrane protrusion and retraction using line scans at regions of interest.

3.3.2 Precise Spatial and Temporal Control of Photoactivation

As described before, limited spatial control can be implemented using the field diaphragm or pinholes in an image conjugate plane. By modulating illumination intensity, low-intensity excitation light at a “safe” wavelength can be used to target and shape the illumination, followed by high-intensity illumination below 500 nm to activate protein. Acquisition and analysis of DIC images can be conducted at cellular regions near the site of illumination, using other parts of the cell body as control regions. Because of the impact of active Rac on actin dynamics, mCherry-actin or Lifeact-mCherry [20] can be used to aid detection of Rac activation. To analyze Rac initiation of downstream signaling, we also tracked translocation of downstream effectors. For wide-field microscopy, artifacts of changing cell volume were avoided using ratiometric imaging. The fluorescence intensity of the tagged target protein was divided by the fluorescence intensity of a separately expressed volume indicator, i.e., yellow fluorescent protein (YFP) or mCherry. As demonstrated previously [15], PA-Rac redistributed slowly out of sites of illumination with a diffusion coefficient of 0.55 $\mu m^2/s$. This led to detectable accumulation of downstream effectors where Rac was activated. Phosphorylation of endogenous PAK can also traced using immunofluorescence of fixed cells after local activation of PA-Rac (*see* Fig. 3). MEF cells stably expressing PA-Rac were plated onto special coverslips with etched grids and numbers (Bellco). The grids and numbers are visible through a 20× phase-contrast objective and can be used to locate the cells that had been irradiated. Cells can be locally illuminated. Immediately after protrusions were induced, the cells were fixed in 3.7 % formalin (Sigma), permeabilized in 0.2 % Triton X-100, incubated with anti-phospho-PAK antibody (Cell Signaling), and finally incubated with Alexa Fluor 594-conjugated secondary antibody (Molecular Probes).

4 Notes

1. The action spectrum of plant phototropin is in the UV-A and blue light range (360–500 nm). We tested several common laser lines for their ability to induce membrane ruffles in MEF cells expressing PA-Rac. The wavelengths 405, 458, 473, and 488 nm all proved to be effective. The power dosage of the PA-Rac to 458 nm line was measured in stable MEF cell lines, where expression levels could be well controlled and the areas of induced protrusions readily measured. A light dose of 6.2 μJ over a 10 μm spot at 458 nm induced a cellular response with a single exposure. This was the lowest power setting (0.1 % of total power on the mW scale) of our Fluoview 1000 confocal microscope at very fast scan rate (10 μs/pixel). Following this exact photoactivation regime but with increasing laser power or scan duration, we determined that the cellular response (protrusion area) stopped increasing when we reached 1,000-fold higher dose.

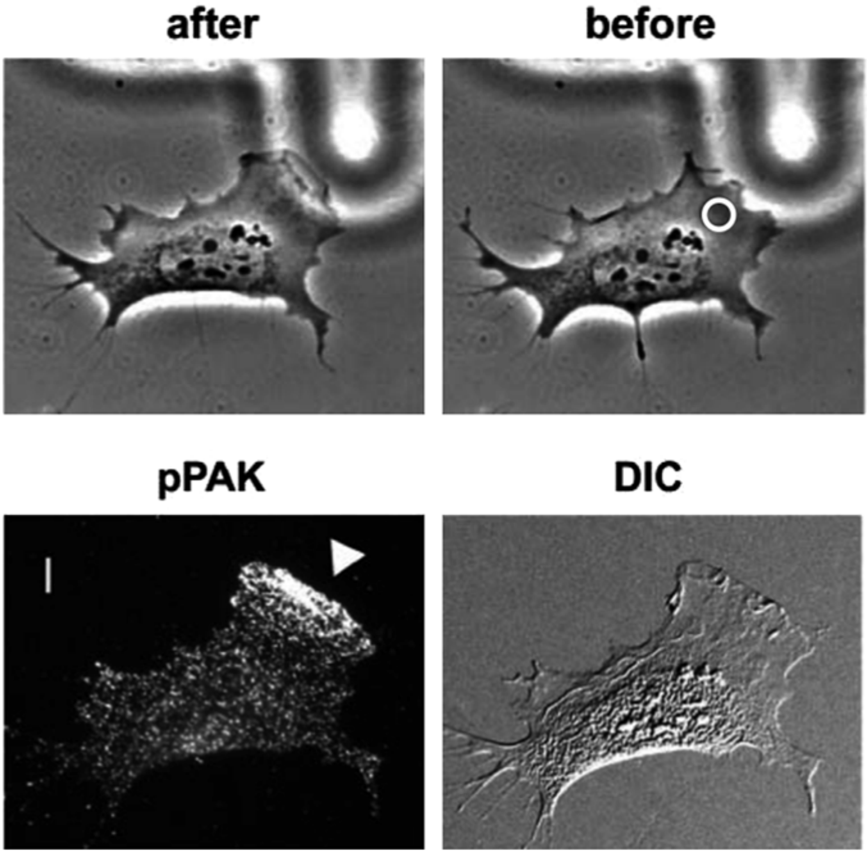

Fig. 3 Local photoactivation of PA-Rac followed by immunocytochemistry. MEF cells expressing mVenus-PA-Rac were plated onto special coverslips that have photoetched grids of numerically labeled squares and were locally irradiated at 473 nm (*white circle*) to generate protrusion (phase-contrast images shown before and after irradiation). The cells were immediately fixed and stained for phospho-PAK. The numbers on the etched grids were used to locate irradiated cells after fixation (DIC). The acute staining of phospho-PAK (*arrowhead*) at PA-Rac-induced protrusions indicates local PAK activation (pPAK). Scale bars, 10 μm

2. The "stage-up" configuration of Nikon microscope refers to an elevated nosepiece (objectives) and sample stage that permit installation of an additional filter block turret in the infinity space of a microscope, benefiting from the use of infinity-corrected objectives.
3. Because of the light sensitivity of the LOV domain, cells expressing PA-Rac should not be exposed to light within the LOV action spectrum (<500 nm) immediately before imaging experiments. It is safe to prepare live samples under yellow or red light, which can be implemented in dark rooms. Even light emitted from bright computer monitors can be of concern, but this is less consequential at a distance. We transferred the cells immediately after transfection into incubators located in

isolated dark rooms to avoid unintended light exposure. In some experiments, extensive manipulations were required prior to imaging. When this was difficult in a dark room, cells could be incubated in the dark for an hour to reduce the effect of prior light exposure and restore responsiveness to photoactivation.

4. For reasons that remain unclear to us, MEF cells selected for stable expression of PA-Rac appeared to downregulate the activity of endogenous Rac, evidenced by the reduction of lamellipodia of these cells prior to induction of expression. In contrast we noticed an upregulation of Rac activity in PA-Rac-T17N overexpressing cells prior to induction of expression. This could be due to mechanisms of cellular compensation. Nevertheless, such phenomena seemed to enhance the effect of illumination to switch on or off Rac in living cells.

Acknowledgments

This work was supported by NIH grant NS071216 and UCHC start-up funds.

References

1. Hell SW (2009) Microscopy and its focal switch. Nat Methods 6:24–32
2. Betzig E, Patterson GH, Sougrat R et al (2006) Imaging intracellular fluorescent proteins at nanometer resolution. Science 313: 1642–1645
3. Salomé R, Kremer Y, Dieudonné S et al (2006) Ultrafast random-access scanning in two-photon microscopy using acousto-optic deflectors. J Neurosci Methods 154:161–174
4. Deisseroth K, Feng G, Majewska AK et al (2006) Next-generation optical technologies for illuminating genetically targeted brain circuits. J Neurosci 26:10380–10386
5. Deisseroth K (2011) Optogenetics. Nat Methods 8:26–29
6. Shimizu-Sato S, Huq E, Tepperman JM et al (2002) A light-switchable gene promoter system. Nat Biotechnol 20:1041–1044
7. Kennedy MJ, Hughes RM, Peteya LA et al (2010) Rapid blue-light-mediated induction of protein interactions in living cells. Nat Methods 7:973–975
8. Wang X, Chen X, Yang Y (2012) Spatiotemporal control of gene expression by a light-switchable transgene system. Nat Methods 9: 266–269
9. Levskaya A, Weiner OD, Lim WA et al (2009) Spatiotemporal control of cell signalling using a light-switchable protein interaction. Nature 461:997–1001
10. Nagel G, Szellas T, Huhn W et al (2003) Channelrhodopsin-2, a directly light-gated cation-selective membrane channel. Proc Natl Acad Sci U S A 100:13940–13945
11. Airan RD, Thompson KR, Fenno LE et al (2009) Temporally precise in vivo control of intracellular signalling. Nature 458:1025–1029
12. Möglich A, Ayers RA, Moffat K (2009) Structure and signaling mechanism of Per-ARNT-Sim domains. Structure 17:1282–1294
13. Swartz TE, Corchnoy SB, Christie JM et al (2001) The photocycle of a flavin-binding domain of the blue light photoreceptor phototropin. J Biol Chem 276:36493–36500
14. Harper SM, Neil LC, Gardner KH (2003) Structural basis of a phototropin light switch. Science 301:1541–1544
15. Wu YI, Frey D, Lungu OI et al (2009) A genetically encoded photoactivatable Rac controls the motility of living cells. Nature 461:104–108
16. Wang X, He L, Wu YI et al (2010) Light-mediated activation reveals a key role for Rac in

collective guidance of cell movement in vivo. Nat Cell Biol 12:591–597

17. Curtis JE, Koss BA, Grier DG (2002) Dynamic holographic optical tweezers. Opt Commun 207:169–175
18. Girkin JM, Poland S, Wright AJ (2009) Adaptive optics for deeper imaging of biological samples. Curr Opin Biotechnol 20:106–110
19. Salomon M, Christie JM, Knieb E (2000) Photochemical and mutational analysis of the FMN-binding domains of the plant blue light receptor, phototropin. Biochemistry 39:9401–9410
20. Riedl J, Crevenna AH, Kessenbrock K et al (2008) Lifeact: a versatile marker to visualize F-actin. Nat Methods 5:605–607

INDEX

Peter J. Verveer (ed.), *Advanced Fluorescence Microscopy: Methods and Protocols*, Methods in Molecular Biology, vol. 1251, DOI 10.1007/978-1-4939-2080-8, © Springer Science+Business Media New York 2015